Understanding volcanic processes using satellite remote sensing and multi-hazard modelling at Manam volcano, Papua New Guinea

Adam Cotterill

University College London

PhD Volcanology

I, Adam Cotterill confirm that the work presented in this thesis is my own. Where information has been derived from other sources, I confirm that this has been indicated in the thesis.

Abstract

Manam is a frequently active open-vent volcano in Papua New Guinea capable of both explosive and effusive eruptions. Ground-based monitoring is challenging due to steep topography, tropical island conditions and frequent eruptions. Remote sensing observations and probabilistic hazard simulations therefore present valuable resources for monitoring and risk reduction at Manam. This thesis aims to: (a) improve understanding of the volcanological processes governing the observed activity at Manam and open-vent systems generally, and (b) quantify the potential spatial distribution of lava flows and tephra deposition and their impact on human activity.

Using satellite remote sensing of thermal and sulphur dioxide emissions and observations of activity, this thesis quantifies Manam's magma budget and variations in excess degassing through time. From these time series, four distinct phases of volcanic activity are identified between 2018 and 2021. This thesis proposes that eruptive activity at Manam during the study period was driven by the injection and eruption of a volatile-rich recharge magma. In this conceptual model, initial eruptions in August 2018 removed previously degassed magma to re-open the conduit and promote efficient fluxing of volatiles through the shallow magmatic system, accounting for the elevated SO_2 fluxes (4.72 kt day^{-1}) observed in May-June 2019. The subsequent eruptions may have been triggered by the formation and eventual failure of conduit plugs formed by degassing-driven dehydration crystallization.

Probabilistic hazard modelling of tephra deposition and lava flow emplacement have been undertaken using *TephraProb* and *Q-LavHA* respectively to constrain the potential exposure of people and assets to these hazards for a range of observed eruption scenarios. Combining simulation results with mapped infrastructure and population data provides insight into the possible impacts of future eruptions at local and regional levels. Consequently, this thesis examines the implications of these results for developing emergency protocols and strategies to improve resilience to Manam's eruptions.

Impact Statement

Volcanic eruptions are capable of directly impacting areas hundreds of kilometres away with an estimated 800 million people estimated to live within 100 km of an active volcano. This intersection of society and volcanic landscapes has many benefits but also places these communities at risk from the effects of eruptions.

This thesis aims to improve the understanding of the processes driving the open-vent volcanism at Manam volcano in Papua New Guinea and assess the hazard posed by ash fall and lava flows from its eruptions. The persistent activity exhibited by open-vent volcanoes presents an opportunity for volcanologists to study, over extended periods, the processes which drive volcanic eruptions. This research has implications at local and regional levels where the insights into the behaviour can aid forecasting of future eruptions and the hazard analysis can be incorporated into emergency planning and efforts to increase resilience of the population and infrastructure. This work also has global scale consequences due to the transferrable findings of volcanic processes to other volcanic systems where future eruptions threaten human life and activity.

A key component of this research is the use of open-access satellite remote sensing techniques to measure the thermal and sulphur dioxide (SO_2) emissions at Manam. This work demonstrates the utility of these methods at remote and inaccessible volcanoes where ground-based monitored may be difficult to not only monitor volcanic emissions but also interpret these signals alongside observed activity in the context of volcanological processes governing the activity.

Volcanoes are a component of the Earth's carbon cycle responsible for releasing carbon stored in the crust into the atmosphere. Carbon dioxide (CO_2) is a long-lived climate forcing atmospheric gas, or greenhouse gas, directly linked to the currently observed global warming. As a global societal issue it is paramount that the contributions of passive and eruptive volcanic activity is understood to prepare for the consequences of future climate change. Manam is one of the top volcanic emitters of CO_2 and so it is necessary to have accurate estimates of its contributions to atmospheric CO_2 levels. Previous estimates have been based on short-term field campaign measures of the volcanic gas plume composition whereby the ratio between CO_2 and SO_2 is used to calculate the CO_2 flux based on the more easily measurable SO_2 emissions. This work presents the first multi-annual SO_2 emission time series for Manam, which in turn has been used to estimated the mean CO_2 emissions over the different phases of observed degassing at Manam.

Overall this thesis presents a comprehensive view of the volcanic hazard posed by Manam at a local and regional level in confluence with new insights into the processes causing its eruptions. Additionally, these findings can be extrapolated for use at other volcanic systems worldwide as well as demonstrating the ability to gain such information at volcanoes where ground-monitoring is precluded. A new view of Manam's CO_2 emissions is also provided which is an important in the face of ongoing climate change due to increasing atmospheric CO_2 levels

UCL Research Paper Declaration Form

referencing the doctoral candidate's own published work(s)

Please use this form to declare if parts of your thesis are already available in another format, e.g. if data, text, or figures:

- *have been uploaded to a preprint server*
- *are in submission to a peer-reviewed publication*
- *have been published in a peer-reviewed publication, e.g. journal, textbook.*

This form should be completed as many times as necessary. For instance, if you have seven thesis chapters, two of which containing material that has already been published, you would complete this form twice.

1. For a research manuscript that has already been published (if not yet published, please skip to section 2)

a) **What is the title of the manuscript?**

b) **Please include a link to or doi for the work**

c) **Where was the work published?**

d) **Who published the work?** (e.g. OUP)

e) **When was the work published?**

f) **List the manuscript's authors in the order they appear on the publication**

g) **Was the work peer reviewed?**

h) **Have you retained the copyright?**

i) **Was an earlier form of the manuscript uploaded to a preprint server?** (e.g. medRxiv). If 'Yes', please give a link or doi)

If 'No', please seek permission from the relevant publisher and check the box next to the below statement:

☐

*I acknowledge permission of the publisher named under **1d** to include in this thesis portions of the publication named as included in **1c**.*

2. **For a research manuscript prepared for publication but that has not yet been published** (if already published, please skip to section 3)

   a) **What is the current title of the manuscript?**

Magma recharge at Manam volcano, Papua New Guinea, identified through thermal and SO_2 satellite remote sensing of open vent emissions

   b) **Has the manuscript been uploaded to a preprint server?** (e.g. medRxiv; if 'Yes', please give a link or doi)

https://doi.org/10.21203/rs.3.rs-3903120/v1

   c) **Where is the work intended to be published?** (e.g. journal names)

Bulletin of Volcanology

   d) **List the manuscript's authors in the intended authorship order**

Adam S. Cotterill, Emma J. Nicholson, Christopher R.J. Kilburn, Catherine S.L. Hayer

   e) **Stage of publication** (e.g. in submission)

Under Review

3. **For multi-authored work, please give a statement of contribution covering all authors** (if single-author, please skip to section 4)

A.S. Cotterill collected, processed, analysed and interpreted all data, and led the writing of the manuscript drafts. E.J. Nicholson contributed to data interpretation and provided written and verbal feedback on the manuscript. C.R.J Kilburn provided written and verbal feedback on the manuscript. C.S.L. Hayer provided code for processing and analysing satellite-retrieved SO_2 data and provided feedback on the manuscript.

4. **In which chapter(s) of your thesis can this material be found?**

Chapter Two – Insights into Manam's Open-Vent Processes Through Remote Sensing of Thermal and SO_2 Emissions

5. **e-Signatures confirming that the information above is accurate** (this form should be co-signed by the supervisor/ senior author unless this is not appropriate, e.g. if the paper was a single-author work)

Candidate	*Supervisor/ Senior Author*
Adam Cotterill	Emma Nicholson
Date:	*Date:*
20/03/2024	20/03/2024

Acknowledgements

I would like to acknowledge first and foremost Dr Emma Nicholson for taking me as your student based on little more than enthusiasm for volcanoes and then relentlessly pushing me to be better and think critically. With the project disrupted by the pandemic, you provided opportunities for me to realise the dreams of a 9 year old Adam of being a volcanologist working in the field, and for that I am especially grateful. I also extend my gratitude to Professor Christopher Kilburn who as my master's supervisor supported my PhD applications and offered valued advice and expertise throughout this ordeal. Further thanks go to Dr Alex Steele who joined the team in the latter stages but had, throughout the PhD, given guidance and well needed perspective which was needed regularly.

Special appreciation is given to my family Mark, Emma, David, Cerys, Ben and Rebecka, who have all encouraged me unceasingly during this endeavour and throughout my life, most especially my parents, who have always supported me along the paths I have chosen and were swifty there when I needed them most. I must recognise Jake, who has ever been my friend and ally, for driving me to persist working towards becoming a volcanologist, for the many memorable years living and adventuring together, and of course providing firm counsel. To Leah, who having burst onto the scene late in the game bringing me great happiness. Thank you for putting up with me as I got increasingly worn down and for ensuring I enjoyed myself even during the final and hardest portion of the PhD.

I next turn to the members of the UCL ES PhD office who have been along for the journey. I think especially of Lily, Will and Eve for the entertainment and discussing the "big" questions, Jonathan for all the deep talks, and my PhD big sister, Kate, who guided me through my initial floundering years. Finally, to the members of TRS, who above all others have shared the trials and tribulations of trying to do a PhD, this would have been an immeasurably less pleasurable experience without you all.

Table of Content

Table of Figures

Table of Tables

1 Chapter One - Introduction

1.1 Prelude

Volcanoes are perhaps the most charismatic geological feature found on Earth, and indeed within our solar system, with over 800 million people living within 100 km of an active volcanic system (Freire et al. 2019). Many choose to do so for reasons such as the agriculture benefits of fertile volcanic soils (Delmelle et al. 2015), religious beliefs and cultural connections surrounding volcanoes (Pardo et al. 2015; Wood et al. 2019a), access to geothermal energy (Shortall et al. 2015; Shortall and Kharrazi 2017) or in the case of volcanic islands, eruptive activity has created the land itself (Wilkinson et al. 2016). These beneficial aspects of volcanic landscapes however come with the threat from the multiple hazards posed by volcanoes. Volcanic hazards such as lava flows, pyroclastic flows and lahars can impact areas up to tens of kilometres from the erupting vent and tephra deposition from large eruptions can affect areas hundreds of kilometres from the eruption site (McGuire et al. 1995). The human impacts of volcanic eruptions include displacement, loss of livelihood, famine, wide ranging health impacts, and loss of life (Auker et al. 2013; Brown et al. 2015).

One such volcano is Manam, an open-vent island volcano approximately 10 km wide with an estimated population of 4,000-7,000 (James Sukua, Pers. Comms.; Sims et al., 2023) and is one of the most frequently active volcanoes in Papua New Guinea (PNG) (Palfreyman and Cooke 1976; Global Volcanism Program 2024). A complicated combination of socio-economic and historical circumstances mean that the residents of Manam have chosen to remain on the island despite often being impacted by the regular explosive and effusive eruptions (Mercer and Kelman 2010;

Connell and Lutkehaus 2017). Compounding this issue was the fact that Manam's on-island monitoring equipment was destroyed by an eruption in 2005 reducing the capability for the Rabaul Volcanological Observatory (RVO) to forecast eruptions (Global Volcanism Program 2005). Fortunately, during the course of this project seismic monitoring equipment was reinstalled on Manam itself (PNG Dept. of Minear Policy and Geohazards Management 2024) .

Typically, volcanic eruptions are often presaged by one, or a combination of, seismicity, surface deformation, degassing fluctuations or surface temperature increases depending on the whether the conduit is open or closed (Acocella et al. 2024). Volcanological monitoring equipment are able to detect pre-eruptive activity and are used to identify eruption precursory signals (Scarpa and Gasparini 1996; Pallister and McNutt 2015). Interpreting monitoring parameter signals can be complex and this is no less true for open-vent systems, like Manam, where precursory signals of the transition from regular activity to paroxysmal eruptions are difficult to identify (Rose et al. 2013; Vergniolle and Métrich 2021). Permanent monitoring allows for the establishment of baselines within these parameters, enabling improved identification of these precursory signals (McGuire et al. 1995; Neuberg 2006; Aiuppa 2015). Therefore monitoring systems are critical to mitigating the impact of volcanic eruptions, but the cost of monitoring equipment and installation, the inaccessibility of many volcanoes, and the risk when installing equipment means that most volcanoes globally are not comprehensively monitored (Wakeford et al. 2019).

The economic limitation often preventing volcanological monitoring is unfortunately compounded by the negative correlation identified between regional development and the number of fatalities caused by volcanic eruptions (Auker et al. 2013). Developing regions such as Indonesia, the Philippines, the eastern Caribbean, and Melanesia rank among the highest for historical volcanic fatalities globally (Auker et al. 2013; Jenkins et al. 2022). The improvement of volcanic monitoring capabilities and understanding potential volcanic hazards in economically developing nations are key factors in reducing the impact of eruptions by building effective community response and increasing resilience (Andreastuti et al. 2019).

Over the last 25 years the quality and accessibility of satellite-based remote sensing of thermal anomalies, gas emissions and ground deformation have bolstered the efforts of volcanologists to monitor and forecast volcanic eruptions (Blackett 2017; Furtney et al. 2018; Poland and Anderson 2020). Open-access online platforms such as *MODVOLC* (Wright et al. 2004; Wright 2016a), *MIROVA* (Coppola et al. 2016) and *MOUNTS* (Valade et al. 2019) automatically process these parameters for volcanoes globally allowing monitoring of non-instrumented volcanoes at a daily frequency.

The body of work seeks to demonstrate the utility of the open-access satellite remote sensing to investigate the volcanological processes responsible for the observed volcanic activity at Manam. This research employs open-source tephra deposition and lava flow models to assess the hazard associated with Manam's explosive and effusive eruptions. The remainder of this chapter will evaluate the literature surrounding mafic open-vent volcanism and volcanic hazard assessments. Manam will then be introduced as the case study volcano, its historical activity and

the impacts its eruptions have had on human activity. Finally, the outline of this thesis will be presented including the overarching project aims and objectives and those of the individual chapters.

1.2 Open-Vent Volcanism

The basic definition of an open-vent volcano is where a long-term direct connection between the magmatic plumbing system and the surface is maintained (Rose et al. 2013) and where outgassing persists alongside mild or low-intensity explosive activity between major eruptions (Andres and Kasgnoc 1998; Vergniolle and Métrich 2021; Edmonds et al. 2022a; Vergniolle and Métrich 2022). Open-vent volcanoes represent a small proportion of the active volcanoes globally (Siebert et al. 2011). However, open-vent volcanoes provide excellent insight into volcanological processes due to the ability to measure long-term timeseries from gas and thermal emissions, geophysical signals, surface activity (Edmonds et al. 2022a). Manam's open-vent state has persisted since at least the 1880s based on historical records and is speculated to go back as far as the 17th century based on accounts from European sailors (Palfreyman and Cooke 1976). Manam is consistently ranked as a top contributor to volcanic emissions globally (Carn et al. 2017; Aiuppa et al. 2019; Fischer et al. 2019a) yet the few studies focused on Manam published in the last 40 years (Mori et al. 1987; Weissel et al. 2004; Tupper et al. 2009; Liu et al. 2020a) investigate Manam's open-vent behaviour (McCormick et al. 2012; Liu et al. 2020a). Given that this research seeks to interpret the processes driving Manam's open-vent behaviour, the literature surrounding open-vent volcanism is here reviewed to allow it to be placed within this wider context.

1.2.1 Maintaining Open Conduits

Open-vent systems exist across the full range of magma viscosities and the manner in which they present at the surface is broadly dependent on viscosity (Rose et al. 2013). More viscous silicic magmas form plugs within the conduit which produce Vulcanian eruptions upon failure (e.g. Tungurahua (Ecuador) - Battaglia et al., 2019; Gaunt et al., 2020; Hall et al., 2015, and El Reventador (Ecuador) - Vásconez et al., 2022) or these magmas can extrude magma to form lava domes that can fail producing Pyroclastic Density Currents (PDCs) and Vulcanian eruptions (e.g. Nevado Del Ruiz (Colombia) - Lages et al., 2024, Popocatépetl (Mexico) - Campion et al., 2018; Gómez-Vazquez et al., 2016, La Soufriere (St Vincent and the Grenadines) - Brazier et al., 1982; Girona et al., 2021, and Soufriere Hills (Montserrat) - Cole et al. 1998; Young et al. 1998). Less viscous mafic magmas are capable of sustaining lava lakes (e.g. Kilauea (Hawaii, USA) - Patrick et al., 2019, Masaya (Nicaragua) - Aiuppa et al., 2018; Pering et al., 2019, Villarrica (Chile) - Liu et al., 2019; Moussallam et al., 2016, Nyiragongo (D.R. Congo) - Barrière et al., 2022; Burgi et al., 2014, Ambrym (Vanuatu) - Firth and Cronin, 2023; Shreve et al., 2022, Yasur (Vanuatu) - Woitischek et al., 2020, Erebus (Antarctica) - Davies et al., 2008; Grapenthin et al., 2022, and Erta Ale (Ethiopia) - Oppenheimer et al., 2004; Spampinato et al., 2008), exposed magma columns (e.g. Manam (PNG) - Liu et al., 2020, Stromboli (Italy) - Vergniolle and Métrich, 2022), or most commonly those that emitting large fluxes of gas (e.g. Bagana (PNG) - McCormick Kilbride et al., 2019, and Etna (Italy) - Aiuppa et al., 2007; Laiolo et al., 2022, 2018).

Lava domes and conduit emplaced plugs are semi permeable allowing the movement of volatiles from the molten conduit to the surface (Gaunt et al. 2014; Calder et al. 2015a; Gaunt et al. 2016). All expressions of open-vent volcanism maintain an open conduit between eruptions and therefore a mechanism providing heat to maintain the liquid state of column magma is required. Three models for this temperature conservation are currently considered as viable explanations.

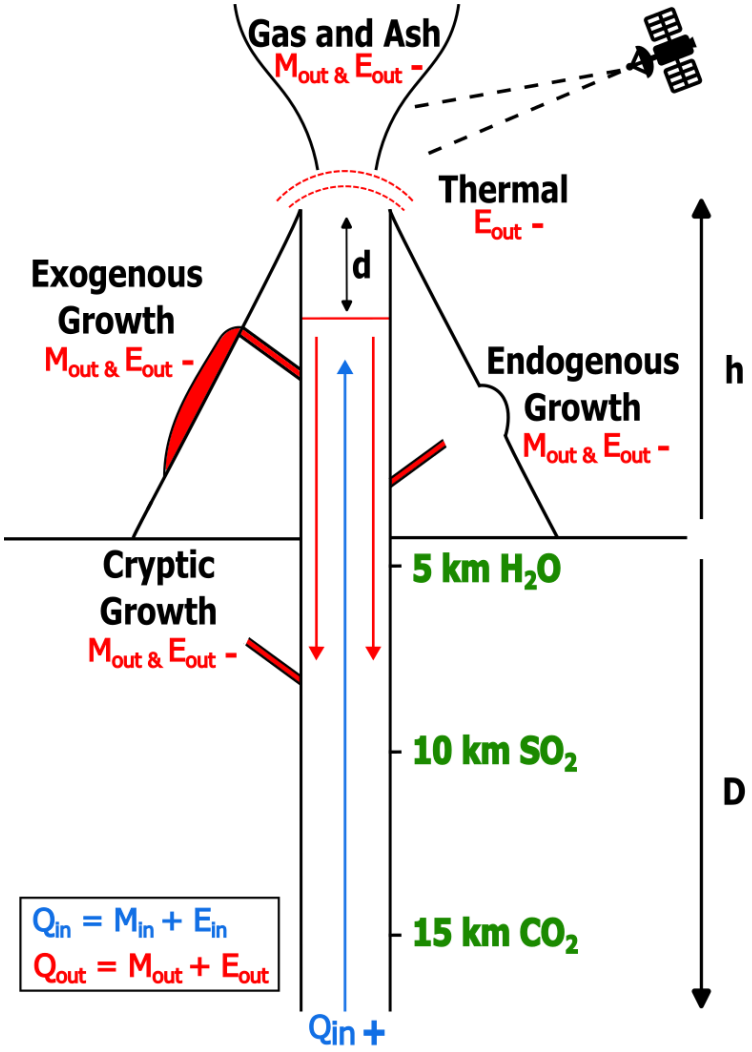

Figure 1.1 A simplified schematic of an open vent volcanic system showing the volcanic edifice height (h), subsurface magmatic system depth (D), and the height of the magmatic column within the conduit (d). Mass (M_{in}) and energy (E_{in}) enter the system in the form of magma (Q_{in}) from depth. Mass (M_{out}) and energy (E_{out}) leaves the system (Q_{out}) through eruption (exogenous growth), intrusion within the volcanic edifice (endogenous growth), or sub-edifice emplacement (cryptic growth). Energy can also be lost by radiated thermal energy with the cooled denser magma sinking to be replaced by less dense hotter magma. Thermal and gas emissions can be measured and used to interpret the mass balance within a volcanic system. Gas composition provides insight into the depth of magmatic degassing and thus the system's eruptive potential

The first and most widely invoked model is that of bi-directional flow where less dense, volatile-rich hot magma ascends replacing the descending more dense, volatile-poor cool magma first proposed by Kazahaya (1994). Magma ascends due to its lower density than the magma above due to its volatile content and the buoyancy affects of exsolved volatiles. As it reaches the upper reaches its volatiles more easily exsolve and this degassed magma now has increased density and in turn sinks to be replaced by fresh magma (Kazahaya et al. 1994; Shinohara 2008; Beckett et al. 2014) (**Figure 1.1**). Experiments have shown that this convective exchange most readily takes the form of a core-annular flow (Stevenson and Blake 1998; Huppert and Hallworth 2007). The exact form of core-annular flow has been shown to be dependent on the viscosity difference between the upwelling and downwelling magmas (Stevenson and Blake 1998). At low viscosity ratios, the descending magma initially flowing in the annulus, along the walls, but detaches midway down the conduit and flows down the core, while the ascending magma moves within the annulus. At higher ratios the descending magma separates into parcels or blobs in the centre of the conduit. At even higher ratios descending magma flows down within the annulus the full length of the conduit, leaving the ascending magma to rise via the core. Further experiments by Hupper and Hallworth (2007) and Becket et al. (2011) identified that a side-by-side flow could form at lower viscosity ratios where both the ascending and descending magma had contact with the conduit wall and one interface between the magma bodies. A transitional side-by-side flow was also found to occur at very low viscosity ratios where core-annular flow occurred in the upper conduit simultaneously with side-by-side flow in the lower conduit (Beckett et al. 2011).

A second model, proposed by Witham et al. (2006), suggests a fluctuating uni-directional flow where volatile-rich magma ascends while volatile-poor magma descends, but critically either the upward or downward flow dominates at any given time. This model specifically attempts to explain the maintenance of lava lakes. While up-flow dominates, the lake fills until reaching a critical depth where the magmastatic pressure (hydrostatic pressure in the experiments) begins to slow the up-flow rate until gas slugs form. These reduce the gas content of the magma when escaping at the surface and allows down-flow to dominate which drains the lake until up-flow reasserts itself due to the decreased magmastatic pressure. This model has so far been shown to be inconsistent with strong gas-driven drainage events at Kilauea's lava lakes (Orr and Rea 2012; Patrick et al. 2016; Moussallam et al. 2016). This may however be a valid explanation for the fluctuations in the height of exposed magma columns but this connection has not yet been made.

The third model hypothesised by Bouche et al. (2010) posits that a bubbly wake forming behind a larger spherical cap gas slug detach from the slug within the lava lake transferring heat to the lake. This model does not require a convective downflow of magma and relies totally on volatiles migrating from deeper sources. It is possible that these three models may be superimposed upon one another likely on different timescales, and should theoretically be distinguishable in the field based on observed gas emissions (Moussallam et al. 2016).

Much of this work deciphering the flow regimes providing sustained heat to open-vent volcanoes is focused on lava lakes (Davaille and Jaupart 1993; Oppenheimer et al. 2004; Harris et al. 2005; Harris 2008; Pering et al. 2019; Campion and Coppola

2023) and strongly degassing non-plugged systems (Kazahaya et al. 1994; Palma et al. 2011; Beckett et al. 2014; Coppola et al. 2022)(**Figure 1.1**). Lava domes are at a basic level slow extrusion of highly viscous magma and the associated continual ascent of magma that feeds the extrusion maintains the open-vent (Melnik and Sparks 2005; Husain et al. 2018). What is yet unclear is what mechanisms maintain heat supply in transiently plugged open-vent systems (Diller et al. 2006; Hall et al. 2015). For example whether bi-directional flow continue beneath the plug driving increasing pressure or does it cease allowing other processes to dominate until the plug fails (Gaunt et al. 2020).

1.2.2 Persistent Degassing

An open-vent provides a direct connection between shallow magma storage and the atmosphere therefore facilitating the free movement of volatiles to the surface. Persistent degassing is a key characteristic of open-vent volcanism across the compositional spectrum (Rose et al. 2013; Edmonds et al. 2022a; Vergniolle and Métrich 2022). Indeed, all three of the models discussed in the previous section explaining the maintaining of open conduits all in some respect aree controlled by magmatic volatile content or the exsolved volatiles themselves (Stevenson and Blake 1998; Witham et al. 2006; Huppert and Hallworth 2007; Bouche et al. 2010).

A common aspect of persistently degassing open-vent systems is that the volume of magma required to supply the observed volatile flux exceeds the volume of magma erupted, commonly referred to as the “excess degassing phenomenon” (Kazahaya et al. 1994; Shinohara 2008). The fate of the unerupted degassed magma is most

often explained by conduit convection (Kazahaya et al. 1994; Edmonds et al. 2010; Palma et al. 2011; Beckett et al. 2014; Coppola et al. 2022; Lages et al. 2024) but intrusion and endogenous crustal growth has also been suggested in some cases (Allard 1997; Coppola et al. 2019; Ruth and Costa 2021). Foundational work in the 1980s and 1990s estimated the mass balance at open vent systems and postulated that the substantial excess non-erupted magma mass found at, Etna (Italy) (Allard 1997), Masaya (Guatemala) (Stoiber et al. 1986), Stromboli (Italy) (Francis et al. 1993; Allard et al. 1994), and Kilauea (Hawai'i, USA) (Francis et al. 1993) were accommodated by sub-edifice intrusive or cryptic growth (Francis et al. 1993; Allard 1997) (**Figure 1.1**). At Etna specifically, this excess magma was found to align with a series of gravity anomalies (Rymer et al. 1995) indicative of plutonic growth from the intruded degassed magma (Allard 1997).

To estimate the extent of the excess degassing phenomenon at a given volcano the volumes of erupted and degassed magmas must be estimated. A widely accepted and utilised approach for calculating the volume of degassed magma is the petrological method (Devine et al. 1984) which requires known or estimated S content in the melt and other magmatic properties. With these properties the observed SO_2 flux can then be used to estimate the volume of magma required to supply the flux (Allard et al. 1994; Andres and Kasgnoc 1998; Shinohara 2008).

The more troublesome aspect is calculating the volume of erupted magma. For effusive eruptions, the physical lava flow deposits can be physically mapped manually or more typically in recent times digital elevation models can be produced from satellite and aerial remote sensing methods allowing more accurate estimate

of emplaced flow volumes (Murray and Stevens 2000; Coltelli et al. 2007; Behncke et al. 2016; Naranjo et al. 2016). Thermal remote sensing has become a prevalent technique for estimating the mass flux at lava lakes and open-vent systems (Harris et al. 1999; González et al. 2015; Laiolo et al. 2018; Coppola et al. 2019, 2022; Lages et al. 2024). This magma output rate is derived from Volcanic Radiative Power (VRP), a measure of radiated energy (Coppola et al. 2012, 2019), based on the relationship between the radiating surface area, surface temperature and discharge rate (Pieri and Baloga 1986; Harris and Baloga 2009a; Coppola et al. 2013). A question surrounding the application of this method at open-vent systems where magma is not physically being expelled from the vent. If convection in the shallow plumbing system is operating and then magma is potentially being recycled and mixed with fresh magma, resupplied with volatiles and subsequently transported back to shallower depths (Harris et al. 1999; Landi et al. 2008; Lerner et al. 2021). The time-scales for such recycling is undoubtably variable between systems, and therefore it is unclear how often the same "parcel" of magma is being measured by remote sensing methods and what the impact of this is on the resulting erupted magma output estimates. Nonetheless satellite-based methods of estimating magma output have repeatedly demonstrated the scale of the excess degassing phenomenon at open-vent systems globally. It has been shown that the volume of degassed magma is often several times greater than the erupted magma (Steffke et al. 2011; Coppola et al. 2019; Laiolo et al. 2022; Valade et al. 2023) with the excess at lava domes potentially several orders of magnitude greater than the extruded magma (Coppola et al. 2022; Lages et al. 2024).

One of the main issues surrounding conduit convection as the mechanism facilitating excess degassing is what happens to the downwelling magma. Conduit convection requires degassed magma to be stored within the shallow crust (Edmonds et al. 2022a) which should result in detectable surface deformation, but inflation is typically followed by deflation at open-vent systems indicative of a transient period of pressure increase rather than an intrusion (Chaussard et al. 2013; Kondo et al. 2019; Shreve et al. 2022). It has been suggested that excess volatiles are supplied by a more primitive, deeply stored magma (Wallace 2001, 2005; Gerlach et al. 2008; Wallace and Edmonds 2011). Edmonds et al. (2022a) propose that plutons forms at depths greater than about 2-3 km accommodated by regional crustal extension. As the plutons crystalise, they undergo second-boiling forming a segregated magmatic volatile phase which is able to migrate upwards independently of magma flow. This model points to deep long-period earthquakes as an indicator of this deep-derived magmatic volatile phase inducing stress changes via their formation (cooling of the plutons) and bubble growth (Aso and Tsai 2014; Melnik et al. 2020; Wech et al. 2020). This model allows for convective processes to dominate in the upper plumbing system but does not require intrusion of the downwelling magma but offers a source for the excess volatiles observed at the surface.

1.2.3 Monitoring Open-Vent Behaviour

As open-vent volcanism can present at low to high viscosity magma systems it follows the associated volcanic hazards at these systems are many. From lava flows at mafic systems (Pieri and Baloga 1986; Kilburn and Guest 1993) to tephra fall and

PDCs from vulcanian and sub-Plinian eruptions typically associated with more evolved magmas (Cioni et al. 2015; Clarke et al. 2015; Arzilli et al. 2019; Sparks et al. 2024). Mafic volcanism is more readily associated with effusive to mild explosive strombolian (Taddeucci et al. 2015; Laiolo et al. 2018; Woitischek et al. 2020b; Métrich et al. 2021) or lava fountaining activity (La Spina et al. 2021; Lamb et al. 2022; Scott et al. 2023) yet basaltic systems have are also capable of sub-Plinian eruptions (e.g. Fuego (Guatemala) Rose et al., 2008) and even Plinian eruptions (e.g. Masaya (Nicaragua) Bamber et al., 2022, 2020; and Tarawera (New Zealand) Carey et al., 2007; Walker et al., 1984). The capability of mafic open-vent volcanoes generating sub-Plinian eruptions (Rose et al. 2008a; Tupper et al. 2009) and the transition from persistent degassing behaviour to explosive paroxysms are often heralded by precursory signals over short timescales. The processes that govern the transition from effusive to explosive in activity are better understood for more silicic magmas than for more mafic magmas (Williamson et al. 2010; Cassidy et al. 2018a).

At closed-vent systems the propagation of magma to the surface can be detected as earthquakes (Endo and Murray 1991; McNutt 1996; White and McCausland 2016; Obermann et al. 2019), surface deformation as magma causes the edifice to inflate (Murray 1995; Mattioli et al. 1998; Hooper et al. 2004; Kilburn 2012; Spaans and Hooper 2016; Morales Rivera et al. 2017), and the onset of degassing (Sparks 2003a; Wallace et al. 2015b). Although these signals might not always precede an eruption they do indicate an increased likelihood of eruptions. Identifying such precursory signals in open-vent systems is more complex as the transitions from

background activity to paroxysms are often sudden to such a degree where there may be no precursory signal (Aiuppa et al. 2021).

At open-vent systems establishing baselines in these monitoring parameters is critical so that deviations from these can be identified (Aiuppa et al. 2007, 2021; Aiuppa 2015; Pallister and McNutt 2015). Multi-annual and multi-parametric monitoring datasets have been used to establish baseline activity and reveal patterns or cycles in open-vent behaviour (Lyons et al. 2010; Flower and Carn 2015; Naismith et al. 2019; Andronico et al. 2021; Valade et al. 2023). For example, Fuego (Guatemala) has been shown to cycle through stages of effusions with subordinate strombolian activity, followed by paroxysmal sustained explosive eruptions, and then periods of discrete degassing explosions (Lyons et al. 2010; Nadeau et al. 2011; Waite et al. 2013). The great benefit of multi-parametric studies are the ability to interpret volcanological processes where a single parameter may only indicate unrest (Taddeucci et al. 2021; Spina et al. 2021; Calvari et al. 2022b, a). The two key parameters used in this work are gas and thermal emissions; the detection and monitoring of these are reviewed in the following sections.

1.2.3.1 Gas Monitoring

The near-continuous gas emissions of open-vent systems provide a reliable source of information about sub-surface activity compared to other monitoring parameters that may be more infrequent. As discussed in section 1.2.2, SO_2 flux can be used to calculate the volume of magma feeding the observed degassing. Ground and satellite remote sensing methods are commonly used to estimate SO_2 emissions at volcanoes due to the relatively low atmospheric SO_2 levels and the strong

absorption of ultraviolet light by SO_2 (Kantzas et al. 2010; Tamburello et al. 2011; Steffke et al. 2011; Theys et al. 2019; Arellano et al. 2021). The high atmospheric H_2O and CO_2 levels make these more troublesome to measure and so do not lend themselves as easily to remote sensing methods. Instead direct sampling of the gas plume is typically required to measure the fluxes of these other gas species. The MultiGAS (Multiple Gas Analyser System) (Shinohara 2005; Aiuppa et al. 2007) enables the direct measurement of SO_2, CO_2, H_2S and the calculation of H_2O from temperature and relative humidity, recorded by the equipment. The ratio of SO_2 versus other species (X/SO_2) are often used to extrapolate the long-term flux in tandem with the remotely-sensed SO_2 flux (Shinohara et al. 2008; Conde et al. 2014; Aiuppa et al. 2014; Lages et al. 2019, 2020). The MultiGAS has also been mounted onto Unoccupied Aerial Systems (UAS) and flown into gas plumes inaccessible by foot to enable quantification of compositions and fluxes (Schellenberg et al. 2019; Liu et al. 2019; Pering et al. 2020; Liu et al. 2020a; Ilyinskaya et al. 2021a; Mason et al. 2021).

As a first order the gas flux itself is an indicator of changing sub-surface activity. An increased SO_2 flux indicates the rise of magma to shallow depths that may become involved in an eruption or a low flux may be linked to reduced eruptive activity (Laiolo et al. 2018; McCormick Kilbride et al. 2023). Decreases in gas flux have also been shown to be related to conduit plugging that temporarily inhibits efficient gas release until the plug fails (Hall et al. 2015; Liu et al. 2020b; Vásconez et al. 2022).

The primary constituents of magmatic gas plumes are H_2O (75-98%), CO_2 (0.3-13%), SO_2 (0.3-3%), and H_2S (0.02-2%) (Gerlach 2004; Fischer and Chiodini 2015; Kern et

al. 2022). Each these gas species have differing solubilities within the melt (Giggenbach 1996) with a exsolve volatile phase shown to exist as magma reaches depths of ~10-15 km which is initially composed of CO_2 (Edmonds and Wallace 2017; Aiuppa et al. 2019, 2021)(**Figure 1.1**). Sulphur species (chiefly SO_2 and H_2S) have been shown generally to exsolve at depths as great as 10 km in H_2O-rich magmas but as shallow as a few hundred metres in H_2O-poor magma (Wallace and Edmonds 2011) (**Figure 1.1**). The solubility of H_2O is such that it exsolves from the melt at depths <5 km (Johnson et al. 2010; Wallace et al. 2015a, 2015b) (**Figure 1.1**). It is through these known solubilities that monitoring of gas plume composition can used to infer the depth of degassing magma (Aiuppa et al. 2007, 2022; Shinohara et al. 2008; Werner et al. 2013) and the change in composition, notably the CO_2/SO_2 ratio, can be identified as a precursor such as the 2015 eruption of Villarrica (Chile) (Aiuppa et al. 2017) and in some cases to forecast eruptions (Aiuppa et al. 2007).

1.2.3.2 Thermal Monitoring

Satellite-based remote sensing of temperature and thermal radiation (often referred to as emissions) for volcanological research has been become prevalent over the last four decades (Rothery et al. 1988; Pieri et al. 1990; Oppenheimer 1991, 1993; Harris et al. 1999; Coppola et al. 2009, 2013; Ramsey and Harris 2013; Laiolo et al. 2018). In the last 20 years ground-based thermal cameras have also been increasingly used for volcanological research providing high spatial and temporal resolution imagery of thermal structures of lava lakes, lava domes, fumaroles and gas plumes (Calvari et al. 2004; Spampinato et al. 2008, 2011; Patrick et al. 2014; Marotta et al. 2019). Despite the benefits offered by ground-based

thermal cameras, the proximity required to capture various volcanic thermal features (Spampinato et al. 2011) and the infrastructure required for permanent installation, means that satellite-based thermal remote sensing remains the most convenient monitoring method at many volcanoes. The volcanological applications of thermal remote sensing has been organised into four themes (Ramsey and Harris 2013; Harris 2013a): 1) the detection of hotspots (Wright et al. 2004; Coppola et al. 2016; Massimetti et al. 2018; Campus et al. 2022), 2) thermal and compositional unmixing of pixel-level data (Harris, 2013b; Lombardo et al., 2006; Rothery et al., 1988)), 3) calculation of heat and mass flux (González et al., 2015; Harris et al., 1999; Harris and Baloga, 2009b), and 4) eruption and unrest investigations utilising thermal time series (Coppola et al., 2012; Girona et al., 2021; Laiolo et al., 2018).

Thermal anomalies are areas on the earth surface at which higher thermal radiation is emitted than the surrounding area. Volcanic temperatures emit most radiation within the thermal infrared (TIR) (8-15 µm) and shortwave infrared (SWIR) (0.9-2.5 µm) portions of the electromagnetic spectrum and it is within these that thermal anomalies are identified (Blackett 2013, 2017). Automatic detection of thermal anomalies from satellite-borne sensors are readily available to the volcanological community through platforms such as *MODVOLC* (Wright et al. 2004) and *MIROVA* (Coppola et al. 2016) covering a large proportion of current and recently active volcanoes. These platforms also classify the intensity of thermal anomalies using Volcanic Radiative Power (VRP), a measure of radiated energy, which was derived from Middle-Infrared (MIR) method of calculation Fire Radiative Power (Wooster et

al. 2003). Changes in VRP are related to changes in temperature, surface area, or emissivity of the radiating body (Coppola et al. 2012).

The volcanological interpretation of a thermal anomaly is the presence of magma at shallow depths which may erupt or indeed its presence at the surface during an eruption (Blackett 2013; Harris 2013a; Coppola et al. 2016). Sub-surface magma heats the surrounding crust and as it reaches shallower depths the surface temperature increases, leading to increased energy radiation from the surface. VRP therefore provides a metric to assess the relative proximity of magma to the surface as the volcanic edifice temperature increases. At the surface VRP provides a measure of the temperature of a fixed-position magma body (i.e. lava domes, lava lakes or exposed magma columns) (Coppola et al. 2022; Campion and Coppola 2023; Lages et al. 2024) or, the relative areal extent or time average discharge rates of lava flows (Coppola et al. 2013). Coppola et. al. (2012) calculated the VRP of magma covering the surface area equal to that of Stromboli's crater rim and how this related to lava overflowing the crater. This method requires the assumption idealised truncated cone crater geometry but could be used to infer the height of lava columns or lakes at volcanoes with flaring cone crater geometry. Changes in lava lake level have been attributed to pressure modulations in magmatic plumbing systems at Kilauea and Nyiragongo (Patrick et al. 2015a; Barrière et al. 2022). This method of remotely inferring lava lake or magma conduit levels could be used to infer pressure dynamics at inaccessible and remote open-vent volcanoes.

Resolving sub-pixel temperatures can be achieved using a technique known as the "dual-band method" (Dozier 1981), which requires a sensor with two SWIR or TIR

bands. The highest resolution open-access satellite-borne thermal sensors currently available have pixel resolutions of several metres to tens of metres in size (Francis and Rothery 1987; Lombardo et al. 2004; Massimetti et al. 2018). Therefore a pixel over a land surface will often contain more than one surface material, each of which will have a specific temperature. The temperature calculated from the pixel radiance is effectively an average of the various thermal contributions from these different materials and the way this is averaged depends on the wavelength of the sensor (Blackett 2013). These are known as brightness or pixel integrated temperatures (PIT). If one part of the pixel is much warmer than the remainder, then it will contribute proportionally more radiance to the signal in shorter wavelengths than in longer wavelengths. Dozier (1981) found that by manipulating the Planck function for different wavelength bands from a sensor it is possible to calculate one of two properties: 1) the radiant temperature of one of the contributing surface materials of subpixel resolution, or 2) the portion of the pixel that each surface material occupies (Chapter 2 for detail).

Rothery et al. (1988) first demonstrated the use of the dual-band method in volcanology by calculating temperatures of volcanic features. Since then, this technique has been widely used to estimate the temperatures of lava flows (Pieri et al. 1990; Oppenheimer 1991, 1993; Oppenheimer et al. 1993; Harris et al. 1999; Flynn et al. 2001; Wright et al. 2002), lava domes and lava lakes (Oppenheimer 1993; Wooster and Kaneko 1998; Harris et al. 1999; Wooster et al. 2000; Gray et al. 2019). For example, studies using the dual-band method have provided insights into the cooling rates of active lava flows from the sub-pixel scale up to flow-wide scale,

allowing the thickness of lava crust to be estimated (Pieri et al. 1990; Oppenheimer 1991). Improvements in the spatial resolution of multi-spectral instruments have allowed the mapping of bifurcation and braiding of subsurface lava tubes using dual-band method providing new understanding of lava field development and propagation (Flynn et al. 2001). The dual-band method has also been applied to estimating the mass flux at active lava lakes at Mt Erebus (Antarctica), Erta Ale (Ethiopia) and Kilauea (USA) (Harris et al. 1999). The dual-band method has also been used to distinguish different volcanic phenomena such as outgassing, lava pooling or lava flows at Mt Etna. This is done by examining the relationship between the temperature of the measured cool component and the proportions of the pixels occupied by the hot and cold components (Lombardo et al. 2004, 2006, 2012).

1.3 Volcanic Hazard Assessments

Despite open-vent volcanoes' proclivity for passive degassing and mild explosive eruptions they are also capable of more substantial eruptions that have often resulted in direct impact to human activity and deaths. Etna has produced lava flows that have destroyed towns and resulted in fatalities (Kilburn and Guest 1993; Branca et al. 2013, 2017), unrest at Nevado del Ruiz in 1985 resulted in lahars that killed at least 25,000 people (Naranjo et al. 1986; Voight 1990), and the 2008 eruption of Fuego left at least 187 dead (Naismith et al. 2019; Jiménez 2020). Fortunately it is increasingly common that the hazard posed by volcanoes is assessed and communicated to neighbouring communities as part of volcanic emergency procedure planning. It has been postulated that there is a link between

the declining rate of volcanic deaths in recent decades and the improvement of hazard assessment and communication, alongside better monitoring capabilities (Brown et al. 2017).

Historically disaster risk reduction (DRR) plans have been based on a zero tolerance of deaths that fail to properly prioritise and protect the livelihoods of volcanic communities (Barclay et al. 2019). This meant that often only an assessment of a probable worst-case scenario was considered to ensure the complete and successful evacuation in emergencies. It has been found that 63% of primary volcanic deaths occur after the first week of activity and 44% of these deaths occur due to people returning to established high hazard zones (Barclay et al. 2019). People often feel compelled to return to do volcanic evacuation zones during crises to collect or protect assets initially left behind or due to socio-economic issues in the areas to which they have been evacuated (Mercer and Kelman 2010; Mei et al. 2013; Connell and Lutkehaus 2017; Barclay et al. 2019; Mafuko Nyandwi et al. 2023). The zero-tolerance of fatality approach typically has lacked an understanding of the priorities of those living alongside volcanoes. This paradigm is slowly being replaced by the sustainable livelihoods approach which involves identifying community priorities, which often prioritise securing livelihoods above all other factors (Kelman and Mather 2008; Few et al. 2017; Barclay et al. 2019; Rozaki et al. 2022; Miller et al. 2022). This approach allows local communities to thrive in their volcanic environment, improving their resilience to volcanic eruptions and understanding their specific socio-economic needs in relation to evacuation to prevent individuals returning to risk zones (Kelman and Mather 2008; Mercer et al.

2009; Barclay et al. 2019). It has been found that DDR planning is more successful when local communities are consulted (Mercer and Kelman 2010; Hicks and Barclay 2018) at the beginning of planning and their priorities are taken in to account (Kelman and Mather 2008). Therefore the impetus on DRR planning should be understanding and managing vulnerabilities and risk in conjunction with local perceptions of vulnerability and risk beyond just threat to life (Kelman and Mather 2008; Mercer and Kelman 2010).

For DDR methods like the sustainable livelihoods approach to be most effective requires accurate assessment of the differing hazards the volcano is capable of producing, under different eruption scenarios and with a view of the probability of these scenarios (Thompson et al. 2015; Barclay et al. 2019; Dewanti et al. 2019). A variety of deterministic and stochastic models have been developed to simulate the various volcanic hazards to provide this view of potential hazard footprints: tephra (Folch et al. 2009; Schwaiger et al. 2012; Biass et al. 2016), lahars (Schilling 1998), lava flows (Harris and Rowland 2001; Crisci et al. 2004; Del Negro et al. 2008; Tarquini and Favalli 2011; Mossoux et al. 2016) and pyroclastic flows (Kelfoun and Druitt 2005; Patra et al. 2005; Sheridan et al. 2005). Hazard maps were previously based on observed phenomenon or inferred from deposits (Yun et al. 2018) but the development of volcanic hazard models has enabled the hazard assessment of speculative scenarios based on analogous systems. The inclusion of possible magnitude scenarios allows not only for proportional evacuations to be planned but also allow policy makers and communities to better prepare. The combination of multi-scenario modelling and effective communication and hazard maps can inform

simple yet effective measures to mitigate the impact of less intense eruptions (Haynes et al. 2007; Calder et al. 2015b; Thompson et al. 2015, 2018; Lindsay and Robertson 2018). For example the application of the sustainable livelihood approach has led to moving high value community and livelihood assets to lower hazard areas or changing to more resilient crop types in higher tephra hazard areas (Kelman and Mather 2008; Connell and Lutkehaus 2017; Few et al. 2017; Barclay et al. 2019).

1.4 Introducing Manam Volcano

Manam is a mafic open-vent island stratovolcano located ~13 km from the northeast of mainland Papua New Guinea (-4.078, 145.038) (**Figure 1.2**). The emergent portion of the volcanic edifice is sub-circular, approximately 10 km in diameter, with the summit reaching to ~1800 m (Palfreyman and Cooke 1976; McKee 1981). Manam is intersected by four radial so-called “avalanche valleys” approximately 90° apart (Weissel et al. 2004) and roughly aligned to the northeast, southeast, southwest and northwest (**Figure 1.2**). All historical lava flows and the majority of pyroclastic density currents (PDCs) are focused down these valleys until ~300 m asl where the valleys open out and the volcanic flows fan out towards the coast (McKee 1981). Four distinct wedges have formed between the valleys, known as planèzes. It is on the coastal margins of these planèzes where most settlements are located (**Figure 1.2**).

Manam has two summit craters from which all historical explosive eruptions have been generated and are also responsible for much of the effusive activity observed

(Cooke et al. 1976; Palfreyman and Cooke 1976; McKee 1981; Tupper et al. 2007; Global Volcanism Program 2024). Main Crater is situated at the northern end of the summit area and has an approximate diameter of 300 m. Its eastern side is completely open to the northeast valley giving the impression that the high western crater wall is the head of the northeast valley. The northeast valley is directly behind the western wall of Main Crater (McKee 1981) (**Figure 1.2**). South Crater is positioned at above the southeast and southwest valleys and has a more confined conical shape than Main Crater (McKee 1981; Liu et al. 2020a). Historically South Crater has varied in size generally, between 70-100m, and has been observed to shift its location slightly from eruption to eruption (Cooke et al. 1976) although the dimensions and location of the crater seem to be relatively stable in more recent decades (Liu et al. 2020a; Global Volcanism Program 2024).

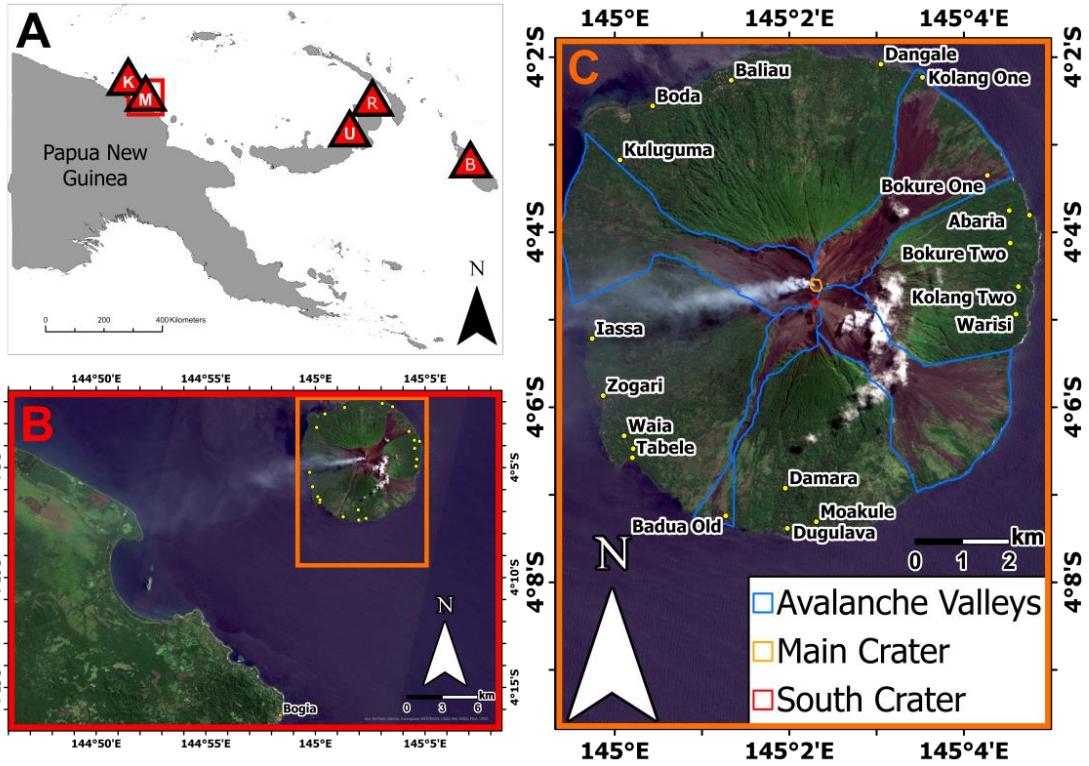

Figure 1.2 A) Location of Manam (M) within Papua New Guinea and other notable volcanoes: Kadovar (K), Ulawun (U), Rabaul (R), and Bagana (B). B) Manan is approximately 13 km from mainland Papua New Guinea. C) Manam island with summit craters and avalanche valleys outlined. Villages locations are shown as yellow dots. Panels B and C use a Sentinel-2 MSI True Colour Image taken on 17 August 2020.

In recent decades Main and South Crater have exhibited different activity. Main Crater hosts a persistent fumarole field and eruptive behaviour has been predominately effusive, with most lava flows issuing from this vent in the last two decades (Global Volcanism Program 2024). South Crater emits a near-constant dense gas plume (McCormick et al. 2012; Liu et al. 2020a) and typically is the vent from which explosive eruptions are generated (Global Volcanism Program 2024).

Another indicator of the direct connection between magma and the atmosphere at Manam is the frequent observation of incandescence at Manam's summit craters, particularly South Crater, outside of eruptions (Global Volcanism Program 2024). A UAS overpass on 22 May 2019 directly observed magma present at shallow depths, passively degassing, within South Crater (Liu et al. 2020a). It remains unclear how

prevalent this state of high standing magma within South Crater is and raises questions surrounding the processes and mechanisms in which Manam transitions from passive degassing to erupting explosively and effusively.

1.4.1 Regional Tectonic Setting

Manam volcano is located on the Adelbert Microplate which is separated from the South Bismarck Plate to the east by the West Bismarck fault (Wallace et al. 2004; Holm and Richards 2013) (**Figure 1.3**). The Adelbert and South Bismarck plates meet the north migrating Australian and Solomon Sea plates at their southern boundary. Here the Australian and Solomon Sea plates have subducted beneath the Adelbert and South Bismarck plates fuelling the Bismarck Volcanic Arc. The arc is divided into eastern and western segments by a volcanically inactive stretch of approximately 100km between Langila volcano and the other volcanoes of New Britain island (Johnson 1977).

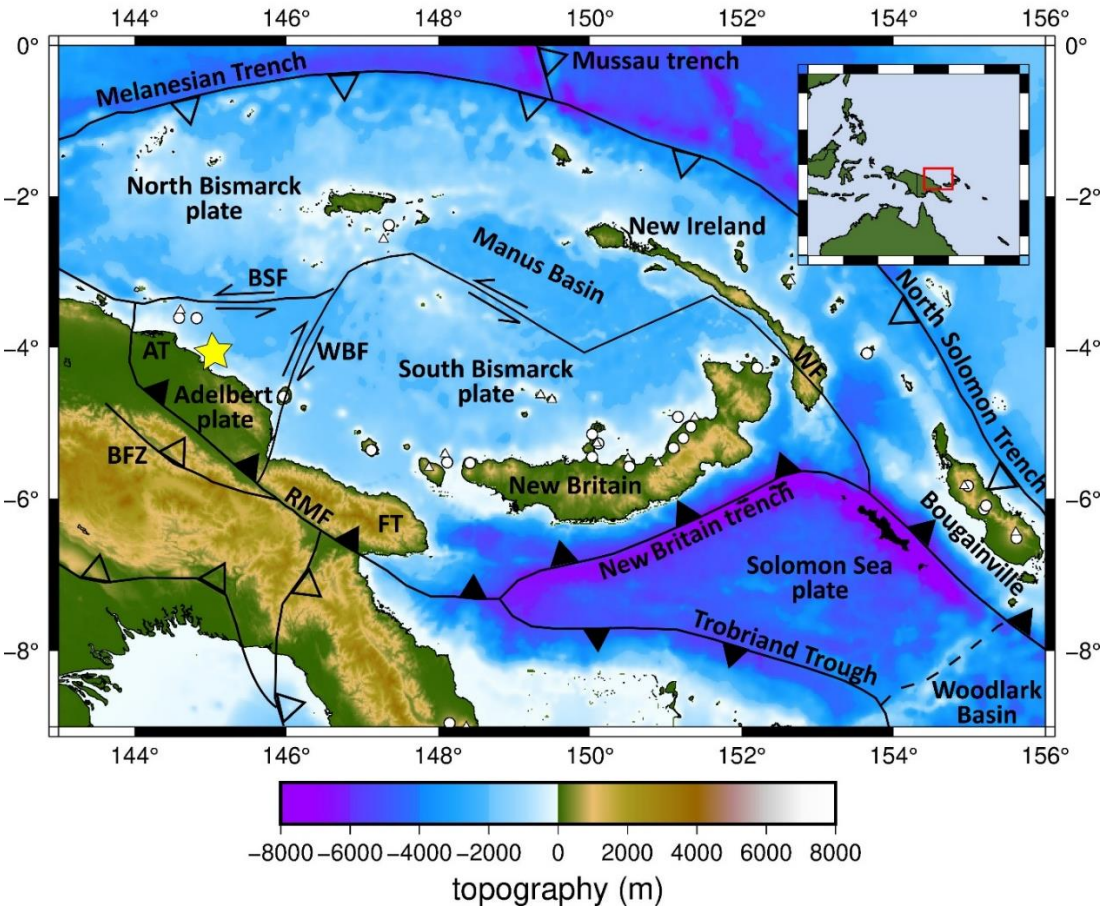

Figure 1.3 Regional tectonic setting from Liu et al. (2020) (used with permission). Manam is shown as a yellow star on the Adelbert Plate. Other volcanoes along the Bismarck Volcanic Arc are marked as white circles. The approximate 100 km gap between the West and East Bismarck Volcanic Arcs can be seen between Langila (furthest west white circle on New Britain) and the other New Britain volcanoes. Abbreviations: AT - Adelbert Terrane, FT – Finisterre Terrane, BFZ – Bundi fault zone, RMF – Ramu-Markham fault, BSF – Bismarck Sea fault, WBF – West Bismarck fault, WF – Weitin fault.

The East Bismarck Volcanic Arc is fuelled by the ongoing northwards subduction of the Solomon Sea Plate beneath the South Bismarck Plate (Tregoning et al. 1999; Cunningham et al. 2012; Tollan et al. 2017). The northwards subduction of the Australian Plate beneath the South Bismarck and Adelbert plates formed the West Bismarck Volcanic Arc. Subduction ceased first in the west around 15 Ma when the Australian plate began to collide with the forearc of the Adelbert Plate, what is now the Adelbert Range (Cloos 2005). The subduction stopped in the eastern West Bismarck Volcanic Arc between 3.7 to 3 Ma due to the collision with the forearc on the South Bismarck plate forming the Finisterre Range (Abbott et al. 1994; Abbott

1995). This forearc now makes up the northern coast of the PNG mainland along the Adelbert and Finisterre Ranges and the Huon Peninsula, what is termed the Adelbert-Finisterre Terrane (Wallace et al. 2004; Abbott 1995) (**Figure 1.3**). The remnants of the subducted oceanic crust which previously divided the Adelbert and South Bismarck plates and the Australian Plate is thought to still be driving volcanism along the West Bismarck Volcanic Arc as it continues to sink into the mantle (Abers and Roecker 1991).

1.4.2 Geochemical Context

The erupted products from Manam include mafic tholeiitic basalts and basaltic andesites (**Figure 1.4**), both of which are notable in the West Bismarck Volcanic Arc for the low TiO_2 content (Johnson et al. 1985). It is thought that the primary melts produced beneath Manam are formed by high degrees of melting in the upper mantle under conditions of slow to negligible subduction and therefore high heat flux (Johnson et al., 1985; Woodhead et al., 2010). The low TiO_2 contents of Manam lavas are indicative of a highly depleted mantle source region (Johnson et al. 1985), and Pb isotope and incompatible trace element data (Woodhead et al. 2010) suggest the addition of a limited terrigenous sediment component. In the context of geophysical constraints, petrological signatures are consistent with progressive heating and melting of a remnant slab into a stagnant mantle wedge no longer rejuvenated by corner flow (Liu et al. 2020a).

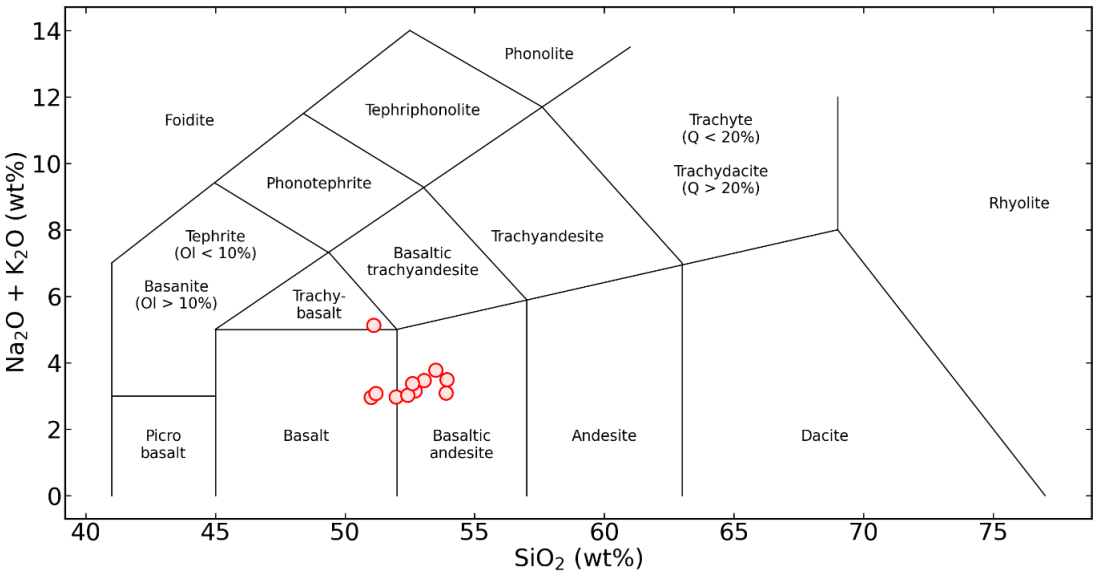

Figure 1.4 Total alkali-silica diagram for Manam lava samples from McKee, 1981; Palfreyman and Cooke, 1976. Manam's erupted lava has broadly been basaltic to basaltic andesite with one outlying sample designated as a trachy-basalt.

1.4.3 Open-Vent Activity

Manam produces a near-continuous gas plume, a phenomenon that has been a common characteristic since the earliest observations in the 17th century (Palfreyman and Cooke 1976). Persistent degassing between eruptions is a defining feature of open-vent volcanism as it indicates the existence of an open pathway for magmatic volatiles to reach the atmosphere (Rose et al. 2013). Both Main and South craters contribute to Manam's prodigious degassing which has been ranked the 11th highest volcanic SO_2 emission source between 2005-2015 at 1480 ± 750 tonnes day^{-1} (Carn et al. 2017). Over the same time interval, Aiuppa et al. (2019) estimated Manam's CO_2 flux at 2760 ± 1570 tonnes day^{-1}, making it the 10th highest volcanic emitter of CO_2 globally. In May 2019, field campaign sampling of Manam's plume using an UAS mounted MultiGAS in May 2019 revealed an elevated average SO_2 flux of 5150 ± [336/733] and CO_2 flux of 3760 ± [313/595] (Liu et al. 2020).

These fluxes would place Manam, albeit transiently, at 2nd and 5-7th respectively for volcanic SO_2 and CO_2 production globally.

1.4.4 Eruptive History

The oldest confirmed observation of Manam erupting was in 1616 followed by a further three observations in 1643, 1700 and 1830 by European sailors (Palfreyman and Cooke 1976). Reliable historical records began in 1887 initially from observations of European missionaries in Haltzfeldhaven and Potsdam on the mainland, Karkar island and Bieng Mission on Manam itself (Palfreyman and Cooke 1976). Scientific observations of Manam began in 1937 initially by the Australian Bureau of Mineral Resources and then RVO following the independence of Papua New Guinea. Since 1887 Manam has produced regular eruptions with the longest period of repose lasting nine years (Palfreyman and Cooke 1976; Global Volcanism Program 2024). Manam's frequent eruptions are typically minor ash-venting episodes ejecting ash 3-5 km asl and this activity generally has very little to no impact on the island's settlements. These low-level eruptions are punctuated by more explosive periods lasting from weeks to years. Manam has been capable of erupting effusively and also producing Strombolian, Vulcanian and sub-Plinian explosive eruption styles (Cooke et al. 1976; Palfreyman and Cooke 1976; Johnson et al. 1985; Tupper et al. 2007; Global Volcanism Program 2024).

The earliest record of a major eruption at Manam was the 11 August 1919 eruption which noted for its violence and is possibly the largest historical eruption based on the speed and the extent to which the ash cloud spread (Palfreyman and Cooke

1976). From 1919 to 2000 there were 11 periods of heightened eruptive (**Figure 1.5**) activity marked by more explosive strombolian or ash-column generating eruptions with both often being accompanied by lava effusions and the latter often producing PDCs. The most notable of these were the 1957/58, 1992/93, 1996, and 1998 eruptions. The 1957/58 eruptions were a period of frequent explosive eruptions generating lava flows and PDCs at both craters lasting from January 1957 to May 1958 (Reynolds 1957; Taylor 1958a, 1958b, 1963). A remarkable feature of this eruption was the only historical observation of a lava flow flowing down the northwest valley (Taylor 1958a). The entire island was evacuated in December 1957 just six weeks before parts of villages around the southwest valley were destroyed by PDCs (Taylor 1958a, 1958b). The 1992/93 eruptions represented a departure from the strombolian activity leading to PDC generating paroxysms that had marked heightened outbursts the interceding years since 1958 (Cooke et al. 1976; Palfreyman and Cooke 1976; Global Volcanism Program 2024) (**Figure 1.5**). This activity began with violent strombolian eruptions but was remarkable for the series of strong explosive eruptions. The largest of these generating a 19 km asl ash column, indicative of a possible sub-Plinian eruption mechanism, and produced a PDC that destroyed 18 buildings (Global Volcanism Program 1992a, b, 1993a, b; De Saint Ours and McKee 1995). The 1996 eruptions culminated in a paroxysmal eruption generating a PDC down the southwest valley spreading 1.5 km either side of the main channel and overran Badua Old village killing 19 people (Global Volcanism Program 1996a). The 1998 eruptions followed a similar pattern as the 1996 unrest and with explosive eruptions in November and December generating PDCs that flowed via the southwest valley (Global Volcanism Program 1998).

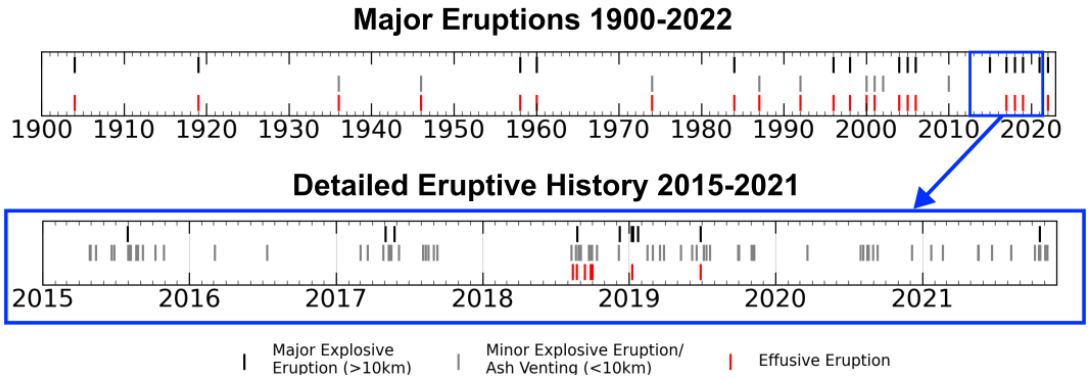

Figure 1.5 Eruptive history of Manam. Top time sees shows notable or major eruptions at Manam between 1900 and 2022. Bottom time series shows a detailed eruptive history of Manam between 2015-2021.

Minor explosive behaviour continued sporadically into the 21st century until the 2004-06 eruptive period which generated eruptions considered comparable to the 1919 and 1957/1958 eruptions (Global Volcanism Program 2004a, b, 2005, 2006). This eruptive phase began in October 2004 following several months of low-level degassing, occasional minor ash emissions and low but steadily rising seismicity (Global Volcanism Program 2004a, 2004c). The eruption was preceded by an escalation in low-frequency earthquakes culminating in a felt earthquake on the island. The eruption began explosively, generating a 10 km ash column from the South Crater and a PDC down the southeast valley to the sea (Global Volcanism Program 2004a, 2004b). The eruption entered a violent Strombolian phase which produced PDCs and lava flows that narrowly missed villages situated in the east of the island. By December 2004, the intensity of eruptions further increased resulting in a mandatory evacuation of the approximately 9,000 inhabitants to the mainland (Mercer and Kelman 2010; Connell and Lutkehaus 2016, 2017).

The 27 January 2005 sub-Plinian phase generated a 21-24 km asl ash column (Tupper et al. 2009) causing ashfall 200 km away on the PNG mainland (Global Volcanism Program 2005) and SO_2 being observed from the eruption 2,200km away (Tupper et al. 2007). Heavy scoria fall injured 14 people and killed one when they returned to their villages on the east of the island and the RVO station near the eastern village of Warisi was destroyed (Global Volcanism Program 2005). Explosive activity continued through 2005 and decreased to a lower intensity following the 27-28 February 2006 eruption which produced a 19 km asl eruption column (Global Volcanism Program 2006). A final explosive outburst produced a PDC on 7 March 2006 killing one person and destroyed numerous homes in Warisi village (Global Volcanism Program 2006).

Following the 2004-2006 major eruptive phase Manam remained persistently active. Through the period 2006-2017 activity at Manam ranged from gentle gas emissions to explosive episodes characterised by ash emissions of up to 8 km asl and PDC generation down the avalanche valleys (Global Volcanism Program 2024). The exception during this period was an eruption on 31 July 2015 which injected ash 19.8 km asl and caused 10-20 cm tephra to fall on the eastern side of Manam (Global Volcanism Program 2017). This eruption lasted 10 days with several days of consistent ash column generation reaching up to 6.7 km asl (Global Volcanism Program 2017).

During 2017-2021 the frequency of large explosive eruptions increased compared to the preceding 10 years. Two large eruptions in May 2017 both generated 12 km asl high ash columns and strong lava fountaining (Global Volcanism Program 2018).

After over a year of relative quiescence a major eruption took place on 25 August 2018, unusually from Main Crater, injecting ash 15.2 km asl into the atmosphere and generating a PDC down the northeast valley that buried 6 houses in Bokure village (Global Volcanism Program 2019a). Further notable eruptions occurred in 23 September, 5 October and 8 December generating 8.5 km asl, 10.4 km asl and 15.2 km asl eruption columns respectively (Global Volcanism Program 2019a). A series of three large eruptions on 7, 11 and 23 January 2019 with the earlier two generating ash columns of 15 km asl and the later eruption reaching 16.5 km asl (Global Volcanism Program 2019b). This continued explosive period led to a three month self-evacuation of a portion of the population (Global Volcanism Program 2019b).

The last major eruption took place in 28 June 2019 which generated an ash column of 15.2 km asl, a ~4 km lava flow in the northeast valley, and PDCs descending down the northeast valley and unusually, the western flank (Global Volcanism Program 2019b). The west and north western areas of Manam have been the main areas of resettlement following the 2004-2005 eruption as they have been less frequently impacted by subsequent eruptions. However, the PDC directed down the western flank destroyed 455 homes and agricultural gardens, and led to the evacuation of 3775 people, the majority of these people living on western Manam (Global Volcanism Program 2019b).

Following this eruption, activity at Manam has generally returned to its state of background persistent degassing, interrupted by sporadic ash venting eruptions and occasional more explosive eruptions. The most notable explosive eruptions reported since the 28 June 2019 occurred on 20 October 2021 (15.2 km asl eruption

column), 22 December 2021 (10.7 km asl eruption column), 8 March 2022 (15.2 km asl eruption column), and 18 April 2022 (13.7 km asl eruption column) (Global Volcanism Program 2021a, 2022a, 2022b).

1.4.5 Anticipating Eruptions and Ordering Evacuations

Manam's eruptions have led to voluntary and mandatory evacuations most notably in 1957 and 2004 (Taylor 1958a; Mercer and Kelman 2010; Connell and Lutkehaus 2017). These two evacuations likely prevented the major loss of life by successfully anticipating a potential climatic eruption. Unfortunately, eruptions at Manam have still resulted in deaths (Global Volcanism Program 1996a, 1998) acting as a reminder that the forecasting of eruptions is inherently difficult. The last evacuation of Manam in 2004 led to a prohibition for residents to return to Manam with it being declared a disaster zone (Connell and Lutkehaus 2016, 2017). Evacuees were housed in several mainland temporary sites, known as care centres, which became essentially permanent as no permanent relocation solution has been decided upon (Connell and Lutkehaus 2016). Issues with neighbouring communities, agricultural practice differences and other socio-economic ramifications of a people removed from their homes long-term led many residents to return to Manam, preferring the threat of ongoing volcanic eruptions to the physical and financial insecurity represented by the care centres (Mercer and Kelman 2010; Connell and Lutkehaus 2017).

Mandatory evacuations cannot be ordered at the smallest sign of unrest as many times these do not culminate in activity that affects the lives of residents. This is

especially true for Manam residents whose previous experience with evacuation has been negative (Mercer and Kelman 2010; Connell and Lutkehaus 2017). The act of ordering perceived unnecessary eruptions leads to mistrust in the capabilities of authorities as was seen after the 1970 and 1983 evacuations of Pozzouli (Italy) after significant uplift that suggested an upcoming eruption within the Campi Flegrei caldera (Charlton et al. 2020; Kilburn et al. 2023). Doubt of scientific competency in understanding volcanic behaviour can lead to non-compliance when an evacuation is ordered (Woo 2008; Bird et al. 2011). This therefore underlines the need for greater understanding of eruptive processes and triggers especially for open-vent systems where pre-eruptive signals can be less clear and for volcanoes where communities live in close proximity like Manam.

1.5 Thesis Outline

This section introduces the two primary aims of this project, which are met through three individual science chapters. The structure of this thesis is then outlined sequentially by chapter, including a brief summary of the aim, objectives (see each chapter for more detail), methods and key findings for each.

1.5.1 Motivation

This project was conceived in response to the impaired monitoring capabilities at Manam following the 2004/05 eruption (Global Volcanism Program 2005) and which meant that those that had returned to Manam in the intervening years did so in spite of the unmonitored, and therefore unpredictable, continued eruptive activity (Kelman and Mather 2008; Connell and Lutkehaus 2017). The ambition was

to utilise satellite remote sensing methods to investigate volcanic processes at Manam and attempt to identify precursory signals. In addition, to this it was hoped that an enhanced view of hazard could be provided by modelling lava flows and tephra deposition produced by Manam. The wider desire was that this work would demonstrate the possibility of monitoring and analysing the activity and assessing the hazard at remote and inaccessible volcanoes in general.

1.5.2 Aims

The overarching aims of this thesis are: (a) to improve understanding of the volcanological processes driving observed transitions between passive, explosive and effusive activity at Manam volcano, and explore the implications for open-vent volcanism more generally, and (b) to quantify the potential spatial distribution of volcanic hazard and risk exposure posed by tephra deposition and lava flows for a range of eruptive scenarios observed in Manam's recent eruptive history. To achieve these aims, this thesis is divided into three chapters that each examine a distinct topic relevant to meeting these aims.

1.5.3 Chapter Two – Remote Sensing of Open-Vent Volcanism

Manam volcano exhibited a period of elevated eruption frequency and intensity between 2015-2021. The aim of Chapter Two is to determine the volcanological processes responsible for driving the observed activity at Manam volcano during this period. The objectives for this chapter are to use open-access satellite remote sensing data to produce a multi-annual timeseries of Manam's SO_2 and thermal emissions; explore the relationships between changes in remotely-sensed emissions

and observed eruptive activity; and interpret these observations in the context of magma storage, ascent and degassing processes to produce a conceptual model of magmatic processes. Together, thermal and SO_2 emissions provide insight into the extent of the "excess degassing" phenomenon at Manam, a key characteristic of open vent volcanoes globally, as well as tracking changes in magma column height within Manam's South Crater, often considered a representative surface proxy for varying pressure in a shallow magma reservoir.

The key findings of this chapter show that a) Manam experienced significant variations in SO_2 flux between 2018 and 2021, b) Manam degassed 0.1 km^3 more magma than it erupted over the same period between March 2019 and December 2021, c) Manam experiences fluctuating pressure within its magmatic plumbing system that appears to have resulted in the level of the magma column rising high enough to appear within the crater on as many as 76 occasions not related to eruptions over the study period. This chapter presents a conceptual interpretive model to explain, in tandem, observed eruptive activity and remotely sensed parameters, which centres on the recharge of volatile-rich magma to shallow depths, commencing some time in 2018. This recharge magma is interpreted to have stimulated renewed eruptive activity from August 2018, ultimately culminating in the major eruption on 28 June 2019. Extensive dehydration-driven crystallisation, due to observed high degassing rates, likely formed transient low permeability plugs in the upper conduit on several occasions. These plugs ultimately failed under the pressure of volatile accumulation beneath, resulting in the series of explosive eruptions observed particularly between August 2018 and August 2019.

1.5.4 Chapter Three – Tephra Deposition Modelling

This chapter aims to place quantitative constraints on tephra hazard, through a probabilistic assessment of the spatial distribution of tephra thicknesses, for a range of relevant explosive eruption scenarios at Manam. The objectives for this chapter are to define realistic explosive eruption scenarios based on the historical eruptive record at Manam; to model the footprint and mass accumulation of tephra deposition under each of these eruptive scenarios using the probabilistic model, *TephraProb* (Biass et al. 2016). These hazard outputs are then combined with geospatial datasets to quantify the exposure of populations, agriculture, buildings and road networks affected under each scenario. This chapter examines how different sectors would be affected by varying accumulations of tephra, and discusses the implications of these results in the context of emergency planning.

Modelling highlighted a seasonal influence on tephra hazard, due to changing prevailing winds on tephra deposition; the wet season (November to April) has a more pronounced east to southeast dispersal compared to the dry season (May to October) which is dominated by a westward dispersal. Bogia is a mainland town that acts as a hub for healthcare and infrastructure to the surrounding district, and is consequently a focal point for emergency response and evacuations of Manam island itself. The results presented in this chapter found that, importantly, during the wet season there is a higher probability of tephra fall impacting Bogia. These findings have implications for emergency and mitigation planning for the region centred around reestablishing transport access to Bogia and ensuring its own resilience and capability to support the wider district during an eruption.

1.5.5 Chapter Four – Lava Flow Modelling

Chapter Four aims to quantify the potential runout lengths of future lava flows at Manam and, from this, assess the hazard posed by effusive eruptions to local settlements and their resident populations. The objectives in this chapter are centred around understanding which vents and what effusion rates are capable of either inundating settlements directly or alternatively reaching the sea and generating secondary hazards such as laze plumes ("lava haze") or littoral explosions. Lava has previously flowed down the northwest valley and outside the bounds of the southwest valley threatening populations. However, repeated instances of these events have not been observed subsequently, raising questions as to whether similar flows may occur in the future and whether they pose a threat to settlements around the northwest and southwest valleys. Additional objectives in this chapter therefore focus on investigating the topographic and eruptive conditions that led to emplacement of these lava flows.

This chapter found that lava flows sourced from summit and upper flanks are not likely to directly impact settlements in their current positions. The biggest direct threat of inundation is found to be the formation of future satellite cones on the lower flanks, which historically have formed much closer to populated areas. However, the probability of future lower flank eruptions is unknown, given the lack of age constraints on previous events. The most likely impact of lava flows at Manam is from the generation of laze from lava entering the sea, either originating from Main Crater and travelling down the northeast valley or from vents within and flowing down the southeast valley. The results in this chapter also provide the basis

for the future creation of hazard communication materials to aid stakeholders (residents and monitoring agencies) to assess whether a lava flow may reach the sea based on the location of the vent.

2 Chapter Two - Insights into Open-Vent Processes Through Remote Sensing of Thermal and SO_2 Emissions

2.1 Introduction

Open-vent activity is sustained by the ascent and degassing of magma at shallow depths (Kazahaya et al. 1994; Harris et al. 1999; Shinohara 2008; Johnson et al. 2010; Palma et al. 2011), with variable contributions from deep-derived segregated fluids that transfer both heat and volatiles to shallow reservoirs (Caricchi et al. 2018; Edmonds et al. 2022b). A common characteristic of open-vent volcanoes is persistent degassing (Rose et al. 2013; Vergniolle and Métrich 2021) where the volume of magma required to supply the observed volatile flux exceeds that of the volume of erupted magma, known as the "excess degassing phenomenon" (Kazahaya et al. 1994; Shinohara 2008). While this strong degassing during interruptive periods is widespread among open-vent systems the eruptive style of these systems is varied and dependent upon each systems magmatic composition. Systems with silica-rich, more viscous, magmas can form lava domes that can collapse with little warning triggering vulcanian eruptions or generating pyroclastic density currents (Stefan 1879; Robin et al. 1991; Wooster and Kaneko 1998; Calder et al. 1999; Young et al. 2003; James and Varley 2012; Mueller et al. 2013; Girina 2013; Flower and Carn 2015; Shevchenko et al. 2020), whereas less evolved, less viscous magmas more typically support persistent gas emissions (Allard et al. 1994; Shinohara 2008; Lyons et al. 2009; Beckett et al. 2014; Liu et al. 2019), in rare examples maintain lava lakes (Moussallam et al. 2016; Gray et al. 2019; Lev et al. 2019) and can produce lava flows or erupt explosively sometimes transitioning between the two (Namiki and Manga 2008; Cassidy et al. 2018b; Viccaro et al. 2021).

Manam has been observed to be persistently degassing since at least 1887 when historical records by European missionaries began (Palfreyman and Cooke 1976). Permanent scientific observation of Manam was established in 1937 and since then observed activity has typically consisted of extended periods of passive degassing, punctuated by explosive eruptions lasting from a few days to weeks interrupted by periods of eruptive quiescence typically lasting several months (Best 1953, 1956; Reynolds 1957; Taylor 1958b; Branch 1965; Palfreyman and Cooke 1976; Global Volcanism Program 2021b). Between 2000 and 2021, Manam has generated 29 major and 139 minor eruptions and produced frequent clusters of thermal anomaly detections in satellite multispectral imagery. During this period, 2014 was the only year which no eruptions or thermal anomalies were reported; however, passive degassing persisted throughout. Over the decade between 2005 and 2015, Manam was the 10th highest volcanic emission source of SO_2 globally as measured by the spaceborne Ozone Mapping Instrument (OMI) (Carn et al. 2016, 2017). Overall Manam's clear patterns of persistent inter-eruptive degassing and sporadic yet frequent eruptions classifies it as a long-lasting open-vent volcano.

Forecasting eruptions at open-vent volcanoes such as Manam present a different challenge to closed systems as the deviations from ongoing activity can be difficult to interpret. For example, at some systems an increase in degassing could represent a precursory signal to an eruption (Johnson and Poland 2013; Hidalgo et al. 2015; Aiuppa et al. 2017) whereas at other systems a decrease in gas emissions may indicate an upcoming eruption (Edmonds et al. 2003b; Campion et al. 2018b). It is therefore critical that the long term behaviour of open-vent systems is understood

through long-term monitoring so that deviations from background behaviour can be identified. Ideally, systems which pose a risk to communities and infrastructure are monitored using multiple parameters such as: gas flux and composition, thermal emissions, seismicity and ground deformation. Ground-based monitoring is often not possible at many volcanoes but advances in satellite-based remote sensing techniques in the last two decades have meant that spatial and temporal resolutions have greatly improved facilitating the measurement of multiple parameters including: ground deformation (Spaans and Hooper 2016; Morales Rivera et al. 2017; Valade et al. 2019), thermal emissions (Wooster and Kaneko 1998; Laiolo et al. 2017; Naismith et al. 2019; Coppola et al. 2019, 2022), lava lake behaviour (Flynn et al. 1993; Harris et al. 1999; Oppenheimer and Yirgu 2002), and SO_2 emissions (Fioletov et al. 2015; Carn et al. 2016, 2017; Laiolo et al. 2018; McCormick Kilbride et al. 2019; Queißer et al. 2019). In particular the daily overpasses of some satellites allow for monitoring of parameters, such as thermal and SO_2 emissions (Wright et al. 2002; Theys et al. 2019).

The major eruption of Manam in 2004/05 was the largest eruption since 1919 based on tephra fall extent (Palfreyman and Cooke 1976; Global Volcanism Program 2024) and destroyed the monitoring station in Warisi village (Global Volcanism Program 2005). This monitoring equipment has not been replaced but Manam has continued to be monitored using the regional seismometer network and an local observer reporting activity to Rabaul Volcanological Observatory (RVO). Therefore, the use of satellite remote sensing monitoring techniques at Manam presents a clear

opportunity to establish a form of permanent multi-parameter monitoring that hasn't been possible since 2005 and to fill in data gaps in the intervening period.

2.1.1 Aims and Objectives

This chapter seeks to understand the volcanological processes responsible for the observed activity at Manam between 2015-2021 using satellite remote sensing of SO_2 and thermal emissions. To do this the following objectives are targeted:

1) Measure the surface temperatures of Manam's two summit craters using shortwave infrared imagery from European Space Agency's (ESA) Sentinel-2 satellite array and utilise the pre-existing *MODVOLC* thermal anomaly detection system to characterise the long-term patterns in thermal radiation emitted.
2) Measure Manam's SO_2 emissions using the TROPOMI sensor carried by the ESA Sentinel-5P satellite to determine how volatile supply and outgassing dynamics fluctuate over multi-annual time periods.
3) Estimate the frequency at which the top of the magma column rises into South Crater using emitted radiance and an assumed simplified crater geometry, and relate this to varying reservoir pressure within Manam's magmatic plumbing system.
4) Quantify the extent of excess degassing at Manam by comparing the total magma input into the shallow plumbing system (estimated from the observed SO_2 emissions) with the observed magma output (from measuring

the geometry of lava flows observable in satellite imagery and deriving the erupted mass from explosive eruptions based on eruption column heights).

5) Establish a conceptual model that invokes volcanological processes to explain the observed activity in the context of varying thermal and SO_2 emissions and changing reservoir pressure, identifying any potential eruption precursory signals.
6) Discuss temporal variability in degassing at open vent volcanoes, and the issues related to extrapolating discrete campaign-based measurements to long-term global inventories of volcanic degassing, by placing Manam's gas emissions in the context of global volcanic emissions.

2.2 Methods

This section outlines the remote sensing methods used to retrieve the Volcanic Radiative Power (VRP), surface temperatures, SO_2 emissions (mass loading and time-averaged fluxes), and to spatially-reference the detected thermal anomalies at Manam volcano.

2.2.1 Thermal Remote Sensing Principles

Thermal remote sensing is based on the principles of electromagnetic radiation. All objects emit electromagnetic radiation according to the kinetic temperature and emissivity of their surface (Jensen 2000; Blackett 2013). As the kinetic temperature of an object increases, its radiance also increases as described by the Stefan-Boltzmann Law (**Equation 2.1**) (Boltzmann, 1884; Stefan, 1879):

$$E = \sigma T^4 \quad (2.1)$$

where E is the measured radiance (W m^{-2}), T is the blackbody temperature (K) and σ is the Stefan-Boltzmann Constant (5.6697 x 10^8 W m^2 K^4). A blackbody is a hypothetical surface that absorbs all incoming radiation, thus heating the blackbody, and then radiates energy with a temperature-defined spectrum and perfect emissivity (ε = 1). As temperature increases, the radiance at all wavelengths also increases but the peak emission shifts to shorter wavelengths (**Figure 2.1**), as described by Wien's displacement law (**Equation 2.2**):

$$\lambda = \frac{b}{T} \quad (2.2)$$

where λ is the peak wavelength (m), T is the blackbody temperature (K) and b is the Wien displacement constant (2.8978 x10^{-3} m K).

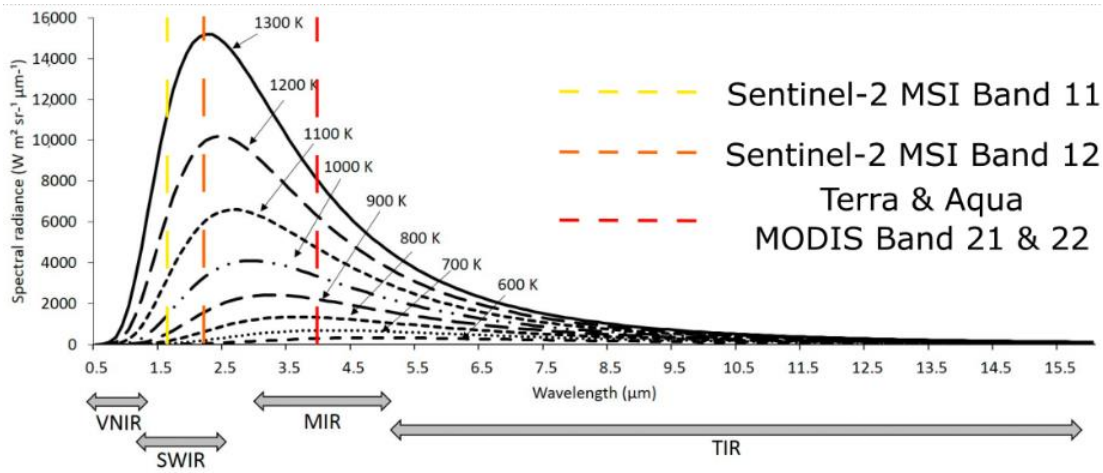

Figure 2.1 Variation of blackbody spectral radiance with temperature. Each line represents the radiation of a blackbody at a given temperature for all wavelengths. The area under the line represents the total radiation emitted by the object. As temperature increases the wavelength at which peak radiance is observed moves to shorter wavelengths (left) (Modified from Blackett. 2017)

The spectral radiance, $L_\lambda(T)$, emitted by a blackbody for a given temperature and wavelength ($\boldsymbol{\lambda}$) can be calculated using the Planck function (**Equation 2.3**) (Planck, 1901):

$$\boldsymbol{L_\lambda(T) = \frac{C_1}{\lambda^5(e\text{^}(C_2 \lambda T) - 1)}} \qquad \textit{(2.3)}$$

Where $\boldsymbol{C_1}$ and $\boldsymbol{C_2}$ are constants of 1.19 x 10^{-16} W m^2 sr^{-1} and 1.44 x 10^{-2} mK, respectively. The temperature-dependence of the peak wavelength means that spectral radiance from very hot surfaces is greater in the shortwave infrared (SWIR) and middle infrared (MIR), 1.3 – 3 μm, compared to the longer-wavelength thermal infrared region (TIR) (**Figure 1**; Blackett, 2013; Kerle et al., 2009). Applied to a practical example, this relationship means that a hot object, such as a lava flow, will emit substantially more energy than its surroundings regardless of its size (Blackett 2013).

2.2.2 Detecting Thermal Anomalies

The *MODVOLC* algorithm was used to measure the radiant heat flux, or volcanic radiative power (VRP) emitted by Manam (Wright et al. 2004; Wright 2016b). *MODVOLC* uses Level 1B products from the MODIS (Moderate Resolution Imaging Spectroradiometer) multispectral instrument onboard the NASA Aqua and Terra satellites providing a 1 km^2 pixel resolution for the infrared bands. Together, these two satellites ensure coverage of most of the Earth's surface every 1 to 2 days. A

thermal anomaly is defined as a pixel(s) in a satellite image that have a higher temperature relative to neighbouring pixels (Wright et al. 2002; Dehn and Harris 2015).

Cloud-covered pixels can have pixel integrated temperatures comparable to pixels containing volcanic products due to their brightness (the term used to describe the intensity of an objects radiance) and therefore interpretation is non-unique (Wright et al. 2002, 2004; Wooster et al. 2003). Similarly, the difference between the measured radiance in the 4 µm and 12 µm centred spectral bands (band 22 [or 21] - band 32) can be similar for pixels containing either a volcanic "hot spot" or meteorological cloud. In order to identify true volcanic thermal anomalies, *MODVOLC* uses the Normalised Thermal Index (NTI) to differentiate between thermal anomalies of volcanic and non-volcanic origin. By normalising the difference between the two bands (**Equations 2.4 & 2.5**), a true hotspot can be distinguished from other elements in the image because the value of this normalised difference increases with the temperature of the emitting surface (Wright 2016b). *MODVOLC* uses a threshold of NTI > -0.80 to define a thermal anomaly. MODIS bands 21 and 22 are both centred on a wavelength of 4 µm; although both bands have the same dynamic range, band 22 is sensitive to pixel integrated temperatures up ~330 K, while band 21 extends to temperatures up to ~500 K. Band 22 therefore has greater spectral resolution than band 21, but is limited by saturation at lower temperatures.

$$NTI = \frac{B_{22} - B_{32}}{B_{22} + B_{32}} \quad (2.4)$$

or *if band 22 is saturated (> 330 K):*

$$NTI = \frac{B_{21} - B_{32}}{B_{21} + B_{32}} \quad (2.5)$$

where 21, 22 and 32 refer to the total spectral radiance emitted in MODIS bands 21, 22, and 32, respectively.

Volcanic Radiative Power (VRP) is the total heat radiated across the area of the anomaly at the time of acquisition, and is expressed in W or J s^{-1} (**Equation 2.6**) (Coppola et al., 2013; Wooster et al., 2003; Wright et al., 2015).

$$VRP\ (\phi_e) = 1.89 \times A_{PIX} \times D_{PIX} \quad (2.6)$$

where 1.89 is a best fit regression coefficient calculated using the MIR method which relates the VRP estimated using the simple power law used by *MODVOLC* to the expected value under the Planck function (Wooster et al. 2003; Wright 2016b), A_{PIX} is the area of the pixel, and D_{PIX} is the above-background MIR radiance of the pixel. When a hotspot is detected in more than one pixel, the total VRP is the sum of the VRP across all pixels. This study uses the volcanic radiative power scale used by *MIROVA* (Middle InfraRed Observation of Volcanic Activity) volcanic thermal anomaly system to provide a simple indicator of relative anomaly intensity (Coppola et al. 2013, 2016). The uncertainty associated with VRP is derived from the contribution of surrounding pixels not identified as thermal anomalies (i.e. background radiance) (Roberts et al. 2005), which is estimated to be as much as ±

30 % (Wooster et al. 2003). This uncertainty is only significant for very weak thermal anomalies with only small differences between signal and background, or for instruments with low spatial resolution (Zakšek et al. 2013).

2.2.3 Locating Thermal Anomalies

Manam volcano has two active summit vents, Main and South Crater, that generally exhibit distinct eruptive styles and pose different hazard footprints. The two vents are within 1 km of each other (i.e. within the 1 km pixel resolution of the MODIS infrared bands) and so the VRP is likely to include thermal contributions from both, should both be radiant simultaneously. To determine the source of each anomaly, or to deconvolve the relative contributions from each vent or from other thermal sources, multi-spectral images from the ASTER (Advanced Spaceborne Thermal Emission and Reflection Radiometer) instrument onboard the Terra satellite and Sentinel-2 are used. The ASTER instrument itself can be tasked to image specific areas of the Earth's surface upon request and therefore does not provide the regular and complete coverage of the Earth's surface compared to the MODIS instrument. However, ASTER level 1T data (Precision Terrain Corrected Register At-Sensor Radiance) band 13 TIR images (11.3 µm centred) have a 90 m resolution, complementing MODIS data by providing higher resolution position information for thermal features (Laiolo et al. 2018). Sentinel-2 is part of the European Space Agency (ESA) Copernicus Earth observation programme and is composed of a constellation of two satellites (Sentinel-2A & -2B), both carrying the Multi-Spectral Instrument (MSI). The MSI provides high resolution (10, 20 & 60 m pixel) imagery across 12 spectral bands ranging from visible to SWIR (443 nm to 2190 nm). True

colour imagery from MSI are also used to determine the location of *MODVOLC* detected anomalies, together with composites imagery using combinations of bands 4 (665 nm), 8 (842 nm), 8a (865 nm), 11 (1610 nm) and 12 (2190 nm) . MSI provides 20 m pixel resolution imagery, providing greater accuracy in thermal anomaly positions, and has a revisit time of 5 days over Manam, providing an additional regular data source (further technical details can be found in **Section 2.4**). Here, I use ASTER and MSI imagery to determine in which of six most likely features each thermal anomaly is located: Main Crater, South Crater or each of the four avalanche valleys (see **Figure 2.2**). Anomalies outside this areas i.e. on the forested flanks are typically related to fires rather than volcanic sources and so have not been considered.

2.2.4 Calculating Surface Temperatures

A semi-automated process has been developed to derive the surface temperature within each of Manam's summit craters from MSI product level 1C Top of Atmosphere Reflectance (TOA). MSI imagery is processed using ArcGIS Pro, automated using the Python programming language. To improve processing time, the island of Manam was divided into 6 regions of interest (ROI) that can be selected individually for processing; the two craters and four avalanche valleys. Each ROI was traced in ArcGIS Pro using a true colour Sentinel 2 image (pixel resolution 10 m) from 17 August 2020 (**Figure 2.2**). The avalanche valleys were delimited based on the valley walls until the points where they open out onto the flatter terrain of the coastal areas of the island. From this point, the extents were extrapolated to the coast using an exaggerated fan geometry guided by pre-existing

lava flows. Only surface temperatures from the Main and South Crater ROIs are analysed in this chapter. All images were processed according the Dual-Band Method implemented by Gray *et. al.* (2019) for MSI imagery. This approach requires pixel integrated temperatures from two SWIR bands, therefore the MSI SWIR bands 11 and 12, which are centred on wavelengths of 1610 nm and 2190 nm, are used. The processing workflow is summarised in **Figure 2.3**.

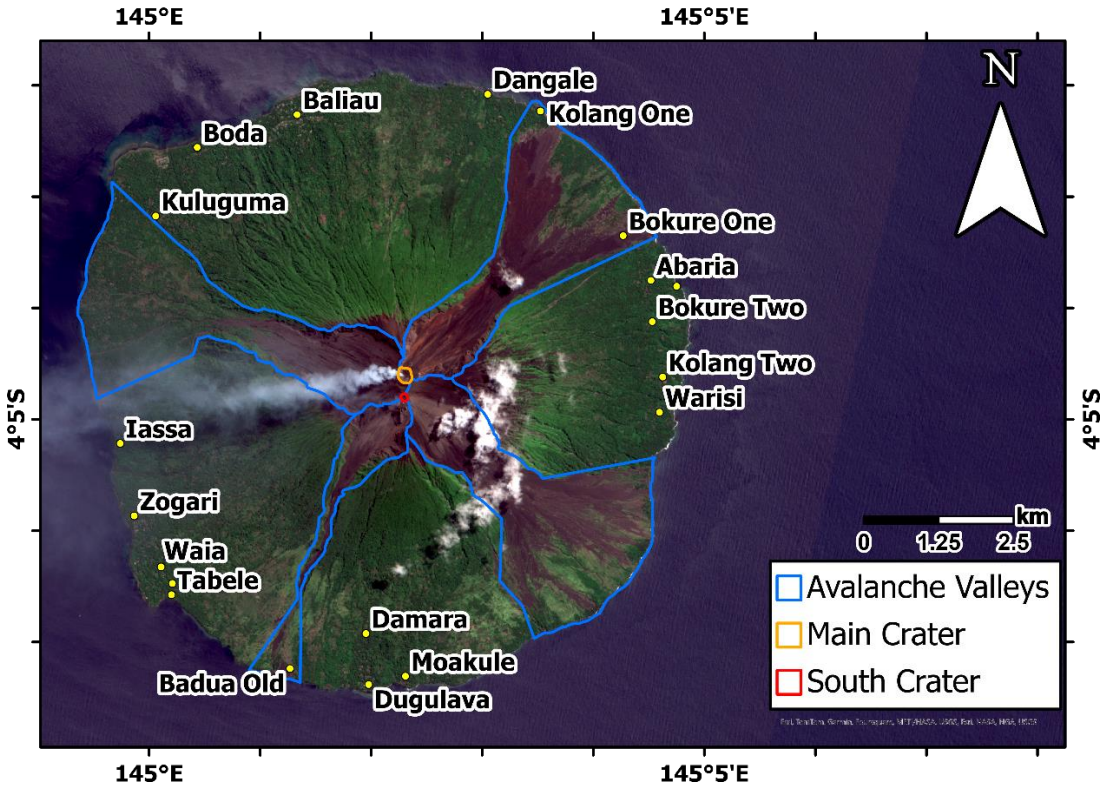

Figure 2.2 True colour image from 17 August 2020 Sentinel-2 MSI overpass with key features of Manam Island with summit craters and avalanche valleys outlined.

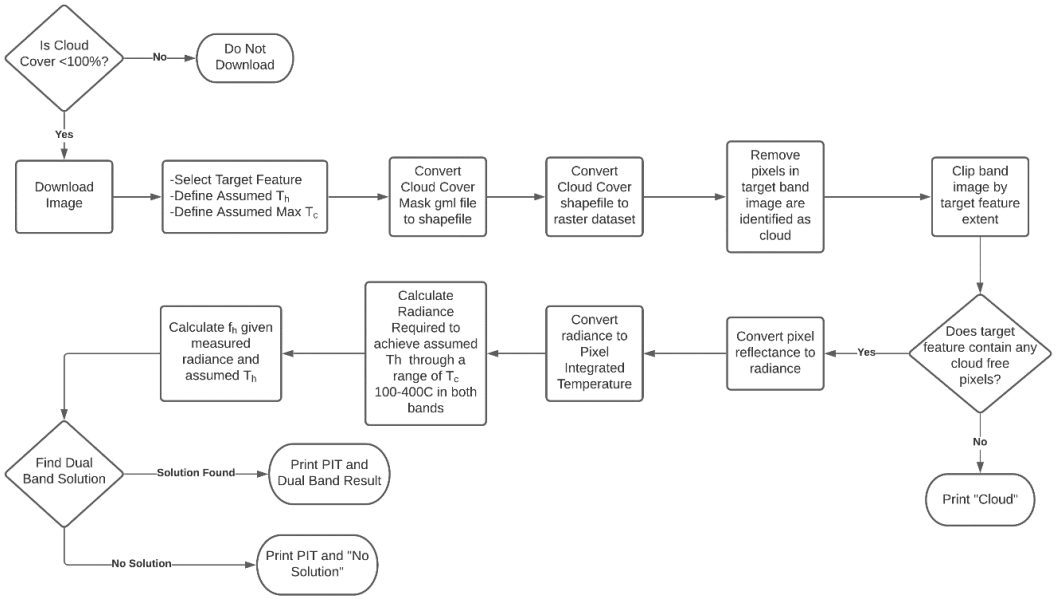

Figure 2.3 Processing workflow for semi-automated dual-band analysis of Sentinel-2 products. Semi-automated processing in ArcGIS Pro begins after images are downloaded from the Sentinel-2 repository.

Any available image tile containing the island of Manam with less than 100 % cloud cover was downloaded from the Sentinel-2 data repository (ESA 2022). Cloud cover regularly hinders satellite measurements in the tropics and combined with the 5-day revisit time of Sentinel-2, cloud cover can produce gaps between summit observations of up to several months. Additionally, cloud cover may only partially obscure the craters and, depending on the part of the crater obscured by cloud, this may reduce the apparent mean temperature. Here, a feature is defined as cloud covered when all pixels within the features boundaries are obscured by cloud. Cloud cover is identified by using the accompanying cloud mask product provided with each MSI image, any pixel identified as being cloud-covered is assigned the digital number “-1” in both bands (11 and 12) so that further processing identifies this pixel as unsuitable for temperature calculations. The band 11 and 12 images with the cloud mask applied are then clipped by the defined target region. When an

object is brighter than the sensors dynamic range, the pixel is designated a digital number of “255”. To avoid ArcGIS erroneously converting this value to a reflectance value, this number is changed to “0” to ensure it is not processed any further. At this point all unusable pixels have been removed and the reflectance value, stored in the pixel digital number, is converted to Top-of-Atmosphere (TOA) radiance (W m^{-2} sr^{-1} μm^{-1}) according to **Equation 2.7**.

$$\boldsymbol{L\lambda = \frac{Q_{cal}E_{e\lambda}(cos\theta)}{\pi\left(\frac{1}{U}\right)}/10^4} \qquad \textit{(2.7)}$$

where $\boldsymbol{Q_{cal}}$ = digital number (DN); $\boldsymbol{E_{e\lambda}}$ = solar irradiance (W m^2); $\boldsymbol{\theta}$ = incidence angle (°), and $\boldsymbol{U}$ = quantification value (converts value to TOA). $\boldsymbol{E_{e\lambda}}$, $\boldsymbol{\theta}$ and $\boldsymbol{U}$ are drawn from MSI metadata associated with each image.

All natural surfaces on Earth reflect some portion of incoming radiation and thus re-radiate <100% of the incoming energy (Blackett 2013). The radiance for a given pixel therefore includes contributions from all the various surfaces within the pixel area. Hot volcanic products emit substantially greater radiation than the cooler surrounding “background” surfaces and so the integrated pixel radiance is weighted heavily towards that of the volcanic products. Pixel Integrated Temperatures are calculated from the pixel-registered radiance; over a homogenous surface, the brightness of the pixel equates to the brightness of the surface and from this the surface temperature can be calculated. However, when a pixel covers two or more surfaces then the brightness of the two surfaces are combined to form a composite signal (Campbell and Wynne 2011; Harris 2013a); therefore the surface temperatures calculated from this can be considered as composite, or integrated,

temperatures. Pixel integrated temperatures were calculated for each band from the radiance values using **Equation 2.8** (adapted for use with MSI imagery from Francis and Rothery, 1987; Rothery, 1988; Harris, 2013), which is derived from the Planck function (**Equation 2.3**).

$$\boldsymbol{T = \frac{C_2}{\lambda l\, n\left(\left[\varepsilon \tau C_1 \lambda^{-5} / 10^6 \pi L_\lambda\right] + 1\right)}} \qquad \textbf{\textit{(2.8)}}$$

where $\boldsymbol{L_\lambda}$ = radiance (Wm^{-2} sr^{-1} µm^{-1}); $\boldsymbol{C_1}$ = 3.742 × 10^{-16} (W m^2); $\boldsymbol{C_2}$ = 0.0144 (mK); $\boldsymbol{\lambda}$ = wavelength (m); $\boldsymbol{T}$ = blackbody temperature (K); $\boldsymbol{\varepsilon}$ = emissivity of the radiating surface; and $\boldsymbol{\tau}$ = atmospheric transmissivity. $\boldsymbol{C_1}$ and $\boldsymbol{C_2}$ are simplified constants representing $\boldsymbol{hc^2}$ and $\boldsymbol{hc/k}$, where $\boldsymbol{h}$ is Planck's constant (6.266 × 10^{-34} J s), $\boldsymbol{c}$ is speed of light (2.998 × 10^8 m s^{-1}) and $\boldsymbol{k}$ is Boltzmann's constant (2987 µm K).

Emissivity for the basalt to basaltic andesite lava erupted at Manam (Palfreyman and Cooke 1976; McKee 1981) is estimated as 0.852 and 0.888 for bands 11 and 12, respectively, based on analogous lavas measured for emissivity in the John Hopkins ECOSTRES Spectral Library (Meerdink et al. 2019). Spectral radiance reaching a satellite sensor is also reduced by atmospheric attenuation and absorption by gases, the degree to which this occurs is known as atmospheric transmissivity. Transmissivity for Manam was estimated using MODTRAN (MODerate resolution atmospheric TRANsmission) system to be 1 and 0.99 for bands 11 and 12 respectively (Berk et al. 2014).

2.2.5 Dual-Band Method

Pixel integrated temperatures provide a useful metric of relative surface temperature change but do not provide an absolute measure of the temperature of specific surfaces within the pixel. Instead, the dual-band method is used to calculate true surface temperatures. The dual-band method assumes that there are only two temperature fields, or components, in a pixel: a target temperature and a background temperature (Dozier 1981; Lombardo et al. 2004; Gray et al. 2019). For example, Crisp and Baloga (1990) model an active lava flow by considering two thermally-distinct radiant surfaces: 1) a spatially larger component corresponding to the cooler crust of the flow ($\boldsymbol{T_c}$) and 2) a smaller, yet hotter, component representing the fractures in the crust ($\boldsymbol{T_h}$), which are assumed to be comparable to the temperature of the inner molten core of a lava body (**Figure 2.4**). The dual-band method involves solving two simultaneous equations **(Equations 2.9** and **2.10)** derived from the Planck function with three unknowns: the hot temperature ($\boldsymbol{T_h}$), the cool temperature ($\boldsymbol{T_c}$) and the fraction of the pixel occupied by $\boldsymbol{T_h}$ ($\boldsymbol{f_h}$):

$$\boldsymbol{L(T_x\lambda_x) = \varepsilon_x\tau_x\left[f_hL(T_h\lambda_x) + (1 - f_h)L\,(T_c\lambda_x)\right]} \quad \textbf{(2.9)}$$

$$\boldsymbol{L\left(T_y\lambda_y\right) = \varepsilon_y\tau_y\left[f_hL\left(T_h\lambda_y\right) + (1 - f_h)L\,\left(T_c\lambda_y\right)\right]} \quad \textbf{(2.10)}$$

Where $\boldsymbol{L}$ is the spectral radiance for a given temperature ($\boldsymbol{T}$ in K) and wavelength ($\boldsymbol{\lambda}$ in nm), $\boldsymbol{\varepsilon}$ is emissivity of the radiating surface, $\boldsymbol{\tau}$ is atmospheric transmissivity and $\boldsymbol{T_x}$ and $\boldsymbol{T_y}$ are the pixel integrated temperatures for bands 11 ($\boldsymbol{x}$) and 12 ($\boldsymbol{y}$) (Lombardo et al. 2006, 2012; Gray et al. 2019). For **Equations 2.9** and **2.10** to be solved, one of the three unknowns must be estimated. Typically, values for $\boldsymbol{T_h}$ or $\boldsymbol{T_c}$

are either estimated or measured (empirically or experimentally) allowing the other to be solved alongside $\boldsymbol{f_h}$. The now known or assumed temperature effectively becomes the background temperature and the remaining unknown temperature is the target temperature. Individually, each equation has multiple solutions of the two remaining unknown parameters but by finding the intersection of these two equations it is possible to derive the unique solution that satisfies both (**Figure 2.5**). Here, it is assumed that the eruption temperatures of lava at Manam do not vary substantially between eruptions and that the temperature of lava crusts would be more insightful as to the state of activity within the summit craters. If the lava crust temperature decreases over time it is assumed that magma supply to the surface is declining, whereas a steady or increasing lava crust temperature over time suggests a stable or increasing surface magma supply. Therefore $\boldsymbol{T_h}$ was estimated at 1142 K (1150°C) as this represents a typical temperature for molten mafic magma, as reported at Manam (Johnson et al. 1985).

A third temperature component representing any background non-lava covered surfaces can be added to the dual-band method allowing the contribution from crustal and molten lava components to be constrained independently of the surrounding land surface (Oppenheimer 1993; Harris et al. 1999). This requires identifying a non-cloud covered lava free surface in every image. Here the two component variant is used, as targeting the craters without needing to identify a background surface allows for automation. The calculation of $\boldsymbol{T_c}$ allows for analysis of relative temperature changes related to the presence of magma at or near the surface. In this scenario cooler $\boldsymbol{T_c}$ values can either represent the heating of the

craters either by subsurface magma or increased magmatic degassing, or a combination of the two and increased $\boldsymbol{T_c}$ values represent the magma at or near the surface.

The two-component thermal assumption of the dual-band method means that the optimal pixels are those that are central to the target feature and do not include any of the surrounding ground within the pixel area (Rothery et al. 1988; Glaze et al. 1989; Oppenheimer 1991, 1993). Unfortunately, most pixels covering volcanic features are not “optimal”, and as such the radiance at each pixel includes contributions from non-volcanic sources. Since the three component variant of the dual-band method is not applied in this work, the contribution of the non-volcanic background temperature is not accounted for here.

This therefore has ramifications for the pixel integrated temperature and dual-band results. With no background temperature component, this method effectively assumes pixels will always be completely filled by a lava body which is not likely to be the case for all pixels even when magma or lava is present within the craters. As such, lower measured pixel integrated temperatures and dual-band results are unlikely to reflect the true temperature but instead indicate the absence of lava. At higher temperatures results will be slightly lower yet overall closer to the actual temperature due to the greater contribution of hotter surfaces total pixel radiance. Thus, high temperature results will indicate the presence of lava and will show the relative change in lava temperatures when present in the craters.

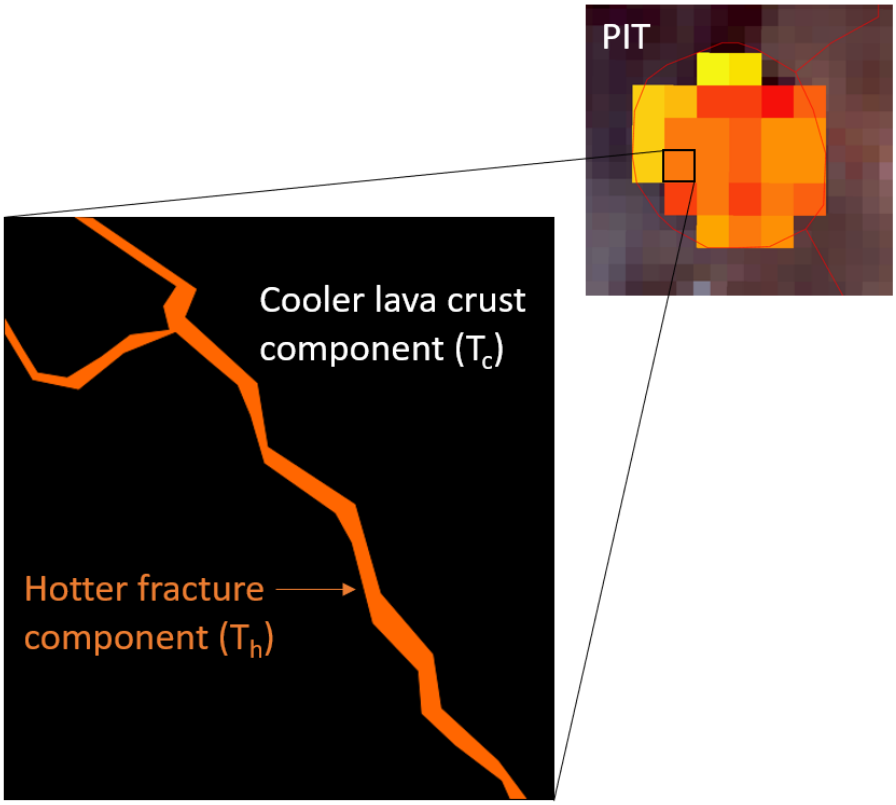

Figure 2.4 Schematic of a lava covered pixel under the two-component model. Most of the pixel is occupied by cooler lava crust and a smaller proportion by hotter fractures. The pixel integrated temperature (PIT) is a function of the temperatures of all radiating surfaces within the pixel (top right) .

The radiance required to achieve a pixel integrated temperature value of 1150°C is calculated in both bands using **Equation 2.8**. This is done using a "Goal-Seek" function built in Python, which finds the value of $\boldsymbol{L_\lambda}$ that allows the function to have $\boldsymbol{T}$ = 1150°C. The required radiance for PIT between 100-600°C in 50°C intervals is also calculated in the same manner; 100-600°C represents a range of possible values of $\boldsymbol{T_c}$ (Flynn et al. 1993; Oppenheimer and Yirgu 2002; Spampinato et al. 2008).

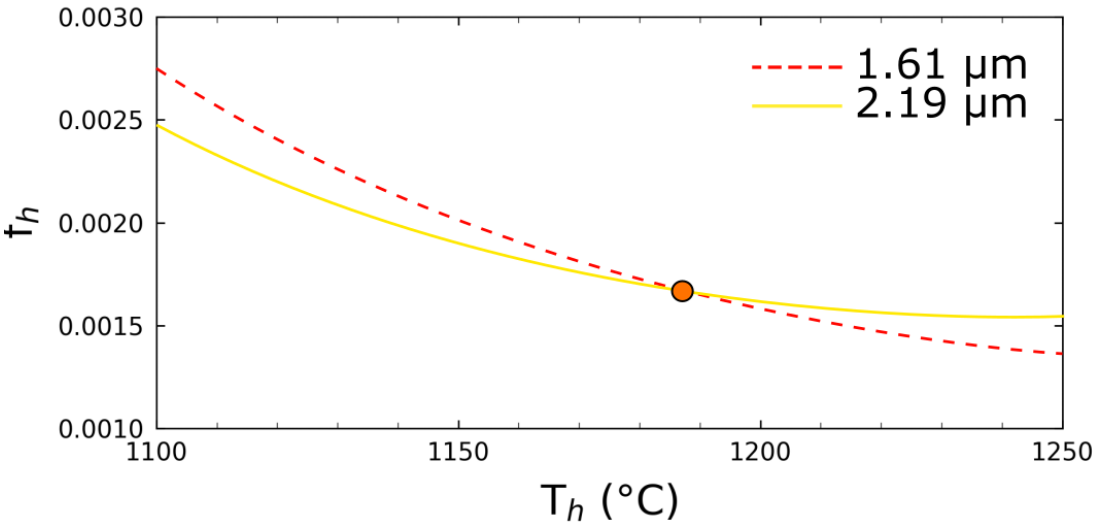

Figure 2.5 Graphical example of a unique solution (orange dot) for T_h and f_h using the dual-band method of SWIR temperature analysis

The value of $\boldsymbol{f_h}$ for each step value in the range of possible $\boldsymbol{T_c}$ values can be calculated using **Equations 9** and **10**, again using the Goal-Seek function. These solutions are then used to interpolate the entire curve that now describes $\boldsymbol{T_c}$ vs $\boldsymbol{f_h}$ (**Figure 2.5)**. The unique solution that satisfies both **Equations 9** and **10** can be found by identifying the point of intersection between the model curves from bands 11 and 12. A solution will not be found if $\boldsymbol{f_h}$ is less than $\boldsymbol{f_{lim}}$, which is the target pixel's radiance divided by the product of the radiance of the hot component of the target band, emissivity and transmissivity and shown in **Equation 2.11** (Flynn et al. 1994):

$$\boldsymbol{f_{lim}} = \frac{\boldsymbol{L_\lambda}}{\left(\boldsymbol{\varepsilon\,\tau\left[L_{(T_h\,\lambda_x)}\right]}\right)} \qquad \textbf{(1.11)}$$

where $\boldsymbol{L_\lambda}$ is the target pixel's radiance, and $\boldsymbol{L_{(T_h\,\lambda_x)}}$ is the radiance of the hot component at a given wavelength. The term $\boldsymbol{f_{lim}}$ can be used as a convergence test

to see whether a dual-band solution can be found. The f_{lim} of band 12 must be greater than the f_{lim} of band 11 in order for convergence to occur and therefore to find a dual-band analysis solution (Flynn et al. 1994). This test was performed during method development and 86% of pixels predicted to have a dual-band solution did find a solution (**Appendix A**, **Figure 7.1, Figure 7.2, & Figure 7.3**).

2.2.6 Quantifying Sulphur Dioxide (SO_2) Emissions

TROPOMI (TROPospheric Ozone Monitoring Instrument) is a spectrometer on board ESA Sentinel-5P polar orbiting platform. TROPOMI has a spectral resolution of 0.25 to 0.54 nm and a spatial resolution of 3.5 × 7 km at launch (Veefkind et al., 2012) and updated to 3.5 × 5.5 km on 6 August 2019. TROPOMI passes over every point on the Earth's surface at least once per day. The TROPOMI Differential Optical Absorption Spectroscopy (DOAS) retrieval algorithm calculates Vertical Column Densities (VCDs) of SO_2 for each pixel within its field of view (Theys et al. 2017); VCD is then converted to column mass (Queißer et al. 2019). The total SO_2 mass loading for a given scene is calculated by summing the column mass of SO_2 contained within each pixel above 3 times the random noise.

The main source of uncertainty in TROPOMI SO_2 retrievals is the altitude of the SO_2 plume, as the instrumental SO_2 response is height dependent. Here ash and eruption plume heights are used as a proxy for the altitude of SO_2 in a given scene. Consistent and accurate plume height estimates are not always available at Manam; the heights of plumes are not regularly reported unless they are notable in magnitude and therefore plume heights from daily background degassing are

mostly unreported. Ash-rich plumes tend to be reported by local observers or by the Darwin Volcanic Ash Advisory Centre (VAAC). However, ground reports tend to underestimate plume heights, especially for plumes >10 km where visibility becomes more difficult (Tupper and Wunderman 2009). Additionally, VAAC reports give plume height in terms of typical commercial aviation flight altitudes rather than the true plume height. These factors mean that there are reasonable estimates available for larger ash rich plumes but there remains ambiguity around the exact altitude of SO_2 in the atmosphere. Additional processing uncertainties include retrieval issues due to cloud cover or choice of air mass factor conversion. Measurements of SO_2 from TROPOMI have been shown to have varying levels of agreement with ground-based estimates of SO_2 (Queißer et al. 2019; Jost et al. 2022). This underlines the importance of a dual method approach where satellite-based derived emission estimates are calibrated and compared to ground-based measurements where possible.

Manam's South Crater lies close to the highest point of the summit region (1807 m asl) and visual observations from May 2019 suggest that, during background degassing between major explosive eruptions, the buoyant gas plume generally rises between a few hundred metres to ~1 km above the summit before dispersing laterally (Liu et al., 2020). Therefore, an altitude of 3 km asl was selected to represent the typical plume height during quiescent phases of activity. Where specific plume heights have been reported by ground observations or VAAC for particular dates (e.g., during explosive eruptions), these values are used to refine the mass loading during these intervals. These plume, or column, heights were

collated from the Smithsonian Institute Global Volcanism Program reports for Manam (Global Volcanism Program 2024) and reports from the Darwin Volcanic Ash Advisory Centre (Darwin Volcanic Ash Advisory Centre 2021) (**Appendix B**, **Figure 7.4**).

Once scene SO_2 mass loadings are calculated, it is important to identify other sources of SO_2 that might contaminate a scene and result in an overestimation of the SO_2 mass flux from Manam. Most contamination sources are other nearby volcanoes, such as Kadovar, ~72 km to the northwest of Manam, which has been outgassing regularly in recent years (Plank et al. 2019, 2020; Global Volcanism Program 2021c), or Ulawun, ~704 km to the east of Manam, which has had 5 confirmed eruptions during the study period (Johnson 2013; Wood et al. 2019b; Global Volcanism Program 2021d; McKee et al. 2021) (**Figure 1.2**).

TROPOMI scenes contaminated by SO_2 from external sources are identified (a) from activity reports for nearby volcanoes and (b) by visual inspection of true colour MSI images and the TROPOMI VCD scene (**Figure 2.6**). When scenes are contaminated by external sources, the areal extent of measurement is focused on Manam or the plume associated with Manam's emissions. If the contaminating plume cannot be clearly distinguished and resolved unambiguously from that of Manam, then the contaminated images are omitted from the results.

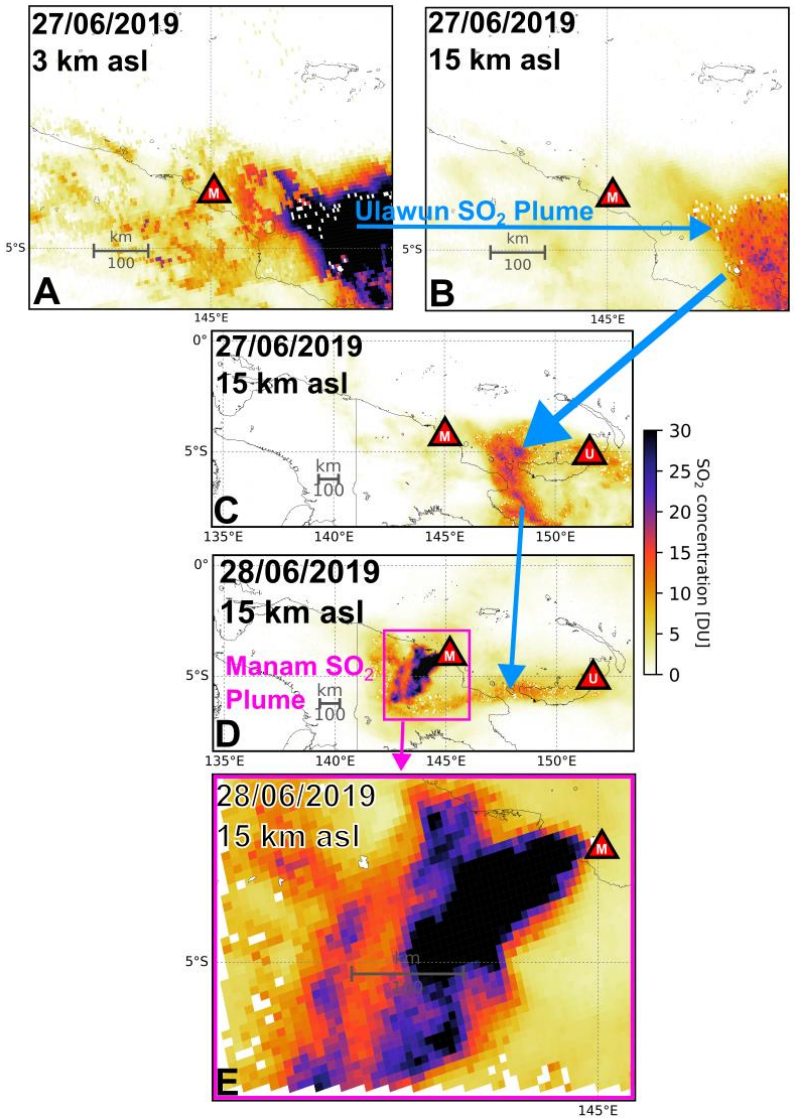

Figure 2.6 TROPOMI SO_2 Vertical Column Density (VCD) over Manam (M) on 27 June 2019 showing high concentrations of SO_2 (interpolated at 3 & 15 km asl, panels A & B respectively). A wider extent view shows that this SO_2 plume is likely sourced from the 26 June 2019 Ulawun (U) eruption (panel C). Wide extent view of the SO_2 plume from 28 June 2019 eruption of Manam and lingering contamination from Ulawun eruption (panel D). Focused extent is therefore used to measure the most SO_2 concentrated part of the Manam plume to avoid as much contamination as possible and to preserve Manam SO_2 signal (panel E) contamination from the SO_2 plume from the 26 June 2019 eruption of Ulawun volcano. The calculated SO_2 mass within this scene and other contaminated scenes are removed from the data set for Manam as it is impossible to distinguish SO_2 emissions from Manam from the plume from Ulawun.

Converting scene SO_2 mass into a flux requires knowledge of the residence time of SO_2 in the atmosphere. If the SO_2 lifetime exceeds 24 hours, then some proportion of the SO_2 mass in a TROPOMI scene will be residual from the previous day. Uncertainties in the lifetime of SO_2 in the atmosphere (especially under different atmospheric conditions) make converting total scene mass to SO_2 fluxes non-trivial

(McCormick Kilbride et al. 2019). Recent studies have attempted to circumvent the need to assume a residence time through a complex back-trajectory model, where TROPOMI retrievals are coupled to a *HYSPLIT* plume dispersion model (Burton et al., 2021; Queißer et al., 2019). Since this study considers SO_2 emissions over a multi-year timescale and is interested in determining gas flux over extended periods, the simplified method proposed by Fioletov et al., (2015) is used where under steady-state emissions the flux ($\boldsymbol{\Phi SO_2}$) and SO_2 mass are related by **Equation 2.12**:

$$\boldsymbol{\Phi SO_2} = \frac{\boldsymbol{MSO_2}}{\boldsymbol{\tau}} \quad \textbf{(2.12)}$$

where $\boldsymbol{MSO_2}$ is SO_2 (tonnes) and $\boldsymbol{\tau}$ is the residence time of SO_2 in the atmosphere. Here, three estimates for residence time were used in an attempt to capture the uncertainty related to this variable: 1, 2 and 3 days based on residence times used in similar studies (Beirle et al. 2014; Laiolo et al. 2018; McCormick Kilbride et al. 2019; Liu et al. 2020a). The maximum atmospheric residence time for SO_2 plumes from Papua New Guinea volcanoes has previously been estimated to be ~18 h with typical ages being < 12 h (McCormick et al. 2012). Therefore, the fluxes based on a 1 day residence time will be used in the discussion. Lastly, time-averaged SO_2 fluxes are calculated by fitting a first-order polynomial to cumulative $\boldsymbol{\Phi SO_2}$.

2.3 Results

This section presents the time series of Volcanic Radiative Power (VRP), dual-band surface temperatures, and SO_2 mass loading. These time series focus on a six-year observation period from 2015 to 2021 that includes several large eruptions with

column heights exceeding 10 km and follows an extended period of relative quiescence.

2.3.1 Volcanic Activity

During 2015 to 2021 there were 86 explosive eruptions ranging from ash venting eruptions to major explosive eruptions generating eruption columns up to ~15 km asl high (Darwin Volcanic Ash Advisory Centre 2021; Global Volcanism Program 2021b). In addition to these explosive eruptions, effusive episodes were reported on seven occasions (Global Volcanism Program 2021b).

Activity during 2015 was marked by a series of 13 minor ash venting eruptions of up to 3 km asl from April to October. On 31 July 2015 a major eruption occurred generating a 19.8 km asl eruption column with 10-20 cm bombs falling on Warisi village on western Manam and ash fall reported in Bogia on the mainland. In contrast to this regular eruptive activity, in 2016 there were only two reported ash venting eruptions on 4 April 2016 and 13 July 2016 both reaching 3 km asl.

More frequent eruptions returned in 2017 with 15 explosive eruptions, two of which were major eruptions generating 12 km asl eruption columns on 4 April 2017 and 26 May 2017. Eruptions began in early march and at least on eruption occurred every month through to September with the exception of July. Following the final eruption of 2017 on 10 September 2017 no eruptions were observed for almost a year until August 2018.

Eruptive activity recommenced at Manam on 10 August 2018 with a small ash venting eruption which was followed 3 days later by a lava flow from Main Crater which moved down the northeast valley. A second effusion flowed down the northeast valley on 23 August 2018 and 2 days later RVO issued a bulletin regarding a major eruption with a 15.2 km asl ash column generated from Main Crater. This eruption saw at least one PDC propagate down the northeast flank and buried 6 houses in Bokure village. Another lava flow issued from Main Crater on 12 September 2018 and lava flows were observed a further four times until 12 October 2018 and it remains unclear whether these were observations of the same advancing flow or separate effusions. Regardless, lava reached within 500 m of the sea and less than 200 m of Bokure village which has subsequently been relocated. A second major eruption occurred on 8 December 2018 with distinct explosions generating a 15.2 km asl and 8.2 km asl eruption column.

After a month long pause in eruptions a major eruption occurred on 7 January 2019 followed by an effusive phase the next day which saw a northeast valley lava flow reach within 400 m from the sea and 1 km from Dangale village. A further 3 days later, on 11 January 2019, a second major eruption occurred (15 km asl eruption column) followed by the last major eruption of January 2019 on 23 January 2019 (16.5 km asl eruption column). Four minor explosive eruptions occurred throughout February and March 2019 followed by a pause throughout April until a solitary minor eruption (5.5 km asl ash column) on 10 May 2019.

More frequent eruptive activity returned in June 2019 with an eruption occurring on average every 7 days from 7 June 2019 to 21 July 2019. The most notable

eruption during this time occurred on 28 June 2019 where a 15.2 km asl eruption column generated PDCs that descend the west and northeast flanks leading to an evacuation of 3775 people and 455 homes destroyed. This eruption also produced a lava flow which terminated approximately 700 m from the sea. Manam produced a further 5 minor eruptions in 2019 in September through to November.

Manam produced less eruptive activity in 2020 than the previous year with a series of minor explosive eruptions in August 2020 being the most notable activity. Infrequent minor eruptions occurred in early to mid 2021 with eruptive activity being observed by residents in August and September 2021 (James Sukua, Pers. Comms.) but not officially recorded by RVO. This activity was reported as “loud continuous rumbling” and at least one “very loud” explosion (James Sukua Pers. Comms.). October 2021 saw a series of eruptions including a major eruption on 20 October 2021 which was followed by another series of eruptions culminating in a major eruption on 22 December 2021.

2.3.2 Thermal Anomaly Detections

Manam has shown enhanced thermal emissions sporadically since regular remote sensing measurements began in 2002 (**Appendix C**, **Figure 7.5**). During the period of observation (2015-2021), thermal emissions are characterised by periods of elevated VRP where thermal anomalies are detected regularly, separated by repose intervals of several months to years with no detectable thermal output (**Figure 2.7**). VRP is a measure of radiated heat and the intensity of an thermal anomaly is classified following Coppola et al (2016; Coppola 2022) : <1 MW = Very Low, ≥1 MW

= Low, ≥10 MW = Moderate, ≥100 MW = High , ≥1GW = Very High and ≥10 GW = Extreme. Most thermal anomalies detected at Manam between 2015 and 2021 have VRP between 10 MW and 93 MW, and are therefore generally classified as "medium"; however, intensity reaches "high" or "very high" on 32 occasions. The time series is grouped into six discrete periods of elevated VRP, hereafter referred to as clusters, where each cluster has a minimum of 5 thermal anomalies separated by no longer than 60 days without a thermal anomaly detection.

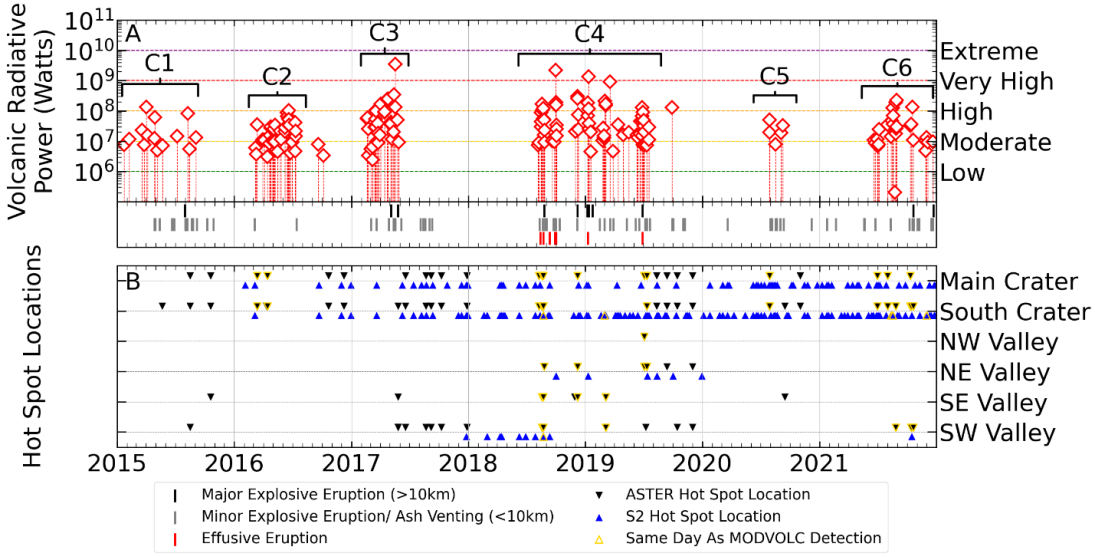

Figure 2.7 A) Timeseries of MODVOLC detected thermal anomalies from 2015 -2021 at Manam and observed activity. Horizontal coloured dashed lines correspond to MIROVA defined Volcanic Radiative Power intensities. B) ASTER infrared imagery used to visually identify the location of anomalies. Black markers indicate an anomaly present in the key region represented by the row marker on the y-axis. Yellow highlighted markers represent an Aster anomaly on the same day as a MODVOLC detection.

Cluster 1 (21 January 2015 – 4 September 2015) began with intermittent low to moderate thermal emissions, and one high intensity detection, with no reported eruptive activity. From April to November 2015, Manam produced 13 minor explosive eruptions (<10 km plume) and one major explosive eruption (>10 km plume) in August. Most of these events were not coeval with thermal anomalies but

low to moderate thermal emissions were detected throughout the period of heightened activity.

Cluster 2 (7 March 2016 – 11 July 2016) is characterised by regular thermal anomaly detections, at a frequency of 9.2 detections per week (compared to 0.88 detections per week in Cluster 1) and a peak intensity of 86 MW recorded on 14 June 2016. Cluster 2 was bracketed by two minor ash venting eruptions on the 4 March 2016 and 13 July 2017 no other eruptive activity was reported during this period**.** Two isolated low intensity anomalies were detected in September and October 2017 with no eruptive activity reported.

Thermal emissions grew progressively more intense during Cluster 3 (18 February 2017 – 29 May 2017), coincident with an escalation in explosive eruptive behaviour that included three episodes of reported strombolian activity and two major explosive eruptions (**Figure 2.8**). Strombolian activity and lava flows in the SW valley coincided with thermal anomalies of 348 MW (14 May 2017) & 135 MW and 3.5 GW (18 May 2017). This very high intensity anomaly on 18 May 2017 was the most intense thermal anomaly during the study period. During the intervening 14 months between clusters 3 and 4 five minor explosive eruptions took place between August and September 2017. No thermal anomalies were detected; however, this is likely due to obscuration from eruption or meteorological cloud cover.

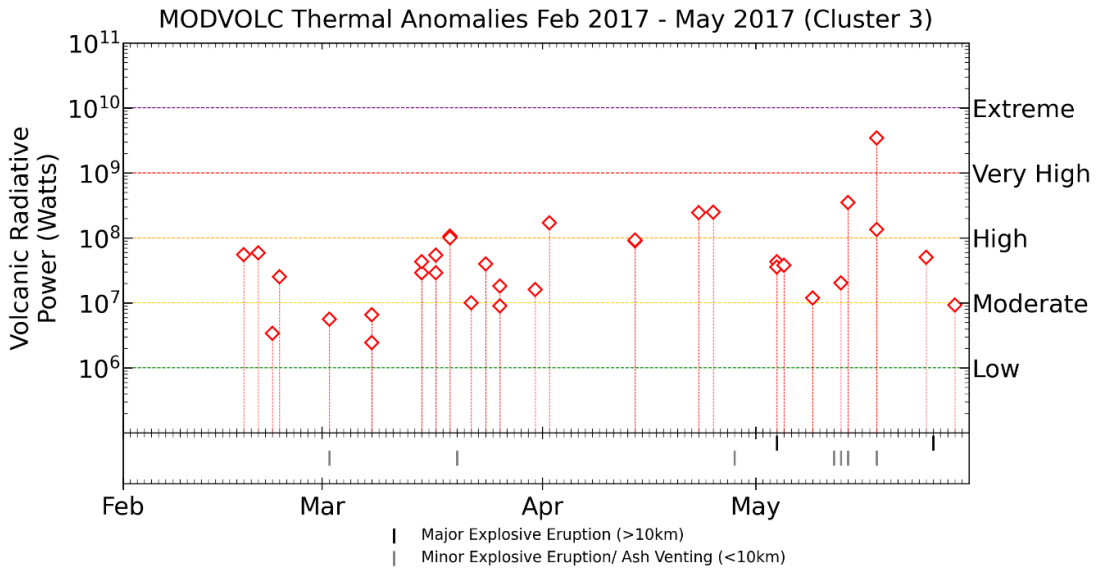

Figure 2.8 Thermal Cluster 3 shown in detail with Tricorn markers indicate eruptive activity style: Black = Major Explosive Eruption, Grey = Minor Explosive Eruption (<10 km plume). Horizontal coloured dashed lines correspond to MIROVA defined Volcanic Radiative Power intensities.

Thermal emissions in Cluster 4 (7 August 2018 – 29 September 2019) coincided with a period of elevated eruptive activity at Manam, which included lava flows and six major eruptions. Of the six days reported with active lava flows, only two occurred coincident with a thermal anomaly detection; cloud cover likely prevented thermal anomaly detections of continuing or cooling flows throughout this period. These two thermal detections were of high (23 August 2018) and very high (1 October 2018) intensity based on their VRP. A moderate thermal emission accompanied a major eruption on 24 August 2018. Two high intensity anomalies were detected on the day of the second major eruption in Cluster 4 (8 December 2018). Manam produced three major eruptions in January 2019 with only eight anomalies detected over this period, including a very high intensity anomaly coincident with the second major eruption (11 January 2019). A high intensity anomaly is recorded on the same day as a reported lava flow in the northeast valley on 8 January 2019. A small cluster of seven anomalies between 23 February 2019 and 5 March 2019 were not

associated with any reported eruptive events, except for a minor explosive eruption on 1 March 2019. Intermittent anomalies were detected from April through to May 2019; the first of these was of high intensity on the day of a minor explosive eruption. Thermal anomaly detections became more frequent through June 2019 from three detections in April and May to 10 in June, with progressively increasing VRP culminating in a high intensity thermal anomaly ahead of a major eruption on 28 June 2019 (**Figure 2.9**). Moderate thermal emissions continued alongside the subsequent minor eruptions, which ceased on 18 July 2019. In the 12 months between Cluster 4 and Cluster 5 only a single high intensity anomaly was detected on 29 September 2019, on the day of a minor explosive event.

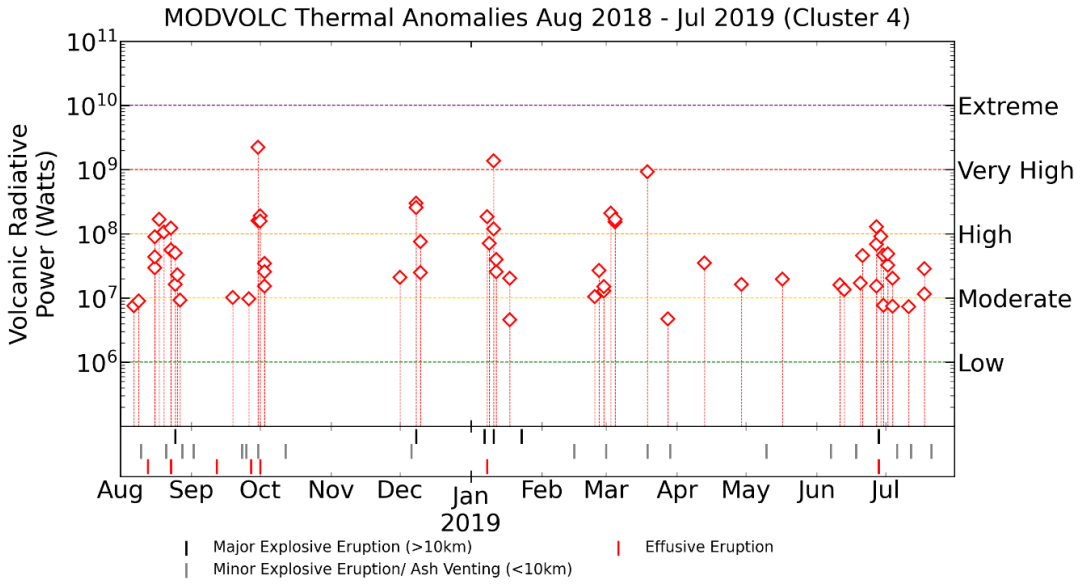

Figure 2.9 Thermal Phase 4 (TP4) shown in detail with Tricorn markers indicate eruptive activity style: Black = Major Explosive Eruption, , Grey = Minor Explosive Eruption, Red = Effusive Eruption. Horizontal coloured dashed lines correspond to MIROVA defined Volcanic Radiative Power intensities.

Cluster 5 includes 5 thermal anomalies and spans a comparatively short interval, which coincides with a period of minor explosive eruptions reported between July and September 2020.

Cluster 6 is associated with a period of unrest at Manam that began in June 2021 and continued throughout the remainder of 2021. Cluster 6 began with a series of low to moderate intensity anomalies following a minor explosive eruption on 23 June 2021. Increased thermal emissions in August 2021 included 11 anomalies including three high intensity detections. Four moderate to high intensity anomalies were detected following reports of Strombolian activity on 18 October 2021 and ahead of the 20 October 2021 major eruption. Several low to moderate anomalies were detected in late November to December in the weeks prior to the 22 December 2022 major eruption.

2.3.3 Spatial Distribution of Thermal Emissions

To resolve the spatial distribution of thermal anomalies, and therefore their sources, higher resolution ASTER and MSI imagery is used. However, the ability for the ASTER platform to be tasked upon request means that ASTER has only passed over Manam 574 times since 2002 and 246 times between 2015 and 2021, of which only 39 (16 %) were on the same day as a *MODVOLC* thermal anomaly detection. Sentinel-2 has a regular 5-day revisit time for Manam; there have been a total of 333 overpasses throughout the study period, of which only 13 (4%) coincide with a *MODVOLC* detection (325 total). Consequently, it is not possible to determine the location of the majority of detected anomalies. Nevertheless, the combined insight from ASTER and MSI shows that both Main and South craters are frequently visible simultaneously in infrared imagery (**Figure 2.7**, example imagery in **Figure 2.10**). In the period 2015-2021 there were 206 days where crater hotspots were visually identifiable from ASTER and MSI imagery; of these 69% showed hotspots in both

summit craters compared to 25% at South Crater only and 6% at North Crater only. Consequently, it is not possible to resolve unambiguously the thermal output from a specific crater; the measured VRP likely includes contributions from both craters, plus any additional activity in the avalanche valleys, due to the large pixel size of MODIS.

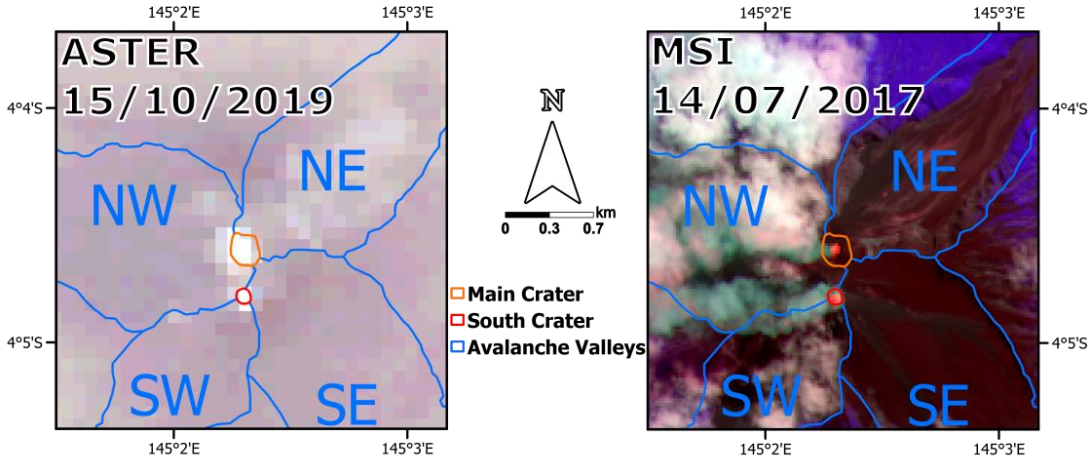

Figure 2.10 Example imagery from ASTER TIR on 15th October 2019 (A) and a Sentinel-2 composite on 14th July 2017 (B) of coeval hotspots at both North and South Craters. ASTER TIR hotspots appear as bright white pixels. Sentinel-2 MSI composite consisting of Bands 4, 8A, and 12. This composite highlights SWIR hotspots which appear as orange-red pixels. Also note the difference in pixel resolution between ASTER (90 m) and Sentinel-2 (20 m).

The distribution of total observed VRP measurements has a mode of 25 MW (**Figure 2.11a**), in close agreement with that of VRP measurements relating to summit activity only (**Figure 2.11b**). Summit-located anomalies at Manam are associated with various types of activity, including ash-venting and Strombolian explosions. Summit activity can generate comparable VRP to flank effusions and there is no clear threshold indicative of a change in eruptive style. However, ≥100 MW anomalies are more likely to be associated with a lava flow (**Figure 2.7**). Lava flows typically produce higher VRP as the greater the radiative surface area, the higher

the energy radiated (Blackett 2013; Harris 2013a). Indeed, the highest VRP measurement in the time series (3464 MW) was recorded during the emplacement of a lava flow that reached 180 m asl. Notably, the two other VRP measurements exceeding 1000 MW were not related to flank effusions but rather major explosive eruptions. However, it is possible that these eruptions were accompanied by lava flows that were not observed on the ground or by satellite due to obscuration by ash clouds.

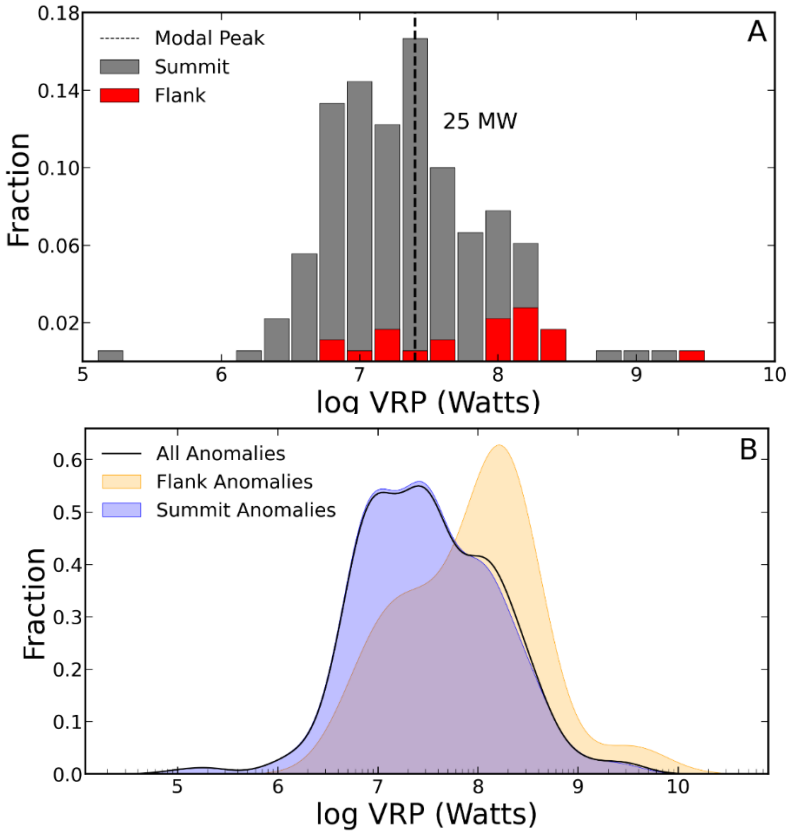

Figure 2.11 Volcanic Radiative Power histograms for 2015-2021 MODVOLC detections. A) MODVOLC detected anomalies that were associated with reported flank effusions or flank hotspots according to ASTER & Sentinel-2 imagery (red) and all other anomalies (grey). The mode of 25 MW is show as the vertical black dashed line. B) Kernel Density plot of MODVOLC detected thermal anomalies (black line), summit anomalies (blue shaded) and Flank Anomalies (orange shaded).

2.3.4 Surface Temperatures

Through the period of observation, Main and South Crater were completely obscured by meteorological or volcanic cloud in approximately 75% of the 277 MSI images available (**Figure 2.12a; Table 1**). Surface temperatures were therefore calculated for Main and South Craters from 68 and 71 images, respectively. The apparent increase in the frequency of cloud cover from late 2017 is due to the Sentinel-2B satellite becoming operational, reducing the Sentinel-2 revisit period from 10 to 5 days.

The daily maximum pixel integrated temperatures for Main and South Craters, derived from MSI data, range from 388°C ± 0.85°C to 509°C ± 1.4°C and 335°C ± 0.81°C to 510°C ± 1.5°C, respectively (**Figure 2.12**). Although the crater with the highest temperature alternates over the study period, the South Crater has a higher maximum temperature on 40 out of the 60 days where the temperature of both craters could be measured together. A notable date where Main Crater measured greater than South Crater was 27 September 2018 by 57°C during the emplacement of a lava flow from Main Crater into the northeast valley. The maximum South Crater pixel integrated temperature during the study period was measured on 20 May 2019; unfortunately, the Main Crater was cloud-covered precluding comparison on this date. However the following measurement of both craters, on 30 May 2019, has an inter-crater temperature divergence of 122°C (**Figure 2.13**). A bright hotspot at South Crater in MSI imagery was observed on this date and follows UAS observations of shallow magma within South Crater on 22 May 2019 (Liu et al. 2020a).

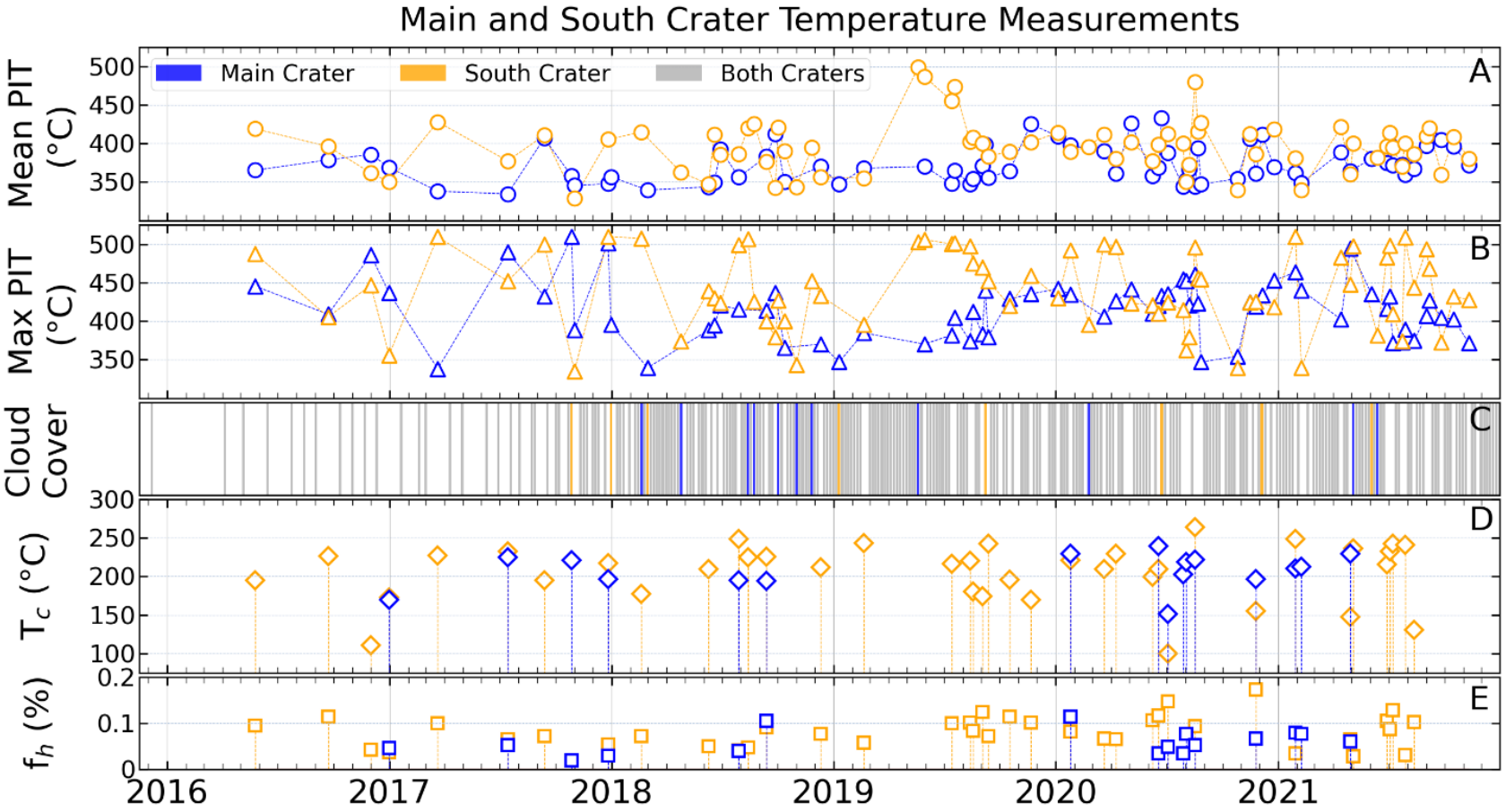

Figure 2.12 Temperature measurements for Manam's Main (blue) and South (orange) craters 2015-2021. Sentinel 2 band 11 (1610nm) A) mean and B) maximum pixel integrated temperature for each crater. C) Cloud coverage indicators for each crater (both: grey) at time of acquisition> D) Calculated surface temperature of the cooler crustal component (T_c) of lava/magma present in each crater. E) Calculated pixel fraction occupied by the hot component (f_h).

Cloud-cover prevented MSI measurements for the entirety of June 2019 and therefore the 28 June 2019 major eruption is not captured in this time series. However, the next two available measurements in July 2019 both exceed 450°C followed by a return to mean temperatures. Interestingly, the mean PITs measured on 13 August 2019 and 18 August 2019 decline more substantially than the maximum temperatures compared to the previous two retrievals. This suggests the ongoing presence of hot material in South Crater, but occupying a smaller portion of the crater.

Crater	Cloud Free		Partial Cloud Cover		Complete Cloud Cover	
	Days	%	Days	%	Days	%
Main Crater	36	13%	32	12%	209	75%
South Crater	51	18%	20	7%	206	74%

Table 2.1 Summary of cloud cover over Manam's summit craters in MSI imagery. Percentages are based on the 277 images (i.e. days) available of Manam between Sentinel 2A becoming operational in November 2015 to December 2021. Partial cloud cover is defined as any image where at least one pixel with the analysis boundary for the crater was not cloud covered and a pixel integrated temperature was able to be calculated.

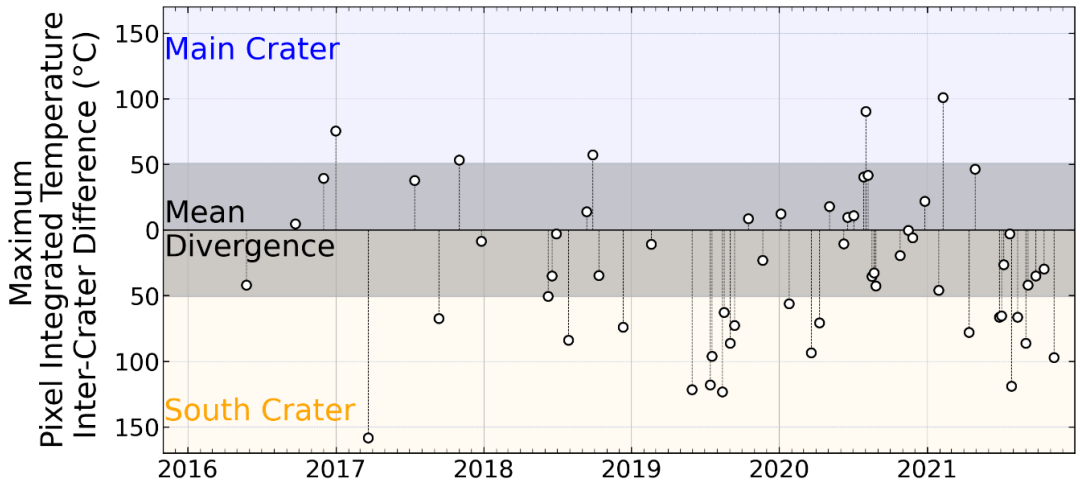

Figure 2.13 Time series showing the difference (or divergence) in inter-crater MSI band 11 pixel integrated temperatures. Mean divergence is 52°C represented by the grey shaded area. South Crater had a higher temperature on 42 (21 above mean divergence) occasions versus 18 (5 above mean divergence) for Main Crater.

2.3.5 SO_2 Emissions

SO_2 mass loadings, determined from TROPOMI satellite data between 6 May 2018 and 31 December 2021, exhibit a mean of 1.1 kt day^{-1} and a median of 0.47 kt day^{-1} (**Figure 2.14**). Notably 75% of daily emissions are below the mean, which is influenced strongly by several short-duration but high magnitude peaks. The timeseries is dominated by an extended interval of above-average emissions that persisted between March and October 2019, during which daily emissions peaked at 58.3 kt before reducing back towards background values (**Figure 2.14**).

A 7-day moving average was used to define four degassing phases (**Figure 2.14**): Phases 1 and 4 appear to characterise the background degassing regime, whilst Phases 2 and 3 capture a period of elevated emissions. The elevated degassing phases are identified by the moving-average exceeding 1 kt day^{-1} and subsequently not dropping below this threshold for more than 8 days. Phase 1 represents a time

period prior to March 2019 (and the subsequent escalation in emissions) when the 7-day average emissions were consistently below 1 kt day^{-1}. Total emissions for Phase 1 equalled 198.8 ± 8.3 kt over 319 days, and are characterised by a time-averaged SO_2 flux of 0.62 day^{-1} (**Figure 2.15**). Effusive activity coincided with two above-average emissions of 8.7 kt and 22.1 kt on 13 August 2018 and 25 August 2018 respectively; the latter of which also coincided with a major explosive eruption. Major eruptions on 11 January 2019 and 23 January 2019 both generated elevated SO_2 mass loadings. Two large eruptions on 19 March 2019 and 20 March 2019 emitted 1.9 and 4.1 kt of SO_2, respectively; following these events, the 7-day moving average exceeded 1 kt day^{-1}, marking the start of Phase 2.

Phases 2 and 3 are defined based on a consistent 7-day moving average SO_2 mass loading in excess of 1 kt day^{-1}. The combined mean daily SO_2 flux during Phases 2 and 3 was 3.2 day^{-1}, with 667 ± 14.7 kt SO_2 emitted over 208 days. During these two phases, SO_2 emissions exceed 10 kt day^{-1} on 14 occasions, a threshold reached only twice during Phase 1 and never in Phase 4. The transition between Phase 2 and 3 is demarcated by a notable change in the gradient of cumulative emissions from 21 July 2019 (**Figure 2.15**). Assuming SO_2 has a 1-day residence time in the atmosphere, Phase 2 has a time-averaged SO_2 flux of 4.72 kt day^{-1} compared to a reduced, but still above-background, flux of 1.5 kt day^{-1} during Phase 3.

The largest SO_2 emission (58.3 kt) during the study period was detected coincident with the 28 June 2019 major eruption, which generated a 15.2 km high eruption column. This eruption, and the following four minor eruptions in July, appear to signal the transition from the elevated SO_2 emissions in Phase 2

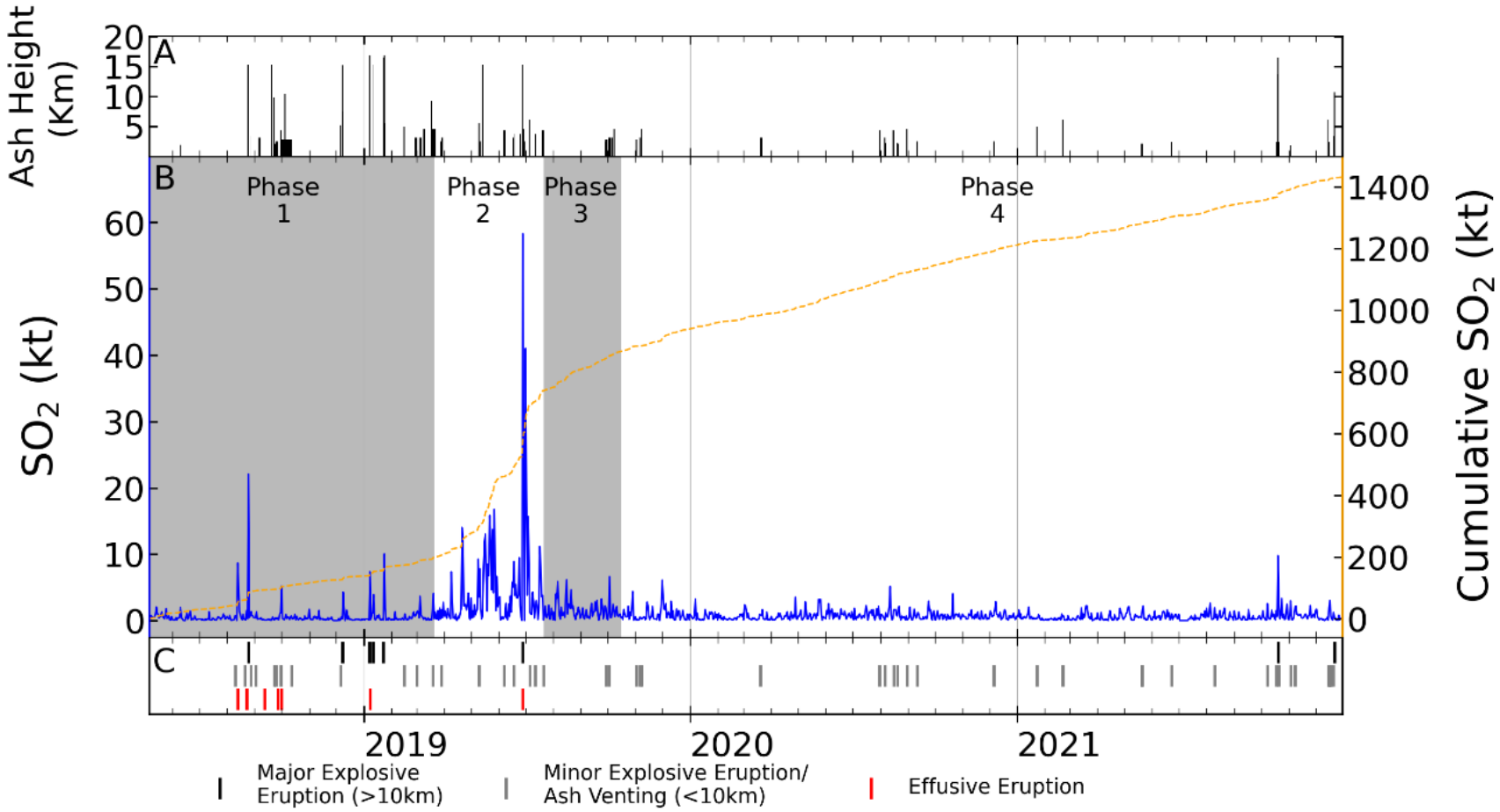

Figure 2.14 A) Ash heights reported by local RVO observers and Darwin VAAC. B) Daily TROPOMI SO_2 mass loading retrievals for Manam 6 May 2018 - 31 December 2021. Time series is annotated with four identified degassing phases. C) Observed eruptive activity.

to the relatively lower emission rate of Phase 3. Interestingly, explosive activity ceased in July 2019 (until October 2019), and yet the 7-day moving average SO_2 mass remained elevated above 1 kt day^{-1} throughout Phase 3, a time-averaged SO_2 flux more than twice that of either Phase 1 or Phase 4.

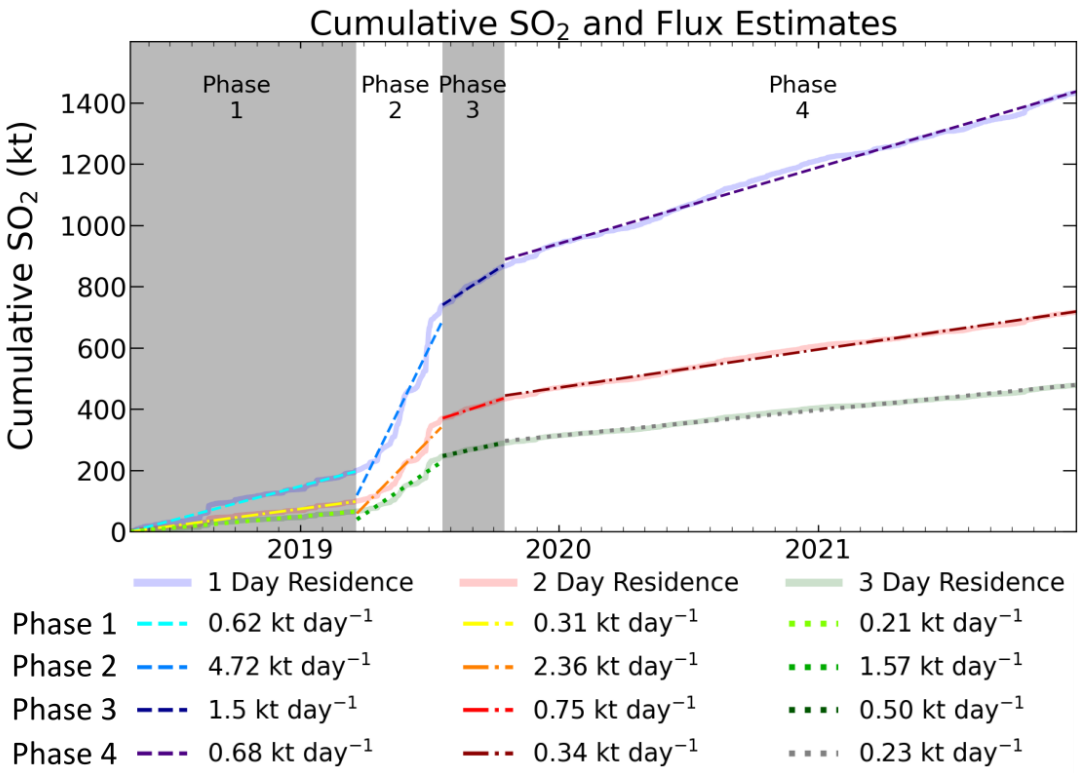

Figure 2.15 Cumulative SO_2 under 1 day, 2 day, and 3 day residence time regimes (solid lines). Each regime is divided by the 4 identified emission phases. A polynomial was fitted for each regime and phase (dashed lines) and the gradient of each line indicates the average daily flux.

Phase 4 began on 17 October 2019 when the 7-day average SO_2 mass loading dropped below the 1 kt day^{-1} threshold for 10 consecutive days. In total, 565 ± 24.9 kt of SO_2 was emitted during Phase 4 with a time-averaged flux of 0.68 kt day^{-1} (**Figure 2.15**), signalling a return to emission rates similar to those Phase 1. A major eruption on 20 October 2021 generated the largest SO_2 mass loading (9.8 kt) of the phase. This event occurred at during a period of heightened emissions between 18 October 2021 and 10 November 2021, where mean daily emissions were 1.5 kt.

2.4 Discussion

Remote sensing observations show that while thermal activity at Manam tends to occur in clusters lasting several months, SO_2 emissions are continuous and persistent. Periods of enhanced thermal emission are often, but not exclusively, concurrent with eruptive activity. For example, numerous thermal anomalies are detected during Cluster 2 during periods with no reported activity and, conversely, eruptive activity between August and September 2017 is not associated with any detected thermal emissions. Unlike the punctuated nature of thermal activity, SO_2 emissions maintain an average daily mass loading over the period of observation of ~1.1 kt, reinforcing the classification of Manam as being in an open-vent state. Four distinct phases are identified within the SO_2 emission time series that highlight fluctuations in volatile supply and transport in the shallow magmatic system over month to year timescales.

Here, the relationship between SO_2 and thermal emissions is examined and the magnitude of excess degassing at Manam is constrained by using these two parameters to estimate the balance between supplied and erupted magma. Additionally, the VRP is used as a proxy for the height of the magma column in Manam's South Crater and discuss the implications of changing magma level for signalling pressure changes within the conduit and shallow magma reservoir system. Next a conceptual model is proposed that attempts to explain the observation co-variation in both gas and thermal emissions, and their relation to the timing of major eruptions. More broadly, the extent to which persistent open vent emissions from Manam contribute to the global emissions budget is quantified

and followed by a discussion of the implications of strongly time-varying behaviour in open vent systems as a source of uncertainty in global degassing inventories based on single or sporadic in situ measurements.

2.4.1 Do gas and thermal emissions exhibit coupled behaviour?

Gas and thermal emissions are two key parameters for monitoring changes in activity at open-vent volcanoes such as Manam, where an established connection exists between a shallow reservoir and the surface (Wright et al. 2004; Sparks et al. 2012; Pyle et al. 2013; Blackett 2013; Aiuppa 2015). The temporal relationship between these two parameters can be used to infer the processes operating in the shallow region of the magmatic plumbing system. Thermal anomalies indicate magma is near or at the surface and therefore represent high pressure in the system, especially those not associated with eruptions (Coppola et al. 2012; Harris 2013a; Dehn and Harris 2015; Laiolo et al. 2018). SO_2 emissions provide insights into conduit permeability (Edmonds et al. 2003b), conduit convection (Shinohara 2008) and deep magma supply (Allard et al. 1994; Aiuppa et al. 2017). Using both monitoring parameters enables more specific processes to be invoked to explain the observed activity at Manam.

Thermal and SO_2 emissions have been shown to display broadly coupled behaviour at other open-vent systems (Flower and Carn 2015; Laiolo et al. 2017, 2018; D'Aleo et al. 2019; McCormick Kilbride et al. 2019; Coppola et al. 2019, 2022), where periods of heightened radiant heat flux tend to be accompanied by above-background SO_2 degassing. At Stromboli (Italy), during the period August 2018-April

2020, periods of elevated thermal flux are accompanied by increased SO_2 fluxes during periods of more intense eruptive activity; however, during extended periods of unrest lasting days to weeks, peak SO_2 emissions lag behind the preceding VRP peak (Coppola et al. 2012; Laiolo et al. 2018, 2022; Viccaro et al. 2021). This relationship has been interpreted as an initial cessation of the convection in the upper conduit during the initially high eruption rate followed by the reestablishment of conduit convection (Laiolo et al. 2022). Conduit convection is the process often invoke to explain the excess degassing observed over long-term periods by recycling magma (Kazahaya et al. 1994; Shinohara 2008; Carey et al. 2013; Coppola et al. 2022). Bagana (Papua New Guinea) exhibits very high daily SO_2 emissions (10 kt day^{-1}) during extrusive periods which suggests a coupling between gas emissions and lava, and therefore thermal emissions (McCormick et al. 2012; McCormick Kilbride et al. 2019, 2023). More generally, coincident enhanced thermal and SO_2 emissions have been observed at other open-vent systems globally, including Batu Tara (Indonesia) (Laiolo et al. 2018), Tinakula (Solomon Islands) (Laiolo et al. 2018), and Etna (Italy) (D'Aleo et al. 2019; Coppola et al. 2019).

Instances where thermal and SO_2 flux timeseries are not well correlated temporally also provide insight into the subsurface volcanological processes that modulate surface activity and the timing of passive to eruptive transitions. Periods of high SO_2 flux but low radiant heat flux during quiescence phases are typically attributed to unerupted magmatic intrusions. For example, SO_2 fluxes at Etna (Italy) were sustained above average for several months in 2005-2006, yet radiant heat flux remained well below average with GPS measured deformation indicating the

intrusion of the degassed magma (Coppola et al. 2019). Conversely, periods of below-average SO_2 flux but high radiant heat flux, often accompanied by eruptions, are commonly explained as the extrusion of residual, previously degassed magma in response to increased pressure in the magma reservoir. This was the case during the prolonged effusive eruption (2006-2012) at Tinakula (Laiolo et al. 2018). The effusive phases each exhibited high VRP typical of lava bodies, however, while the earliest phase in 2006-2007 had above background SO_2 emissions, the final phase (2011-2012) emitted markedly less SO_2. It has therefore been suggested that the initial phase of volatile rich magma tapped an older relatively degassed residual magma which eventually was extruded in the final phase (Laiolo et al. 2018).

Here, the degree to which co-variation in SO_2 and thermal emission timeseries at Manam is coupled for each of the four defined degassing phases that have been characterised by distinct rates of SO_2 emission is evaluated. Specifically examined is the relationship between the frequency and magnitude of the daily SO_2 mass loadings and the intensity of thermal VRP for the period 6 May 2018 to 31 December 2021, as this spans the time for which both Sentinel 5P TROPOMI and MODIS data are available for direct comparison.

The combined timeseries for SO_2 emissions and VRP shows that the relationship between these two parameters is not immediately clear (**Figure 2.16a**). Thermal anomalies typically begin to be detected in the weeks prior to peaks in SO_2 mass loading (broadly defined as above the long-term average of 1 kt day^{-1}) and they peak in magnitude relatively closely, within days to weeks, of major eruptions. The exact timing of VRP maxima is often somewhat ambiguous to define, due to the

frequent cloud cover and the presence of ash in eruptive plumes, both of which obscure the thermal signal leading to data gaps.

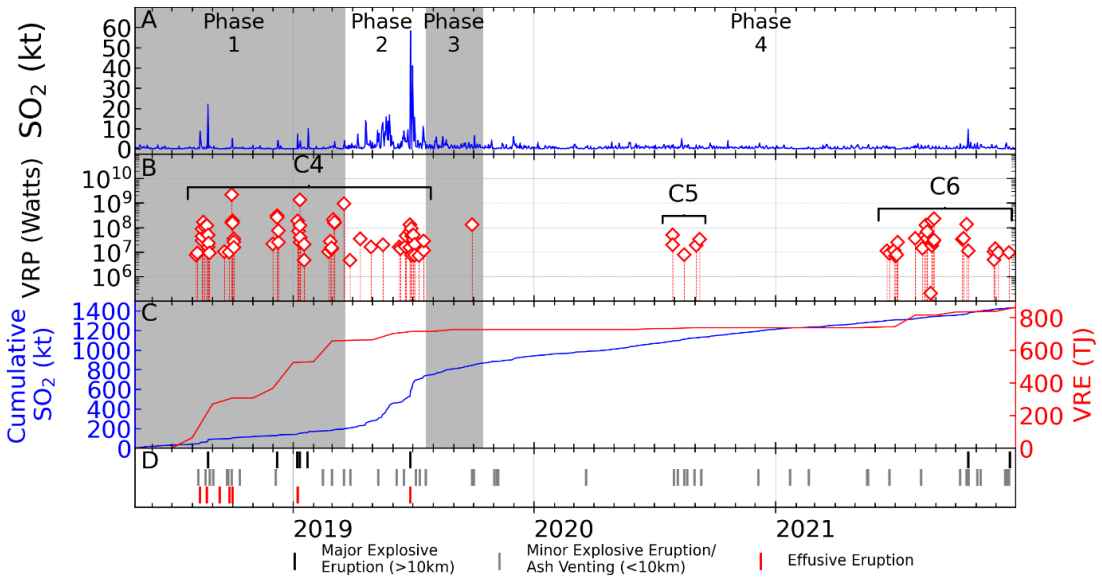

Figure 2.16 Combined timeseries of SO_2 emissions (A), thermal anomaly detections (B), cumulative SO_2 emissions (blue) and thermal energy (red) (C) and reported activity (D).

Of the three most intense thermal anomalies (~1000 MW), which all occur during degassing Phase 1, two are coincident with long lava flows that reached within 500 m of Manam's coastline. The major eruption on 28 June 2019 produced the largest lava flow in terms of inundation area (1.63 km^2), and yet is associated with a measured VRP of only 90 MW. A substantial portion of the radiance from this effusive eruption was likely obscured by the ash-rich eruption column and subsequent overpasses of MSI reveal that meteorological cloud cover was substantial during the following days, therefore it is probable that the true VRP would have been greater. Given the intensity of the third of the peak thermal emissions reaching 1000 MW (19 March 2019), it is likely that this was also

associated with an unreported lava effusion that was not captured in MSI, ASTER or OLI satellite imagery due to a combination of cloud cover issues and no overpasses near the *MODVOLC* detection date.

Cumulatively, Manam emitted a total SO_2 mass of 1432 ± 480 kt and radiated 86 ± 26 x 10^{13} J between 6 May 2018 and 31 December 2021 (**Figure 2.16c**). By expressing both gas and thermal time series in the form of cumulative outputs, it is clear that relative timing of peak emissions between these two parameters are temporally offset during the study period. Increases in the cumulative VRP are most pronounced during Phase 1, and yet are accompanied by only a modest increase in cumulative SO_2 associated with sustained background emissions. Conversely, in Phase 2, SO_2 emissions show a steep increase in cumulative mass loading with a more gradual increase in emitted thermal energy. The cumulative thermal emission curve levels off in Phase 3, indicating negligible thermal energy release during this period, and remains flat throughout most of Phase 4. In contrast, cumulative SO_2 emissions continue to increase steadily throughout Phase 3 but at a reduced rate; reestablishment of the cumulative gradient similar to that observed in Phase 1 signals the beginning of Phase 4 and a return to background emissions (**Figure 2.16c**).

The correlation between total weekly SO_2 emissions and total weekly volcanic radiative power is strongest during Phase 1 with a Pearson's correlation coefficient (r) of 0.27, which implies a weak positive relationship between SO_2 and thermal emissions during this period (**Figure 2.17**). Although the co-variation is not well fit by a simple linear relationship, relative changes appear broadly coupled; days

where SO_2 emission is elevated above background are generally associated with greater, but highly variable, VRP.

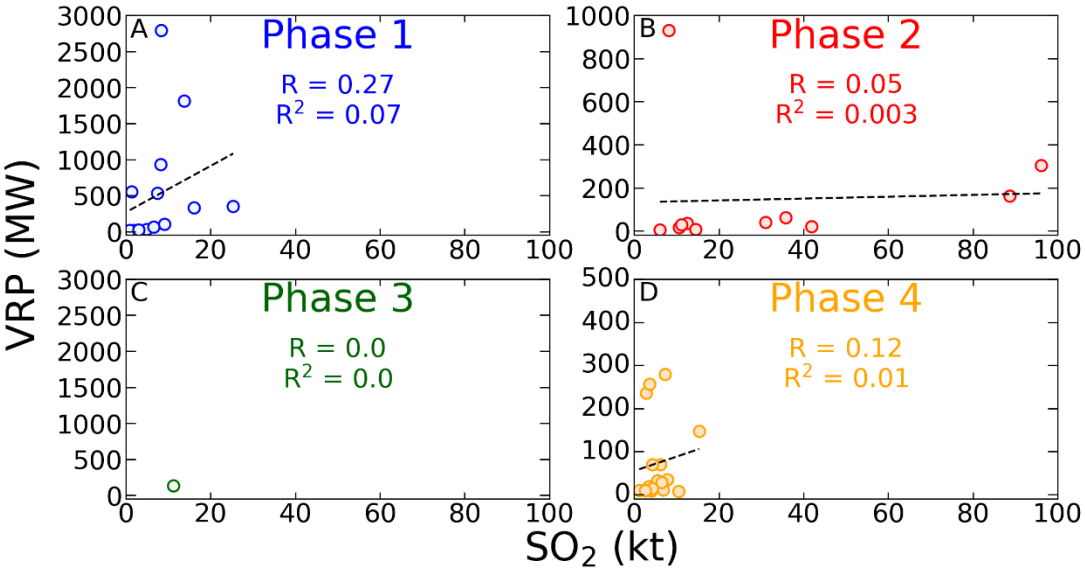

Figure 2.17 Weekly total SO2 emissions versus weekly total volcanic radiative power. R and R^2 values calculated using Pearson's Correlation by degassing phase.

2.4.1.1 Phase 1

A clearer relationship exists between the timing of emission peaks of the two parameters during Phase 1. Throughout this period, peaks in SO_2 emission occur coincident with periods of heightened radiant flux, and are typically aligned with an observed eruption (**Figure 2.18**). On five occasions thermal anomalies begin to be detected days to weeks ahead of an eruption that is also coincident with elevated SO_2 emission (e.g., August 2018, October 2018, December 2018, January 2019 and March 2019; **Figure 2.18**)). Volcanic radiative power tends to peak close to the time of eruption and then reduces rapidly, with further thermal anomalies ceasing within days. The notable exception to this pattern is the 23 January 2019 eruption where SO_2 emissions peak with no anomalies detected which could potentially be due to obscuration of the thermal signal by meteorological or volcanic cloud.

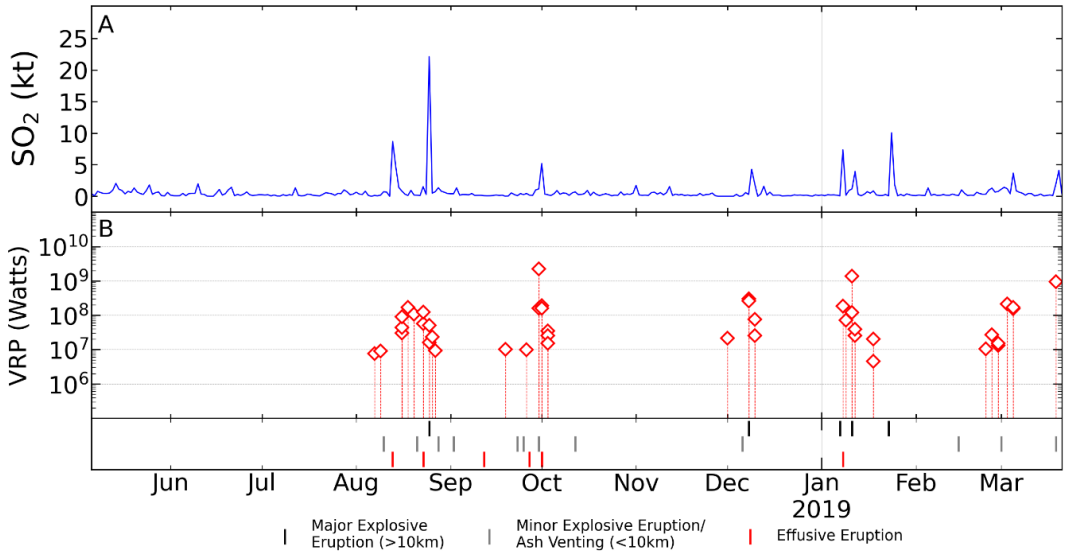

Figure 2.18 Focused view of SO_2 mass and volcanic radiative power during gas emission Phase 1. The peak deviations from background emissions of both parameters are linked temporally with peak SO_2 emissions regularly coinciding with eruptions. Thermal anomalies tend to appear in the days to weeks before eruptions, peak around the time of the eruption and then disappear in the following days.

2.4.1.2 Phase 2

Phase 2 is characterised by several months of elevated outgassing, yet few reported eruptions prior to that occurring on 28 June 2019 (**Figure 2.19**). Only four thermal anomalies were detected from March through May 2019, of which only one was coincident with a peak in SO_2 emission and none with an eruption. Magma was observed in situ at shallow depths within South Crater on 22 May 2019 by an UAS (Liu et al., 2020) during a month of sustained increased SO_2 emission. No anomaly was detected on the day of the field observation. However, a hotspot was observed in the SWIR in MSI imagery on 20 May 2019 and 30 May 2019, both with relatively high PITs, which suggests the same anomaly was likely present on 22 May 2019 (**Figure 2.12**) but was most likely obscured by cloud cover over the summit at the time of satellite overpass (E. Nicholson, Pers. Comms.).

SO_2 emissions in June 2019 were lower than in May but remained above background levels. The major eruption on 28 June 2019 produced the greatest daily mass loading observed throughout the study period (58.3 kt). Thermal emissions increased in the days to weeks prior to and including 28 June 2019, with increasing VRP from 10 to 100 MW. Following the major eruption, SO_2 emissions remain elevated until early July before reducing abruptly, while VRP declined more gradually back to 10 MW.

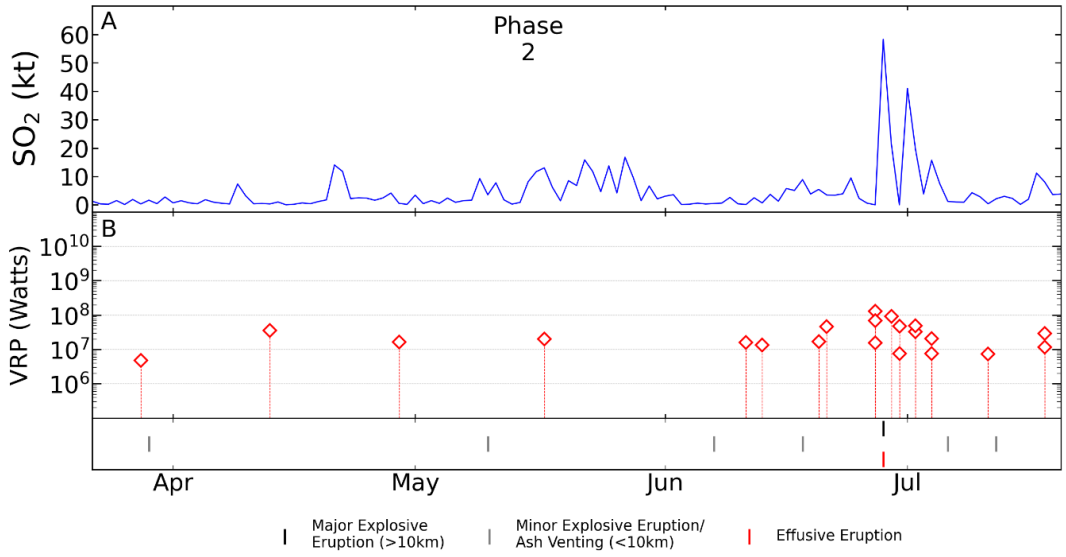

Figure 2.19 Focused view of SO_2 mass and volcanic radiative power during gas emission Phase 2. During this phase elevated SO_2 emissions do not coincide with the relatively sparse thermal anomalies detected in March and May. The two parameters exhibit coupled behaviour around the renewed period of eruptive activity in June which culminated in the major eruption on 28th June 2019.

Throughout Phase 2, co-variation in gas and thermal emissions do not appear to be well correlated, with the exception of maxima in both parameters during the 28 June 2019 eruption (**Figure 2.19**), and there is essentially no correlation between the magnitudes of total weekly emissions (**Figure 2.17**). However, the persistent cloud cover affecting MIS imagery (**Figure 2.12**) during Phase 2 suggests that cloud obscuration is likely to have similarly affected the MODIS acquisitions used by the

MODVOLC system. This therefore suggests that there is likely to have been a under-reporting bias in the frequency of thermal anomaly detections, and an under-estimation of the VRP for those detected, during this time.

2.4.1.3 Phase 3

Phase 3 continues to be a period of elevated SO_2 emissions though to a lesser degree as Phase 2 with time-averaged emissions during this period being 1.5 kt day^{-1} down from 4.72 kt day^{-1}. Phase 3 is notable as only one thermal anomaly was detected on the day of a minor eruption on 29 September 2019 but coinciding with an SO_2 emission of 1.9 kt. In contrast, a SO_2 emission of 7 kt on 3 October 2019 following a minor eruption the previous day did not coincide with a thermal anomaly detection. Therefore, like Phase 2, Phase 3 represent an extended period where gas and thermal emissions appear to be decoupled.

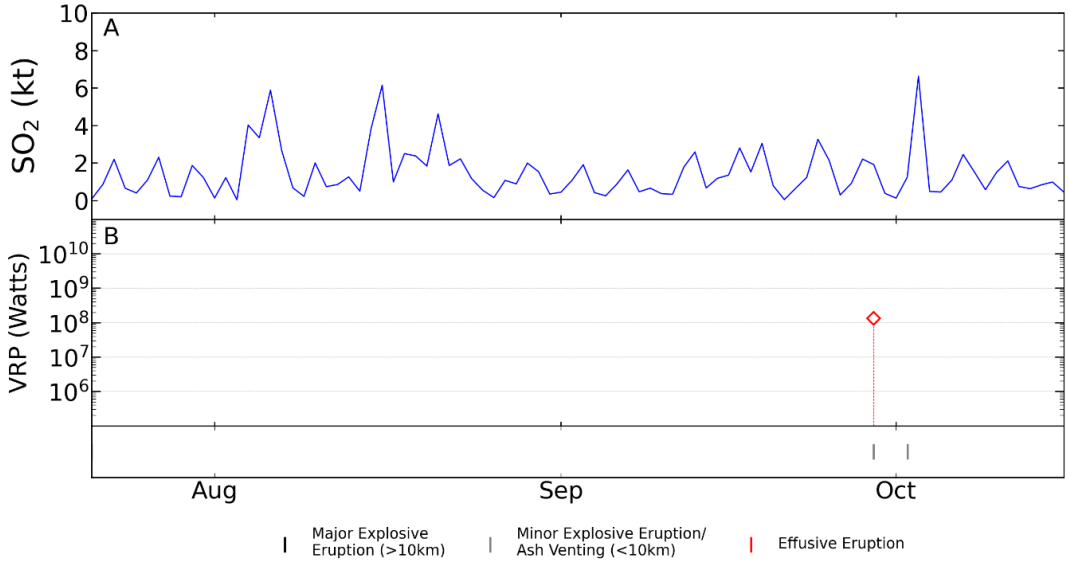

Figure 2.20 Focused view of SO_2 mass and volcanic radiative power during gas emission Phase 3. During Phase 3 thermal and SO_2 emissions are strongly decoupled. Only one thermal anomaly was detected while SO_2 emissions continued to be elevated above background emissions.

2.4.1.4 Phase 4

Phase 4 is the longest period lasting just over 2 years and 2 months with average daily SO_2 emissions returning to the ~0.6 kt background level last seen during Phase 1 (**Figure 2.21**). A small cluster of thermal anomalies (Cluster 5) coincided with a series of minor eruptions in August-September 2020, but where SO_2 emissions exhibit only very minor increases from background at this time. Following Cluster 5, there are nine months with no detected thermal anomalies accompanied by background degassing fluctuations. There is a strong possibility that cloud cover hindered thermal anomaly detections but the consistency of no anomalies being detected suggests that thermal activity was, at most, at a low level.

Thermal activity recommences in June 2021 and continues intermittently until the end of the study period, 31 December 2021. These renewed thermal emissions are associated with an intensification in eruptive activity through June to end August 2021, with progressively increasing peak VRP that reaches a maximum concurrent with visual observations of incandescence and audible intra-crater explosions (most likely Strombolian) in August. Again, only very minor increases in SO_2 are observed (**Figure 2.21**). Another small cluster of thermal anomalies occurred in October and peaked in VRP during the major eruption of 20 October 2021. This eruptive event generated the largest SO_2 mass loading of Phase 4 of 9.7 kt but is still far more modest than that emitted during major eruptions throughout Phases 1-3. A further series of anomalies occurred in late November through December 2021 alongside minor increases in SO_2 emissions, peaking at only ~3 kt. Reports of visible eruptive activity began in mid-December 2021 and culminated in a major eruption on 22

December 2021, which is associated with a relatively modest VRP of 10 MW and 1.2 kt SO_2 emission.

Although Phase 4 is a return to the background degassing levels seen during Phase 1 it does not appear that the thermal and SO_2 emissions returned to the coupled state observed in Phase 1. Thermal anomalies in Phase 4 were often linked with eruptions but the accompanying SO_2 emissions were relatively modest. Indeed the fluctuations in SO_2 emissions also occur during periods of eruptive quiescence and absences of thermal anomalies (**Figure 2.21**). Therefore the thermal and SO_2 emissions during Phase 4 appear to be decoupled as in phases 2 and 3.

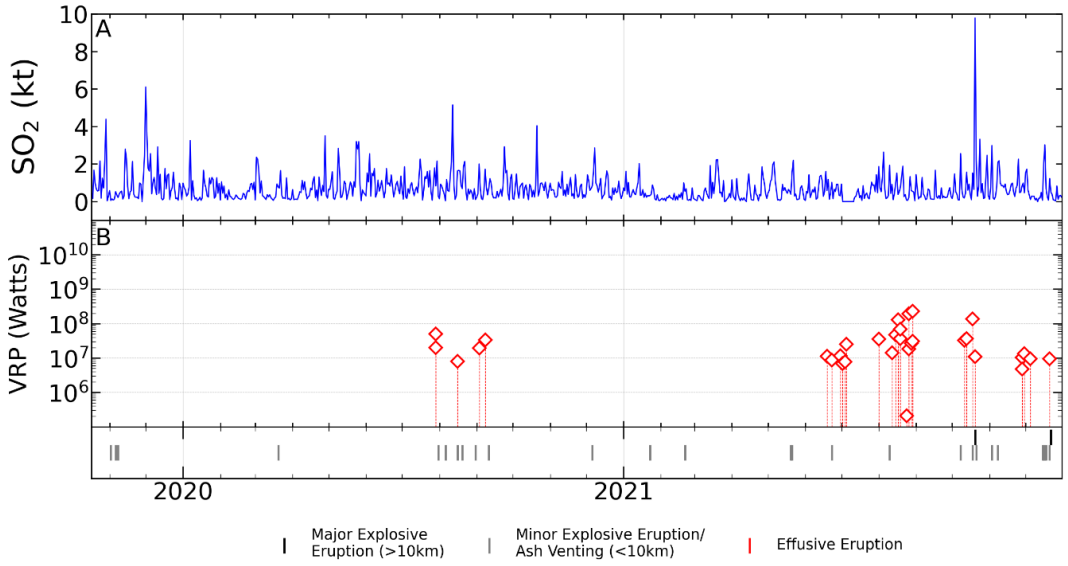

Figure 2.21 Focused view of SO_2 mass and volcanic radiative power during gas emission Phase 4. This phase represents a return to background SO_2 emissions where peaks in these emissions are coupled with thermal anomaly detections generally related to eruptions.

	SO_2 Emissions	Thermal Emissions	Coupled /Decoupled
Phase 1 (6 May 2019 – 21 March 2019)	Low background emissions peaking during eruptions	High Thermal Activity	**Coupled**
Phase 2 (22 March 2019 – 20 July 2019)	Elevated above background	Moderate Thermal Activity	**Decoupled**
Phase 3 (21 July 2019 – 16 October 2019)	Above background but reducing over time	Very Low Thermal Activity	**Decoupled**
Phase 4 (17 October 2019 – 31 December 2021)	Low background emissions fluctuating mostly independently of eruptions	Initially Low but later increasing to moderate thermal activity	**Decoupled**

Table 2.2 Summary table of SO_2 and thermal emissions characteristics by phase.

From these observations, I propose that there are two regimes during the study period, where SO_2 and thermal emissions are coupled or decoupled. Phases 1 operates under the coupled regime, where peaks in the two parameters are well correlated in time but not in absolute magnitude. In contrast, Phases 2, 3 and 4 show little to no correlation between either the timing or magnitude of thermal and gas emissions and therefore represent a decoupled regime (Table 2.2).

2.4.2 Is persistent outgassing balanced by magma flux?

Mass balance calculations at mafic open vent volcanoes globally suggest that the amount of magma required to sustain observed gas fluxes is generally far greater than that erupted (Kazahaya et al. 1994; McCormick et al. 2012; Laiolo et al. 2022).

This is sometimes referred to as the excess degassing phenomenon and is a key characteristic of open-vent volcanism (Stevenson and Blake 1998; Shinohara 2008; Vergniolle and Métrich 2021). Constraining the mass balance of magma in terms of total inputs and outputs, and how this varies over time, is key to relating observed gas emissions to the magmatic and eruptive processes operating at Manam, and at open-vent volcanoes more generally. Space-borne measurements of SO_2 emissions and radiant flux can be used to infer the amounts of magma supplied to the shallow magmatic system (input) and erupted (output), respectively. Here a mass balance approach is used from the TROPOMI derived SO_2 time series and combined with estimates of erupted volumes from plume heights reported in Volcanic Ash Advisory Bulletin (Darwin VAAC) and lava flow inundation areas calculated from MSI satellite imagery using ArcGIS.

The volume of magma required to generate the observed SO_2 emissions is calculated using **Equation 2.13**:

$$\boldsymbol{V = \frac{f}{c\,\rho\,\gamma\,\Delta S} \times 10^{-9}} \qquad \textbf{(2.13)}$$

where V = magma volume (km^3), f = measured SO_2 flux (kg d^{-1}), c = S to SO_2 conversion constant (c = 2), ρ = magma density (2640 kg m^{-3}), γ vesicularity (expressed as melt fraction i.e. 1 = 0% porosity, 0.7 = 30% porosity), and ΔS = degassed sulphur (ppm $\times$ 10^{-6}). Density is calculated using the method of Bottinga and Weill (1970) using bulk rock compositions are from Palfreyman and Cooke (1976) and McKee (1981). Values of vesicularity and both initial and degassed melt sulphur contents are unconstrained for recent eruptive products; therefore, the

vesicularity term is varied between 0 and 30%, and the total degassed sulphur is approximated as 0.2 ± 0.02 wt %, based on the range of undegassed S contents in melt inclusions from arc magmas (Lloyd et al. 2014; Taracsák et al. 2022). Manam emitted 1432 ± 48 kt of SO_2 between 6 May 2018 and 31 December 2021, based on cumulative TROPOMI mass loadings. This mass of exsolved SO_2 implies degassing of 0.12 ± 0.01 to 0.22 ± 0.01 km^3 of magma (**Equation 2.13**). Examining the peak emissions observed during Phase 2 in more detail, the magma volume required to produce the 540 ± 11 kt of SO_2 emitted during this period is between 4.6 – 8.1 × 10^{-2} km^3, which translates to a mean flux of between 3.8 ± 0.1 × 10^{-4} and 12.1 ± 2.4 × 10^{-4} km^3 day^{-1} to supply the time-averaged SO_2 flux of 4.72 ± 0.09 kt day^{-1}. The magma volumes required to yield the cumulative SO_2 emissions for each degassing phase are summarised in **Table 2.3**.

Phase	Duration (days)	Total SO_2 Emitted (kt)	Mean Daily SO_2 Flux (kt day^{-1})	Total Magma Volume (km^3)	Mean Magma Volume (km^3 day^{-1})
1	319	199 ± 8	0.62 ± 0.03	1.7 – 3.0 × 10^{-2}	0.5 – 1.7 × 10^{-4}
2	120	540 ± 11	4.72 ± 0.09	4.6 – 8.1 × 10^{-2}	3.8 – 12.1 × 10^{-4}
3	87	128 ± 4	1.5 ± 0.05	1.1 – 1.9 × 10^{-2}	1.3 – 3.9 × 10^{-4}
4	806	565 ± 25	0.68 ± 0.03	4.9 – 8.5 × 10^{-2}	0.6 – 1.9 × 10^{-4}
All	1332	1432 ± 48	1.1 ± 0.04	1.2 –2.2 × 10^{-1}	0.9 – 2.9 × 10^{-4}

Table 2.3 Summary of SO_2 emissions by phase and the calculated magma required to supply observed SO_2 emissions.

2.4.2.1 Effusively Erupted Magma Volume

The volume of erupted lava has not been routinely quantified at Manam with the distance travelled being the chief parameter recorded. In order to estimate the effusively erupted volumes, lava flows were identified in true colour, SWIR and TIR satellite imagery from Sentinel 2, Landsat 7 & 8 and ASTER (**Figure 2.22**). Six lava flows were clearly identifiable in satellite multispectral imagery between May 2018 – December 2021 and the area inundated by each flow was measured using ArcGIS. The volume of each lava flow was calculated using by using the average thickness of the lava flow from the September – October 2018 lava flows of approximately 3.5 m. The average thickness of this lava flow was measured by creating an digital elevation model using Agisoft Metashape from images extracted from a UAS video of Manam's northeast valley. Several transects were drawn across the lava flow from points of equal elevation either side of the flow and then the elevation every 1 m along the transect was extracted. The elevation at the side of each transect was then subtracted from the lava surface elevation to give a thickness and then the mean thickness was calculated for the flow (**Figure 2.23**). A pycnometer measured porosity of 18.77% from a sample from the 28 June 2019 lava flow was applied to the volumes to give the dense rock equivalent (DRE). The measured inundation areas and estimated volumes of the lava flows are given in **Table 2.4**.

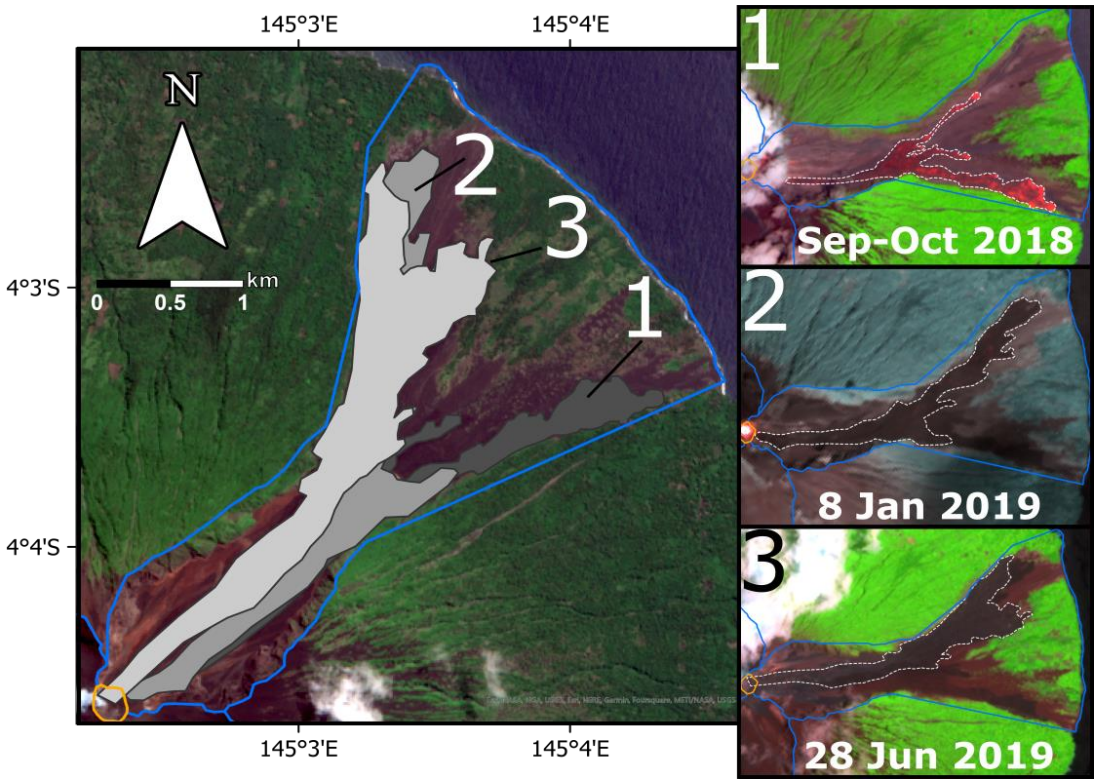

Figure 2.22 Inundation areas of the three largest lava flows during 2018-2021. 1) - 1h September –1 October 2018 (dark grey) MSI composite image Bands 4, 8A And 12 from 2 October 2018 overpass. 2) 8 January 2019 (middle grey) Landsat 8 composite Bands 5 and 7 – 22 January 2019 (light grey). Background imagery MSI composite image Bands 4, 8A And 12 from 13th August 2019 overpass.

Date	Valley	Area (m^2)	Volume (m^3)	DRE (km^3)
12/09/2018-01/10/2018	Northeast	0.89×10^6	3.13×10^6	2.55×10^{-3}
08/01/2019	Northeast	1.39×10^6	4.89×10^6	3.98×10^{-3}
28/06/ 2019	Northeast	1.63×10^6	$5{,}68 \times 10^6$	4.62×10^{-3}
13/08/2019	Northeast	0.17×10^6	0.59×10^6	4.81×10^{-4}
26/08/2021	Southwest	0.23×10^6	0.80×10^6	6.51×10^{-4}
21/08/2021	Southwest	0.05×10^6	0.16×10^6	1.29×10^{-4}

Table 2.4 Satellite measured lava flow inundation areas with volumes calculated from mean thickness of the September - October 2018 lava flows (Figure 2.23). Dense rock equivalent was calculated by removing the porosity of a sample from the 28 June 2019 lava flow as measured by pycnometer.

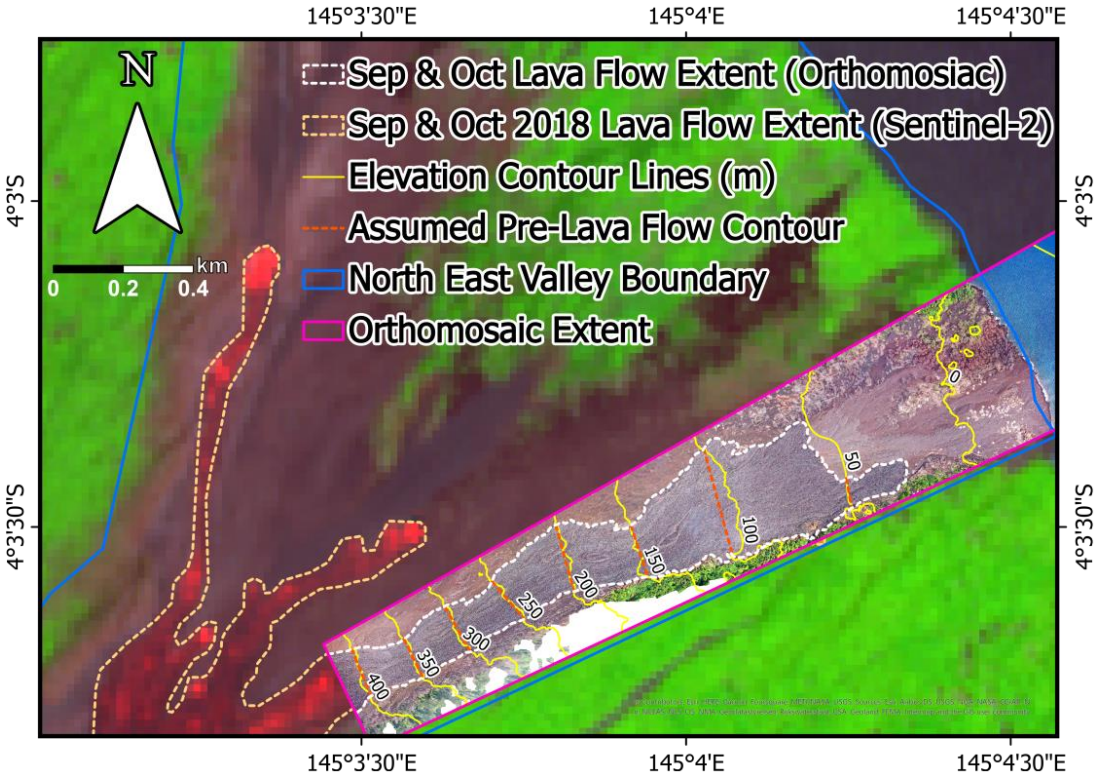

Figure 2.23 The lower portion of the September & October lava flow (extent marked in light orange dashed lines) identified in composite MSI imagery on 2 October 2018. Overlain is the orthomosiac of the lava flow (limits marked by pink bounding box) constructed from UAS imagery from late October 2018 (courtesy of Dr Keiran Wood, University of Manchester, UK and Dr Emma Nicholson, University College London). A DEM was constructed using this orthomosaic corresponding to the same pink bounded area. Lava flow thickness estimates produced using the difference between the measured elevation of the lava flow surface and the approximated straight continuation (dark orange dashed lines) of the elevation contours (yellow lines). Full method detail given below.

2.4.2.2 Explosively Erupted Magma Volume

The erupted mass from explosive eruptions is typically estimated by exhaustive field collection of tephra samples to create a total grain size distribution (TGSD) and performing inversion modelling (Connor and Connor 2006). Complete and representative TSGDs are difficult to collect due to inaccessibility of proximal areas immediately following a volcanic crises and the fast erosion of the finest grained material in distal locations. Ideally, collection of TGSD samples should happen in as soon as possible after an eruption to reduce the impact of erosion on the tephra

deposits however this is rarely possible. The mathematical description of the thinning of tephra deposits is required to calculate the volume erupted magma from an explosive eruption. However, this cannot be done using a simple exponential decay and requires more complex, and it some cases multiple, trends to provide realistic estimates of erupted volumes from a TSGD (Bonadonna and Houghton 2005). A considerable issue for coastal and island volcanoes like Manam is that a substantial portion of the erupted tephra falls out over the ocean making it virtually impossible to create a complete TGSD for these eruptions. Sampling for TGSD is typically only carried out for eruptions with a large tephra fall footprint; examples of TGSD are uncommon. Additionally, frequently erupting volcanic systems also present difficulties due to the regular contamination of one ash deposits by subsequent eruptions, especially in proximal areas. These considerable difficulties mean that TGSDs are not available for the majority of volcanoes globally and commonly TGSDs from analogous volcanic systems are used in tephra deposition modelling.

With TGSDs being unavailable for most volcanoes an alternative method for estimating the erupted volume is needed. Mastin (2009) examined the relationships between the eruption plume heights, erupted volumes, and eruption rates from a range of eruptions where these parameters and other eruption source parameters were published. The eruption catalogue includes moderate to large explosive eruptions and spans low to high silica content magmas. Plume height observations within this catalogue were ascertained by ground-based or airborne observations, radar measurements or cloud satellite temperature. A positive correlation was

identified for the 34 eruptions in the catalogue with measured plume heights, *H* (km), and estimated erupted volumes, V (km^3 DRE), with the following line of best fit:

$$H = 25.9 + 6.64\log_{10}(\mathrm{V}) \qquad \textbf{(2.14)}$$

This correlation between plume height and erupted volume has been interpreted as the conduit widening and associated increases in mass discharge rate with time (Carey and Sigurdsson 1989; Mastin et al. 2009). **Equation 2.14** is used to calculate the erupted volumes at Manam based on RVO observation and reported heights from the Darwin VAAC reports. The uncertainty with using **Equation 2.14** to calculate erupted volume from plume height is estimated to be approximately one order of magnitude (L. Mastin, Pers. Comms.) caused by outliers in the catalogue. Examples of outliers in the dataset are a) long-lasting eruptions producing with modest eruption plume heights erupt a much greater volume than would normally be expected of small to medium plume heights due to their extended duration, or b) very large eruptions with eruption plumes of over 25 km where the erupted volume is not as great as the line of best fit would forecast such as the 1991 Pinatubo eruption. The longest duration eruption at Manam in the last 22 years was the climatic phase of the 2004-05 eruption, which lasted for approximately 15 hours and producing a plume with a maximum height of 24 km (Tupper et al. 2009; Global Volcanism Program 2021b). This is also the highest recorded plume altitude this century and so it is assumed that Manam's erupted volumes are more likely to follow the identified trend (**Equation 2.14**) than to tend towards the outliers in

eruption catalogue. Therefore it is reasonable to use **Equation 2.14** to estimate the erupted volumes from observed plume heights at Manam.

2.4.2.3 Magma Balance at Manam

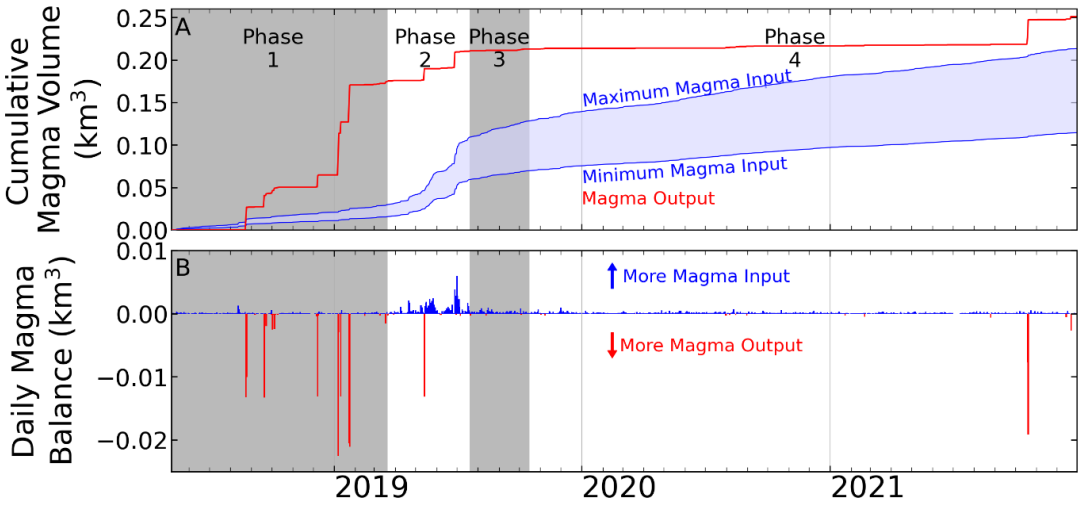

Figure 2.24 A) Cumulative magma output (i.e. effusively and explosively erupted magma) (red) and cumulative magma input (magma reaching the exsolution level for SO_2 at depth) (blue). The minimum and maximum magma input values are based on varying the assumed sulphur content (1000-2500 ppm) and vesicularity (0-30%) (Liu et al. 2020a) of the melt used in the petrological method to calculate magma volumes from SO_2 flux (Shinohara 2008). B) The daily net magma balance.

The balance of magma entering and leaving Manam's plumbing system is calculated by subtracting daily magma input from output and is characterised by a near-constant low input as seen in Phases 1 and 4 (**Figure 2.24**) punctuated with substantially larger output of magma in both effusive and explosive eruptions. It is difficult to draw conclusions over longer timescales, especially those that encompass different eruptive and degassing phases. However, by using the four previously defined degassing phases it is possible to gain further insight into the changing open-vent behaviour at Manam. For instance, 70% of erupted magma over the time series was during Phase 1 where it is likely that degassed magma from the previous eruptive phase in 2017 was forced out of the plumbing system to

accommodate the increased pressure resulting from the arrival of fresh magma deeper in the plumbing system. With the removal of this degassed and therefore more crystallised magma, it became easier for exsolved volatiles to flux through the plumbing system. **Figure 2.24** suggests that more magma was erupted (~0.25 km^3) than the maximum estimate of magma entering the system (~0.22 km^3) which is very unlikely at an open-vent system. Though these values do remain within the associated errors. However, if it is accepted that the erupted magma during Phase 1 is indeed from a previous batch of unerupted magma, potentially associated with the 2017 eruptive period, then this phase can be set aside and only consider Phase 2 onwards. The total magma volume of magma entering the system from Phase 2 to 4 is 0.18 km^3 and the volume of erupted magma is 0.08 km^3. These values indicate the return of more efficient movement of volatiles through the system as Manam began to exhibit excess degassing that is commonly observed at open-vent volcanic systems.

2.4.3 Can thermal emissions provide a proxy for magma column height?

Observations have shown that the level, or heights, of magma columns and lava lakes can vary substantially over days to months. In particular cases these variations in magma height within the conduit or crater have been shown to be precursors to eruptions. Changes in magma column height are thought to reflect the pressure within the magmatic reservoir with rises indicating increased risk of paroxysms. For example the 2015 paroxysmal eruption of Villarrica (Chile) was preceded by a rapid magma column rise inferred using infrasound (Johnson et al. 2018). At Stromboli (Italy) the rise of the magmatic column and resulting lava effusions are thought to

have triggered the 2003 and 2007 paroxysms (Calvari et al. 2011). Drops in magma column level can indicate potential drainage events that may manifest as flank effusions. This has been shown to be the case at the lava lakes at Kilauea (USA) (Patrick et al. 2015b, 2019a) and Nyriagongo (D.R. Congo) (Barrière et al. 2022) where lake levels have varied over multi-year periods and decreases have been linked to extrusions and deep intrusions.

Typically magma column heights are observed or inferred using infrasound but due to Manam's regular activity, direct observations into the crater are not possible and Manam is not monitored by infrasound equipment. However, the daily coverage of Manam by MODIS can potentially be used to infer the height of the magma column. Coppola et al. (2012) demonstrated that the theoretical VRP of a magma filled crater at Stromboli could be calculated by assuming temperature and knowing the surface area occupied by magma in a completely filled crater. This section will explore the use of this method to estimate the magma column height within Manam's South Crater and how this can be used to gain insight into the processes driving activity at Manam.

VRP provides a means to quantify temporal variability in the thermal energy radiated by Manam. Changes in VRP can be explained by changes in the temperature of the radiating body, the emissivity of the radiating surface, or the surface area of the radiating body. In closed volcanic systems, an increase in VRP indicates a corresponding increase in the temperature of surface rocks. This temperature increase commonly provides an early signal of unrest, potentially signalling the ascent of magma or hot exsolved fluids which progressively heat

surface rocks via conduction. At open-vent systems where the magma column is observable by the satellite the change in VRP can also be linked to a change in magma temperature and also the surface area occupied by the magma column either in the conduit or the crater.

Where lava is directly observable by MODIS, VRP can be linked to an active lava area ***A*** (or any volcanic target with a temperature greater than 300°C) through the Stefan-Boltzmann law (**Equation 2.15**) (Coppola et al. 2013):

$$VRP = A\sigma\varepsilon T_e^4 \qquad \textbf{(2.15)}$$

where σ is the Stefan-Boltzmann constant (5.67 x 10^{-8} W m^{-2} K^{-1}), ε is the emissivity, T_e^4 (K) is the effective radiation temperature (i.e., the area-weighted temperature of the active lava surface that radiates an equivalent heat power). Active lava bodies are most commonly lava flows or lava lakes but also include situations where the top of the magma column is present at very shallow depths within the conduit or filling a portion of the crater (as observed at Manam on 22 May 2019; (Liu et al. 2020a), allowing it to be directly observable by in situ observations or by satellite-based sensors.

Adapting the method of Coppola et al., (2012), the measured VRP is related to the surface area of lava exposed within the South crater of Manam and, for a range of crater geometries, show how variations in VRP may signal changes in the height of the magma column. It should also be noted that the height of the magma column within the crater in combination with the satellite viewing or zenith angle can result in impaired line of sight of the magma body producing the thermal signal (Dehn et

al. 2002). This could produce a smaller estimated intra-crater magma height under this method but this is not considered here but could be investigated in further work developing this technique. These changes in magma column height within the South Crater are then put in the context of observed eruptive activity. It should also be noted that the height of the magma column within the crater

2.4.3.1 Estimating the Geometry of South Crater

The geometry of Manam's South Crater is not well understood and so I approximate it here using a conical frustrum (i.e. a truncated cone). True colour satellite imagery from MSI shows that the crater is approximately circular in shape, with crater rim area of 6983 m^2 calculated using ArcGIS software, and relatively steep walls (**Figure 2.25**). Approximating the crater as a perfect circle, this area translates to a radius of 47.15 m and provides constraints on the top dimensions of the conical frustrum. In June 1987 South Crater was estimated to have a depth of ~60 m based on aerial observations (Global Volcanism Program 1987). This report didn't report the size of the bottom of South Crater and so information from analogous open vent volcanoes are used to estimate the dimensions of the base of the crater and the flare angle. The flare angle is the angle between the crater base and the walls, and in situ observations during lava lake drainage events that expose the lower regions of the craters at Villarrica, Nyiragongo, Kilauea, and Erta Ale indicate that this angle can vary widely between 30° and 90° (Bouche et al. 2010; Spampinato et al. 2013; Burgi et al. 2014; Qin et al. 2018). Wide-based craters typically have shallower flare angles tending towards 90°, whilst those craters with smaller bases often have steeper crater walls with flare angles of <45° (Qin et al. 2018). Here, Villarrica (Chile) is used

as an analogy to Manam due to its similar eruptive behaviour and crater geometry. Villarrica's conduit is estimated to be between 10 and 20 m in diameter, transitioning to a crater with steep walls and a relatively small flare angle (Moussallam et al., 2016), approximated experimentally as 30° (Qin et al., 2018). Visual comparison of the craters at Villarrica and Manam's South Crater suggests that while similar, Manam has a narrower crater geometry. As such, the flare angle is varied between 15° and 30° for use in subsequent calculations to capture this uncertainty.

Using the upper and lower limits estimated for flare angle and conduit width, alongside the measured radius of the top of South Crater, the height of the crater can be calculated according to the cross section of a conical frustrum (**Figure 2.26**). First, the measured VRP is related to the surface area of the radiating magma by rearranging **Equation 2.15** to **Equation 2.16**.

$$A = \frac{VRP}{\sigma \div \varepsilon \div T_e^4} \qquad \textit{(2.16)}$$

With the area of the magma surface assumed to be circular, finding the radius of this circle from the calculated area (**Equation 2.16**) provides $\mathbf{R_3}$, the radius of the magma surface (**Figure 2.26**) (**Equation 2.17**).

$$r = \sqrt{\frac{A}{\pi}} \qquad \textbf{(2.17)}$$

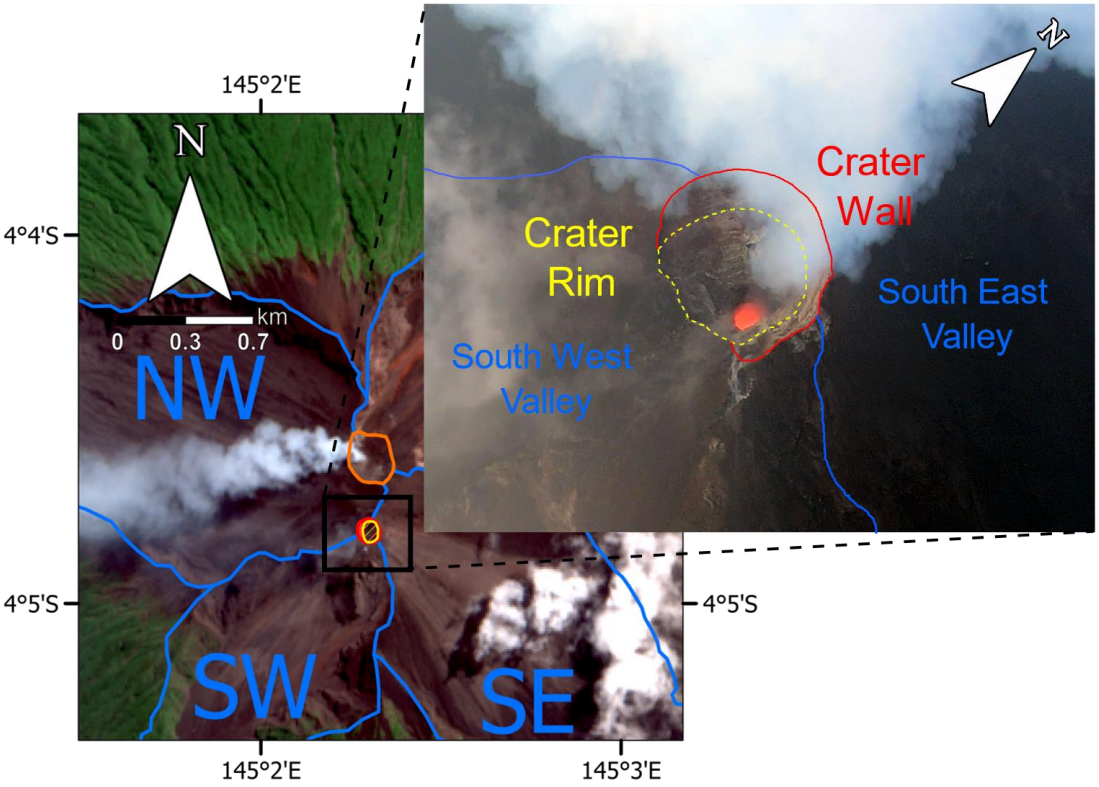

Figure 2.25 Measurement of South Crater's rim in ArcGIS (left) and zoom box showing the structure of South Crater. Yellow represents the crater rim in both images. The measurement of the crater rim perimeter is approximate due to the 10m pixel resolution of the MSI true colour imagery. The red marked areas in both images demark the crater wall which rises above the crater rim on all sides except on the southwestern side.

Once $\mathbf{R_3}$ is known, $\mathbf{a_2}$ is calculated according to **Figure 2.26** allowing the height of the magma in the crater ($\mathbf{h_2}$) to be calculated. The volume of the magma present in the crater (V) is then calculated using **Equation 2.18**:

$$V = \frac{1}{3} \times \pi \times h_2 \times ({R_1}^2 + R_1 \times R_3 + {R_3}^2) \quad \textbf{(2.18)}$$

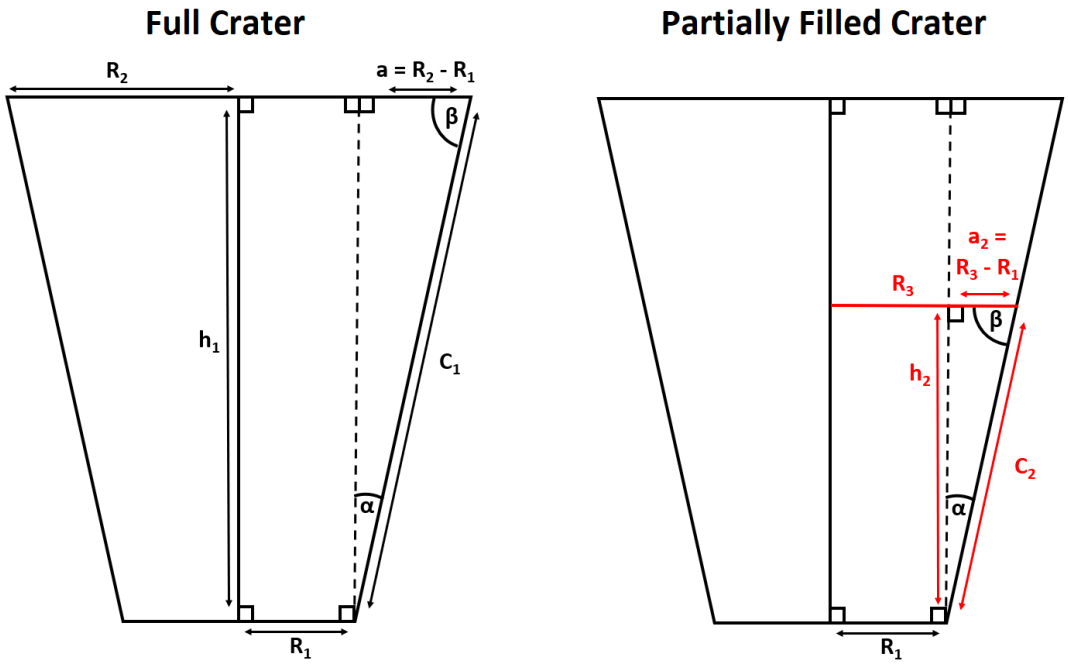

Figure 2.26 Left - Cross section of a truncated cone used to represent the geometry of a volcanic crater. Right - Cross section of a truncated cone partially filled by magma. ***R₁*** *= radius of the cone bottom representing the magma conduit,* ***R₂*** *= radius of the top of the cone representing the top of the crater,* ***R₃*** *= radius of the surface area of the magma body,* ***a*** *= the difference between* ***R₂*** *and* ***R₁,*** ***a₂*** *= the difference between* ***R₃*** *and* ***R₁,*** ***α*** *= flare angle,* ***h₁*** *= crater height,* ***h₂*** *= level or height reached by the in-crater magma,* ***C₁*** *= length of crater walls,* ***C₂*** *= length of the crater walls from base to magma height.*

Using the upper and lower estimated limits for flare angle (15-30°) and magma conduit radius (5-10 m), generates four potential geometries for Manam's South Crater (Table 2.5) including calculated height and total volume.

Smaller flare angles and conduit radii require larger crater heights to meet the measured crater area (6983 m^2) and calculated rim radius (47.15 m). This is because the rate at which a crater widens is less at smaller flare angles, so greater crater heights are required to accommodate this and similarly more widening is required from smaller conduits (**Table 2.5**). Varying the flare angle has a greater impact on crater height and volume than varying the conduit width: crater height and volume are 215% larger for a flare angle of 15° compared to 30°, whereas a change in magma conduit diameter from 10 m to 20 m produces a difference of less than 1%.

The largest crater geometry is therefore produced using a flare angle of 15° and a conduit radius of 10 m and the smallest geometry using a 30° flare angle and 20 m conduit radius. Assuming the depth of South Crater has not changed substantially since the observation in June 1987 then the two geometries based on 15° flare angles have heights that are 132-162% larger than the estimated 60 m. Comparatively, two 30° flare angles based geometries are much closer (64-73 m) and being within the same order of magnitude are reasonably within the uncertainty associated with a visual estimation. Therefore these two smaller geometries are taken forward into the calculation of intra-crater magma calculations in the next section.

Flare Angle	**Conduit/ Crater Bottom Diameter ($2 \times R_1$) (m)**	**Crater Height (h_1) (m)**	**Crater Volume (m^3)**
15°	10	157	409,069
15°	20	139	405,649
30°	10	73	189,849
30°	20	64	188,262

Table 2.5 Estimated heights and volume of South Crater, Manam based on a measured crater top area of 6983 m^2 and varied between the assumed upper and lower limits for flare angle and the conduit/crater base radius. See main text for details.

2.4.3.2 Calculated Intra-Crater Magma Heights and Volumes

The final calculation of intra-crater magma height must also consider whether radiance detected by the MODIS satellite and converted into VRP by *MODVOLC* is derived from a magma body located within South Crater. There are three situations where thermal emissions may be partially or entirely external to South Crater:

(a) During eruptions, extruded lava and tephra contribute considerable thermal energy to the overall heat budget. Therefore data is omitted from dates with reported effusive or explosive eruptive activity to improve the likelihood that detected thermal radiance is centred on Manam's craters.

(b) The VRP reported by *MODVOLC* for a given overpass includes a thermal radiance contribution from Main Crater. 94% of MSI and ASTER overpasses during the study period show a visible hotpot over South Crater compared to 75% over Main Crater. Although this indicates that there is a considerable overlap between the emitted thermal energy from both craters, visible hotspots at South Crater generally appear far larger and brighter in composite imagery (**Figure 2.27**). Since MODIS pixels are large enough to cover both craters it is not possible to resolve the relative contributions of each crater to overall VRP. Therefore, for the purposes of this calculation, it is assumed that all detected thermal energy originates from South Crater but recognise that this is likely to be an overestimate.

(c) In this method the assumed conduit width is used as the diameter for the base of the crater. This means that a calculated intra-crater magma height of 0 m indicates that the magma column height has not exceeded the point

where the conduit begins to flare outwards $\mathbf{R_1}$ (**Figure 2.26**). Assuming the conduit has a constant diameter means the surface area of the top of the magma column is constant regardless of depth. As such it means that a calculated height of 0 m not only represents the magma column reaching the base of the crater $\mathbf{R_1}$ but also a detection of the magma column at any depth with in the constant width portion of the conduit. Since this method relies on relating the magma surface area to the height within an idealised constantly widening crater, it is not possible to estimate the depth of the magma column in the conduit. Therefore any VRP measurements that produce in-crater height value of ≤0 are not reported in the results.

As with the thermal anomaly detections from which this method relies, cloud cover can obscure the thermal signal from the view of the MODIS instrument meaning that magma with South Crater may not be identified.

The timeseries of intra-crater magma heights, calculated for a 10 m diameter conduit based geometry, shows that there are 76 instances where magma is calculated to have been present within South Crater during the period 2015-2021, compared to 19 instances for the 20 m diameter conduit geometry (**Figure 2.28**). Therefore, depending on the true geometry of South Crater, between 13 and 54% of total non-effusive or explosive eruption related thermal anomaly detections are linked to the magma column rising to at least the base of Manam's South Crater.

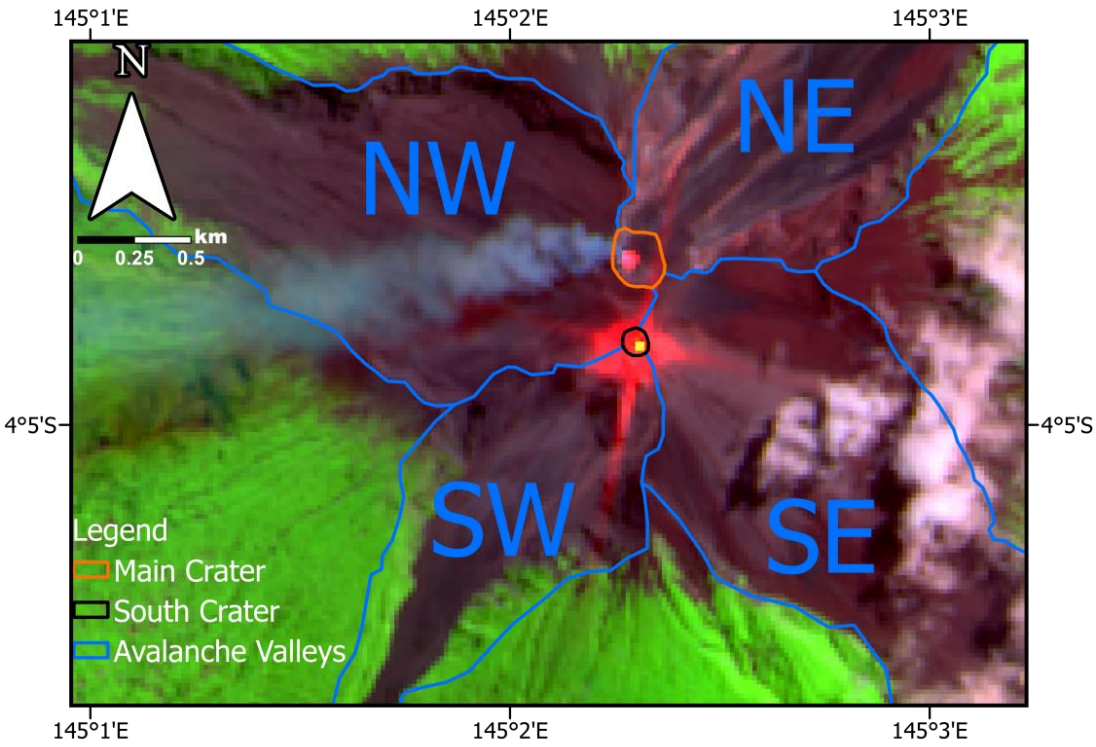

Figure 2.27 Example of the relative greater brightness and size of hotspot over South Crater (black) compared to Main Crater (orange). MSI composite image using Bands 4, 8a and 12 from 17 August 2020.

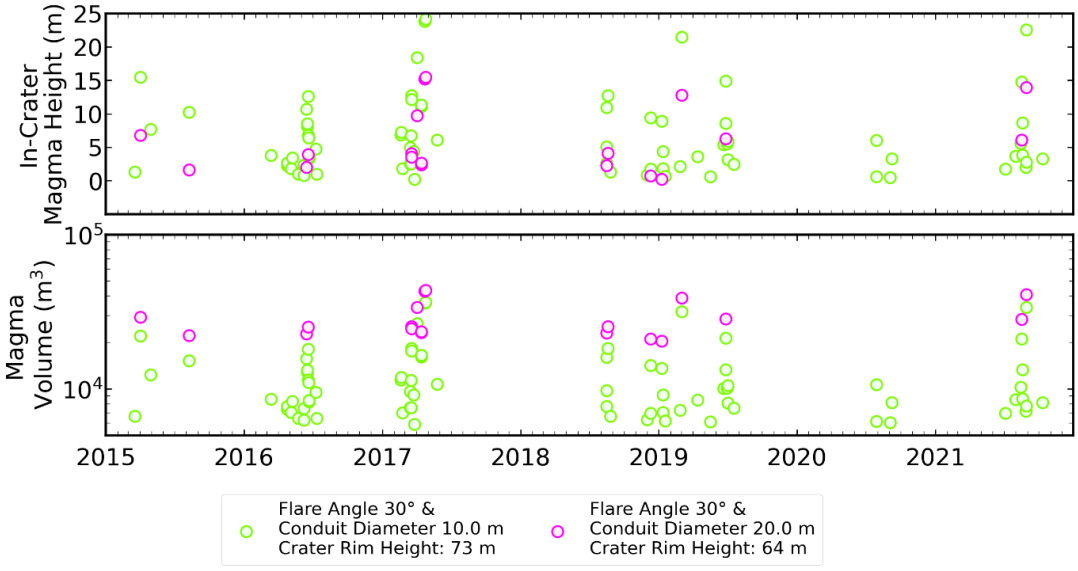

Figure 2.28 Calculated intra-crater magma heights (top) and volumes (bottom) based on VRP as measured by MODVOLC using the two assumed upper and lower geometry sizes: (1) flare angle = 30° and conduit diameter 10 m (green), (2) flare angle = 30° and conduit diameter 20 m (gold).

The maximum intra-crater magma heights are 24 m and 15 m in under the 10 and 20 diameter conduit defined craters respectively, which both equate to 49 m below the full height of South Crater depending on the geometry. Although dates where lava flows are recorded have been filtered out of the data set, there are no instances where VRP values suggest that the magma level within South Crater approaches the rim. This suggests that lava flows within the southwest and southeast avalanche valleys within the study period did not originate from overtopping of South Crater, and is instead consistent with observations that lava flows extrude principally from either Main Crater (**Figure 2.22**) or a lateral flank fissure or vent at the head of the southwest and southeast avalanche valleys (Global Volcanism Program 2021b).

Magma was observed in situ at low levels within South Crater on 22 May 2019 (**Figure 2.29**; Liu et al., 2020) and provides the only opportunity to ground-truth which of the proposed crater geometry end-members is the most realistic. No thermal anomaly was detected on 22 May 2019 this is likely due to be cloud cover during the overpass times of the Terra and Aqua satellites (10.30 am and 13.30 pm), during which time thick cloud was reported by the team responsible for the observation of the crater in the early morning (Liu, Pers. Comms.). The closest anomaly detection was two days earlier on the 17 May 2019 with a VRP of 19.75 MW. Without evidence to the contrary, it can be assumed that the level of the magma column on 17 May 2019 was similar to the level observed on 22 May 2019, but recognise that the height of a magma column or lava lake can change considerably between even consecutive days (Patrick et al. 2015b, 2019b; Lev et al.

2019). The thermal anomaly on 17 May 2019 represents a 1 m intra-crater magma height based on the 10 m diameter conduit based geometry, whereas magma is not calculated to be present within the crater if the conduit diameter is instead taken to be 20 m. Therefore, this suggests that of the two end member geometries tested, the 10 m diameter conduit flare angle is closer to the true geometry of Manam's South Crater. There are 10 reported observations of summit incandescence that are not related to eruptive activity during the period 2018-2021 (Global Volcanism Program 2021b) (**Figure 2.30**), although this record is potentially subject to an under-reporting bias. Nonetheless, most of these reported observations do not coincide with thermal anomaly detections at Manam and so may represent additional magma high stands within South Crater on days where satellite observations were obscured.

The level of the magma surface in open-vent systems is considered to reflect either pressure changes within the underlying magmatic system, such as through magma recharge or the accumulation of an exsolved volatile phase in a shallow reservoir, or variations in gas flux through the conduit, not necessarily mutually exclusive (Patrick et al. 2015b; Moussallam et al. 2016; Lev et al. 2019). Pressure increases within closed-vent volcanic systems may result in inflation of the volcanic edifice observed as ground deformation (Murray 1995; Mann et al. 2002; Dzurisin 2003; Kilburn 2012; Chaussard et al. 2013; Morales Rivera et al. 2017; Ebmeier et al. 2018; Caricchi et al. 2021), even accounting for the compressibility of gas-rich magmas (Kilbride et al. 2016). In open-vent systems, however, increases in reservoir pressure can be at least partially accommodated by a rise in the height of the

magma column. The appearance and ascent of magma within summit craters has been demonstrated as an eruptive precursor at several mafic open vent volcanoes e.g. Villarrica (Chile) (Johnson et al. 2018) and Stromboli (Italy) (Viccaro et al. 2021; Andronico et al. 2021) and can be detected by the appearance of night time incandescence, as enhanced thermal emissions in remote sensing time series (Coppola et al. 2012; Laiolo et al. 2018), and by changes in the frequency content of independent monitoring data sets such as infrasound (Johnson et al. 2018; Battaglia et al. 2019).

The level of lava lakes has been observed globally to have variations which occur over varying timescales from shorter (minutes to hours) to longer (days to months) phases (Tilling 1987; Peters et al. 2014; Richardson et al. 2014; Vergniolle and Bouche 2016; Patrick et al. 2019b; Lev et al. 2019). Shorter-term lake levels fluctuations are associated with outgassing cycles, known as gas piston activity (Orr and Rea 2012; Patrick et al. 2016, 2019a; Vergniolle and Bouche 2016; Smets et al. 2017) whereas longer-term variations are related to changing pressure in the magmatic system linked to the magma ascent rate (Richardson et al. 2014; Patrick et al. 2019a; Lev et al. 2019). These temporally differing lava lake level fluctuations can be superimposed upon one another leading to very high stands or very low stands if the peaks and troughs in the cycles align respectively (Patrick et al. 2019a). It is not possible to determine at what point in these cycles the MODIS overpasses captured but these may help explain the scatter in **Figure 2.28 & Figure** 2.30**.** The clusters of intra-crater magma likely represent the peaks in the longer-term, magmatic system pressure related cycles, whereas the scatter within these cycles

may reflect the shorter-term gas piston activity. The under-sampling resulting from the 1 to 2 MODIS overpasses a day mean that the shorter-term fluctuations are not observed and so there is some uncertainty around the timescales at which Manam's magma column height changes.

Figure 2.29 Observation of magma present within South Crater from a fixed-wing drone overpass on 22 May 2019 (Liu et al., 2020).

At Manam, no robust correlation exists between the intra-crater magma heights and emitted SO_2 (**Figure 2.30**); several magma high stands coincide with above-average SO_2 emissions (e.g. June 2019), whilst others occur when SO_2 emissions remain at background levels (e.g. August 2021). This uncorrelated relationship suggests that gas flux cannot be the dominant control over the magma column

height. Instead, here it is proposed that variations in pressure within the shallow magma storage system over weeks to months modulate the magma column height and can explain the clusters of thermal anomalies observed at Manam.

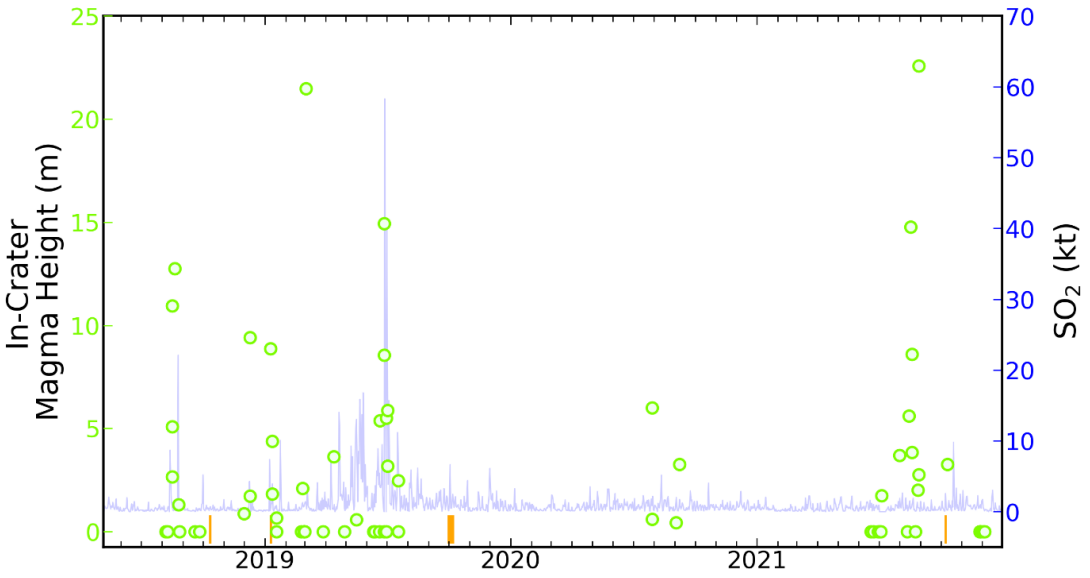

Figure 2.30 VRP-derived in-crater magma heights (green) based on a 30° flare angle and 10 m diameter conduit based geometry for South Crater plotted over the SO_2 mass emissions (blue) and observed incandescence (orange bars).

An increase in system pressure can be caused by a number of factors but primarily these are the arrival of new magma from depth and exsolution of volatiles by decompression during ascent or by second boiling (Chaussard et al. 2013; Caricchi et al. 2021). Decompression triggered exsolution typically requires the release of a lithostatic load, such as the removal of a crystallised plug, lava dome, a landslide or the removal of magma during an effusion (Edmonds and Woods 2018). However, systems that have an unobstructed conduit that allows the free movement of the magma column, as is thought at Manam, do not have a long-lasting cap or plug of cooled rock substantially blocking the conduit. As such, it is unlikely that lithostatic load changes are happening over days to weeks as suggested by the estimated magma column height changes (**Figure 2.30**). Therefore pressure changes due to

exsolution are more likely to be driven by second boiling during isobaric cooling and crystallisation. The accumulation of an exsolved volatile phase from second boiling resulting from the ascent of new magma and in conjunction the associated pressure increases from the ascending recharge magma are the proposed primary mechanisms for modulating the height of magma within Manam's South Crater. Next the occurrences of high system pressure are considered within the context of the previously defined SO_2 emission phases and recorded eruptions using heightened magma column as a proxy for high pressure. Prior to the onset of eruptive activity on 10 August 2018 no thermal anomalies were detected between 25 May 2017 and the start of thermal anomaly Cluster 1 on 7 August 2018, indicating that magma was not present in South Crater nor at the near surface and therefore it is inferred that pressure was not high during this period.

Phase 1 is suggested as a period of coupled thermal and SO_2 emissions and so like the majority of anomalies during this phase, the estimated presence of magma within South Crater also coincide with peaks of SO_2 emissions and eruptions. It is clear that pressure within Manam's plumbing system was elevated due to the regular thermal anomalies and eruptions during Phase 1 and so the estimated magma heights within South Crater underline that high pressure was often maintained between eruptions throughout this period.

Emissions in Phase 2 are decoupled as evidenced by the elevated SO_2 emissions during March-May 2019 which are accompanied by just four detected anomalies during this period. Of these, two represent days where the magma column may have been high enough to enter South Crater with magma rising an estimated 4 m

into South Crater on 13 April 2019 and 1 m 17 May 2019 (**Figure 2.30**). These two dates alongside the observation of magma within the crater on 22 May 2019 indicates that pressure was periodically high during this period. Six instances of intra-crater are identified in June 2019 alongside the explosive eruptions during this time indicating that high pressure was sustained despite the regular removal of magma from the system. As previously shown only one thermal anomaly was detected during Phase 3 and VRP of this anomaly did not indicate the potential for magma to be present within South Crater. The reported incandescence between 1-8 October 2019 and the five eruptions suggest that while pressure likely dropped following the June 2019 eruptions, there were still some isolated periods of heighted pressure in Phase 3.

Manam's SO_2 and thermal emissions return to a coupled state in Phase 4 and so the thermal anomalies which indicate the potential for magma within South Crater occur around eruptions. Four of the five anomalies detected in 2020 indicate magma as present within South Crater alongside a period of six eruptions between 31 July 2020 and 11 September 2020. The series of anomalies in August 2021 coincide with the reported eruptive activity (James Sukua Pers. Comms.) and so cannot be reliably used to indicate the rise of magma into South Crater. The presence of magma up to 3 m within South Crater on 11 October 2021 (**Figure 2.30**) alongside the series of eruptions including the major eruption on 22 October 2021, suggests that pressure was high during this time.

There is a clear transition between periods of higher and lower pressure around the series of eruptions in June & July 2019. During Phases 1 and 2 there were 23

potential instances of intra-crater magma identified in 439 days compared with 14 instances in the 839 days of Phases 3 and 4. Therefore, this suggests that broadly Phases 1 and 2 represent periods of relatively sustained high pressure, which is corroborated by the increased thermal activity and number of eruptions in these phases. Conversely, Phases 3 and 4 represent periods of prolonged low pressure punctuated by short discrete periods of elevated pressure. Thermal anomaly Cluster 6 and the intra-crater magma identifications within could indicate a renewed period of sustained increased pressure.

2.4.4 A Conceptual Model of Manam

This section proposes a conceptual model of processes operating in Manam's shallow plumbing system that are responsible for the observed activity, thermal anomalies and SO_2 emissions between 6 May 2018 and 31 December 2021. The last eruptive period prior to this study period ended with a minor eruption on 10 September 2017 after which Manam entered a period of relative quiescence until the 10 August 2018 (**Figure 2.7**). During this time observations indicate that Manam's characteristic persistent degassing was maintained (Global Volcanism Program 2021b). Pressure in the shallow plumbing system was low during this period as evidenced by absence of thermal anomalies throughout the inter-eruptive period (**Figure 2.7**). The observed persistent degassing and low pressure suggests that the residual magma from the 2017 eruptions continued to degas throughout this period driving a sluggish convection of magma within the shallow plumbing system (Kazahaya et al. 1994; Allard 1997; Witter et al. 2004; Beckett et al. 2014).

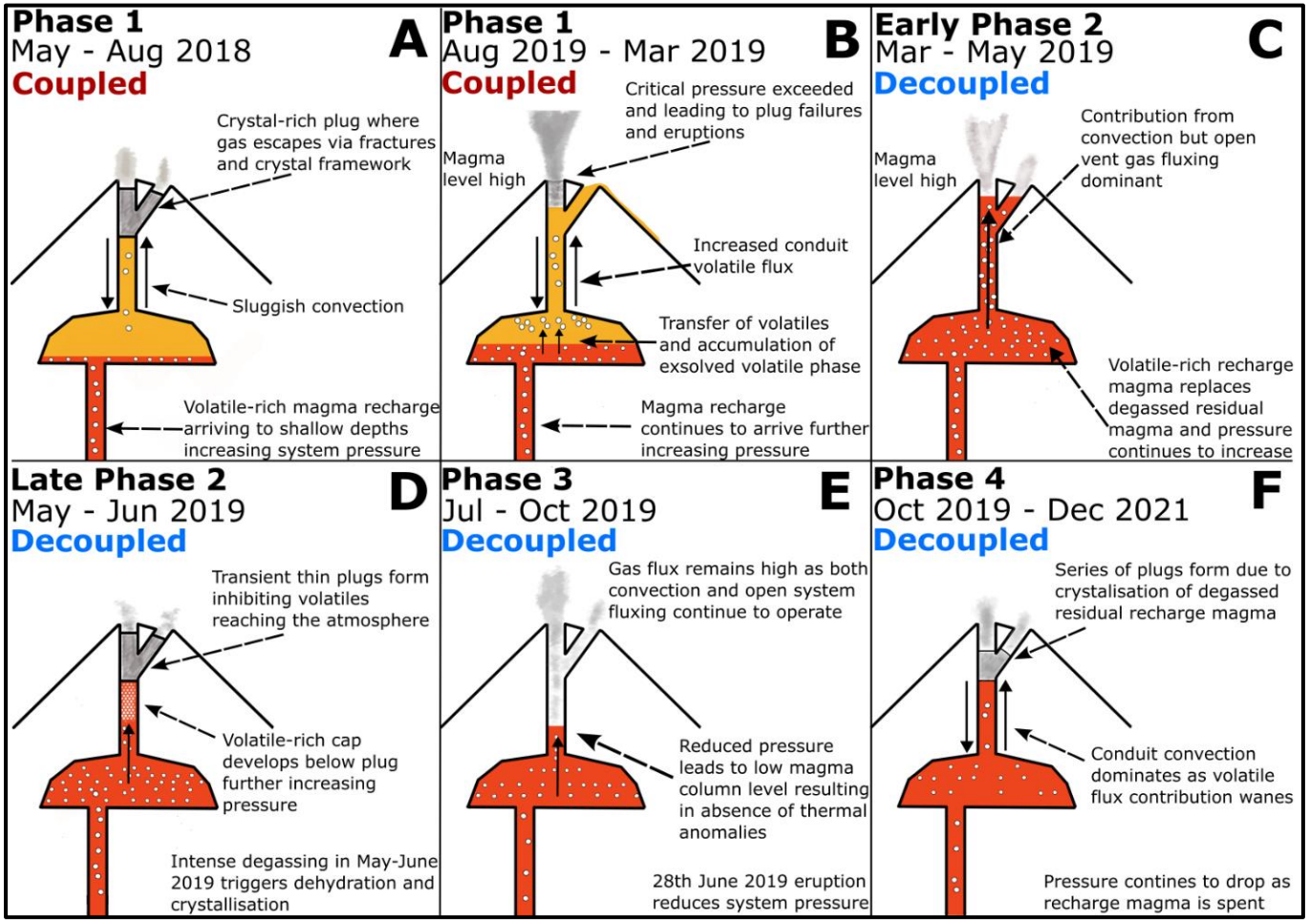

Figure 2.31 Conceptual model of Manam's shallow plumbing system and processes responsible for the observed activity, thermal anomalies and SO_2 emissions. "Coupled" and "Decoupled" indicates the broad state of thermal and SO_2 emissions during each phase.

Various models have been suggested to explain the persistent repeated mild explosions seen at volcanoes like Manam. Some invoke a degassed and crystalised highly viscous magma at the top of the conduit or magma column which is thin enough to be broken by gas slugs which trigger discrete strombolian explosions (Gurioli et al. 2014). This style is associate with low viscosity basaltic magmas, typical at Stromboli (Italy), which allow for the movement of gas slugs and so is unlikely to the mechanism at Manam. The most likely is the pressure build up model where a thicker plug of degassed magma forms in the upper conduit which causes pressure to build up beneath as magma and volatiles are unable to leave the system efficiently (Stix et al. 1997; Melnik and Sparks 2002; Yokoo et al. 2009) as proposed at Arenal (Costa Rica) (Valade et al. 2012) or Tungurahua (Ecuador) (Hall et al. 2015).

As this residual magma becomes depleted in volatiles it cools and crystallises forming a crystal-rich plug in the upper conduit (Stix et al. 1997; Diller et al. 2006; Hall et al. 2015; Gaunt et al. 2020) and this effective partial closing of the conduit also could be responsible for the absence of thermal anomalies. However, this plug must remain permeable to allow the continually observed degassing through networks of fractures (Edmonds et al. 2003b). Indeed it is thought that these networks allow the plug to act as a valve and control degassing periodicity which can be detected through seismic and infrasound signals (Hellweg 2000; Johnson and Lees 2000; Lesage et al. 2006). This ongoing degassing of the residual magma in the upper reaches of Manam's plumbing system alongside cooling and crystallisation of

magma in the upper conduit is the proposed state of the system leading into Phase 1.

At the start of Phase 1 background SO_2 emissions of ~0.62 kt day^{-1} are maintained indicating that volatiles likely sourced from second boiling of the cooling residual magma were able to migrate through the semi-permeable plug to the atmosphere (**Figure 2.31A**). Pressure within the shallow plumbing system began to increase as evidenced by the anomaly detections in Cluster 4 beginning 7 August 2018 (**Figure 2.9**), the presence of magma within South Crater (**Figure 2.30**), and the series of explosive and effusive eruptions in August to September 2018 (Global Volcanism Program 2019a). The arrival of a volatile-rich magma recharge to the shallow storage region below Manam is a likely candidate for the cause of the increase in pressure (Andronico and Corsaro 2011; Viccaro et al. 2015; Patrick et al. 2015b, 2019a; Grapenthin et al. 2022). The magma recharge would have begun to reach Manam's shallow magma storage regions in the months prior to the return of eruptive activity in August 2018 based on estimates from similar systems (Cannata et al. 2018; Aiuppa et al. 2021; Petrone et al. 2022). This bottom up increase in pressure in tandem with emplaced semi-permeable plug restricting volatile migration would have greatly increased the pressure in the system while the plug remained stable (Diller et al. 2006; Battaglia et al. 2019) (**Figure 2.31a**). However as the new magma continued to ascend the associated pressure increase exceeded the strength of the plug formed in the conduit (Woitischek et al. 2020a). The initial weakening of this plug is likely indicated by the two thermal anomalies detected on the 7 and 9 August 2018 as magma began to slowly rise with the breakdown of the

lower plug. The minor ash venting eruption on 10 August 2018 signals the initial failure of the plug as the volatile-depleted residual magma at the top of the column is depressurised and fragments (Battaglia et al. 2019). With the plug removed the pressure sourced from the incoming new batch of magma is partially relieved by the removal of magma in the form of the lava flow observed on 13 August 2018 (Global Volcanism Program 2019a) (**Figure 2.31b**).

During Phase 1, 0.18 km^3 of magma was erupted whereas 0.03 km^3 entered the system based on SO_2 emissions and the discrepancy between the effective input and output of magma during this phase implies that the majority of the magma erupted was degassed prior to eruption. Therefore it is assumed that the magma erupted during Phase 1 was primarily unerupted residual magma from the 2017 eruptive period that had been continuing to degas during the interruptive period. This process of removal of the degassed residual magma by way of explosive and effusive eruptions continued throughout August to September 2018 including the major explosive eruption on 25 August 2018 and the intermittent effusive phase from 9 September to 1 October 2018 (Global Volcanism Program 2019a). The removal of the residual magma reduced the lithostatic load in the upper plumbing system promoting the continued ascent of the recharge magma (Calvari et al. 2011) and allowing for the transfer of volatiles between the two magma batches which partially fuelled the series of explosive eruptions observed during Phase 1 by the fluxing of volatiles through the residual magma in the conduit (Edmonds et al. 2022a) (**Figure 2.31b**). The accumulation of volatiles at the top of a storage reservoir as an exsolved foam and subsequent destabilisation may also explain the

larger explosive eruptions throughout this period (Allard et al. 2005) although this is not possible to confirm. The cycle of reduced permeability from crystallisation of cooling stagnant magma in the upper plumbing system, leading to increased pressure from continued degassing and fresh magma arrival, culminating in an eruption is repeated throughout Phase 1 until the older degassed magma from 2017 is expelled from the system.

The eruptions in January 2019, including 3 major eruptions, removed 0.11 km^3 of residual magma (42% of total erupted material during this study) likely representing the majority of remaining residual magma. The removal of the degassed residual crystal-rich magma meant that: a) the permeability in the upper plumbing system increased allowing for more efficient transport of volatiles to the surface and, b) allowed a new magma batch to further ascend to shallow depths and thus providing increased volatile supply as it decompresses. The minor eruptions throughout February and March 2019 (Global Volcanism Program 2019a, 2019b) seem to have fully opened the conduit where convection alongside fluxing of deeper sourced volatiles facilitated the elevated SO_2 emissions observed during Phase 2 (4.72 kt day^{-1}).

During Phase 2 0.08 km^3 of magma entered the shallow plumbing system based on the SO_2 emissions compared to 0.04 km^3 erupted indicating Manam was in state of excess degassing typical of open-vent volcanic systems. Indeed, over Phases 2-4 this persistent excess degassing was maintained as 0.18 km^3 of magma entered the system versus 0.08 km^3 erupted. During early Phase 2 (March-May 2019) the system was likely under a state of relative high pressure (**Figure 2.31c**) despite the

sparsity of anomalies as many that were detected indicate magma likely to be present within South Crater. The observation of magma on 22 May 2019 (**Figure 2.29**) alongside two South Crater high surface temperature retrievals on 20 and 30 May 2019 (**Figure 2.16**) suggest at least transient periods of high pressure raising the magma column. The decoupled state of emissions during Phase 2 as well as sparse detection of thermal anomalies and infrequent eruptions indicate that reservoir pressure was highly variable during May 2019.

These incidents of high pressure are likely to be due to the continued arrival of volatile-rich magma to shallow depths replacing the removed residual magma (Patrick et al. 2019b) with a minor contribution from the expansion of gas bubbles due to decompression during ascent (Sparks 2003a; Gonnermann and Manga 2007; Rutherford 2008; Burgisser and Degruyter 2015). The decoupled SO_2 and thermal emissions during Phase 2 underline the importance of fluxing of volatiles through Manam's upper plumbing system. The increased volume of exsolved gases within the conduit would promote an increase in pressure accommodated by a rise in the magma column height but the detected anomalies, intra-crater magma estimates and observations do not suggest a persistent high stand of magma within the conduit. Therefore, the fluxing of volatiles independent of ascending magma in conjunction with convection within the conduit is required to explain the enhanced SO_2 emissions during this period without regular thermal anomalies and eruptions (Edmonds et al. 2022a).

Late Phase 2 (June-July 2019) exhibited an increase in thermal emissions and eruptive activity compared to early Phase 2 (March to May). This period of also saw

the continuation of high surface temperatures at South Crater alongside relatively lower temperatures that began in May, suggestive of magma at very shallow depths (**Figure 2.12**). These high temperatures and thermal anomalies not directly related to eruptions indicate magma near the surface and therefore that the system was in a state of heightened pressure. Increases in pressure require a process acting at depth such as a greater rate of magma entering the system or a process acting to alter the plumbing system that impedes volatiles from reaching the atmosphere. The marked decrease in daily SO_2 emissions at the beginning of June and subsequent return to elevated emission alongside the minor eruption on 7 June 2019 (**Figure 2.14**) suggest that the conduit was obstructed briefly and then reopened by the eruption. It is therefore proposed that the intense degassing during early Phase 2 led to the dehydration of magma in the upper conduit triggering crystallisation (Lipman et al. 1985; Couch et al. 2003; Applegarth et al. 2013b; Gaunt et al. 2020) and the formation of another plug which reduced the ability for the exsolved gases to reach the atmosphere and therefore increasing pressure. Due to the continuing elevated volume of degassed volatiles the pressure build-up quickly exceeded the critical pressure of the plug leading to the three minor explosive eruptions on 7, 8 and 18 June 2019 which all failed to completely remove the plug of crystallised magma in the conduit. Subsequently the pressure continued to increase, with the possible formation of a volatile-rich cap of magma beneath the plug (Stix et al. 1997; Sparks 1997; Burgisser et al. 2011) (**Figure 2.31d**), until the 28 June 2019 eruption where the plug failed completely and led to rapid decompression within the conduit driving the explosive activity that generated a 15.2 km eruption column and a lava flow in the northeast valley which reached

within 700 m of the coastline. Three further minor eruptions followed the 28 June 2019 and in total an estimated 0.021 km^3 of magma was erupted during June and July 2019 with 0.018 km^3 erupted on the 28 June 2019 itself, 7% of the total erupted magma volume during this study period.

SO_2 emissions during Phase 3 remained above background levels but reduced from 4.72 kt day^{-1} to ~1.54 kt day^{-1}. This reduction in SO_2 emission rate is interpreted as the gradual depletion of volatiles in the new magma batch within the shallow magmatic system. The state of decoupled SO_2 and thermal emissions from Phase 2 continued into Phase 3 as indicated by the near total absence of thermal anomalies and eruptions alongside the continuing above average SO_2 emissions. To explain the near low frequency of thermal anomalies and eruptions in Phase 3 it is inferred that the removal of substantial volume of magma and volatiles during June and July 2019 reducing pressure in the shallow magmatic system and thus the height of the magma column (Anderson et al. 2015; Patrick et al. 2020; Barrière et al. 2022) (**Figure 2.31e**). The continued elevated degassing, albeit substantially reduced compared to Phase 2, indicates the combination of conduit convection and volatile fluxing remained active during this period to facilitate the observed SO_2 emissions. Manam maintained a state of open-vent excess degassing during Phase 3 with SO_2 emissions indicating that 0.02 km^3 of magma was supplied with just 0.002 km^3 being erupted.

The average daily SO_2 emissions in Phase 4 were ~0.68 kt day^{-1} similar to Phase 1 (~0.62 kt day^{-1}) and so it can be considered this represents a return to background emissions. Thermal anomalies detections were sparse between November 2019 to

May 2021 with just the five anomalies of Cluster 5 occurring during this time (**Figure 2.7**) indicative of low reservoir pressure during this period. The reduction in pressure identified in Phase 3 continued in Phase 4 and was accompanied by the decrease in SO_2 emissions which likely indicates that the initially volatile-rich magma recharge which arrived in Phase 1 had become relatively depleted in volatiles. The contribution of volatile fluxing to SO_2 emissions is likely to have waned during this period with conduit convection being the dominate process responsible for the transport of volatiles albeit returning to a less energetic state than in Phases 2 and 3 (**Figure 2.31e**). As in Phase 3, a state of excess degassing continued in Phase 4 despite the decrease in the rate of SO_2 emitted with 0.09 km^3 of magma supplied and 0.04 km^3 erupted. Notably ~75% of the erupted material in this phase occurred in the 5 months from August to December 2021.

The decoupled SO_2 and thermal emissions during Phase 4 indicate that there were sporadic instances of high pressure during Clusters 5 and 6 where the magma column rose to shallow depths including 14 instances of where magma is estimated to have been present in South Crater. Instances of high pressure coincided with several explosive eruptions associated with isolated high SO_2 emissions. Additionally, the highest estimated intra-crater magma height of 23 m occurred on 29 August 2021 (**Figure 2.28**) around the time of a series eruptions reported by Manam's Disaster Preparedness Committee (James Sukua Pers. Comms.). It is possible that the renewed eruptive activity in 2021 during Phase 4 is result of the arrival of a new batch of magma arriving at depth as is postulated to explained the activity in Phases 1 and 2. However, this explanation is unlikely as no lava flows

were reported during 2021 suggesting that the increase in pressure was not as a result from a magma body applying pressure from below. Rather, the more likely explanation for the increased pressure is reduced conduit permeability resulting from crystallisation due to the continual volatile depletion and dehydration of the cooling residual magma. This would lead to another phase of repeated partial closing or restriction of the conduit with eruptions resulting from the built up pressure exceeding the strength of the crystal-rich magma (Applegarth et al., 2013; Lipman et al., 1985). It is probable that more substantial plugs were able to form prior to the major eruptions on 20 October 2021 and 22 December 2021. These more established plugs would have required relatively higher pressures to fail which could explain the apparent increased magnitude of these two eruptions.

This interpretation of the processes responsible for Manam's presented in **Figure 2.31** suggests that a volatile-rich body of magma began to reach Manam's shallow plumbing system around August 2018 leading to an increase in pressure which caused the removal of crystal-rich relatively degassed magma in the conduit through a series of explosive and effusive eruptions from August 2018 to March 2019. With the conduit fully reopened degassing rates at Manam became elevated as volatiles were able to exsolve and rise efficiently through the plumbing system through a combination of fluxing and conduit convection. The upper reaches of the magmatic system became dehydrated after several weeks of intense degassing causing crystallisation and the formation of a plug which began to restrict the efficient movement of volatiles through the conduit and increasing pressure. After a series of partial failures of this plug the major eruption on 28 June 2019 erupted

0.021 km^3 of magma and substantially reducing pressure in the plumbing system. Following this the remaining portion of the 2018 magma batch continued to degas until the leading to repeated cycles of plug formation and plug clearing eruptions most notably from July 2021 to the end of the study period in December 2021.

2.4.5 Global context and broader implications

The last ground-based measurements of Manam's SO_2 emissions were taken during May 2019 yielded an average SO_2 flux of 5150 ± [336/733] tonnes day^{-1} (Liu et al. 2020a). This campaign measured flux would place Manam as the 2nd highest emitter of volcanic SO_2 within the ranking of volcanic SO_2 emissions compiled by Carn et al. (2017) and the derived CO_2 flux of 3760 ± [600, 310] tonnes day^{-1} would place it 5th-7th globally (Aiuppa et al. 2019). The time series of SO_2 emissions at Manam presented in this chapter demonstrates the variability of volcanic volatile emissions over months to years. Specifically these campaign measurements were taken during Phase 2 where SO_2 emissions were substantially greater than background emissions during this study period. This therefore raises questions over the reliability of placing individual volcanoes within global volcanic emission inventories based solely on campaign-style measurements. Long-term satellite remote sensing of emissions provides the ability to assess the temporal variability of volcanic emissions and appropriately place an individual volcanoes emissions into the global context.

The time average SO_2 fluxes based on a 1 day residence time for each phase (**Figure 2.15**) are presented alongside the annual mean daily SO_2 emissions (2005-2015) presented by Carn et al. (2017) in **Figure 2.32**. The mean annual daily SO_2 emissions

(2005-2015) for Manam is 1.48 kt day^{-1} which places Phases 1 (0.62 kt day^{-1}) and 4 (0.68 kt day^{-1}) below this long-term average, Phase 3 (1.5 kt day^{-1}) around this average and Phase 2 (4.72 kt day^{-1}) substantially higher than the identified average. The time-averaged emissions in Phase 2 represents the highest period of SO_2 emissions exceeding the 3.52 kt day^{-1} observed in 2005. Additionally, Carn et al. (2017) identified a declining trend in annual SO_2 emissions and the inclusion of the data from this study shows this declining trend despite the elevated emissions during 2019 (**Figure 2.32**). This once again highlights the remarkable increase in emissions during Phases 2 and 3 which are above the background for the study period, above the annual mean daily emissions and do not follow the observed long term trend.

Considering each SO_2 emission phase in the global context indicates would place Manam as low 31st largest contributor to global volcanic SO_2 emissions based on Phase 1 and as high as 3rd during Phase 2, with Phase 3 ranking 10th globally and Phase 4 placing 25th (**Table 2.6**). If Manam's more recent background emissions in Phases 1 and 4 are representative of it's long term emissions, then at 25th to 31st highest SO_2 emitter globally, Manam continues to be a major contributor to global volcanic SO_2 emissions.

CO_2 fluxes per phases are calculated per phase using the average May 2019 CO_2/SO_2 ratio measured by Liu et al. (2020a) (**Table 2.6**). These fluxes place Manam as high as 6th-7th globally for volcanic CO_2 emissions during Phase 2 and as low as 46th-51st during Phase 1 based on two compilations of volcanic CO_2 emissions (Aiuppa et al. 2019; Fischer et al. 2019b). The application of the May 2019 CO_2/SO_2 ratio across all

phases is problematic as CO_2/SO_2 ratios vary with degassing pressure as well as eruptive style (Moretti and Papale 2004; Burton et al. 2007; Aiuppa et al. 2010; Aiuppa 2015).

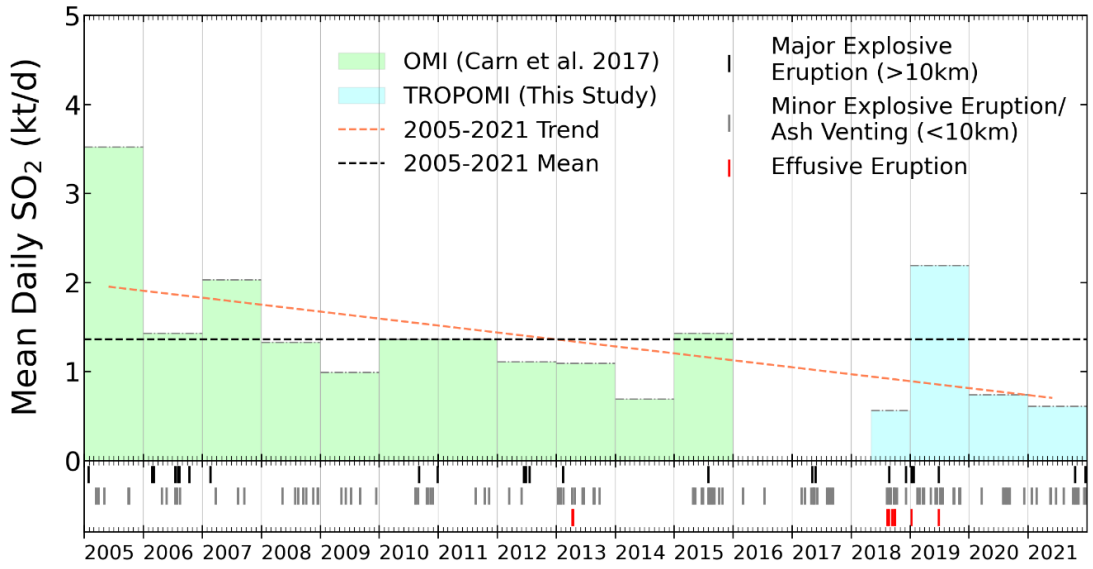

Figure 2.32 Manam annual daily SO2 emissions (kt/d) measure by OMI (green) (Carn et al. 2017), TROPOMI derived annual daily SO_2 emissions based a 1 day residence time (blue), trend (red dotted line) and mean annual emissions 2015-2012 – 1.36 kt/d (black dotted line).

Based on the observed variation in SO_2 emissions and the invoked magma recharge event suggests that the CO_2/SO_2 ratio would not have remained stable. The average CO_2/SO_2 ratio for May 2019 of 1.07 ± 0.06 indicates a relatively CO_2 poor composition. Low CO_2 alongside high SO_2 is normally indicative of degassing of a shallow depth magma but during Phase 2 fluxing of deeper derived volatiles is assumed to be the process facilitating the elevated SO_2 emissions. Manam's low CO_2 signature has been attributed to the limited or carbon-poor sediment supply to the subduction trench along the inactive portion of the Western Bismarck arc (Liu et al. 2020a). The low carbon supply to Manam means that the CO_2/SO_2 ratio is likely to remain low even during periods where degassing may be enhanced by fluxing of deeper derived volatiles. As such, Phases 1 and 4 would likely have lower CO_2/SO_2

ratios as the composition would be relatively dominated by the SO_2 degassing from shallow unerupted magma (Aiuppa et al. 2021). This therefore underlines the uncertainty around the derived CO_2 fluxes especially for Phases 1, 3 and 4 where magmatic processes and eruptive activity differ from Phase 2 where the utilised CO_2/SO_2 ratio was measured.

Phase	Time-averaged SO_2 emissions (kt day^{-1})	Global SO_2 Rank	Derived CO_2 Flux (kt day^{-1})	Global CO2 Rank
1	0.62 ± 0.03	31	0.46 ± 0.03	46 – 51
2	4.72 ± 0.09	3	3.3 ± 0.2	6 – 7
3	1.5 ± 0.05	10	1.1 ± 0.07	=19 – 23
4	0.68 ± 0.03	25	0.52 ± 0.04	41 – 46

Table 2.6 SO_2 and CO_2 emissions by phase and ranked against global inventories. SO_2 Carn et al. 2017, CO_2 Auippa et al. 2017 & Fischer et al. 2019.

Manam's SO_2 emissions have been shown to be highly variable over month to year timescales which make placing it amongst global volcanic volatile inventories difficult. For example the climatic eruptions at Manam in 2005 are likely to have greatly increased Manam's SO_2 emissions that year to 1285 kt which has strongly influenced Manam's SO_2 emission rankings for 2005-2015 (Carn et al. 2017).

Similarly, Phase 2 of the SO_2 timeseries in this study also presents a remarkable deviation from background emissions which taken in isolation would rank Manam much higher compare to Phases 1 and 4. This highly variable behaviour has been documented at other volcanoes including Anatahan (Northern Mariana Islands) and

Miyakejima (Japan) which like Manam experienced exceptional emissions related to eruptions which elevated their placement in global rankings despite marked decline in emissions in the following years (Kazahaya et al. 2004; McCormick et al. 2015). Variability in emissions have been identified at Bagana (Papau New Guinea) where degassing substantially decreased for an extended period in 2019 to 2021 before returning to more normal higher emissions (McCormick Kilbride et al. 2023). Following the 2015 East Rift eruption, Kilauea (USA) has shown a notable decline in SO_2 emissions as it's lava lake was drained (Kern et al. 2020). Conversely, systems, like Turrialba (Costa Rica), can reawaken after long-term repose and rapidly become a dominant source of volcanic volatiles regionally and globally (de Moor et al. 2016). The widely observed variations in degassing rates across systems worldwide underscore the importance of regular reassessment of global volatile inventories and the limitations of placing volcanoes within these based on limited-term measurements of emissions. This also underlines the potential role that satellite remoting sensing of volatiles can play in providing an ongoing assessment of volcanic degassing globally in a similar way to thermal emissions are monitored by open access platforms such as *MODVOLC* (Wright et al. 2004; Wright 2016b), *MIROVA* (Coppola et al. 2016) and MOUNTS (Valade et al. 2019). Additionally, this emphasises the need for a multi-parametric approach to interpreting changes in degassing behaviour and eruptive activity at open vent volcanic systems, as the processes responsible for modulating degassing are varied and interpretations potentially ambiguous when derived from emission rates alone.

2.4.6 Limitations and Future Work

A key feature of this chapter is the use of satellite remote sensing alongside observed activity to demonstrate the possibility of interpretation of volcanological processes without ground-based data. The logical next step is to this satellite only approach is to extend the thermal anomaly and SO_2 emission timeseries from 2022 onwards to further calibrate the framework presented in section 2.4.4. This work captured a substantial increase in SO_2 emissions during 2019 but it is unknown how often Manam exhibits this type of behaviour so in addition to extending the combined timeseries forward, it would also be beneficial to extend it backwards to pre-2018. The MODIS-based *MODVOLC* thermal anomaly detections are available from 2000 onwards. The SO_2 emission and surface temperature time series from this chapter are only available back as far as 2018 and 2015 respectively; the operational start dates for the Sentinel-5P (TROPOMI) & Sentinel-2 (MSI) missions respectively. It would therefore require the integration of other satellite-based sensors like NASA's OMI which can be used to resolve SO_2 emissions (at lower resolution than TROPOMI) as far back as 2003 (Carn et al. 2013) and NASA's Landsat 7 Enhanced Thematic Mapper Plus (ETM+) and Landsat 8 Operational Land Imager (OLI) which combined would be able to SWIR data as far back as 1999 (Flynn et al. 2001; Blackett 2014). The production of a multi-decadal timeseries from satellite remote sensing data would provide the opportunity to identify repeated cycles or other exceptional periods of emissions from which to modify the model suggested here of Manam's activity.

A key enhancement to this satellite-based approach to understanding Manam's sub-surface processes would be to integrate satellite derived deformation data. Deformation of volcanic edifices is now regularly performed through Interferometric Synthetic Aperture Radar (InSAR) methods (Klees and Massonnet 1998; Valade et al. 2019; Poland and Zebker 2022; Grapenthin et al. 2022) and have been able to show the inflation and deflation of volcanoes indicative of arrival of magma to the near-surface (Chaussard et al. 2013; Morales Rivera et al. 2017; Albino et al. 2020; Grapenthin et al. 2022). At Manam, this parameter could provide insights into the potential arrival storage of degassed magma prior to eruptions (Scott and McKee 1986; Ramayanti et al. 2022) and reveal further evidence towards how Manam facilitates the magma responsible for its excess degassing and elevated SO_2 emissions.

The method presented in section 2.4.3 uses an assumed simplified geometry of South Crater to estimate the occurrences of magma rising into the crater itself. A future avenue of work would be to further test this method at volcanoes where the height of magma columns or lava lakes has been recorded or estimated by other geophysical signals such as Villarrica (Chile) (Johnson et al. 2018) and Kilauea (USA) (Patrick et al. 2015b). This would enable calibration of this method for use at volcanoes where magma level is not easily observable and provide a remote-sensing method for evaluating the pressure state at remote volcanoes.

2.5 Conclusions

A magma recharge event at Manam has been identified using satellite-based remote sensing of thermal and SO_2 emissions. This recharge magma arrived in in the shallow plumbing system in 2018 increasing pressure causing the removal of residual crystal-rich magma from the 2017 eruptive period in a series of explosive and effusive eruptions from August 2019 to March 2019. With the removal of the crystal-rich residual magma Manam's conduit became more permeable allowing the efficient transport of volatiles through the shallow plumbing system resulting in the observed above-background emissions in Phases 2 and 3. The considerable degassing throughout this period caused dehydration and crystallisation leading to a plug of crystalised magma forming in the upper conduit. This restricted degassing and therefore increased system pressure until this plug failed causing rapid decompression of volatile-rich magma below the plug triggering the 28 June 2019 major eruption. Following this eruption pressure in the system was relieved and background levels of SO_2 emissions were re-established as the recharge magma became relatively depleted in volatiles.

Manam's frequent eruptions have for the first time been placed in the context of a long-term timeseries of thermal and SO_2 emissions by the application of satellite-based remote sensing methods. The timeseries has revealed four distinct phases of SO_2 emissions with background emissions of ~0.62-0.68 kt day^{-1} identified based on Phases 1 and 4. Elevated emissions in Phase 2 (4.72 kt day^{-1}) during which the major 28 June 2019 eruption occurred followed by the transitory Phase 3 where emissions were above background (1.5 kt day^{-1}) but steadily reduced during this period.

The excess degassing phenomenon has been quantified over an extended time period at Manam with an estimated excess of 0.10 km^3 of unerupted degassed magma during Phases 2-4. Phase 1 saw more magma erupted than estimated to have been supplied to the shallow plumbing system. This is explained by the fact that Phase 1 saw the removal of 0.18 km^3 of volatile depleted residual magma from the 2017 eruptive period. Therefore it is suggested that the fate of unerupted degassed magma at Manam, and potentially other excessively degassing volcanoes, is its removal through several eruptions over a period of months caused by the arrival of recharge magma. The regularity of this process is unknown at this point as only one magma recharge event has been identified at Manam. Therefore it is recommended that the examination of SO_2 and thermal emissions at Manam be continued. Additionally, it remains unclear to what extent degassed magma is intruded at Manam and this represents an avenue of future research by reintroducing ground deformation monitoring to Manam.

Unlike other open-vent systems (e.g. Villarrica (Chile) (Palma et al. 2008) and Fuego (Guatemala) (Lyons et al. 2009; Naismith et al. 2019)) no clear patterns of activity were identified at Manam over this period. It may be that any cycles at Manam occur over long time periods again supporting the notion to continue monitoring these parameters into the future. Despite the lack of identified cycles, eruptions at Manam are triggered by the emplacement and subsequent failure of crystal-rich plugs during this study period (Battaglia et al. 2019). As such a reduction in SO_2 emissions may indicate the reduction in conduit permeability resulting from the formation of a plug, and therefore may be a potential precursory signal.

Manam has previously been placed in the top 10 for global SO_2 and CO_2 emissions (Carn et al. 2017; Liu et al. 2020a). This chapter confirms that Manam is a top contributor to global volcanic emissions but also highlights that the variable SO_2 emissions measured place Manam as high as 3rd and as low as 31st globally. Derived CO_2 fluxes using measured CO_2/SO_2 ratios and the observed SO_2 emissions place Manam as high as 6th and as low as 51st. These results underline the uncertainty involved with placing volcanoes such as Manam which have highly variable SO_2 emissions over month to year timescales, using campaign measurements alone.

Finally this chapter demonstrates the importance of monitoring and understanding the fluctuations in gas emissions at open vent volcanic systems. The gas emissions of persistently degassing volcanoes are the most abundantly available monitoring parameter and with proper analysis can provide insights into the eruptive potential of the system. Increases or decreases in flux, from an established long-term background level, can indicate changed conditions that may lead to eruption. At Manam both of these are shown with the increased SO_2 emission period alongside the transient flux decreases here associated with sealing of the conduit. Additionally, changes in gas plume compositional changes can indicate the arrival of new magma at depth that can trigger eruptions.

3 Chapter Three - Tephra Deposition Modelling and Impact Analysis

3.1 Introduction

Explosive volcanic eruptions generate tephra as magma is disintegrated during fragmentation (Heiken and Wohletz 1991; Kaminski and Jaupart 1998; Gonnermann 2015; Schmith et al. 2018). Volcanic plumes from explosive eruptions represent buoyant mixtures of tephra particles, magmatic gases and entrained ambient air, which rise in the form of an eruptive column over the vent before spreading laterally as a form of gravity current on reaching the level of neutral buoyancy in the atmosphere (e.g., Bursik, 2001; Sparks, 1997). Away from the column, the dispersion of volcanic plumes is controlled by the wind field and the physics of particle sedimentation (Carey and Sparks 1986; Bursik et al. 1992; Folch 2012; Woodhouse et al. 2013). Tephra particles will settle out of a volcanic plume largely according to gravitational settling, potentially accelerated by turbulent atmospheric instabilities, aggregation or wet depositional processes (Brown et al. 2012; Manzella et al. 2015; Poulidis et al. 2018).

Of all volcanic hazards, tephra deposition typically has the largest spatial extent and therefore produce the most widespread societal and environmental impacts. Tephra can be classified by particle size into three categories: bombs and blocks (>64 mm), lapilli (2-64 mm) and ash (<2 mm) (Wilson et al., 2015). Bombs and blocks will typically follow a ballistic trajectory and generally accumulate within 5 km of the vent (Blong 1984; Taddeucci et al. 2017). In contrast, lapilli and ash are carried to greater altitudes by convecting eruption columns and may be transported laterally many tens to hundreds of kilometres from the volcano before being deposited (Bursik 1998; Stevenson et al. 2012; Matthews et al. 2012; Bonadonna et

al. 2015b; Cashman and Rust 2020). This chapter focusses on modelling of the large-scale transport and deposition of particles within convecting volcanic plumes and therefore the use of tephra hereafter implies reference to ash and lapilli only.

Tephra is the fifth most common cause of fatality associated with volcanic activity between 1500 and 2017 and the most common in terms of maximum recorded distance a fatality has occurred from the source volcano (Brown et al. 2017). However, overall, the total number of recorded fatalities associated with tephra (4,315 individuals) is relatively low when compared to those caused by pyroclastic density currents (59,958), volcanogenic tsunami (56,822), and lahars (49,938). Deaths caused due to tephra fall tend to occur close to the source volcano where accumulation is greatest and are typically the result of roof or structural collapses, asphyxiation or burial (Spence et al. 2005; Brown et al. 2017). Tephra fall rarely poses an immediate direct risk to life during an eruption (Wilson et al., 2015). Instead, it is the accumulation of tephra on the ground and on structures, and the long-term remobilisation of these deposits, that cause the most significant and prolonged impacts to human life and activity (Brown et al. 2015; Loughlin et al. 2015).

Thick accumulations of tephra can lead to roof collapse and other structural damage to buildings rendering them unsafe for human occupation, especially if the deposits become water-saturated (Spence et al. 1996; Blong 2003; Hayes et al. 2019). Moderate accumulations of a few centimetres can cause the failure of critical infrastructure such as electrical grids and telecommunication systems, largely due to the electrically insulating properties of tephra (Bebbington et al. 2008; Wardman

et al. 2012; Wilson et al. 2014). Even thin deposits of tephra can cause widespread damage to crops and vegetation (Craig et al. 2016, 2021), transport infrastructure (Brown et al. 2015) and public health (Wilson et al. 2013; Damby et al. 2013). A key aspect of eruption preparedness and risk reduction is therefore to establish the likelihood of various thicknesses of tephra accumulation (i.e. the production of hazard maps) for a range of realistic eruption scenarios (Connor et al. 2001; Mastrolorenzo et al. 2008). These mapping products can inform assessments of the potential exposure of populations and economic assets, and highlight societal vulnerabilities (e.g. access bottlenecks that may affect evacuation or aid delivery) in the regions surrounding active volcanoes (Calder et al. 2015b; Jenkins et al. 2022).

3.1.1 Tephra Deposition on Manam and Mainland Papua New Guinea

Tephra deposition is the most common hazard produced by eruptions at Manam, and accumulation can range from thick deposits exceeding 100 mm on the island itself to very thin “dustings” of ash <1 mm that, depending on the magnitude of the eruption, can reach the coastal mainland or potentially 100s of kilometres inland (Best 1956; Taylor 1958a, b; Branch 1965). Few tephra deposits from Manam have been recorded and most reports do not provide adequate information on the extent of the deposits nor thicknesses at multiple locations. The only published map of tephra deposition, to the best of my knowledge, on Manam was produced following four “major” eruptions occurring between December 1957 and March 1958. These events affected an area corresponding broadly to an east to west band across the middle of the island, and represented deposits exceeding 10 inches in thickness (254 mm) (Taylor 1958b). Since these deposits were an amalgamation of

tephra from multiple eruptions it is difficult to draw conclusions as to the hazard represented by one independent eruption, or indeed to estimate the magnitude of one or more of these eruptions; this is a frequent limitation in the reconstruction of past eruption dynamics from older deposits (Pyle 2016). However this example of multiple successive tephra deposition events is an issue that remains as Manam has continued to frequently erupt explosively within days to weeks in recent years (Global Volcanism Program 2021b).

Historically, tephra deposition has caused the collapse of roofs and buildings on Manam (Palfreyman and Cooke 1976; Global Volcanism Program 2004b). Although the repair of traditionally-built timber buildings can be relatively quick, promoting relatively short timescales of recovery, the damage from tephra fall on the agricultural gardens can have much longer-term impacts on food security (Mercer and Kelman 2010). Thin deposits of ash can damage or destroy crops but often do not significantly impact the growth of replacement crops. However, thicker deposits of scoria-sized particles (2-64 mm) do not erode as quickly and therefore can prevent impacted areas from being agriculturally productive for multiple seasons (Taylor 1958b; Mercer and Kelman 2010).

3.1.2 Tephra Transport and Dispersal Models

Given the widespread impacts tephra deposition is capable of causing at local, regional and global scales it is important to assess the potential hazard footprint (Bonadonna et al., 2021; Wilson et al., 2014; Wilson et al., 2015). Future extents of tephra deposition can be estimated by the mapping of deposits from previous

eruptions (e.g., Pyle, 1989a). However, this approach relies on the assumption that future eruptions will be similar to those that have occurred in the past, and can be challenging in regions of poor preservation where deposits are remobilised rapidly by wind or water. Numerical plume models that include particle sedimentation allow a probabilistic assessment of tephra deposition, even where previous deposits have not been mapped or they are not preserved (Biass et al. 2017; Warwick et al. 2022; Buckland et al. 2022). For volcanoes where little or no field-based mapping of tephra deposits have been undertaken, such as Manam, tephra transport and dispersal models (TTDMs) represent an opportunity to fill in this gap in volcanic hazard assessments.

TTDMs are a sub-type of atmospheric transport models that are designed to model the airborne transport and sedimentation of particles, such as tephra and aerosols. These transport models have three principle components: 1) an emission source that defines the release of the substance of interest in time and space, 2) an atmospheric model, and 3) a transport model that describes the movement and removal of the substance from the atmosphere (Folch 2012). A transport model uses either a Eulerian or Lagrangian method. While Eulerian models solve for variables (e.g. particle properties) and at fixed locations or grid points, Lagrangian models calculate the accumulation by tracing paths of an “ensemble” of particles and compute the mass concentration by averaging over fixed background cells (Folch 2012). Eulerian models adapt the Advection-Diffusion-Sedimentation (ADS) equation (**Equation 3.1**), which is derived from the general principle of mass

conservation of particles within a fluid. Ignoring particle inertia and particle-particle interactions the ADS equation is expressed as:

$$\frac{\partial C}{\partial t} = \nabla \cdot (uC) + \nabla \cdot (K\nabla C) - \nabla \cdot (u_s C) + S_0 + S_K \qquad (3.1)$$

where t = time, C = particle mass concentration, u = $(u_x u_y u_z)$ wind velocity, K = turbulent diffusivity tensor (accounting for unresolved-scale turbulent wind fluctuations), u_s = particle sedimentation velocity, S_0 = (x, y, z, t) source term (accounting for the production of particles) and, S_K = (x, y, z, t) sink term (accounting for the destruction of particles) (Folch 2012; Bonadonna et al. 2015b). The three righthand terms in Equation 1 describe the advection of particles by wind, turbulent diffusion of particles and particle sedimentation respectively (Folch 2012; Bonadonna and Costa 2013).

Lagrangian models are most commonly used for modelling the atmospheric dispersal of tephra due to their particle tracing capability. Notably, they are used by various Volcanic Ash Advisory Centres (VAAC) for forecasting potential disturbance to air transport; for example, *HYSPLIT* (Draxler and Hess 1998) and *NAME III* (Jones et al. 2007). This type of transport model is not typically used for ground-based tephra hazard assessment as prediction of ash cloud location over time is the primary concern of the aviation related organisations that tend to develop these kinds of models.

Models that solve the ADS numerically are able to provide time-dependent airborne tephra concentration and ground mass accumulation from any type of eruption and particle size (Folch 2012). Examples of numeric TTDMs are *FALL3D* (Costa et al.

2006; Folch et al. 2009) and *ASH3D* (Schwaiger et al. 2012; Mastin et al. 2013). *FALL3D* is a Eulerian model that allows the user to define the horizontal and vertical diffusion rates and has multiple uses for operation forecasting (Folch et al. 2008), modelling of past events (Folch et al. 2010; Costa et al. 2012) and tephra hazard assessment (Folch and Sulpizio 2010; Scaini et al. 2012; Barsotti et al. 2018). *ASH3D* is a finite volume Eulerian model capable of global scale modelling of tephra dispersal and deposition and critically to predict ash concentration and deposition during eruptions (Schwaiger et al. 2012).

Gaussian TTDMs were developed under the premise that under certain circumstances the ADS can be solved using an analytical solution in the form of a Gaussian function. The assumptions required are that: 1) the vertical wind and vertical diffusion (K_v) are negligible i.e. $u_z = 0$ and $K_v = 0$, 2) the horizontal wind components of the wind field are homogeneous and steady i.e. $u_x = u_x(z)$ and $u_y = u_y(z)$, 3) the horizontal turbulent diffusion is constant i.e. $K_h(x, y, z) = K$, 4) the term accounting for divergence of the settling velocity can be neglected and, 5) particles are emitted instantaneously as point sources along a vertical line, i.e. $S_0 = \delta_0(x_0, y_o, z_o)$ (Folch 2012). Given these assumptions **Equation 3.1** simplifies to:

$$\frac{\partial C}{\partial t} = u_x \frac{\partial C}{\partial x} - u_y \frac{\partial C}{\partial y} - u_z \frac{\partial C}{\partial z} + K\left(\frac{\partial^2 C}{\partial x^2} + \frac{\partial^2 C}{\partial y^2}\right) + \delta_0 \qquad \textbf{(3.2)}$$

And the Gaussian function which serves as an analytic solution is as follows (Macedonio et al. 2005):

$$\boldsymbol{C(r,t) = \frac{1}{4\pi Kt}\, exp\left[\frac{(x-x_0-u_x t)^2 + (y-y_0-u_y t)^2}{4Kt}\right] \delta(z - z_0 - u_s t)} \qquad \textbf{(3.3)}$$

Equation 3.3 describes the dispersal of particles in a horizontal layer that settles at velocity u_s. The topography is assumed to be flat and the atmosphere is divided into discrete vertical layers allowing the Gaussian function to spread and settle as its centre of mass translates under the effect of the winds in each layer and settling velocity (Suzuki 1983; Folch 2012). Models that use this approach include *Tephra2* (Bonadonna et al. 2005, 2014a) and *ASHFALL* (Hurst and Turner 1999; Hurst and Smith 2004). These Gaussian TTDMs are computationally light and lend themselves to multiple uses including probabilistic hazard modelling (Volentik et al. 2009; Biass et al. 2016), inversion modelling of ground deposits to infer eruption characteristics (Connor and Connor 2006).

3.1.3 Aims and Objectives

The aim of this chapter is to place quantitative constraints on tephra hazard, through a probabilistic assessment of the spatial distribution of tephra thicknesses, for a range of relevant explosive eruption scenarios at Manam. In the framework of the resulting tephra accumulation probability maps, this chapter will quantify the extent to which populations and assets may be exposed to different thicknesses of tephra accumulation, and the resulting impacts to society and the environment. This will be achieved through targeting the following objectives:

1) Identify a range of explosive eruption scenarios based on Manam's eruptive history, and define a corresponding suite of input parameters to initialise the *TephraProb* TTDM (Biass et al. 2016).

2) Model the extent and mass accumulation of tephra deposition across Manam and mainland Papua New Guinea resulting from the defined eruption scenarios, and the role of seasonality on dispersion characteristics.
3) Assess the impact of tephra deposition by analysing population, structures, land cover, road network exposure datasets in conjunction with the modelled tephra isopachs in ArcGIS
4) Evaluate the potential impacts of varying tephra accumulations on human activity and infrastructure in the context of published tephra impact frameworks (Wilson et al. (2015b).
5) Discuss the emergency planning considerations arising from tephra hazard assessment including: food security issues, construction-based resilience measures, the ramifications of a compromised road network during an emergency and examining potential evacuation and relocation sites for displaced Manam residents.

3.2 Methods

This section outlines the procedure used to assess tephra accumulation impacts at Manam. This includes an overview of the selected tephra transport and dispersal model (*TephraProb*), the pre-defined eruption scenarios and model starting conditions for each, the population and infrastructure data, and the framework for the exposure analysis conducted in ArcGIS.

3.2.1 *TephraProb*

TephraProb (Biass et al. 2016) has been used to assess the impact of tephra deposition from eruptions of Manam. *TephraProb* is an opensource toolbox that produces scenario-based probabilistic assessments of ground tephra accumulation based on the *Tephra2* model (Bonadonna et al. 2005, 2014b, a). Given a range of probabilistic eruption scenarios, *TephraProb* creates distributions of eruption source parameters (ESPs) that are run in *Tephra2* and provides results in the form of exceedance probability maps, probabilistic isomass maps and hazard curves for defined locations. *TephraProb* was selected over other TTDMs due to its simple graphical user interface (GUI), which allows for non-specialists to leverage the *Tephra2* model with relative ease and low computing power requirements.

The *Tephra2* model uses an analytical solution to the advection-diffusion equation to compute the tephra mass accumulation according to eruptive and wind conditions (Bonadonna et al. 2005; Connor and Connor 2006; Volentik et al. 2009; Bonadonna and Costa 2012). It adopts a Eulerian approach, solving variables in the ADS equation at fixed locations or grid points (Folch 2012; Constantinescu et al. 2021). The size of the grid cells and therefore the distance between grid points is definable through the *TephraProb* GUI. The key components of *Tephra2* include: i) grain-size-dependent diffusion and particle density, ii) a vertically stratified wind profile, iii) particle diffusion within the rising plume, and iv) settling velocities that include variations in the Reynolds number depending on whether particles follow a laminar or turbulent flow regime (Bonadonna et al. 2005; Biass et al. 2016). *Tephra2* requires three input files: a) a configuration file, which details the eruption source

parameters and the surrounding atmosphere (specific details provided further in this chapter), b) a table of locations where specific tephra accumulations are to be calculated, and c) a table of wind speeds and directions at varying altitudes throughout the atmosphere (Biass et al. 2016).

3.2.2 Modelling Parameters and Eruption Scenarios

Five distinct eruption scenarios are defined that broadly encompass the range of explosive eruptions observed at Manam since the early 1900s (Palfreyman and Cooke 1976; McKee 1981; Global Volcanism Program 2021b). These scenarios range from minor (<10 km asl eruption columns) vulcanian eruptions to major (>10 km asl eruption column) vulcanian and sub-Plinian eruptions.

The NOAA Reanalysis II dataset (Kanamitsu et al. 2002) was used to provide the stratified wind profiles, accessed using the *TephraProb* GUI. Reanalysis II provides global coverage of atmospheric conditions four times daily and data specifically from 2000-2021 were used. Each eruption scenario was modelled for both the wet and dry seasons. It should however be noted that the parameters of the 100 runs for each scenario are independently sampled for each season resulting in two sets of 100 runs. As these runs are randomly sampled it means that the tephra deposition for each season per scenario are not strictly directly comparable as they are not based on the same eruption source parameters. While this doesn't undermine the validity of either season's results it should be kept in mind when comparing the seasonal outputs.

In Madang province, where Manam is located, the dry season typically runs from May to October and the wet season from November to April (Pereira et al. 2019). The final atmospheric parameter common to all scenarios is the height of the tropopause, which is estimated to be around 18,500 m asl at the latitude of Manam (-4.078, 145.038) (Feng et al. 2012).

Tephra2 accounts for the two regimes of particle sedimentation based on the terminal fall velocity of particles (Bonadonna et al. 2005). As such, *Tephra2* requires the definition of the fall-time threshold acting as a threshold for the sedimentation of small particles (power-law diffusion) and large particles (linear diffusion) for which a diffusion coefficient must be specified. Ideally these parameters should be estimated by inverting tephra fall field data (Connor and Connor 2006); however, since no comprehensive studies of tephra accumulation from eruptions of Manam exist, the parameters measured from an analogous volcano are used instead. Therefore, parameters from the 1974 eruption of Fuego (Guatemala) were selected: fall-time threshold = 5000 s and diffusion coefficient = 4900 m^2 s^{-1} (Biass et al. 2016). The eddy constant parameter was set to 0.04 m^2 s^{-1} (Suzuki 1983).

The pumice density was set to 1000 kg m^{-3} and the lithic density 2500 kg m^{-3} based on typical values for basaltic andesite tephra (Wehrmann et al. 2006). The column integration steps and TGSD integration steps were both set to 80 (S. Biass, Pers. Comms.). The probability of tephra being released from the eruption column at some vertical height above the vent is controlled by a beta probability density function **(Equation 3.4)** (Biass et al. 2016):

$$P(x) = \frac{(1-x)^{\beta-1}x^{\alpha-1}}{B(\alpha,\beta)} \quad \textbf{(3.4)}$$

where x is a dimensionless height normalised to the plume height and $B(\alpha, \beta)$ represents the beta function defined by two parameters α and β, both greater than 0. Here we use α = 3 and β = 1.8 which shifts the release patter of particles towards the top of the plume. The shape of the beta probability density function is shown in **Figure 3.1**.

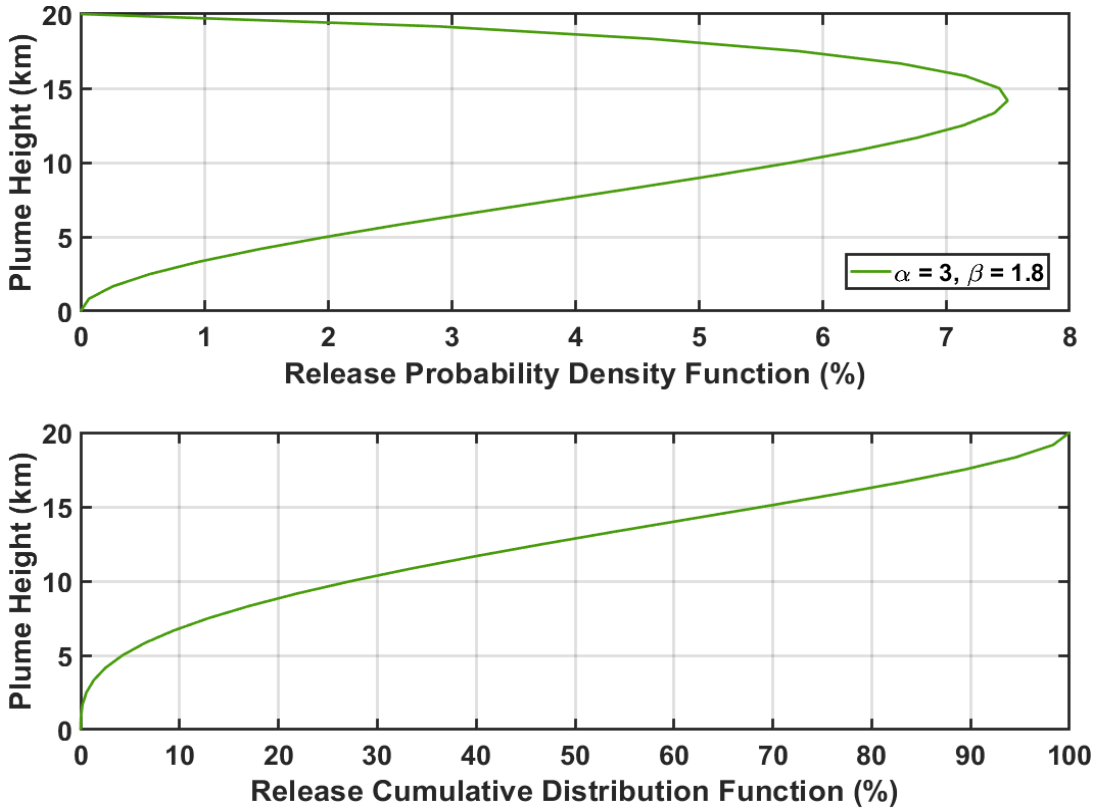

Figure 3.1 Example of release probability density function (PDF) and cumulative distribution function (CDF) of a 20 km eruption column α = 3 and β = 1.8 in the beta PDF that controls the probability of a particle to be released at a given altitude from the plume (Equation 4).

The five eruption scenarios modelled were divided into three Vulcanian and two sub-Plinian scenarios. As such two different TGSDs were used for each of the two eruption types to represent the difference in the particle size distribution that Vulcanian and sub-Plinian style eruptions would produce. As previously mentioned

no TGSD analyses have been undertaken on the tephra deposits of Manam's previous eruptions and so TGSD from analogous volcanoes and eruptions are used (Table 1). The Vulcanian scenarios use the TGSD from the 1974 Vulcanian eruption of Fuego (Guatemala) (Rose et al. 2008b) and the sub-Plinian scenarios use the TGSD from the 1854 sub-Plinian eruption of Hekla (Iceland) (Gudnason et al. 2018).

	Fuego (Rose et al., 2008)	**Hekla (Gudnason et al., 2018)**
Eruption Composition	Basaltic Andesite	Basaltic Andesite
Eruption Date	1974	1854
Eruption Type	Vulcanian	Plinian
Column Height (km)	10	19
Total Grain Size Distribution		
Max Phi	-2	-5.5
Min Phi	10	8
Min Median Phi	-1.9	-4
Max Median Phi	5	4
Min Standard Deviation Phi	0.4	1
Max Standard Deviation Phi	3.2	4

Table 3.1 Total grain size distributions of the 1974 Vulcanian eruption of Fuego (Guatemala) and the 1854 Plinian eruption of Hekla (Iceland) used as analogues for the tephra deposition modelling of Manam eruptions.

TephraProb requires a minimum and maximum repose interval between explosions to be defined when modelling Vulcanian eruptions—this information is not available for Manam. Dominguez et al. (2016) showed that for eruptions where the timing of individual explosions had been recorded, the repose intervals were typically minutes long with a few cases where several hours separated explosions. Therefore, the minimum repose interval was selected as 10 minutes and a maximum of 1 hour.

Each sub-Plinian scenario in *TephraProb* requires a minimum and maximum erupted mass but again no such estimates exist for past eruptions at Manam. Therefore the erupted mass ranges for the sub-Plinian scenarios were calculated by using the relationship between eruption plume height and volumetric flow rate (VFR) identified from a catalogue of historic explosive eruptions (Mastin et al. 2009) shown in (**Equation 3.5**)**:**

$$H = 2.00\ V^{0.241} \qquad \textbf{\textit{(3.5)}}$$

where H is the eruption column height (km) and V is VFR in Dense Rock Equivalent (m^3 DRE s^{-1}). This value is multiplied by the minimum and maximum eruption durations to give the minimum and maximum estimated total erupted volume. These volumes are then multiplied by the assumed density (2500 kg/m^3) to give the range of erupted mass for each scenario.

3.2.2.1 Scenario 1 Ash Venting – Minor Vulcanian Eruption

This scenario is based on the relatively frequent ash venting and minor explosive eruptions that represent most of the reported activity at Manam (Palfreyman and

Cooke 1976; Global Volcanism Program 2021b). Typically, these small-scale eruptions produce eruption clouds reaching to ~3000 m asl but can extend up to ~5000 m asl for longer duration events. These altitudes are used as the minimum and maximum eruption column heights respectively. The smallest of these eruptions are limited to a few consecutive explosions with the larger eruption containing series of explosions lasting between 1-3 hours. Here we model the duration of this style of eruption with a minimum of 30 minutes and a maximum of 3 hours.

3.2.2.2 Scenario 2 Minor Vulcanian Eruption

Scenario 2 represents Vulcanian eruptions of increased intensity and duration compared to scenario 1. This type of eruption is modelled as producing eruption columns between 5000 and 10,000 m asl and having a duration between 3 and 5 hours. In Manam's recent history, 23 eruptions of this magnitude occurred during period 2018 - 2021. An example of this type of eruption is the 23 September 2018 eruption, which generated a 8500 m asl ash column (Global Volcanism Program 2021b).

3.2.2.3 Scenario 3 Major Vulcanian Eruption

Major Vulcanian eruptions are those generating eruption columns greater than 10,000 m asl and longer in duration than scenario 2 events. Scenario 3 is modelled with a minimum eruption column height of 10,000 m asl and maximum 15,000 m asl and duration ranging from 5 to 10 hours. Between 2018 – 2021, 7 eruptions generating >10,000 m asl eruptions columns are likely to have been Vulcanian style

eruptions. Notable eruptions of this kind have occurred on 25 August 2018 and 20 October 2021, which both produced ~15,000 m asl eruption columns (Darwin Volcanic Ash Advisory Centre 2021).

3.2.2.4 Scenario 4 Major Sub-Plinian Eruption (28 June 2019 Style Eruption)

Sub-Plinian eruptions are much less common at Manam and between 2018 and 2021 only 2 or 3 are thought to have occurred. This scenario represents an eruption similar to that of the 28 June 2019 eruption, which generated a ~15,000 m asl eruption column and pyroclastic flows on the western and northeastern flanks destroying 455 homes and agricultural gardens (Global Volcanism Program 2021b). This scenario is modelled with column heights ranging between 10,000 and 15,000 m asl, and a duration between 5 and 10 hours. The calculated erupted mass range for these eruptions is $3.58 \times 10^{10} – 3.85 \times 10^{11}$ kg.

3.2.2.5 Scenario 5 Major Sub-Plinian Eruption (2004/2005 Style Eruption)

Scenario 5 represents the largest known sub-Plinian eruptions of Manam. An example of this category is the 2004-2005 series of eruptions, in which the climatic event lasted up to 15 hours and generated a 21,000-24,000 m asl eruption column (Tupper et al. 2009). The only other eruption during historical times that may have been similar in magnitude was the 1919 eruption; however, the description of the eruption does not provide enough detail to confirm this (Palfreyman and Cooke 1976). This scenario is modelled with an eruption column height range of 15,000 to 25,000 m asl and a duration of between 10 and 15 hours. The resulting calculated erupted mass range for this eruption scenario is $3.85 \times 10^{11} – 4.81 \times 10^{12}$ kg.

	Scenario 1	Scenario 2	Scenario 3	Scenario 4	Scenario 5
Equivalent VEI	1	1-3	3-4	3-4	4-5
Equivalent Magnitude	0-2.1	2.1-3.6	3.6-4.6	3.6-4.6	4.6-5.7
Modelled Eruption Style Condition	Vulcanian	Vulcanian	Vulcanian	Sub-Plinian	Sub-Plinian
Min Height (m asl)	3,000	5,000	10,000	10,000	15,000
Max Height (m asl)	5,000	10,000	15,000	15,000	25,000
Min Mass (kg)	-	-	-	3.58×10^{10}	3.85×10^{11}
Max Mass (kg)	-	-	-	3.85×10^{11}	4.81×10^{12}
Min Duration(h)	0.5	3	5	5	10
Max Duration(h)	3	5	10	10	15
Min Repose Interval (mins)	10	10	10	-	-
Max Repose Interval (mins)	60	60	60	-	-

Table 3.2 Summary table of modelled scenario input parameters. TephraProb does not require erupted mass estimates for Vulcanian eruptions. Equivalent magnitude calculated as per Pyle (2015)

3.2.2.6 Sampled Erupted Masses

For sub-Plinian eruptions (scenarios 4 and 5) *TephraProb* randomly samples the plume height, wind speed and mass eruption rate and duration and then calculates the erupted mass per run. Only parameters resulting in a erupted mass that falls within the pre-defined minimum and maximum erupted mass range (Table 3.2) are selected to be run through the *Tephra2* model. For Vulcanian eruptions a range of

erupted masses is not predefined as the erupted mass is calculated in a different manner to sub-Plinian eruptions which does not require this constraint. Vulcanian eruptions are modelled as a series of discrete explosions, the number of which are defined on the random sampling of the repose interval and eruption duration ranges defined by the user. Each explosion is considered as instantaneous thermal emission as opposed to the sustained emission of a sub-Plinian eruption. The total erupted mass of a Vulcanian eruption is the sum of the erupted mass of each explosion. The mass of one explosion is directly related to the plume height by the thermal equation of Bonadonna et al. (2002) (**Equation 3.6**):

$$H_{vp} = 55M^{0.25} + H_V \quad \textbf{(3.6)}$$

where H_{vp} is plume height (m asl), M is plume mass (kg) and $H_V$is vent height (m asl). The modelled erupted masses for all scenarios and divided between the dry and wet seasons are shown in **Figure 3.2**. It should be noted that the parameters are randomly sampled and validated to enable 100 runs for each season. This is due to the need to randomly sample wind speeds from the prospective season. This therefore results in two independent sets of 100 runs of randomly sampled runs, this is evident in **Figure 3.2** where the distribution of erupted masses are different between seasons in each of the scenarios. This means that the tephra deposition for each season per scenario are not strictly directly comparable as they are not based on the same eruption source parameters. While this doesn't undermine the validity of either season's results it should be kept in mind when comparing the seasonal outputs.

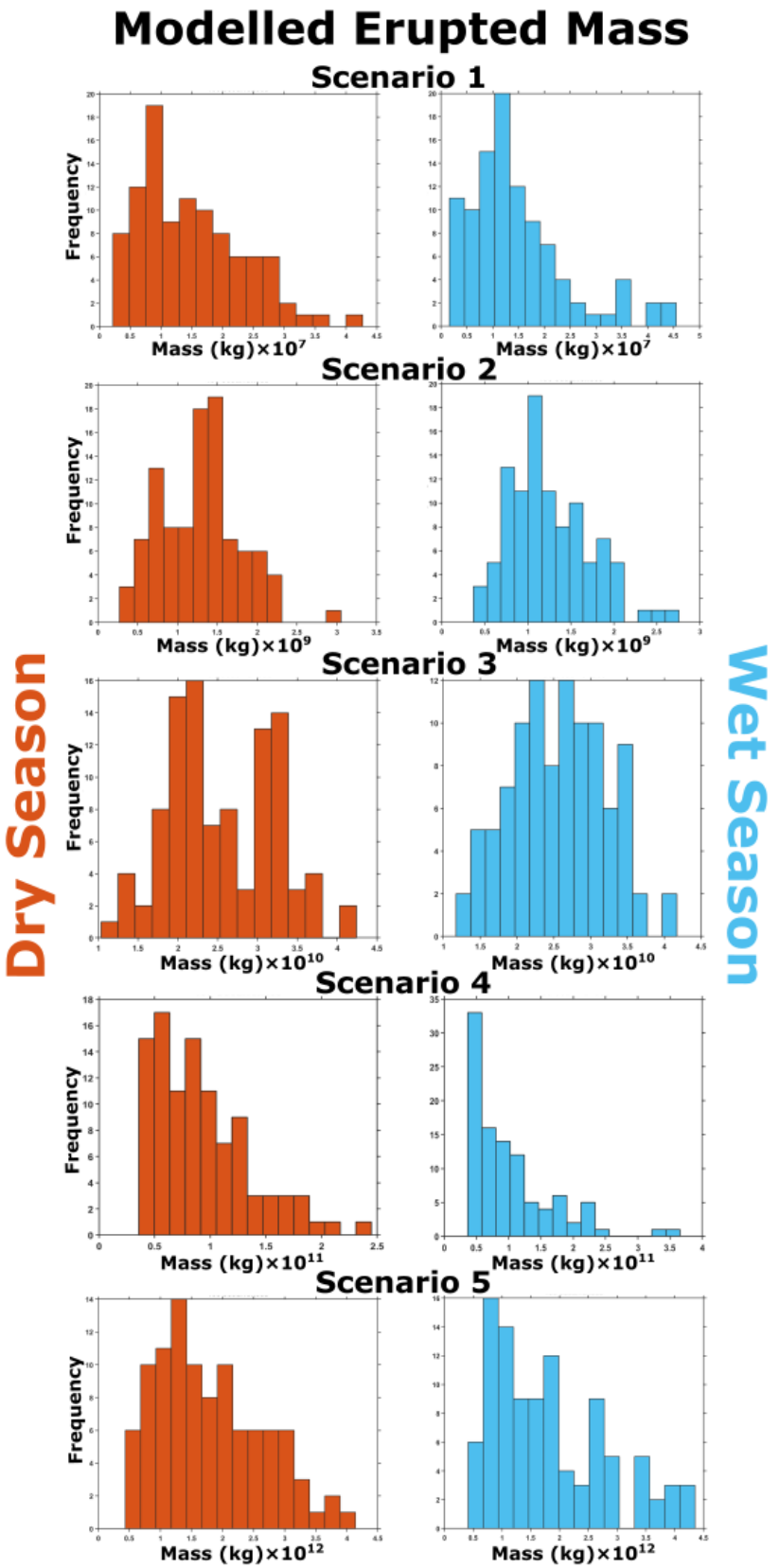

Figure 3.2 – Histograms showing the erupted masses of each scenario by season. The bin widths of each scenario's histograms are 0.25 multiplied by the x axis exponent. The distribution of erupted masses are different between the season within each scenario due to each scenarios season consisting of 100 independently sampled model runs.

3.2.3 Tephra Accumulation Impact Analysis

To assess the impact of the tephra accumulation from the modelled eruption scenarios requires (a) probabilistic tephra accumulation maps, (b) a framework outlining the effects of tephra accumulation on different aspects of human activity, and (c) locations of exposed assets (i.e. populations, buildings, infrastructure and agriculture). Here, the overview of ash fall impacts on different sectors of society produced by Wilson et al. (2015b) is used to assess how the modelled accumulations would impact communities and infrastructure. This framework categorises tephra accumulations into five thickness classes: Trace to Light (>0.1 mm), Thin (>1 mm), Moderate (>10 mm), Thick (>100 mm), and Very Thick (> 1000 mm). The impacts of these tephra deposit thicknesses on buildings, infrastructure, and agriculture are summarised in **Table 3.3**.

The modelled outputs from *TephraProb* include tephra accumulation contours for the following selected masses and equivalent thicknesses: 0.25 kg m^{-2} (0.1 mm – Trace to Light), 2.5 kg m^{-2} (1 mm – Thin), 25 kg m^{-2} (10 mm – Moderate), 250 kg m^{-2} (100 mm – Thick), 2500 kg m^{-2} (1000 mm – Thick). The equivalent thicknesses are calculated using the lithic density parameter selected (2500 kg m^{3}). The isomass contours representing 90% and 50% probability thresholds were used for the impact analysis as they represent high and moderate likelihood distributions, respectively. These isomass contours were digitised into an ArcGIS Pro workspace and overlaid on spatial population and infrastructure datasets to quantify the potential exposure of various assets and therefore the corresponding impacts of the five eruption scenarios.

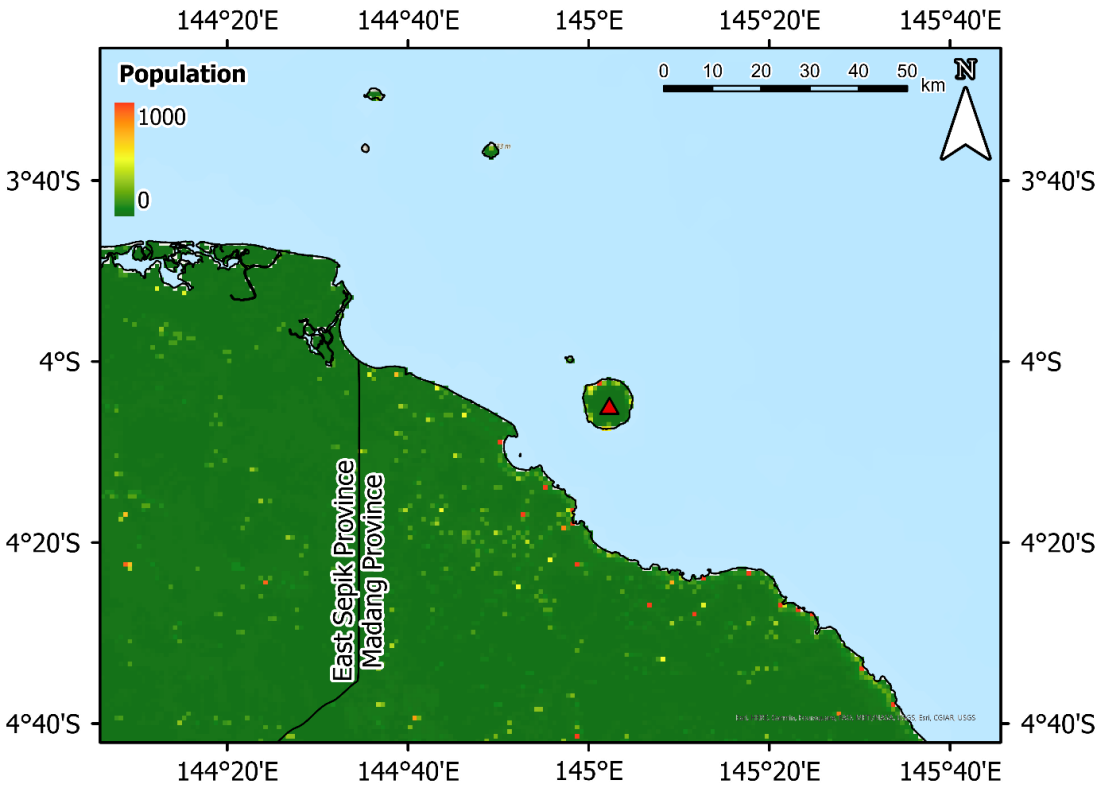

Figure 3.3 Map of population in East Sepik and Madang provinces of Papua New Guinea in the region surrounding Manam (red triangle). Population estimates are derived from the Oak Ridge National Laboratory LandScan Global Data Set (Sims et al., 2023) as "ambient" population over a 24 hour period. Pixels are 1 km by 1 km.

Localised high spatial resolution exposure data was not available for northern mainland Papua New Guinea provinces of Madang and East Sepik. Therefore, global open-access population, land cover, road networks and buildings data sets were used. Population data is derived from the Oak Ridge National Laboratory LandScan Global Data Set (Sims et al. 2023). This data set disaggregates census population figures across 1 km pixels by combining geospatial science, remote sensing techniques and machine learning algorithms to produce a 24-hour average "ambient" population per pixel. The population of Manam had been suggested to be around 4,000 people in 2021 (James Sukua, Pers. Comms.) and the LandScan 2022 data estimates this at 6,349 people (**Figure 3.3**). These two estimates are broadly in agreement and, without census data available specifically for Manam

island, this suggests that the LandScan data are reliable for this region of Papua New Guinea.

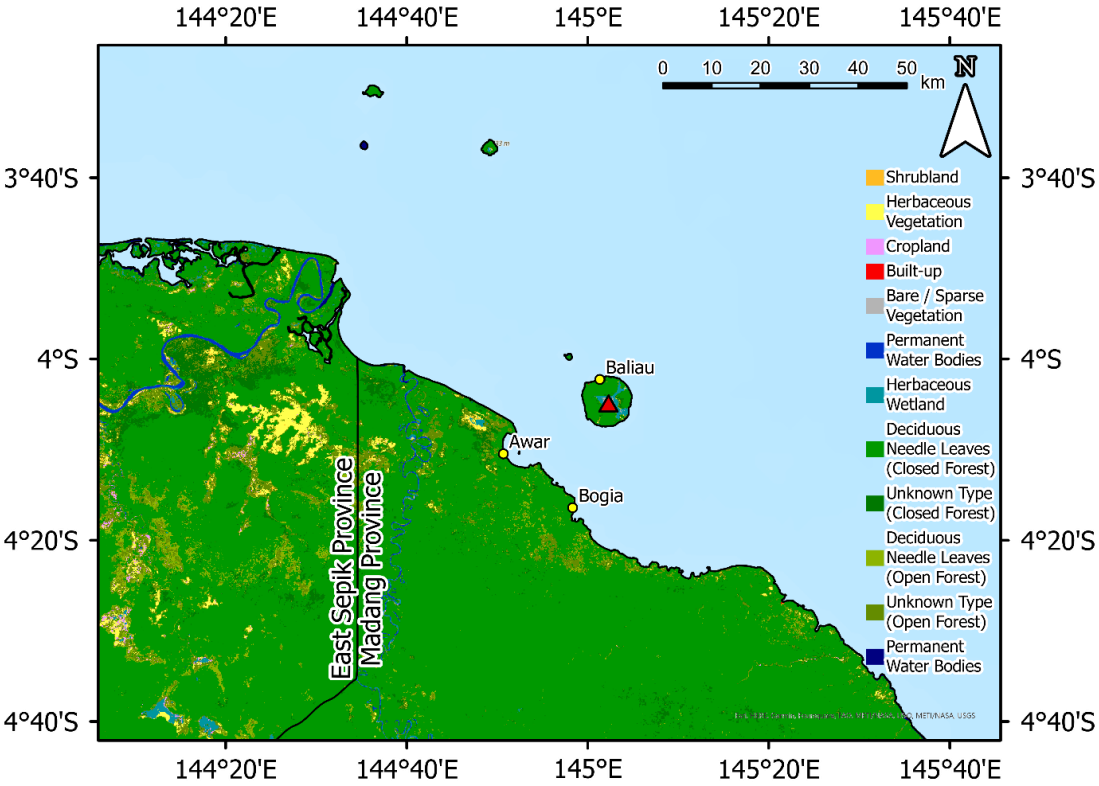

Figure 3.4 Map showing the land cover in East Sepik and Madang provinces in the region surrounding Manam (red triangle). Land cover pixels are 100 m by 100 m from the Copernicus Global Land Service Global Land Cover v3 dataset ("Copernicus Global Land Service," 2020).

Land cover data is useful for determining the specific impact that ashfall will have on a given area. For example, while thin ashfall may cause very little damage or disruption to robust structure in an urban area, it may be enough to cause the failure of crops in an agricultural region (Jenkins et al. 2015). The Copernicus Global Land Service Global Land Cover v3 (Buchhorn et al. 2020) data set provides 100 m pixel resolution land use data from 2019. The Land Cover v3 dataset is produced using the MultiSpectral Imager (MSI) on the European Space Agency's Sentinel-2 satellite to identify the predominant vegetation or land cover within the 100 m pixels (**Figure 3.4**). For the exposure analysis herbaceous vegetation, shrubland and

bare/sparse vegetation are included alongside the cropland designation as potential crop-covered land. This is due to the fact that these landcover types are difficult to distinguish from each other solely using satellite remote sensing but also that areas where non-forest vegetation dominates is likely to be a result of human cultivation in these regions of Papua New Guinea where forest is the dominant landcover class (Biass et al. 2022).

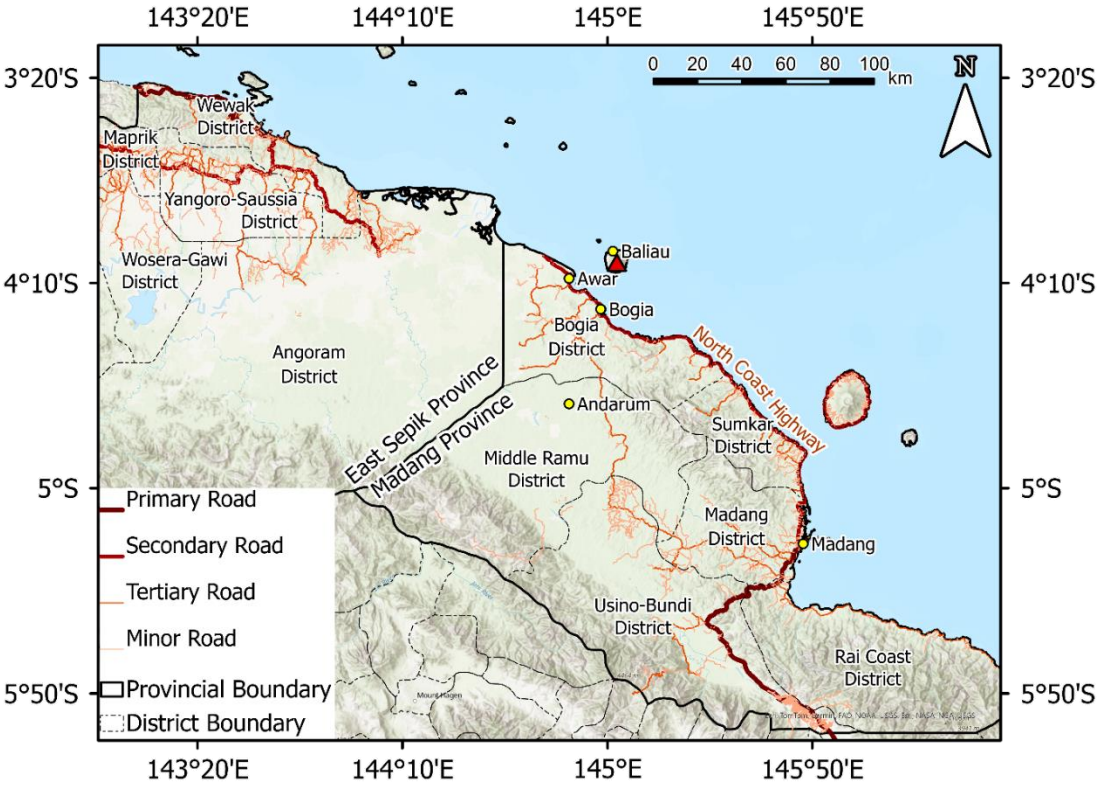

Figure 3.5 The road networks of Madang and East Sepik provinces in the region surround Manam (red triangle). Road network was produced by the Open Street Map (OpenStreetMap contributors 2023). The North Coast Highway (secondary road – brown text highlight) runs along the coastline from Madang via Bogia and Awar to the northwest of Bogia district. The second route from Madang to Bogia runs inland through the Madang, Middle Ramu and Bogia districts. Madang is the largest mainland settlement close to Manam, to Madang the provincial capital of Madang province. Bogia is the district capital of Bogia district which Manam is located in.

Road networks are key transport links in Papua New Guinea, and in Madang and East Sepiks provinces these are the main way in which towns and villages are connected. Road networks represent the primary routes used for evacuations before and during volcanic crises but also for aid to arrive to affected areas in the

aftermath of volcanic eruptions. Here the OpenStreetMap (OSM) road network data (OpenStreetMap contributors 2023) is used for this analysis (**Figure 3.5**).

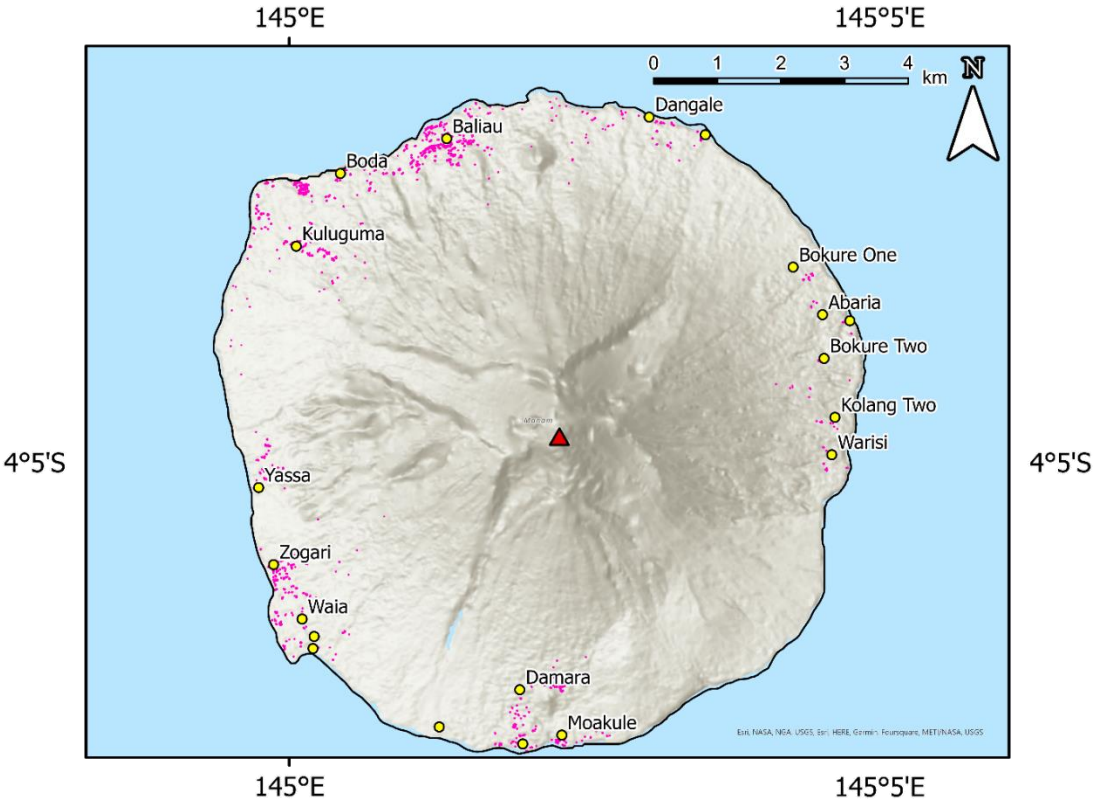

Figure 3.6 Buildings on Manam according to Open Street Map data (OpenStreetMap contributors 2023).

The OSM building data (OpenStreetMap contributors 2023) is used to analyse how many buildings are affected by the tephra accumulation from different scenarios. This data set only contains the footprint of the buildings and not any construction-type or structural information. Additionally, while this data set is generally quite comprehensive and includes coverage of Manam Island (**Figure 3.6**), it does not include any buildings along the coast of the mainland closest to Manam, including towns such as Bogia. While this limits the ability to assess number of buildings impacted in this area, the Land Cover v3 dataset includes a “built-up” classification referring to areas containing predominantly human structures and urban land use.

Category	Sub-Category	Trace to Light (>0.1mm)	Thin (>1mm)	Moderate (>10mm)	Thick (>100mm)	Very Thick (>1000mm)
Buildings	**Structural**	None	**Unlikely to be a problem** at this tephra hazard intensity.	In rare instances, **non-engineered and long-span roofs may be vulnerable to damage**, particularly when tephra falls wet or is subsequently wetted by rainfall.	**Structural damage due to excessive tephra loading. Very thick tephra deposits (>100 mm) may cause roof collapse**.. Non-engineered, long-span and low-pitched roofs are typically the most vulnerable.	**Structural damage to most buildings likely.**
	Non-Structural	**Minimal.** Tephra may also accumulate in gutters and possible corrosion of metallic elements.	Tephra may **block gutters and downpipes, leading to localized flooding and damage. Roofing materials may be abraded or damaged** by human actions **during tephra removal**.	**As above, with higher likelihood of more severe impacts.**	**Non-structural elements**, such as gutters, **are more vulnerable to failure**. Gutters may accumulate tephra from the roof.	
	Contents and Furnishings	Tephra **may contaminate building interiors** leading to risk of adverse health impacts for building occupants.	Heating, ventilation and air-conditioning **(HVAC) systems can be disrupted by obstructed filters**, condensers and air intakes.	**As above, with higher likelihood of more severe impacts.**	**As above, with higher likelihood of more severe impacts.**	

Infrastructure	**ALL**	N/A	Corrosion and/or abrasion of paintwork, windscreens, metallic elements, some air-handling, mechanical and electrical equipment or engines etc. Potential clogging of air and oil filters.	N/A	N/A	**Structural damage to all structures possible. Expect most systems to be disrupted for extended periods. Ground transport networks likely to be impassable.**
	Ground Transport	Transport networks possibly affected by reduced visibility. Roadway and railway may experience reduced surface traction.	**Visibility from direct fall and remobilization**; reduction in traction; most road markings obscured; increased wear of engine and brakes; possible signal failure on railway lines.	**Ground transport networks disrupted by visibility and traction problems.**	**Transport networks severely affected by reduced traction**; very thick tephra falls may create **extra loading on bridges**, especially when wet.	
	Power System	None	**Flashover of power line and transformer insulators may occur with <3 mm of tephra fall**. Hydroelectric plants may see abrasion damage to turbines. Thermal plants may be vulnerable to blockage of air intakes.	**Insulator flashover** is the most likely impact. **Tephra accumulation may also overload lines**, **weak poles and light structures**, and cause **additional tree-fall** onto lines.	**Structural damage to lightly engineered components and buildings possible**. Substantial clean-up of sites required. Most generation plants likely to be disrupted.	
	Water Supply	None	Raw water sources: probable increase in turbidity; **possible increase in acidity and levels of soluble elements**. Tephra-induced electricity outages are the most common cause of disruptions to water production. Demand may remain high for	**Possible damage to water and wastewater** networks if tephra enters systems, such as pumping equipment, hydraulic seals, water treatment plants,	**Significant contamination of exposed surface waters**. Probable **blockage or sedimentation of water supply pipes** or canals, storm drains and/or	**Structural damage to all structures possible. Expect most systems to be disrupted for extended periods. Ground**

			months afterwards if water is needed to dampen downwind remobilized ash.	waste-water treatment plants, etc. **Possible blockage of storm drains, ditches and/or sewers, leading to surface flooding**.	sewers, **leading to surface flooding**. **High risk of severe damage to water- and wastewater- treatment plants** if volcanic ash enters systems.	**transport networks likely to be impassable.**
	Waste Water	None	**Tephra may enter sewer lines** where there is inflow or infiltration. Volcanic tephra may form unpumpable masses in sewer lines. Mechanical pre-treatment and treatment equipment is highly vulnerable to damage from ash-laden raw sewage at wastewater treatment plants.			
	Telecoms	None	**Possible damage to external telecommunication components and power cables.**	As above	**Possible damage to communication dishes and microwave towers** due to excess tephra loading.	**Structural damage to all structures possible. Expect most systems to be disrupted for extended periods. Ground transport networks likely to be impassable.**
	Airports	**Airports are very sensitive to tephra fall.** They may close, due to reduced runway friction reduced visibility when tephra on the ground. **Almost always requires clean-up.**	**As above, with higher likelihood of more severe impacts.**	**Airports closed for clean-up.**	**As above, with higher likelihood of more severe impacts.**	

Agriculture	**Pastoral Farming & Horticultural Farming**	**Likely to be minimal**; but could include coverage of feed supplies or produce and contamination of water supplies.	Volcanic ash coverage of crops, **may lead to discoloration of leaves and fruits**; coverage of livestock feed; possible leachable element toxicity hazards. **Generally minor health hazards for livestock.**	Volcanic ash coverage of crops may lead to **structural damage and more severe UV blockage**. Coverage of livestock feed more intense and longer duration.	**Burial of pasture and most crops**. Loading damage to tree crops likely. Soil's fertility may wane over time as key soil processes are broken by volcanic ash blanket **Damage/burial of farm assets**.	**Total burial of crops/pastures**. The buried soil's fertility will decrease over time as key soil processes are sealed off. Tree damage likely in production forests.
	Forestry (Silviculture)	N/A	N/A	N/A	**Tree damage possible** in production forests.	**Total burial of crops/pastures**. The buried soil's fertility will decrease over time as key soil processes are sealed off. Tree damage likely in production forests.

Clean-up		Usually no action required. Suspended ash **may require removal from closed environments**, particularly for people susceptible respiratory illness.	**Minor clean-up required**: sweeping of roads, paved areas and roofs/gutters usually sufficient. **Tephra falls of only a few mm depth will generate large volumes of volcanic ash for collection and disposal**.	**All roads and paved areas on public and private properties require cleaning**; private properties usually require assistance with clean-up/disposal.	**As above, but with much larger volumes** which will require greater resources and/or cleaning time; vegetated areas (e.g., parks and gardens) may require cleaning too.	**As above, but with much larger volumes** which will require greater resources and/or cleaning time.

Table 3.3 Impacts on different parts of human activity and infrastructure by thickness of accumulated ash deposits. This is a abbreviated version adapted from Wilson et al. (2015b).

3.3 Results

In this section, differences in the seasonal wind directions and velocity are described first to provide context for the subsequent tephra transport distribution. The modelled tephra thicknesses for each scenario at both 50% and 90% probability, in both the wet and dry seasons, are presented. The potential exposure of populations and assets are then quantified based on the overlap between these datasets and particular tephra thickness contours. Interpretation of these results in the context of the tephra impact framework (Wilson et al., 2015) and emergency planning will be included in the discussion.

3.3.1 Seasonal Wind Directions

The NOAA Reanalysis 2 wind data (Kanamitsu et al. 2002) from 2001-2021 (**Figure 3.7**) used in the *TephraProb* modelling indicates that there are marked differences in median wind direction between the dry and wet seasons most notable at altitudes of 0-10 km asl and at >15 km asl. The seasonal difference in median wind speeds is less pronounced than those of wind direction with differences of <5 m/s between the two seasons at most sampled altitudes except 16.6 and 26.4 km asl where the difference is 5 m/s. Overall these inter-seasonal wind speed differences across all altitudes are minor and so it is expected that the main influence on inter-seasonal ash accumulation is wind direction. Therefore wind direction differences within each altitude band analysed by *TephraProb* will be highlighted here. For clarity, wind directions here describes the direction that the wind is moving toward

rather than provenance to remain consistent with descriptions of modelled tephra deposition distributions.

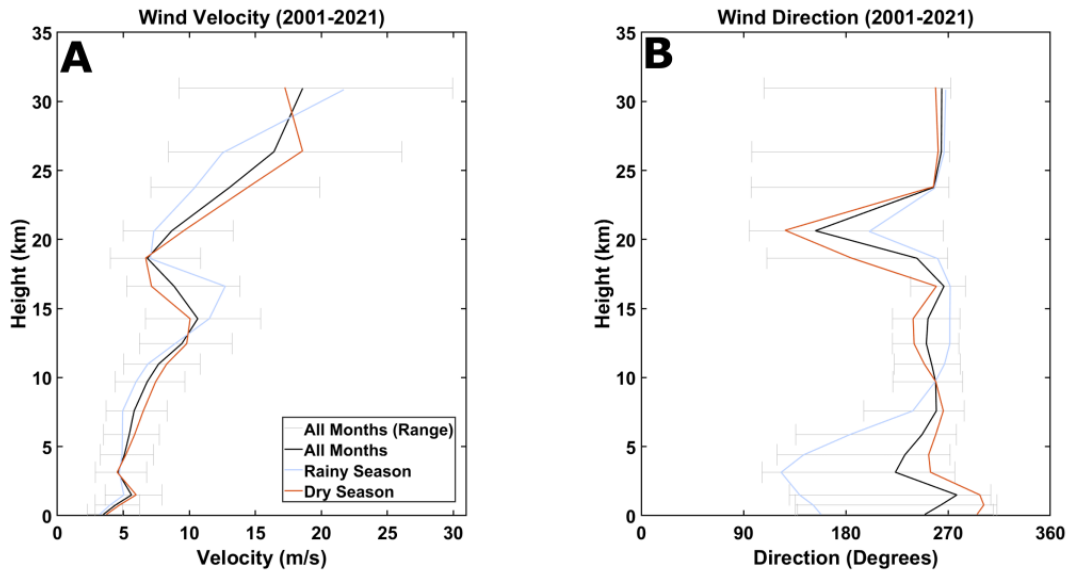

Figure 3.7 Profiles of wind velocity (A) and direction (B) by altitude around Manam according the NOAA Reanalysis 2 dataset (Kanamitsu et al. 2002) for the years 2001 to 2021. All months (black), dry season (brown), and wet season (blue).

The most prominent seasonal difference in wind direction is in the 0.1 – 4.4 km asl altitude band where the two seasons have effectively diametrically opposed wind directions (**Figure 3.7**). During the dry season the wind direction is dominated by west to northwest winds (west - 14%, 17.5% - west-northwest, and 17% - northwest). In contrast, the wet season is dominated by east to southeast winds (east – 11%, east-southeast – 13.5%, and southeast - 11%) with some lesser contribution to westward winds. The influence of wind direction at these altitudes have a significant role in determining the distribution of tephra from all eruption scenarios which all inject tephra into or above these altitudes. However, the most impacted scenarios by the wind directions at these altitudes are those where the

majority of ash injection occurs within these, which are scenarios 1 and 2 which have a modelled eruption column height of 3-5 km asl and 5-10 km asl respectively.

The wind directions in the 5.9 – 9.7 km asl altitude bands are more similar between seasons that those at lower altitudes, with both dominated by westward tending winds (**Figure 3.7**). In the wet season the winds transition from the south to southeast dominated winds at altitudes >5km asl towards those with a westward component (west-southwest – 12%, west – 16%, west-northwest – 12%) but still with a notable eastward component (east-southeast – 5.5%, east – 7%, east-northeast – 6%) (**Figure 3.8).** The dry season however has a negligible eastward component and more substantial westward element (west-southwest – 18%, west – 27%, west-northwest – 16%).

At altitudes of 11 – 14.3 km asl wind directions of the two seasons are both mainly composed of westward bound winds (**Figure 3.7**). The main distinction between the two seasons being the skew towards northwest winds in the wet season and southwest winds during the dry season (**Figure 3.8**). The most substantial wet season components are west (26%), west-northwest (21%), and west-southwest (13%) winds while the dry season winds skew more to the west-southwest (25%) and southwest (18%). The winds at this altitude influence dispersal of ash from scenarios 3, 4 and 5 which include the largest Vulcanian scenario and the sub-Plinian scenarios. These scenarios produce the most ejected mass and inject material in or above 11 – 14.3 km asl altitudes and so these winds greatly determine the dispersal before the more varied directional winds at lower altitudes impact dispersal.

The wind directions at altitudes of 16.6 – 18.6 km asl only impact tephra dispersal from the scenario 5 sub-Plinian eruption, which has a modelled eruption column height of 15-25 km asl. The wet season has a major westward directional component (38%) with the west-southwest and west-northwest components contributing 15% and 17% respectively (**Figure 3.8**). The eastward directional winds contribute only a small portion of the total winds observed at these altitudes. Overall, the dry season has is dominated by winds ranging from southwest to southeast (west – 21%, west-southwest – 14%, and west-northwest 10%) but a notable east component exists which isn't present in the wet season (east – 10%, east-southeast – 7.5%, and east-northeast 4%).

As with the 16.6 – 18.6 km asl altitude winds, those at 20.6 – 23.8 km asl also only influence the dispersal pattern of scenario 5 eruptions. The winds at these altitudes only impact modelled eruptions which were sampled to have eruption columns >20 km asl. Compared to the 16.6 – 18.6 km asl altitudes winds, the 20.6 – 23.8 km asl winds are relatively more balanced between eastward and westward bound winds. While 46% of wet season winds are westward due to 36% from directly west winds with minor contributions from west-southwest (6%) and west-northwest (4%), 34% of the total winds are contributed by east-southeast to east-northeast winds (east – 15%, east-southeast – 11%, and east-northeast – 8%) (**Figure 3.8**). Similarly, the proportion of wind directions in the dry season for these altitudes are relatively balanced. The westward contributions are the same as the wet season (46%) but the eastward contributions are greater with a total of 44% from east-northeast to east-southeast, notably 26% from east bound winds (**Figure 3.8**).

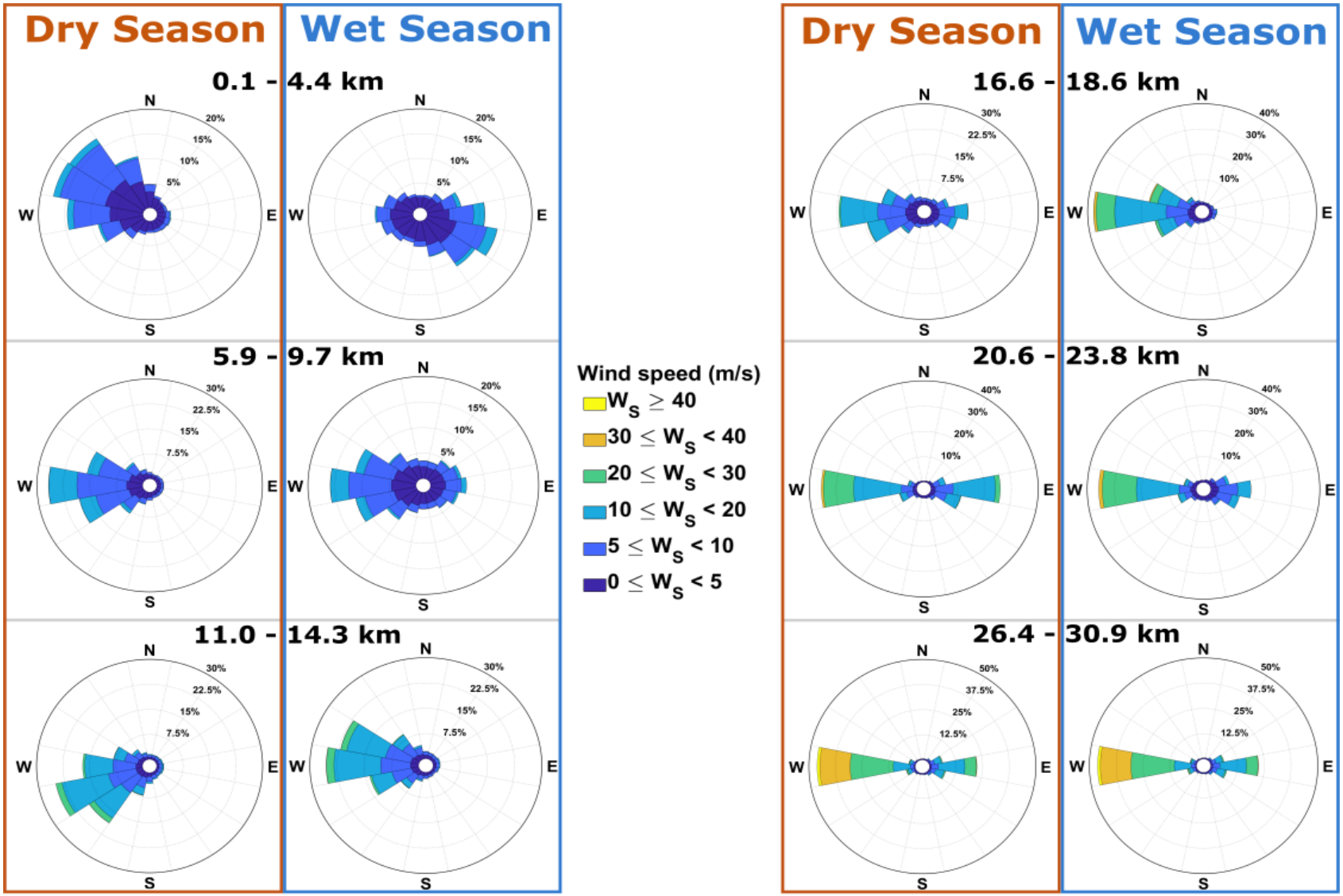

Figure 3.8 Roses showing the proportion of wind direction and speeds around Manam at the wind profile sampling heights defined by TephraProb for the years 2001-2021 according to the NOAA Reanalysis 2 data set (Kanamitsu et al., 2002).

3.3.2 Probabilistic Tephra Deposition Modelling

Here the results from the *TephraProb* probabilistic modelling of the five eruption scenarios are presented in the form of ash thickness isopach maps converted from isomass deposition maps using the lithic density value used (2500 kg m^3, **Table 3.2**). Each isopach is labelled indicating the minimum mass expected within that area depending on the exceedance probability of the deposition map (either 50% or 90%). For example, the 10 mm isopach in a 90% exceedance probability map indicates that anywhere within the isopach has a 90% chance of an accumulation of 10 mm or greater, whereas the area outside the isopach has a less than 90% chance of a 10mm or greater tephra accumulation. Importantly, there is still a chance that a 10 mm accumulation may occur outside the isopach, and this should be kept in mind when interpreting probabilistic tephra modelling outputs.

3.3.2.1 Scenario 1

The modelled output for scenario 1 suggests that no tephra accumulations equal to or greater than 0.1 mm (0.25 kg/m^2) are expected at either the 90% (high) or 50% (moderate) exceedance probabilities.. However, to demonstrate the extent of very fine ash dispersal from these short-lived eruptions, the 50% exceedance contour for deposition of 0.1 kg/m^2 (or 0.04 mm) is shown in **Figure 3.9**. This very fine ash deposit for both seasons extends predominantly southward but remains confined to Manam's flanks and does not reach the coast. Although subtle, the deposit distribution in the dry season has a slight westward skew relative to the wet season which has a more easterly direction; controlled largely by the contrasting prevailing wind directions in the lower atmosphere between the two seasons (**Figure 3.8**).

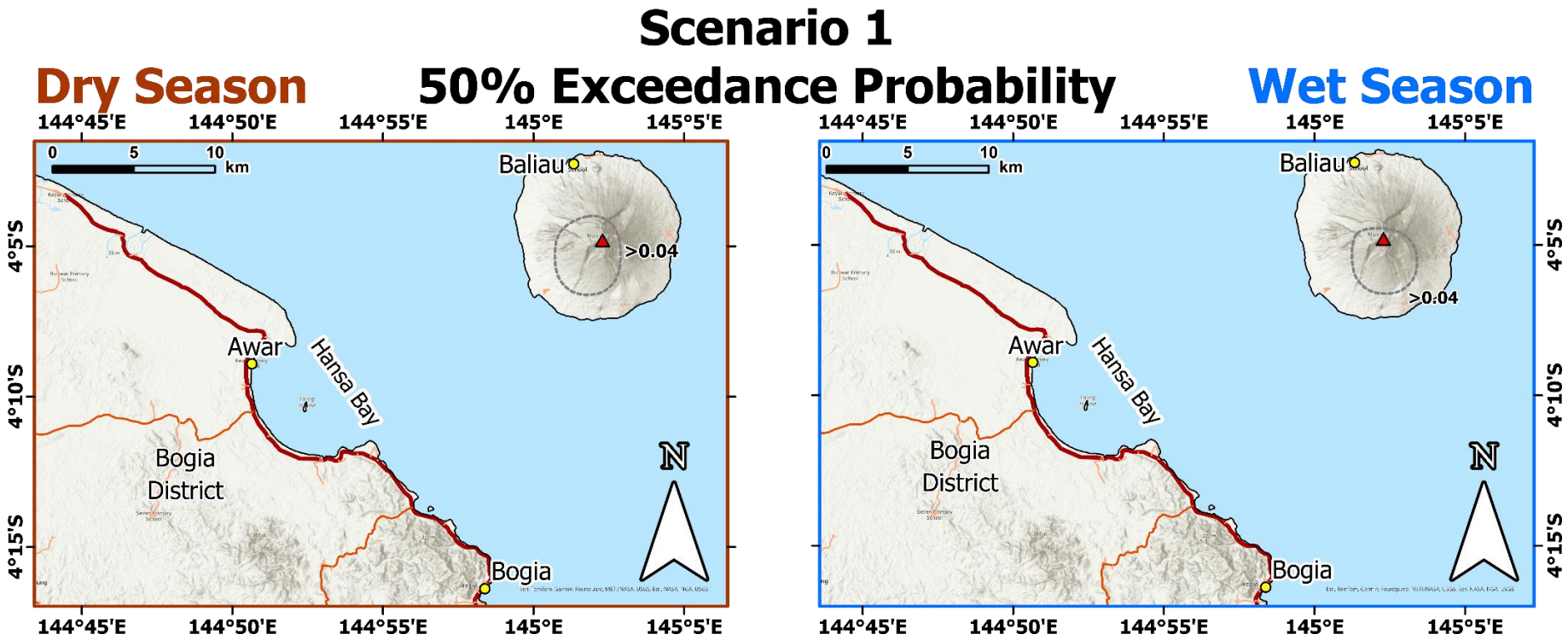

Figure 3.9 Probabilistic modelled results for Scenario 1 which represents ash-venting or minor vulcanian explosions in the dry season (left) and wet season (right). The contours here represent a 50% probability that deposited tephra will exceed the thickness (in mm) indicated by the contour label/

3.3.2.2 Scenario 2

For scenario 2 eruptions during the dry season, there is a 90% chance that the western half of Manam would receive at least 0.1 mm of tephra accumulation (**Figure 3.10**). Manam's northeastern, eastern and southeastern coastlines and the mainland all fall outside the 0.1 mm isopach under 90% exceedance probability, indicating a <90% probability of seeing this thickness of ash accumulating there (**Figure 3.10**). Visualised as the 50% exceedance probability, the 0.1 mm isopach covers the entirety of Manam and the southern tip of Boisa Island to the northwest of Manam but does not reach the mainland (**Figure 3.10**). Central and western Manam fall within the 1 mm isopach but Baliau and other northern Manam settlements remain outside of this isopach (**Figure 3.10**). Therefore, there is a 50% probability that central and western Manam will receive at least 1 mm of ash, with the remainder of the island receiving ≥ 0.1 mm of ashfall. Most of Manam, except the most northern regions (including Baliau) and the western coastal areas, has a 90% likelihood of experiencing at least 0.1 mm of tephra accumulation (**Figure 3.10**). The 0.1 mm isopach for a 50% exceedance probability encapsulates the entirety of Manam island indicating that there is a moderate chance in all parts of the island to receive at least 0.1 mm of ash during a scenario 2 eruption (**Figure 3.10**). An area covering most of the southern half of Manam, and much of the slopes of the volcano itself, has a 50% probability of accumulating tephra at a thickness of 1 mm or greater (**Figure 3.10**). During the wet season, accumulation of at least 0.1 mm is not expected on the mainland or Boisa Island, at 50% probability (**Figure 3.10**).

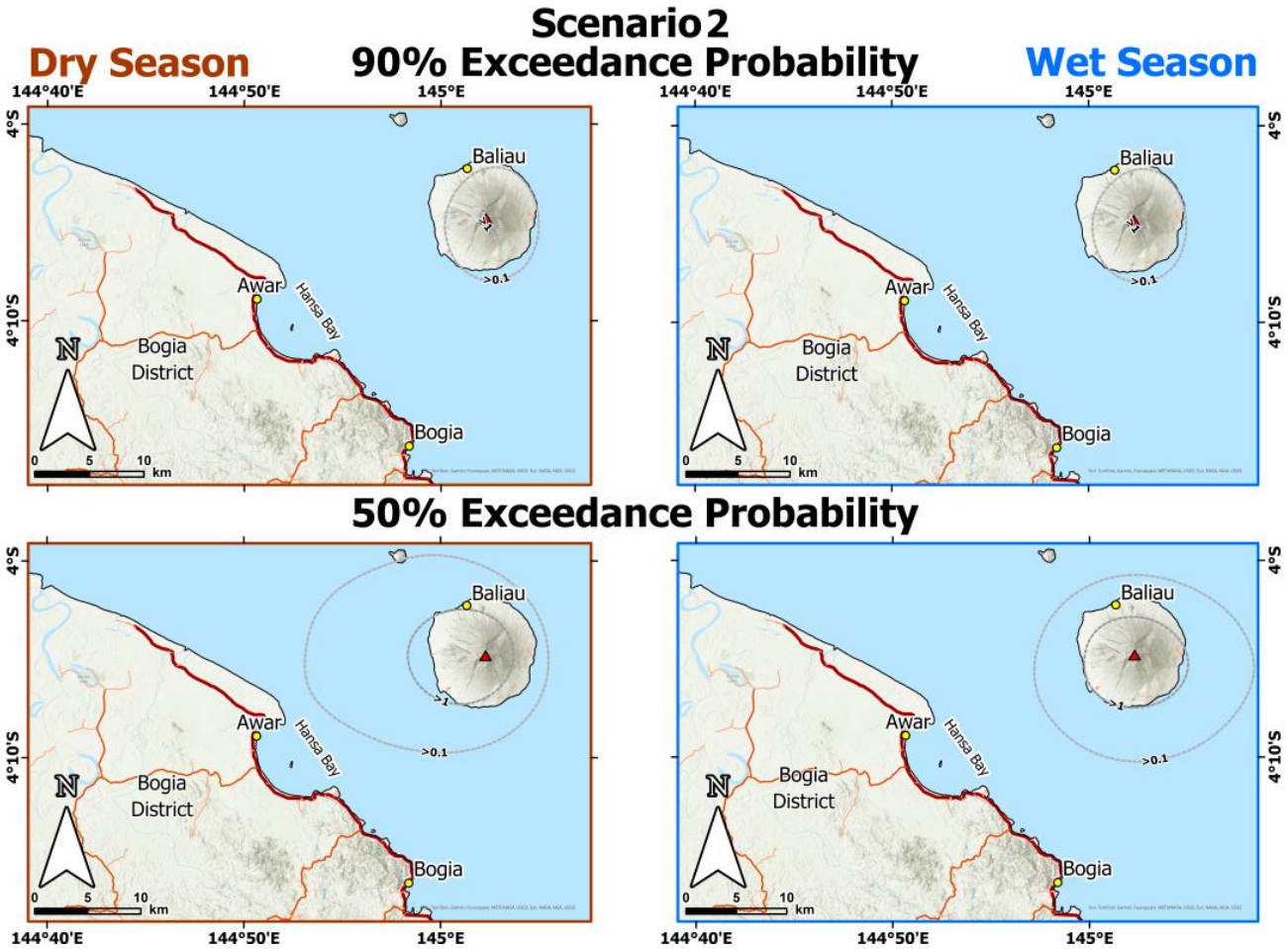

Figure 3.10 Probabilistic isomass plot for Scenario 2 during the dry season (left column) and wet season (right column). Scenario 2 is a Vulcanian eruption lasting 3-5 hours generating an 5-10 km eruption column. The contours here represent a 90% (top row) or 50% (bottom row)probability that deposited tephra will exceed the thickness (in mm) indicated by the contour label.

As in scenario 1, there is a distinct difference in the general trending direction of tephra deposition between the two seasons. During the dry season, the prevailing tephra dispersal is almost directly due west (**Figure 3.10**), whereas the expected deposit in the wet season has a more southeasterly trending shape (Figure 3.10). Scenario 2 eruptions all generate eruption plumes that reach between 5 and 10 km asl, yet despite the westerly prevailing winds in the 5.9 – 9.7 km asl altitudes (Figure 3.8) the southeasterly prevailing winds in at 0.1-4.4 km asl Figure 3.8) during the wet season seem to have the strongest influence on tephra dispersal direction. The wind direction in both these two altitude bands are both predominantly westerly during the dry season.

3.3.2.3 Scenario 3

The scenario 3 90% exceedance probability dry season results show that the western half of Manam (inclusive of Baliau) would accumulate a thickness of at least 1 mm of tephra (**Figure 3.11**). There is a high probability that 0.1 mm or more will accumulate on the eastern half of the island, and the northern and southernmost coasts, as well as on Boisa Island. The northern half of Hansa Bay also falls within this isopach, as does part of the North Coast Highway (**Figure 3.11**). At 50% exceedance probability, the area of potentially impacted land expands considerably. The 0.1 mm isopach extends 63 km to the west of Manam's south crater and reaches Bogia to the south (**Figure 3.11**). All roads from Bogia and Madang to the communities north of Bogia have a moderate probability of being impacted by at least 0.1 mm of ash accumulation. The settlements around Hansa Bay, including Awar Plantation, all have a high probability of experiencing at least 1

mm of ashfall. Manam Island itself falls entirely within the 1 mm isopach, with the central and western portions (including Baliau) having a 50% chance of 10 mm or greater of tephra deposition.

The modelled results for scenario 3 eruptions during the wet season show that there is a 90% probability for anywhere on Manam island to receive 1 mm or more of tephra accumulation as a result of this type of eruption (**Figure 3.11**). The 0.1 mm isopach based on a 90% exceedance probability does not reach the mainland but does intersect the southeastern coastline of Boisa Island (**Figure 3.11**). The 50% exceedance probability plot (**Figure 3.11**) for the wet season scenario 3 eruptions shows that there's the majority of Manam, excluding the northeast coastal areas, have a moderate probability of at least 10 mm of ash accumulation. The northeastern coastal areas fall with within the 50% and 90% 1 mm isopach indicating there is high probability of experiencing 1 mm or more of ashfall. Boisa island falls wholly within the 50% exceedance probability 1 mm isopach which falls just short of the mainland (**Figure 3.11**). The 50% exceedance probability 0.1 mm isopach reaches 43 km to the west, 24 km to the east and around 30 km to south. This isopach is closer to a symmetrical distribution that its dry season counterpart and impacts Bogia and the North Coast Highway between Bogia and Hansa Bay. The secondary roads leading from Madang also have a moderate chance of being affected by 0.1 mm or greater of tephra accumulation.

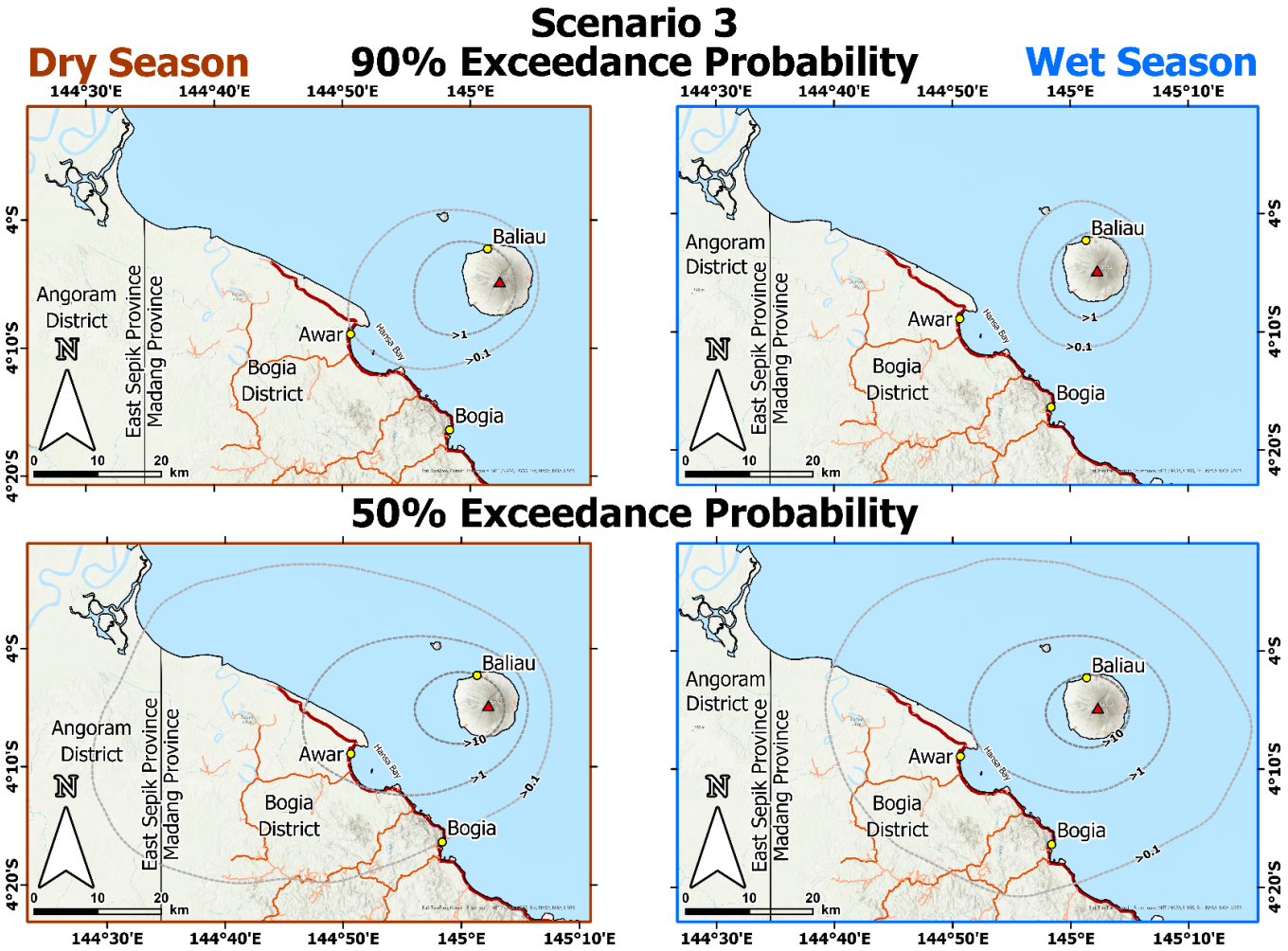

Figure 3.11 Probabilistic isomass plot for Scenario 3 during the dry season (left column) and wet season (right column). Scenario 3 is a Vulcanian eruption lasting 5-10 hours generating an 10-15 km eruption column. The contours here represent a 90% (top row) or 50% (bottom row)probability that deposited tephra will exceed the thickness (in mm) indicated by the contour label.

The dry season tephra accumulation isopachs at both the 90% and 50% probabilities show a more pronounced westward skew than their wet season counterparts (**Figure 3.11**). The wet season dispersal pattern has a more symmetrical distribution than the dry season while still maintaining a slight westerly skew (**Figure 3.11**). The winds between 5.9-9.7 and 11.0-14.3 km asl are broadly westward dominated year round. Therefore the opposing wind directions in the lowest altitude band (**Figure 3.8**), must be those influencing the dispersal pattern the most. The wet season wind directions in these altitudes range between northeastern through to southeastern and since all tephra particles must move through this layer these eastward trending low altitude winds are able to balance out the influence of the westward dominated higher altitude winds.

3.3.2.4 Scenario 4

The scenario 4 90% exceedance probability plot (**Figure 3.12**) indicates that there is a high chance that anywhere on Manam will be impacted by at least 1 mm of tephra accumulation. Additionally, the majority of the island excluding the northeast, east and south east coastlines have a 90% chance of receiving at least 10 mm of ashfall with the central and western slopes of Manam likely to be inundated by 100 mm or more of deposited ash (**Figure 3.12**). Neither Boisa Island or the mainland have a 90% probability of receiving at least 0.1 mm.

A large portion of Manam covering central, western coast and the north and south slopes fall within the area indicated as having a 50% chance of receiving 100 mm of tephra from a scenario 4 type eruption (**Figure 3.12**). The rest of Manam has a 50% chance of experiencing 10 mm of tephra accumulation and under the same

exceedance probability Boisa Island falls within the 1 mm contour. The 0.1 mm contour in the 50% exceedance probability contour extends over the mainland, south of Hansa Bay and towards the Ramu river in the west, approximately 37 km from Manam. There is a moderate chance of receiving 1 mm along the entire stretch of the North Coast Highway north of Bogia. Bogia has a less than 50% chance of receiving 0.1 mm of ash during this intensity of sub-Plinian activity (**Figure 3.12**).

During the wet season scenario 4 eruptions have a 90% chance of depositing 100 mm or more of tephra on central Manam on the upper slopes of the volcano itself (**Figure 3.12**). The majority of the island except the most northeastern and northwestern coastal areas have a high probability of accumulating at least 10 mm of tephra during a scenario 4 sub-Plinian eruption. The northeastern and northwestern coasts of Manam have a 90% probability of 1 mm of tephra under this scenario. No areas outside of Manam have a 90% probability to receive any thickness of ash during the wet season.

The area with a 50% probability of receiving 100 mm or more of ash corresponds to most of southern Manam as well as the northern, eastern and western slopes of the volcano itself (**Figure 3.12**). Northern Manam and the most southwestern coastal areas all fall within the 10 mm isopach in the 50% exceedance probability output (**Figure 3.12**). Boisa Island is shown to have a 50% chance of receiving at least 0.1 mm of tephra accumulating. No part of the mainland is falls within any of the isopach in **Figure 3.12** indicating there is less than 50% probability that 0.1 mm as will fall in these areas.

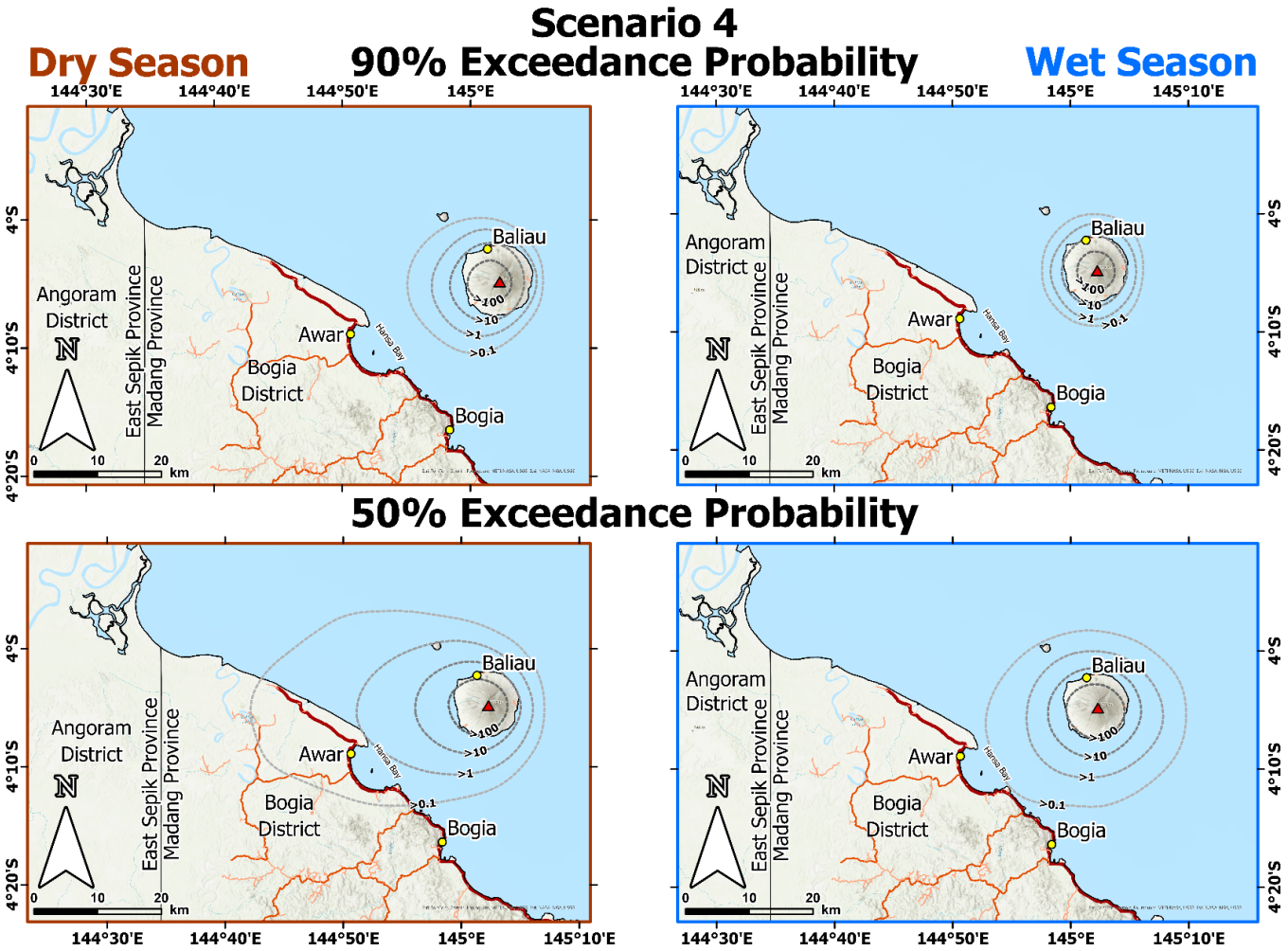

Figure 3.12 Probabilistic isomass plot for Scenario 4 during the dry season (left column) and wet season (right column). Scenario 4 is a sub-Plinian eruption lasting 5-10 hours generating an 10-15 km eruption column. The contours here represent a 90% (top row) or 50% (bottom row)probability that deposited tephra will exceed the thickness (in mm) indicated by the contour label.

Like the previous scenarios there is a clear difference in the general dispersal patterns between the two seasons. The dry season has the westerly dominated distribution seen in the other scenarios, as mentioned, reaching 37 km towards the Ramu River (**Figure 3.12**). In the 50% exceedance probability plot (Figure 3.12) the 0.1 mm isopach extends some 15 km south onto the mainland but does not reach Bogia and the most easterly extension of the tephra dispersal pattern is limited to 9 km. The wet season dispersal pattern shown in (**Figure 3.12**) has a relatively symmetrical shape compared to the dry season. The 0.1 mm isopach extends 12 km to the north and 15.5 km to the south and not making landfall. Similarly this contour extends 17.5 km to the west and 14 km to the east. Like with previous scenarios it is easterly winds in the lower 5 km that are likely responsible for the more symmetrical dispersal pattern seen in the wet season. Notably the scenario 4 dispersal pattern has a smaller extent than that of scenario 3 despite having larger erupted masses.

3.3.2.5 Scenario 5

The modelled results for scenario 5 indicate that other than the most northeastern coastal areas, there is a high probability Manam will receive at least 100 mm of tephra deposition from this type of eruption (**Figure 3.13**). Furthermore, a large portion of the island including the centre, west and southern slopes have a 90% probability for 1000 mm ash to accumulate in these areas and the northeast coast falls within the 10 mm isopach (**Figure 3.13**). While the 90% exceedance probability isopachs do not reach the mainland, Boisa island is intersected by the 1 mm isopach giving the south of the island a 90% chance of seeing at least 1 mm of ash

deposition with the north of this island would expect to receive at least 0.1 mm of tephra (**Figure 3.13**).

The 50% exceedance probability plot for the dry season (**Figure 3.13**) shows a larger area than any of the previous scenarios with a moderate chance of 0.1 mm of ash accumulating during a scenario 5 type eruption. The 0.1 mm isopach extends up to 79 km in the west and 72 km to the southwest of Manam (**Figure 3.13**). The North Coast Highway 10 km south of Bogia has a moderate chance of at least 0.1 mm of ash accumulation (**Figure 3.13**). The 1 mm isopach also extends inland over Hansa Bay for 46 km and passing < 1 km north of Bogia. Manam itself is completely encompassed by the 100 mm isopach with the majority of the island, excluding the eastern coastal areas, have a moderate chance of receiving at least 1000 mm of ash during a sub-Plinian eruption represented by scenario 5. Boisa Island has a 50% probability of receiving at least 10 mm of tephra deposition from a scenario 5 type eruption. Northern Hansa Bay and Awar Plantation situated approximately centrally on Hansa Bay falls within the 10 mm contour (**Figure 3.13**).

The 90% exceedance probability plot of distribution of tephra fall from a wet season scenario 5 eruption shows that no where on the mainland has a high probability of receiving at least 0.1 mm of tephra (**Figure 3.13**). The majority Boisa Island falls within the 0.1 mm isopach with the southern tip of the island being within the 1 mm isopach. The entirety of Manam has a 90% chance of 100 mm or greater of tephra accumulation (**Figure 3.13**). The 1000 mm isopach covers central Manam including all flanks of the volcano but all the coastal regions fall outside of this area (**Figure 3.13**).

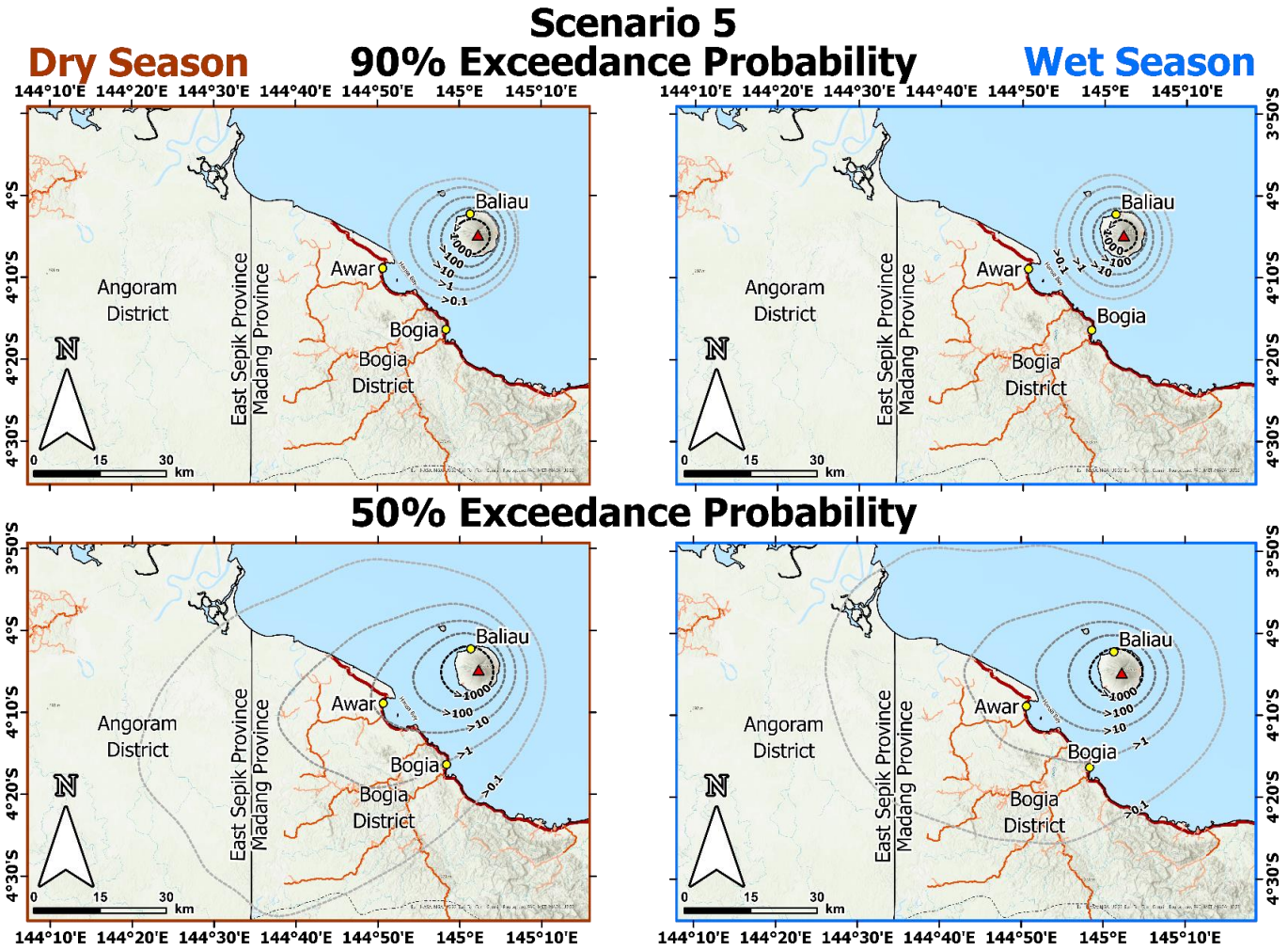

Figure 3.13 Probabilistic isomass plot for Scenario 5 during the dry season (left column) and wet season (right column). Scenario 5 is a sub-Plinian eruption lasting 10-15 hours generating an 15-25 km eruption column. The contours here represent a 90% (top row) or 50% (bottom row)probability that deposited tephra will exceed the thickness (in mm) indicated by the contour label.

Like the dry season, the 50% exceedance probability plots (**Figure 3.13**) provide a indication of how great the tephra deposition extent of these more intense sub-Plinian eruptions could be. The 0.1 mm isopach extends furthest to the southwest and west at 45 km and 67 km respectively. The eastward extent of this isopach is 23.5 km from Manan and 34 km to the Northwest (**Figure 3.13**). The westward extent reaches beyond the Ramu river into East Sepik province. Bogia has a moderate chance of at least 0.1 mm of ash though the 1 mm isopach is positioned less than a kilometre to the north suggesting that greater accumulations in Bogia may still have probabilities approaching 50% (**Figure 3.13**). Awar Plantation and the wider Hansa Bay fall fully within the 1 mm isopach while Boisa Island sits within the 10 mm isopach (**Figure 3.13**). The most northeasterly coastlines of Manam have a moderate probability of receiving at least 100 mm of ashfall while the rest of the island has a 50% probability for 1000 mm or more of tephra to accumulate as a result from a scenario 5 sub-Plinian eruption (**Figure 3.13**).

Comparing the dry and wet season 50% exceedance probability maps for scenario 5 shows a difference in the general dispersal pattern to those observed in the other scenarios (**Figure 3.13**). However, the difference between the two seasons does not follow the general trend observed in the other scenarios. In scenarios 2-4, the dry season typically has a exaggerated western dispersal pattern when compared to the more symmetrical pattern seen in the wet season modelled runs. Like other scenarios the dry season eruptions have a strong westerly component to the disperse pattern, in this case 70km west of Manam (**Figure 3.13**). However, in this scenario the dispersal pattern is dominated by southwestern component which

reaches as far as 80 km from the eruption source. Unlike the other scenarios, the wet season dispersal pattern has a substantial westerly component that reaches 67 km from Manam, similar to the 70 km observed in the dry season modelling (**Figure 3.13**). The wet season also has a southwestern component that reaches 50 km as well as direct southerly component reaching 32 km. The wet season dispersal pattern also reaches further to the north, northwest and east than in the dry season but with only the areas around the mouth of the Sepik river being potentially impacted by dispersal in the northeast direction these are less important (**Figure 3.13**).

3.3.2.6 Quantitative Exposure Analysis

The results of intersecting the exposure data sets reveal the extent that explosive eruptions at Manam would impact the local and regional communities of Madang and East Sepik province. The exposure sets analysed geospatially in ArcGIS Pro were: Madang and East Sepik population, roads, and land cover in addition to buildings on Manam itself. These datasets are not comprehensive and the analysis of these do not provide a holistic view of the impact of eruptions of Manam but they do provide a useful basis to quickly quantify the relative impacts of the different eruptions scenarios. Further implications of the deposition of the varying ash thicknesses on these different exposure data sets will be discussed in the context of the tephra impact framework (Wilson et al. 2014) in the discussion section. In this section the quantitative analysis of these data is presented. The modelled ash deposition of scenario 1 eruptions do not intersect with any of the exposure data sets and so this section focuses on scenarios 2-5.

Minor Vulcanian eruptions represented by scenario 2 are not expected to deposit tephra on the mainland. The impacts of these eruptions are therefore localised yet there is a notable difference in the 90% probability seasonal estimates of population affected where 2,717 people would be affected during the wet season vs 5,324 as the northeast of Manam only has a high probability of tephra accumulation in the dry season (**Table 3.4**). This disparity is also reflected in the anticipated number of buildings affected with just 324 impacted during the wet season and 1,184 during the dry season. However the 50% probability results do not show this disparity with almost equal populations (~6,300) and buildings (1,276) affected (**Table 3.4**). There is a 50% chance of 3 km^2 of cropland being covered by 0.1 mm or more of ash on Manam during a dry season scenario 2 eruption. However, this is likely to be an underestimate as the agricultural gardens typical of Manam and northern Papua New Guinea are planted within forested areas rather than the forest being cleared and so the satellite-based remotely sensed land cover data set would likely designate this as forest. The 0.2 km^2 of urban land impacted by scenario 2 eruptions (**Table 3.4**) is Baliau and the nearby villages on Manam's north coast.

The modelled results from a scenario 3 major Vulcanian eruption indicate that there is a 50% probability that 35,654 could be affected by tephra fall during a dry season eruption or 30,130 during the wet season (**Table 3.4**). An eruption in either season has a moderate chance of depositing ash along 120 km of the road network including the North Coast Highway as far south as Bogia in the dry season and beyond Bogia in the dry season. On Manam itself, 157 buildings fall within the 90%

exceedance probability 0.1 mm tephra isopach and 1,079 within the 1 mm contour during dry season modelling, and these become 197 and 1,226 buildings in the 1 mm and 10 mm contours respectively for the 50% exceedance probability results. During the wet season 1,275 buildings fall within the 1 mm 90% probability isopach and for the 50% probability 50 fall within the 1 mm isopach and 1,226 in the 10 mm isopach. Dry season eruptions have a moderate probability to inundate 40 km^2 of cropland compared to 11.6 km^2 during the wet season (**Table 3.4**).

Scenario 4 sub-Plinian eruptions have a 90% chance to impact the entire population of Manam (6,349) in either season (**Table 3.4**). The 50% probability that the mainland will be impacted by a dry season eruption of this type means that 15,682 people are moderately likely to be exposed to tephra and 48 km of roads. In the dry season there is a 50% chance that 531 buildings will be in areas where at least 100 mm will be deposited and a further 748 where 10 mm or more will fall (**Table 3.4**). These numbers are fairly similar to the wet season where 414 buildings would expect to receive 100 mm or more of tephra, and 863 buildings would be located in areas expecting to see 10 mm or more of tephra.

In scenario 5 sub-Plinian eruptions there is a 90% probability that the populations of both Manam and Boisa would be impacted by some level of ash deposition (**Table 3.4**). Notably, 1,574 people have a high probability of being directly impacted by at least 1000 mm of tephra accumulation during a dry season eruption due to the westerly shift in wind and tephra dispersal during this season (**Table 3.4**). When considering the 50% exceedance probability plot the total population that has a moderate chance of experiencing at least 0.1 mm of tephra deposition is 51,000

during the wet season and 58,000 during the dry season (**Table 3.4**). In either season all buildings on Manam would expect to receive at least 100 mm of tephra with a 50% chance that the vast majority of buildings will be inundated by at least 1000 mm (**Table 3.4**). The 50% exceedance probability results show that 235 km of roads are moderately likely to be covered by tephra during a dry season eruption and 195 during a wet season eruption. In both seasons the North Coast Highway south of Bogia has a 50% chance of tephra accumulating along its length, as well as the unnamed road that runs inland from Madang to Bogia. Finally there is a moderate chance that 100 km^2 of cropland would be affected by ash during a dry season eruption compared to 67 km^2 if the an eruption takes place during the wet season (**Table 3.4**).

Scenario	Season	Exceedance Probability	Thickness (mm)	Population	Inundated Roads (km)	Manam Buildings	Urban Land (km^2)	Cropland (km^2)	Forests (km^2)
Scenario 2	Dry Season	50%	0.1	3,419	-	564	0.1	1	18
			1	2,942	-	712	0.1	3	46
			10	-	-	-	-	-	-
			100	-	-	-	-	-	-
			1000	-	-	-	-	-	-
			Total	**6,361**	**-**	**1,276**	**0.2**	**3**	**64**
		90%	0.1	5,324	-	1,184	0.1	3	57
			1	-	-	-	-	-	-
			10	-	-	-	-	-	-
			100	-	-	-	-	-	-
			1000	-	-	-	-	-	-
			Total	**5,324**	**-**	**1,184**	**0.1**	**3**	**57**

Scenario	Season	Exceedance Probability	Thickness (mm)	Population	Inundated Roads (km)	Manam Buildings	Urban Land (km^2)	Cropland (km^2)	Forests (km^2)
Scenario 2	Wet Season	50%	0.1	3,508	-	779	0.1	0.1	15
			1	2,841	-	497	-	3	49
			10	-	-	-	-	-	-
			100	-	-	-	-	-	-
			1000	-	-	-	-	-	-
			Total	**6,349**	**-**	**1,276**	**0.1**	**3**	**64**
		90%	0.1	2,717	-	324	-	2	51
			1	-	-	-	-	1	-
			10	-	-	-	-	-	-
			100	-	-	-	-	-	-
			1000	-	-	-	-	-	-
			Total	**2,717**	**-**	**324**	**-**	**3**	**51**

Scenario	Season	Exceedance Probability	Thickness (mm)	Population	Inundated Roads (km)	Manam Buildings	Urban Land (km^2)	Cropland (km^2)	Forests (km^2)
Scenario 3	Dry Season	50%	0.1	24,360	97	-	-	32	1,210
			1	6,476	24	197	-	5	84
			10	4,809	-	1,079	0.1	3	49
			100	-	-	-	-	-	-
			1000	-	-	-	-	-	-
			Total	**35,645**	**121**	**1,276**	**0.1**	**40**	**1,343**
		90%	0.1	2,903	4	157	-	0.4	24
			1	4,996	-	1,118	0.1	3	50
			10	-	-	-	-	-	-
			100	-	-	-	-	-	-
			1000	-	-	-	-	-	-
			Total	**7,899**	**4**	**1,275**	**0.1**	**3**	**74**

Scenario	Season	Exceedance Probability	Thickness (mm)	Population	Inundated Roads (km)	Manam Buildings	Urban Land (km^2)	Cropland (km^2)	Forests (km^2)
Scenario 3	Wet Season	50%	0.1	23,658	121	-	0.1	8.2	640
			1	191	-	50	-	-	3
			10	6,281	-	1,226	0.1	3	63
			100	-	-	-	-	-	-
			1000	-	-	-	-	-	-
			Total	**30,130**	**121**	**1,276**	**0.2**	**11.6**	**705**
		90%	0.1	12	-	-	-	-	0
			1	6,349	-	1,275	0.1	3	64
			10	-	-	-	-	-	-
			100	-	-	-	-	-	-
			1000	-	-	-	-	-	-
			Total	**6,361**	**-**	**1,275**	**0.1**	**3**	**64**

Scenario	Season	Exceedance Probability	Thickness (mm)	Population	Inundated Roads (km)	Manam Buildings	Urban Land (km^2)	Cropland (km^2)	Forests (km^2)
Scenario 4	Dry Season	50%	0.1	9,219	48	-	-	5.94	210
			1	114	-	-	-	-	1
			10	3,186	-	748	-	-	-
			100	3,163	-	531	0.1	0.4	17
			1000	-	-	-	-	-	-
			Total	**15,682**	**48**	**1,279**	**0.1**	**6.36**	**228**
		90%	0.1	-	-	-	-	-	-
			1	876	-	99	-	0.2	6
			10	5,192	-	1,097	0.1	1	35
			100	281	-	82	-	3	23
			1000	-	-	-	-	-	-
			Total	**6,349**	**-**	**1,278**	**0.1**	**3**	**64**

Scenario	Season	Exceedance Probability	Thickness (mm)	Population	Inundated Roads (km)	Manam Buildings	Urban Land (km^2)	Cropland (km^2)	Forests (km^2)
Scenario 4	Wet Season	50%	0.1	114	-	-	-	-	1
			1	-	-	-	-	-	-
			10	4,030	-	863	0.1	0.1	16
			100	2,319	-	414	-	3	48
			1000	-	-	-	-	-	-
			Total	**6,463**	**-**	**1,277**	**0.1**	**3**	**65**
		90%	0.1	-	-	-	-	-	-
			1	337	-	154	0.1	-	2
			10	6,009	-	1,124	-	1	42
			100	3	-	1	-	3	20
			1000	-	-	-	-	-	-
			Total	**6,349**	**-**	**1,279**	**0.1**	**3**	**64**

Scenario	Season	Exceedance Probability	Thickness (mm)	Population	Inundated Roads (km)	Manam Buildings	Urban Land (km^2)	Cropland (km^2)	Forests (km^2)
Scenario 5	Dry Season	50%	0.1	32,455	129	-	0.1	86	2,421
			1	15,533	92	-	-	10	590
			10	3,948	14	-	-	0.1	30
			100	1,122	-	149	-	0.2	8.1
			1000	5,227	-	1,127	0.1	3	56
			Total	**58,285**	**235**	**1,276**	**0.2**	**100**	**3,104**
		90%	0.1	-	-	-	-	-	-
			1	114	-	-	-	-	1
			10	1	-	-	-	-	0.1
			100	4,774	-	905	0.1	0.5	24
			1000	1,574	-	376	-	3	40
			Total	**6,463**	**-**	**1,281**	**0.1**	**3**	**65**

Scenario	Season	Exceedance Probability	Thickness (mm)	Population	Inundated Roads (km)	Manam Buildings	Urban Land (km^2)	Cropland (km^2)	Forests (km^2)
Scenario 5	Wet Season	50%	0.1	32,464	137	-	0.1	60	1,741
			1	11,684	58	-	-	6	245
			10	114	-	-	-	-	1.0
			100	57	-	27	-	-	0.9
			1000	6,292	-	1,248	-	-	-
			Total	**50,611**	**195**	**1,275**	**0.1**	**67**	**1,988**
		90%	0.1	102	-	-	-	-	1
			1	12	-	-	-	-	0.2
			10	-	-	-	-	-	-
			100	6,292	-	1,268	0.1	1	36
			1000	57	-	7	-	3	28
			Total	**6,463**	**-**	**1,275**	**0.1**	**3**	**65**

Table 3.4 Summary table of the estimated exposure of population, road network, Manam buildings, urban areas, cropland, and forests to the modelled tephra deposition of scenarios 2-5. The modelled tephra dispersal from scenario 1 is minimal and has no impact on these data sets. All estimates were calculated by intersecting the tephra deposition thickness contour lines with the relevant data set

.

3.4 Discussion

The probabilistic modelled tephra deposition results presented in the previous section indicate that eruptions of Manam volcano are capable of impacting mainland Papua New Guinea up to several tens of kilometres from Manam itself. Each eruption scenario has a differing deposition pattern that varies in shape, distance from Manam and the thicknesses of tephra deposited. Wind direction is known to have strong influence on tephra dispersal (Carey and Sparks 1986; Bursik 1998; Davies et al. 2010; Poulidis et al. 2018) and as the wind directions in the lower 5 km of the atmosphere are diametrically opposed between the dry and wet season over Manam and the surrounding regions (**Figure 3.8**) the spatial distribution of deposited tephra is markedly different depending on which season an eruption occurs.

This difference is even perceptible when comparing the modelled tephra deposition results for scenario 1 where very little ash is deposited (**Figure 3.9**). This result replicates closely the observations of these type of eruptions where tephra deposition and any impact on human activity is not mentioned in reports. Given the low erupted masses in these eruptions it is probable that any impacts are very minor and potentially considered common place or unremarkable by residents and the RVO observer on Manam, and therefore are not recorded. The potential that these impacts are not noteworthy gives some confidence to the modelling of this scenario as the impacts from the modelled accumulation would be very minor in severity and extent. The modelled results for scenario 2 show that that there is

likely to be thin deposits of ash (≥0.1 mm) with a deposits of ≥1 mm having a 50% probability on the majority of the island.

Another notable finding is the dispersal footprint of the Vulcanian scenario 3 is larger than the sub-Plinian scenario 4 despite being the less explosive eruption style. Both scenarios share the same range of duration and plume heights but the range of modelled erupted masses is greater for scenario 4 than scenario 3 (**Table 3.2**). These two scenarios use two different TGSDs taken from a Vulcanian eruption of Fuego (Guatemala) and a basaltic andesite sub-Plinian eruption of Hekla (Iceland) (**Table 3.2**). The Vulcanian Fuego TGSD range (10 ϕ – -2 ϕ) is shifted towards finer particles than the sub-Plinian Hekla TGSD (8 ϕ – -5.5 ϕ) and as finer particles are more easily transported longer distances this explains the larger footprint of the scenario 3 modelled eruptions (Pyle 1989b, 2016; Sparks et al. 1992). The generally more coarse particles in the scenario 4 modelling in tandem with the greater erupted mass explains the greater thicknesses deposited closer to the volcano in this type of eruption.

The results also show that Scenario 5 eruptions have the largest area of dispersal and produce the thickest tephra deposits unsurprisingly due to it having the largest erupted mass ($\bar{x}$ = 0.41-4.35 × 10^{12} kg), plume heights (15-25 km) and durations (10-15 h). However, the high probability that the whole of Manam will receive 100 mm or more of ash and indeed moderate probability that 1000mm will accumulate island wide are findings that necessitate serious consideration for emergency planners and implementation of mitigation strategies. This is the case especially

considering the 50% probability outputs indicate much of the mainland including Bogia and the North Coast Highway will also be impacted by tephra fall.

The remainder of this section will consider the impacts of the modelled tephra deposition looking through various key aspects of human activity including health infrastructure and food security. Then the implications these issues for emergency planning at mitigation strategies will be assessed and then recommendations for future tephra impact studies at Manam and elsewhere will be discussed.

3.4.1 Tephra Impact Assessment

The modelled results indicate the potential severity of each eruption scenario but from a hazard assessment and mitigation perspective it is important to consider the results in the context of the likelihood of each scenario occurring. Between 2002 and 2021 there were 100 eruptions that fall under the description of scenario 1 eruptions, 36 scenario 2 type eruptions and four scenario 5 eruptions (Darwin Volcanic Ash Advisory Centre 2021; Global Volcanism Program 2021b). It can be difficult to distinguish scenario 3 and 4 eruptions based solely on the reports and as such with there are five eruptions which do not provide enough detail to determine the eruption style. When including these with the seven clear scenario 3 type eruptions and one scenario 4 type eruption we see a general trend of reducing frequency with intensity of eruption scenario (Darwin Volcanic Ash Advisory Centre 2021; Global Volcanism Program 2021b). This analysis indicates the thicknesses of tephra deposited from given scenario, yet the activity of Manam presented in Chapter 1 shows that Manam can experience multiple eruptions within days to

weeks. Tephra from multiple eruptions will stack if not removed during post-eruption clean up resulting in potential greater loads of tephra exacerbating the impact of previous eruptions. Here, the ramifications exposure analysis results (**Table 3.4**) will be explored by considering the implications of tephra accumulation from single eruptions in the context of the Wilson et al. (2015b) impact framework (**Table 3.3**) and the wider literature. The sectors considered will be population and health, buildings and infrastructure, agriculture and food security, and transport systems.

3.4.1.1 Population and Health

Madang province has a population of 493,906 (National Statistics Office [PNG] 2011) making it the fourth most populous province in Papua New Guinea. While Scenario 2 eruptions are anticipated to only impact the population of Manam itself (6,349) Scenario 3 and 4 eruptions also have a 50% chance to impact up to an estimated 35,645 and 15,682 people between the mainland and Manam itself (Table 3.3). Critically, the dry season scenario 5 result show there is a 50% probability that tephra fall will directly impact 58,285 people, 12% of the provincial population (Table 3.3). All projected impacted populations represent a substantial number of people which may need support in some capacity and the scenario 5 potentially impacted populations are a considerable portion of the provincial population that would likely stretch the resources of provincial and national governments responding to the eruption. The impacts on other sectors will be discussed in following sections and here the impacts on population health will be considered.

The economy of Madang province is based on outdoor industries including mining, agriculture, fisheries and tourism (Madang Provincial Government 2024) meaning that beyond the evident interruption to these industries due to heavy tephra fall, many people would be exposed to airborne tephra through their occupations even during light tephra fall. This is especially true for Bogia district in which subsistence agriculture is the primary basis of the districts economy and where access to amenities such as clean water, healthcare and education is limited (Madang Provincial Government 2024). The most common health issues are due to inhalation of fine ash particles, with particles <10 μm in diameter able to penetrate into respiratory pathways as far as the bronchioles, causing acute effects that include asthma attacks and bronchitis as well as coughs, breathlessness and chest pains (Horwell and Baxter 2006). Particles <4 μm are classed as respirable as they are able to enter the alveoli, and pass chemicals into the bloodstream and most seriously silicosis, the scarring of the lungs, due to exposure long-term (months to years) to fine ash particles with high concentrations of crystalline silica (Horwell and Baxter 2006). Other health impacts of tephra fall include eye trauma from tephra becoming lodged in eye sockets (Fraunfelder et al. 1983; Hansell et al. 2006) and leaching of toxic chemicals (e.g. Flourine) into drinking water (Ayris and Delmelle 2012; Arnalds 2013; Ruggieri et al. 2023).

The sub-10 μm tephra particles responsible for respiratory diseases have been shown to be at high levels even after relatively light tephra accumulations of 500-1500 g m^{-2} (Andronico and Del Carlo 2016) and that dangerous levels of fine ash particles pose a threat to health even at the distal reaches of deposits (Newnham et

al. 2010). Therefore the modelled tephra deposits for eruptions of Manam show that it is not only the proximal regions with thicker deposits where respiratory issues will be experienced (Barsotti et al. 2010; Gudmundsson 2011).

3.4.1.2 Buildings and Infrastructure

Roof collapse have only been responsible for 2% of recorded volcanic fatalities yet they are reported as a cause of death in 21% of volcanic eruptions (Simkin et al. 2001; Spence et al. 2005). Most buildings on Manam have a timber constructed frame with a sloping coconut frond roof, with larger communal buildings incorporating a corrugated iron roof (Connell and Lutkehaus, 2016). The scenario 2 modelled tephra deposition indicate a 50% probability that 1 mm or more would accumulate across the majority of the island, which would not be expected to cause any structural damage but may result in drainage infrastructure becoming blocked, causing localised flooding, and flashover of electricity cables resulting in loss of power **(Table 3.3**). Scenario 4 eruptions are anticipated to produce accumulations of >10 mm across the majority of the island during the dry season and virtually the entire island in the wet season (**Figure 3.12**). 10 mm of ash may cause the collapse of long span roofs and non-engineered roofs (Jenkins et al., 2015; Wilson et al., 2015), especially when the tephra deposits become wet which is very likely during the wet season (Macedonio and Costa 2012; Williams et al. 2021). Furthermore, with the likelihood of widespread roof and structure issues resulting from the projected tephra deposition it suggests that there would be limited appropriate shelter airborne tephra during an eruption and remobilised tephra post eruption (Wilson et al. 2011; Liu et al. 2014). The results also indicate that only a scenario 5

eruption would be likely be capable of producing accumulations of ≥10 mm and this would be on the northern areas of Hansa Bay (**Figure 3.12**).

The results show that structure threatening thicknesses of ≥100 mm can be produced by scenario 4 and 5 eruptions but only on the island of Manam itself (**Figure 3.12 & Figure** 3.13). Structural damage to majority of the buildings in these zones would be expected where deposits reach thicknesses of ≥100 mm (Biass et al., 2022; Blong, 2003; Wilson et al., 2015). During the 1994 Rabaul (Papua New Guinea) timber frame buildings suffered from roof collapse at ~100 kg m^{-2} (Blong 2003) or 40 mm. Total collapse of timber frame buildings were recorded from ~765 kg m^{-2} (Blong 2003) or ~300 mm of Manam tephra. Therefore it is expected that structural damage would be expected to most buildings (Table 3.3, Wilson et al., 2015). Indeed on Manam itself large portions of the island have a moderate likelihood of being covered by >1000 mm of ash (**Figure 3.13**). Which would most likely result in complete structure failure of the timber framed buildings on Manam (Blong 2003; Hayes et al. 2019).

3.4.1.3 Agriculture and Food Security

Thin deposits of tephra have been shown to cause aesthetic decolouration of leaves and fruit of horticultural crops and potential leaching of toxic elements into the soil and plants (Arnalds, 2013; Ligot et al., 2022; Wilson et al., 2015). Thick deposits can bury or structurally destroy crops causing, in the most extreme cases, total loss of harvests (Wilson et al., 2015). Agriculture underpins the economy of Madang province and within Bogia district subsistence agriculture is the primary source of income and food (Madang Provincial Government 2024). The subsistence farming

methods of Manam island itself follow traditional, low technological methods, that involve planting food crops in cleared areas of forest (Connell and Lutkehaus 2016, 2017). The impacts of tephra fall have been shown to be more severe where farms do not have access to technological improvement assets i.e. farming technologies (Craig et al. 2016). Therefore probabilistic modelling of tephra fall provides a view of hazard to the agricultural industry and subsistence farmers who are vulnerable to this hazard.

Scenario 2 eruptions have a 50% probability of at least light tephra deposition across Manam with the majority of the island shown to receive at least 1 mm. The area likely to receive 1 mm of tephra includes all the slopes of Manam which is typically where the largest agricultural gardens are located (Mercer and Kelman 2010; Connell and Lutkehaus 2016, 2017). The agricultural gardens would experience some minor productivity loss and disruption of harvests due to issues with equipment and access rather than widespread loss of plants (Jenkins et al. 2015). While the turbidity in natural water sources, which have their source on Manam's slopes would increase to an unsafe level for consumption with just 1 mm of deposited tephra (Wilson et al., 2015) underlining the need for covered storage of water to mitigate this issue.

Scenario 3 and 4 eruption scenarios have the potential to affect between 3-40 km^2 of cropland depending on the time of year (Table 3.4) which would only see loss of crops as most of these fall within areas likely to see 0.1 mm of tephra fall. Scenario 3 eruptions have a 50% chance of depositing 10 mm of ash on Manam (**Figure 3.11**) causing structural damage to crops, especially low lying plants, resulting in an

estimated <50% productivity loss (**Table 3.3**) (Jenkins et al. 2015). Whilst a scenario 4 eruption would cause burial of most crops under 100 mm of tephra across a large portion of Manam with the most northerly areas still experiencing reduced productivity and structural damage (**Figure 3.12**). This would require significant long-term remediation for any cash crops but critically on Manam, this would necessitate food supplies from the mainland over a sustained period as clean-up and recovery of the soils.

A scenario 5 eruption would have a 50% probability of depositing 1000 mm across most of the island resulting in total burial of crops, pastures and water sources are likely under this level of inundation with long-term clean up required to remove the large volumes of deposited material (**Table 3.3**, Wilson et al., 2015). This type of eruption has the largest potential area affected by tephra fall with 67-100 km^2 of cropland on the mostly on the mainland (**Table 3.4**). Any loss of harvest has an direct and immediate impact on communities, especially island communities such as Manam, but the impact to harvests has potential far reaching ramifications for food security in the region following an eruption.

3.4.1.4 Transport Network

Long distance transport options in Bogia district are limited to the road network (**Figure 3.5**) with boats used in the district typically only capable of shorter distance journeys along the coast or to Manam and other islands. This makes the two road routes that link Bogia district to Madang town are vital as Madang town is the location of the nearest airport and hospitals. The first is via the North Coast Highway, a single lane secondary road (OpenStreetMap contributors 2023), which

runs directly between Madang town and Bogia along the coastline for 184 km. The ~3 hour car journey is the quickest route. The second route is a tertiary road of unknown quality running inland between the Finisterre mountains and the central Highlands coming to Bogia from the south. As the North Coast Highway is classed as the highest graded road and has a short journey time it is considered the most important transport link to Bogia and any closure of this road would represent a major issue for the economy and delivery of aid during an eruption. It has been demonstrated that <0.1 mm of tephra can cover road markings which can lead to disruptions and accidents (Blake et al. 2016) and traction issues for vehicles begin with <1mm (Biass et al., 2017; Wilson et al., 2015) and obstruction of vehicles at 10 mm (Blake et al., 2016; Jenkins et al., 2015; Wilson et al., 2015).

Tephra fall from scenarios 1 and 2 are not expected to reach the mainland and therefore do not impact the road network. Scenario 3 eruptions have a 50% probability of depositing at least 0.1 mm of tephra on 121 km of roads (Table 3.4). The westward dominated dispersal during dry season eruptions would cause traction issues along roads in northwest of Bogia including the North Coast Highway which could see deposition of at least 1 mm around Hansa bay likely hampering efforts to transport relief to communities in these areas. Whist the southward extension of the wet season dispersal would cause traction issues on roads south of Bogia including both key routes to Madang.

The smaller extent of tephra deposits expected from scenario 4 eruptions compared to scenario 3 results in a 50% probability of the 48 km (Table 3.4) of road network north of Bogia impacted by >0.1 mm of tephra but only in the dry season, as wet

season winds would impede tephra from reaching the mainland (**Figure 3.11**). The 50% probability results indicate that scenario 5 eruptions are likely to disperse tephra over the furthest distances impacting 195 km of roads in the wet season or 235 in the dry season (**Table 3.4**). In both seasons, 0.1 mm of tephra is expected to be deposited on the two routes to Madang south of Bogia and 1 mm impacting the coastal area, again impeding the access via the North Coast Highway (**Figure 3.13**). Further to this 10mm or more of ash could be expected along the coast around Hansa Bay during the dry season (**Figure 3.13**).

3.4.2 Implications for Emergency Planning

Volcanic islands, like Manam, are amongst the most vulnerable environments due to the exposure to multiple hazards and the socio-economic context associated with isolation from the mainland or other nations (López-Saavedra and Martí 2023). As such they are locations where established disaster risk management is most vital (Miller et al. 2022; López-Saavedra and Martí 2023). This need for clear emergency protocols is compounded by the fact that scenarios 3, 4 and 5 type eruptions also capable of depositing impactful accumulations of tephra on the nearby mainland. This therefore requires cohesive regional level emergency plans to provide sufficient support to the mainland and island communities of Madang province due to eruptions of Manam. This section will discuss some considerations regarding enhancing community and regional level resilience to tephra fall as well as evaluating potential evacuation locations.

3.4.2.1 Food Security

Agriculture plays a critical role in the economy of Madang province (Madang Provincial Government 2024) yet up to 100 km^2 of cropland could be impacted by tephra fall from an eruption of Manam. Alongside this economic agricultural impact, 92% of people in Madang province also producing their own food (National Statistics Office [PNG] and ICF 2019). After the 2021 eruption of La Soufriere (St. Vincent and the Grenadines) 81% of food producers reported that food production was negatively impacted by the eruptions and 68% reported overall decreased productivity of cropland due to ash fall (Augustus et al. 2023). When residents are unable to produce crops and economic access also becomes impossible food security must be alleviated by reserves or external aid until agricultural practices can be restored (De Haen and Hemrich 2007). An additional consideration is that inhabitants of volcanic islands and coastal regions suffering from acute food security issues caused by natural disasters often become more reliant on coastal fishing (Connell and Lutkehaus 2016; Steenbergen et al. 2020) yet if this reliance becomes long-term, this causes pressures on fish stocks, compacting food security issues if other food sources are not restored (Steenbergen et al. 2020). As such the possibility of food scarcity in Manam and Bogia district should be a major concern for emergency planners.

Food security studies in less economically developed countries consistently emphasise the importance of community level planning with local governance assistance to improve resilience to food supply issues (Pothukuchi 2004; Texier-Teixeira et al. 2014; Rachmawati et al. 2017; Rozaki et al. 2022). Best practice is to

perform a guided Community Food Assessment with the goal of achieving community food security and should include planning for cessation of food production and access (Pothukuchi 2004). Local communities and authorities should be encouraged to maintain reserves of long lasting, ideally canned, food to alleviate initial food availability issues as crops are destroyed by tephra, and transport issues inhibit access to markets and while food aid delivery is pending (De Haen and Hemrich 2007; Augustus et al. 2023). Larger farms have been shown to be more resilient to impacts of volcanic activity (Rozaki et al. 2022) and that agricultural growth, physically and technologically, are critical to reducing food poverty in developing nations (De Haen and Hemrich 2007). Pre-emptive food security improvement measures targeting the root causes of food supply issues during disasters have been highlighted as a key target for in rural Papua New Guinea (Jackson et al. 2020). Therefore, where possible, investment in both economic and subsistence agricultural practices should be encouraged. Communities farmers should also be encouraged include building protective structures over smaller crops which are typically more heavily impact by smaller tephra accumulations or undertake early harvests of near mature produce if pre-warning an eruption is provided in any way (Ligot et al., 2022).

3.4.2.2 Construction Issues

Roof collapse are only responsible for 2% of volcanic fatalities they are reported as a cause of death in 21% of volcanic eruptions (Simkin et al. 2001; Spence et al. 2005). While roof collapses are a low contributor to volcanic fatalities, the loss of shelters during and post-eruption causes displacement of people adding pressures to

resources while clean-up and rebuilding take place. On Manam specifically, the mass evacuation led to myriad socio-economic problems due to the number of people displaced into care centres (Mercer and Kelman 2010; Johnson 2013; Connell and Lutkehaus 2016, 2017). Therefore when structures are able to withstand the roof loading from tephra fall and inhabitants are able to stay in their own homes this can reduce the potential humanitarian issues post-eruption.

Experiments have shown that tephra accumulations of 100-300 mm will likely slide off common modern roof construction types that have an angle of ≥35° and that metal roofs require a shallower ≥32° angle to shed deposited tephra (Osman et al. 2023). The traditional Manam construction of timber frame have sloping coconut frond roofs designed to allow accumulations of ash to slide off (Connell and Lutkehaus 2016), this roof type however was not tested by Osman et al. (2023) but it is likely that they would be less efficient than corrugated metal roofs at shedding tephra. During the 1994 Rabaul (Papua New Guinea) eruption roof collapses occurred where loads of >4 kN m^{-2} (200-300 mm) had been deposited and complete structural collapses began with at least >7.5 kN m^{-2} (460 mm). Assuming building practices in Rabaul and Bogia District are similar some recommendations can be made to improve building resilience to tephra accumulation. Ideally all roofs should have slope angles of ≥35° and where possible be constructed from corrugated metal, though it is recognised that in remote villages like those on Manam where metal roofs are seen as a status symbol (Connell and Lutkehaus 2017), this may not be economically possible. At the 2011 Cordón-Caulle (Chile) and 2021 Tajogaite (La Palma, Canary Islands) eruptions it was shown that roofs may not be the failure

point in structure damage (Elissondo et al. 2016; Barragan et al. 2022). It has been shown that clearing of tephra during eruptions significantly reduces the risk of building failure (Hayes et al. 2015). Therefore to reduce the risk of roof or structural collapse, residents should be encouraged to clear their roofs, when it is safe to do so, as well as removing ash from around houses that may act as buttresses and prevent ash from sliding from roofs.

Nonetheless it is highly likely that many buildings on Manam itself will experience roof or structural collapse under the level of tephra deposition (10-1000 mm) expected from major eruptions of Manam (Blong 2003; Jenkins et al. 2015). The potential widespread roof and structural issues anticipated as a result from the projected tephra deposition Scenario 3-5 eruptions suggests that there would be limited appropriate shelter during eruptions of these magnitudes and therefore local or regional level evacuations may be necessary.

3.4.2.3 Maintaining Transport Access to Bogia District

It has shown that tephra deposits of <0.1 mm are capable of causing disruption to surface transport networks by obscuring road markings and decreasing vehicle traction (Blake et al. 2016, 2017) requiring reduced speed to safely navigate and thus slowing evacuations, arrival of first responders and delivery of aid (Hayes et al. 2022). The modelled results have shown that scenario 5 sub-Plinian eruptions of Manam are capable of depositing ≥0.1 mm of tephra across the majority of western Bogia district covering 38% of the district's road network (Table 3.4). The northwestern portions of Bogia district will potentially receive 1 mm and areas around Hansa Bay, including the North Coast Highway, could be inundated by 10

mm. Thicknesses of 1 mm are shown to exacerbate traction issues and 4 mm (10 kg m^{-2}) can render a road impassable to non-specialised vehicles (Jenkins et al. 2015; Blake et al. 2016). This means that the areas furthest from Bogia and Madang could be isolated by tephra fall with disrupted escape routes leading to fatalities as people are unable to leave unsafe areas and first responders are unable to gain access (Kim et al. 2019).

Critically, the two routes between the towns of Madang and Bogia, the North Coast Highway and the inland route, are both potentially impacted by tephra fall. The link between these two towns is vital during a volcanic emergency as these are the only terrestrial routes available for evacuation and access to the affected areas. As the district capital and largest mainland town close to Manam, Bogia is a hub for facilities including health care and financial services for the population of this part of northwestern Madang province. Access to Manam is typically provided via boat services from Bogia due to its relatively well established maritime infrastructure, including multiple jetties. The North Coast Highway runs through Bogia as well as linking it to other secondary roads to inland settlements. It is for this reason that previous evacuations of Manam have been via Bogia where evacuees are transferred to terrestrial transport and future evacuations would likely follow this procedure.

Bogia represents a vital provider of non-emergency infrastructure to the region and a key location for evacuations. Therefore it is paramount that road access to Bogia is maintained during volcanic crises so that evacuation along the North Coast

Highway is possible but also so that humanitarian aid can also reach the areas likely to be affected by Manam's eruptions.

3.4.2.4 Evaluating Proposed Resettlement Sites as Evacuation Destinations

The hastily organised mandatory evacuation of Manam in 2004 demonstrated how unplanned emergency responses can turn a environmental crisis into a human crisis as more people died as a result of poor health and violence than directly from the eruption itself (Connell and Lutkehaus 2017). The perceived poor management of the evacuation and humanitarian effort following the 2004-05 eruptions has severely impacted trust in government involvement in volcanic emergency response (Mercer and Kelman 2010). Rural residents have been shown to be less likely to follow government emergency plans and evacuation orders (Bird et al. 2011) but the involvement of local leadership and experiential knowledge has been shown to shape views around hazard and risk (Martinez-Villegas et al. 2021). Therefore future volcanic emergency response plans should be created in consultation with local communities and leadership structures to ensure the planned responses, including evacuation, meet the communities needs during the next emergency (Bonadonna et al. 2021b).

Official relocation plans are often refused as they do not provide to the needs of the community as seen in the settlements around Merapi (Indonesia) (Mei et al. 2013; Jumadi et al. 2017). The problem of locating temporary accommodation for evacuees is an ongoing issue following the 2004 evacuation to three sites along the mainland coast in Potsdam, Asuramba and Mangem (Connell and Lutkehaus 2016). Some residents still remain in these care centres and issues with land ownership

and conflict with locals alongside other emergent social issues (Mercer and Kelman 2010; Connell and Lutkehaus 2017) suggest that these locations would not be suitable for another large scale evacuation. Two other options for relocating these remaining evacuees have been postulated.

The first is a site in Andarum, approximately 30 km inland from Bogia (**Figure 3.5**), which has enough land to facilitate the permanent relocation of Manam's entire population (Connell and Lutkehaus 2016). As of 2016 this option had been the national government's preferred option but had not yet provided the funding to realise this solution (Connell and Lutkehaus 2016). If the Andarum solution was realised it would provide a location with resolved long-term land rights for current islanders to remove to during major eruptions. However, a 30 km inland journey during an eruption may prove to be difficult logistically at short notice. The issues surrounding different agricultural practices on Manam versus the mainland that were experienced in the care centres would require education to allow the residents to support themselves over extended periods. This is compounded by the fact that Manam islanders are reliant on sea fishing, a lack of access to the coastal areas would further inhibit them to support themselves (Connell and Lutkehaus 2017) and contribute to feelings of displacement and disconnection from place identity. Overall, the Andarum location faces ongoing funding issues (Connell and Lutkehaus 2017) and does not provide a convenient destination during an ongoing eruption and so does not represent a viable option for an evacuation destination.

The second previously suggested option is allow Manam residents to settle on the disused Awar Planation and surrounding land on the north of Hansa Bay (**Figure**

3.5), a short journey from Manam by boat (Connell and Lutkehaus 2016). The plantation itself has been given to residents of Awar for redevelopment (pngbuzz 2020; Loop PNG 2024) but another site around Hansa Bay could serve a similar function. Andarum is currently not accessible by a maintained road whereas Hansa Bay is served by the North Coast Highway and so would require less investment to construct evacuation care centres. Manam residents would more easily be able to travel to Manam post-eruption to begin to restore island settlements allowing a somewhat self-sufficient return to Manam over time. A key issue with Hansa Bay is that it has a 50% probability of receiving >10 mm of tephra during a dry season scenario 5 type eruption (**Figure 3.13**) and >1 mm during the wet season (**Figure 3.13**). This makes it possible that under a major sub-Plinian eruption like in 2004/05, Hansa Bay could require at least short term relief making it unfit for an evacuation destination in this scenario.

Ultimately, due to the low likelihood of being affected by tephra fall, the ideal location for evacuation from Manam are locations along the mainland coast to the southeast, as was done in 2004. However, previous experiences from the care centres mean that evacuation to these areas may not be well followed by evacuees nor would they be well suited for Manam residents as previous experience has shown (Mercer and Kelman 2010; Connell and Lutkehaus 2017). As a result a site on Hansa Bay, may represent the simplest and most cost effective solution but the probability of also being impacted by large eruptions, albeit to a lesser degree than Manam, makes this a non-ideal solution. Despite this, Awar represents a location that would allow Manam residents to restore their villages and agricultural gardens

themselves as aid to do so is unlikely while Manam remains a designated disaster zone by the national government.

3.4.3 Limitations and Future Work

3.4.3.1 Data Availability

This chapter has used open source data sets to estimate the exposure to, and impacts of tephra ground accumulation. While open source data is often found to be more up to date and accurate than proprietary data sets (Hayes et al. 2022), it is recognised that the Open Street Map buildings dataset (OpenStreetMap contributors 2023) does not contain information for settlements in western Bogia district, despite having good coverage on Manam. No other dataset was available to fill these gaps and since structural integrity threatening accumulations of tephra were modelled to predominantly impact Manam it was decided that digitised mapping of Bogia district buildings using recent satellite images was outside the scope of this work. However, it is recognised that a more comprehensive dataset would improve the comprehension of tephra risk to buildings and so work to fill this data gap would be beneficial.

In a similar vain impacts on the traditional timber framed buildings with coconut frond roofs are based on damage to similar buildings during the Rabaul (Papua New Guinea) 1994 eruption reported by Blong (2003) and the reported resilience of these buildings to tephra loading on Manam itself (Mercer and Kelman 2010). Recommendations to roof and structural designs were made considering the findings of Osman et al. (2023) where the effects of tephra loads on different roof

types were tested. This did not include frond roof types and so future work could include following the same methodology to test frond roofs response to tephra accumulation. Future improvements to this could include using remote sensing to estimate ash deposition from future events using muography (Tanaka 2020) and combining it with satellite-based assessment of building damage (Williams et al. 2020) in order to enhance understanding of vulnerability of structures to tephra deposition in Madang province.

Land cover information was also limited the relatively coarse Copernicus land cover data set (Buchhorn et al. 2020). For future uses of the process used in this chapter finer landcover datasets could be created using classified (requiring fieldwork), unclassified and machine learning remote sensing methods (Mitchell et al. 2013; Kadavi and Lee 2018). Though it is recognised that implementation of these methods in places like Papua New Guinea where rainforest canopies dominate the land cover making fine scale classification difficult.

A crucial facet of improving a community's resilience to volcanic hazard is an understanding of that group's vulnerability which can be defined as the potential for loss (Cutter 1996). The risk posed by a given hazard is a product of the intensity of the hazards impact and the vulnerability of the population that would be affected by that hazard. Therefore to provide a true view of risk to the tephra hazard posed by Manam requires a view of the vulnerability of the population of western Madang province, especially in Bogia district. Vulnerability and Capacity Assessments enable quantification of population vulnerability and can be assigned easily communicable levels for decision-making (Yoon 2012; Fuchs et al. 2012; Nguyen et al. 2019).

Vulnerability and Capacity Assessments in data scarce regions threatened by volcanic eruptions are difficult to undertake as baseline information population statistics may not available or recent enough (e.g. Democratic Republic of Congo (Michellier et al. 2020), Indonesia (Siagian et al. 2014) or the Philippines (Gaillard et al. 2001)). However, the integration of remote sensing data sets (e.g. the LandScan population data set (Sims et al. 2023) used in this chapter) have been used to mitigate data availability issues (Michellier et al. 2020; Crummy et al. 2023).

3.4.3.2 TGSD Limitations

The tephra deposition modelling of Vulcanian and sub-Plinian eruptions of Manam is able to provide insight into the likely dispersal and accumulation which can be used to inform volcanic emergency protocols. TGSDs are known to strongly influence plume dynamics (Girault et al. 2014; Costa et al. 2016; Connor et al. 2019), therefore it must be recognised that this modelling is limited due to the use of proxy TGSDs as no published TGSDs for Manam exist. It should be noted there are relatively few volcanoes with sufficient tephra deposit information to estimated erupted volumes or calculate TGSDs (Green et al. 2016). TGSDs were selected from analogous volcanoes and eruptions to represent the likely parameters and conditions of Manam's future eruptions (Table 3.1). However, even within these results the influence of different TGSDs can be seen in the difference in the lateral spread of the 0.1 mm contours in the scenario 3 and 4 modelling. Both scenarios shared the same duration and plume height ranges but the sub-Plinian scenario 4 were modelled with potential erupted mass range an order of magnitude greater. Despite this the modelled Vulcanian scenario 3 dispersal pattern covers a greater

area than scenario 4 eruptions (**Figure 3.12**). This is because of the TGSD used for Vulcanian eruptions in this study have a more substantial composition of finer grained particles compared to the sub-Plinian eruptions (Table 3.1). This demonstrates the sensitivity the model towards to selected TGSD. While this doesn't invalidate the results of this study it does indicate the benefits of using TGSDs from the study volcano itself. Ideally for future iterations of this study would include field work to determine the TGSD of eruptions of Manam and where possible distinguish between different eruptive styles as has been attempted here with the two different proxy TGSDs. However, given Manam is an island, a portion of the any substantial tephra fall will be deposited into the ocean leaving any TGSDs for Manam incomplete. Additionally, Manam and mainland Madang province are heavily forested and the dense vegetation would likely impede as access to suitable sampling sites, especially on Manam where this would be coupled with the steep slopes of the volcanic flanks and the inaccessible summit region. In other settings it is possible to quantify or recognise the uncertainty around TGSD due to incomplete ground deposit sampling (Bonadonna et al. 2015a; Pyle 2016; Alfano et al. 2016) and it has been shown that determination of TGSDs are more sensitive to uncertainties relating to proximal and medial deposits (Alfano et al. 2011). Therefore, as proximal and medial tephra deposition from eruptions at Manam will be on the island itself and the ocean, critical components of the ground deposits would be missing from any attempts to calculate a TGSD for Manam.

3.5 Conclusions

The aim of this chapter was to understand the tephra hazard associated with explosive eruptions of Manam and what impacts the deposited tephra might have on human activity in the affected areas. Five eruption scenarios, based on the observed activity at Manam since the early 20th century, were modelled using the probabilistic tephra deposition model *TephraProb*. Ash venting eruptions (scenario 1) are shown to deposit trace thicknesses of tephra around the summit of Manam, not affecting the coastal populations of the island. Minor Vulcanian eruptions have a 50% likelihood to deposit ≥1 mm of ash on central and southern areas of the island, and are not anticipated to impact the mainland. Major Vulcanian eruptions (scenario 3) are shown to have a moderate chance of depositing trace thicknesses on several 10s of kilometres into the mainland and ≥10 mm on Manam itself threatening structural damage to the traditional timber buildings of Manam, especially during the wet season. Less intense sub-Plinian eruptions (e.g. 28 June 2019 eruption) are shown to have a 50% probability of depositing ≥100 mm across large parts of Manam causing significant damage to island infrastructure and agriculture as well as trace ash deposits on the mainland during the dry season. More intense sub-Plinian eruptions (e.g. 2004/05 eruptions) will have a moderate chance to inundate most of Manam with ≥1000 mm effectively rendering the island unhabitable and long distance dispersal of fine ash onto the mainland westerly into the neighbour East Sepik province.

Using *TephraProb* has provided a method to understand the hazard at Manam in a probabilistic manner by way of randomly sampling eruption source parameters

from predetermined ranges. Additionally it has allowed the comparison of the deposition of tephra from the same eruption scenario but during the dry and wet seasons of Papua New Guinea. This has revealed a dominant westward dispersal of ash during dry season eruptions with a more symmetrical distribution during the wet season predominantly due to changing wind patterns in the lower 5 km of the atmosphere. While the dry seasons impacts tend to affect a larger area, the wet season winds cause tephra from scenario 3 and 5 eruptions to reach the key mainland town of Bogia and the North Coast Highway that is the key route to the provincial capital Madang.

This work has shown that with careful parameter selection that modelling of the tephra hazard of volcano with sparse data relating to the deposits of previous eruptions. However, improvements to this work include field-based characterisation of tephra deposits of previous Manam eruptions to provide more specific parameters for future modelling of Manam's tephra hazard. This would include collating new Manam specific TGSDs but also enable inversion modelling of previous eruptions to ascertain eruption source parameters of these historical events, to then further validate the *TephraProb* model specifically to eruptions of Manam (Connor and Connor 2006; White et al. 2017).

Another recommendation for future work is to survey buildings on the mainland in either in the field and by digitising recent satellite imagery. A field-based survey would allow or improved records of construction types allowing for improve impact assessments whilst digitising recent satellite imagery would provide the widen scope of tephra deposition affects beyond Manam itself.

In conclusion, this chapter has provided the first known assessment of tephra deposition and associated impacts to infrastructure and livelihoods from eruptions of Manam volcano across a range eruption scenarios. It has demonstrated a methodology that can be used at other under studied yet frequently eruptive volcanoes to provide first order assessment of tephra hazard. This probabilistic tephra deposition assessment has also provided information from which volcanic emergency protocol best practices can be developed, including evaluation of potential evacuation locations and the highlighting of Bogia as the key to emergency response and thus the need to improve resilience of the town and transport links to the provincial capital Madang

4 Chapter Four - Lava Flow Modelling and Hazard Assessment

4.1 Introduction

Lava flows are frequent products of volcanic activity, especially for mafic volcanism, and cover an estimated 70% of the Earth's surface (Kilburn 2000). Basaltic lava flows can erupt at temperatures as high as 1200°C and move at speeds in excess of 15 km hr^{-1} (Baloga et al. 1995; Kilburn 2000; Griffiths 2000). The 1977 Nyiragongo (D.R. Congo) lava flows inundated ~20 km^2 of land in less than an hour and tragically resulted in around 100 fatalities (Tazieff 1977; Komorowski 2002; Favalli et al. 2009), highlighting the lethal potential of effusive volcanic eruptions. Lava flows pose a hazard to large part of the global population with 47 million living within 5 km of a volcanic vent (Cottrell 2015). Fortunately, most lava flows are slower than the highly mobile Nyiragongo flows and advance slowly enough to be evaded on foot (Peterson and Tilling 2000). Even so, lava flows have killed 659 people between 1500 and 2017 including one fatality 29 km away from the source of the flow (Brown et al. 2017). However, it is the immovable assets such as buildings and infrastructure that is most vulnerable to the often inexorable advance of lava. This damage to the built environment then has cascading societal and economic repercussions, with long post-eruptive recovery periods. As development and spread of human settlements increase, so has the number of lava flows impacting the built environment over time: 50% of occurrences recorded over the last ~5500 years have occurred in the last 110 years (Meredith et al. 2024).

Recent examples where lava flows have resulted in substantial damage to homes and other critical infrastructure include Fogo 2014-2015 (Cape Verde) (Jenkins et al. 2017), Kilauea 2018 (USA) (Meredith et al. 2022), Nyiragongo 2021 (Congo) (Mafuko

Nyandwi et al. 2023), and Tajogaite 2021 (La Palma, Spain) (Biass et al. 2024). Many of the examples given here are from island volcanoes where populations live in proximity to volcanic hazards by virtue of the land they live on being formed by the very volcano that poses a threat. A secondary hazard posed by lava flows is its interaction with sea water which produces a volcanic gas plume known as laze (i.e. lava haze) (Kullman et al. 1994; Sansone et al. 2002; Williams-Jones and Rymer 2015). Lava-seawater interaction can release toxic gases such as chlorine and metal aerosols, capable of being transported by the wind to areas far from the lava flow itself (Resing and Sansone 2002; Edmonds and Gerlach 2006; Mason et al. 2021). The generation and transportation of laze is currently a less understood facet of volcanic eruptions and often overlooked in hazard assessments. It is particularly hazardous at island volcanoes where lava-seawater interactions are not uncommon. Recent notable examples are the 2018 Kilauea (USA) (Mason et al. 2021) and 2021 Tajogaite (La Palma, Spain) (González-Santana et al. 2022) eruptions where laze plumes were generated in proximity to inhabited areas. As with all populations living in close proximity to volcanoes, an understanding of lava hazards is critical to inform decisions by residents and policy makers before, during and after eruptions (Blong 1996; Felpeto et al. 2001; Yoon 2012).

4.1.1 Lava Flow Modelling

Lava flow hazard assessments have historically been based on mapping of previous flows to identify preferred flow routes and runout distances (Crandell and Mullineaux 1978; Guest and Murray 1979). Since the 1980s however this approach has been increasingly complemented by the application of numerical models (Yun

et al. 2018). Modern models treat lava flows as gravity currents that spread under their own weight and are slowed by their own rheology and underlying slope, whilst also taking into account the yield stress of lava and a non-flowing basal profile section (Cordonnier et al. 2016). Cooling and effusion rate are primary controls on lava advance. Cooling increases viscosity through crystallisation and is a function of thermal conductivity, specific heat and density (Stasiuk et al. 1993; Diniega et al. 2013; Harris and Rowland 2015a; Cordonnier et al. 2016). The effusion rate controls the rate a flow grows and spreads (Walker 1973; Kilburn and Lopez 1988; Kilburn 2000; Harris and Rowland 2009). It also influences how easily surface crust can break to expose underlying lava (Kilburn 2004, 2022) and, hence also, the rate at which lava flows cool (Dragoni 1989; Crisp and Baloga 1990; Harris et al. 1998). Additional factors that models must consider are the initial eruptive temperature of the lava, vent geometry, thermal boundary conditions at the top and base of the flow, and the control of temperature on the physical and rheological properties of the lava, as well as the underlying surface topography (Costa and Macedonio 2005; Cordonnier et al. 2016).

Several lava flow models are available for investigating lava flow dynamics and producing hazard maps (see Cordonnier et al. (2016) and Costa and Macedonio (2005)). One group of models includes those that that confine the flow into a channel, allowing it to flow downslope in one direction, and thereby sacrificing the complexities of the physical processes of flow emplacement (e.g. spreading) in order to focus on modelling more nuanced thermal processes. *FLOWGO* (Harris and Rowland 2001, 2015b) is the most prominent channelled flow model, which

simulates the flow of a finite-mass parcel down a levee-contained channel (see **section 4.2.1.1** and Harris and Rowland, 2001, 2015b for more detail). This method allows for fast computational times and is available to run in widely-available software including Microsoft Excel (Harris et al. 2016), Python (Chevrel et al. 2018) and within the probabilistic lava flow model *Q-LavHA* (Mossoux et al. 2016). The flexibility and fast computational time of *FLOWGO* has made it a popular tool for the assessment of lava inundation probability and maximum runout lengths (Rowland et al. 2005; Wantim et al. 2013; Rodriguez-Gonzalez et al. 2021; Prieto-Torrell et al. 2021; Derenius and Gao 2022; Ramayanti et al. 2022) including during crises such as the 2018 Piton de la Fournaise (La Reunion) eruption (Harris et al. 2019).

Another common approach to lava flow modelling is the cellular automata method. Here, a 2D grid of cells is populated with properties including elevation, lava height and temperature and the advance and cooling of the lava flow is determined by the evolution of the cells' properties (Cordonnier et al. 2016). Cellular automata models, such as *SCIARA* (Crisci et al. 2004) and *MAGFLOW* (Del Negro et al. 2008; Cappello et al. 2016) rely on a physical model of the thermal and rheological evolution of lava flows (Del Negro et al. 2008), which allows them to model flow spreading and the emplacement of successive flows (Cappello et al. 2016). As such these type of models are capable of not only forecasting lava flow hazard footprints (Herault et al. 2009; Rongo et al. 2016) but also flow thicknesses (Crisci et al. 2004; Avolio et al. 2006; Vicari et al. 2007; Del Negro et al. 2008).

Probabilistic, or stochastic, models use probability distributions to determine the movement of lava from cell to another (Favalli et al. 2005; Mossoux et al. 2016). This is achieved by assigning a probability to each of the cells (pixels of the underlying DEM) surrounding the flow representing the likelihood that the flow will move to that cell. This probability typically relates to the difference in elevation between cell occupied by the flow front and each of its surrounding cells (Tarquini and Favalli 2010; Mossoux et al. 2016). The *DOWNFLOW* model (Favalli et al. 2005; Tarquini and Favalli 2016) is able to forecast lava emplacement while accounting for probabilistic lava flow length (Tarquini and Favalli 2013; Harris and Rowland 2015b). *Q-LavHA* is a probabilistic modelling platform (provided as a plugin for QGIS) that combines the probabilistic model of Felpeto et al. (2001) with deterministic flow length constraints including *FLOWGO* (Mossoux et al. 2016). Stochastic models have fast computational times and are therefore typically used to simulate different lava flow scenarios as part of operational or responsive hazard assessments (Rodriguez-Gonzalez et al. 2021; Vilches et al. 2022; Verolino et al. 2022; Derenius and Gao 2022; Németh and Moufti 2023).

Lava flow models are effective tools for not only understanding the processes governing emplacement (Lev et al. 2012) but also for critically assessing the spatial extent of lava flow hazard to inform pre-emptive land use planning, eruption preparedness, crisis response management planning, and syn-eruptive monitoring. Lava flow hazard assessments based on modelling have become integral to improving the resilience of communities on or close to volcanoes, especially on volcanic islands (Rowland et al. 2005; Favalli et al. 2009; Rodriguez-Gonzalez et al.

2021; Vilches et al. 2022; Verolino et al. 2022). In this chapter, probabilistic lava flow modelling will be applied to Manam volcano, where lava flows are frequent in the historical eruptive record. Here, current hazard perception is primarily based on experiences learned from previous flows (Palfreyman and Cooke 1976; Mercer and Kelman 2010). It is therefore hoped that numerical modelling can enhance hazard awareness by highlighting locations that are potentially vulnerable to lava flow inundation but have not previously experienced them in the recent past.

4.1.2 Lava Flows on Manam

A key part of hazard assessments is not only representing the potential extent a hazard may impact but also the likelihood a certain event or scenario may occur (Marzocchi et al. 2004; Connor et al. 2015). This section examines historical lava flow activity on Manam with the intent of understanding the frequency of which lava flow runouts of differing magnitude have occurred in the past. It is also necessary to consult the historical record to identify previous sources of lava flows which may reactivate or provide insight into the location of future vents. This section also attempts to provide context for the need for numerical lava flow modelling at Manam by highlighting the impacts of lava flows on settlements in the past. The frequent effusion of lava flows at Manam has been well documented since at least 1887 (Palfreyman and Cooke 1976). The ability of lava flows to reach and enter the ocean is not uncommon, with a flow during the major 1919 eruption doing so alongside probable sub-Plinian explosive activity (Fisher 1939). McKee (1981) mapped the historically-emplaced lava flows (**Figure 4.1**) showing how the four radial “avalanche valleys” generally confine the flows in their upper reaches

until ~400 m asl, below which the valleys open onto the shallower sloping coastal regions (**Figure 4.1**). The exception to this is the southeast valley, which currently broadens out much lower down at ~200 m asl. Interestingly, the mapped flows here are well outside the current confines of the valley and more recent pyroclastic deposits (**Figure 4.1**), suggesting a change in topography since these undated lava flows were emplaced. The term "avalanche valley" likely comes from the fact pyroclastic material has been observed to flow down the valleys in a manner visually similar to snow avalanches. Indeed, accumulations of lava emplaced at the head of the southeast valley were reported to become unstable and move down slope "as avalanches" (Reynolds 1957). Pyroclastic density currents (PDCs) are also common, especially Block and Ash Flows (BAF) that move rock or debris flows (Cole et al. 2002; Charbonnier and Gertisser 2008), and deposit blocky pyroclastic material on the lower flanks (Taylor 1958a).

The settlements on Manam are located in the coastal regions of the planèzes, the wedge shape-landforms between the eroded avalanche valleys, away from the areas with pyroclastic deposits (Best, 1953 ; McKee, 1981; Palfreyman and Cooke, 1976) (**Figure 4.1**). These locations are supposedly chosen specifically based on knowledge of the hazard posed by volcanic flows directed down the avalanche valleys (Mercer and Kelman 2010). Both lava flows and PDCs become unconfined towards the coast where they are able to fan out from the end of the valley to the ocean. This has resulted in settlements closer to the coast being threatened or inundated by lava flows in recent decades such as Bokure and Kolang (Global Volcanism Program 1992c, 2019a, 2019b, 2019c).

The potential for lava flows to directly threaten settlements situated between the avalanche valleys is demonstrated most clearly by five satellite cones of unknown dates that also are located between the avalanche valleys (**Figure 4.1**). These cones are situated stratigraphically on top of unmapped lava flows and are thought to have been built during a closing phase of explosive activity following initially effusive eruptions (McKee 1981). No published work exists, to the best of my knowledge, that considers the threat posed by future flank eruptions. Yet, despite the prevailing hazard posed by the frequent summit eruptions at Manam, the geological record of the island indicates clearly that flank eruptions represent an eruptive scenario that cannot be ignored.

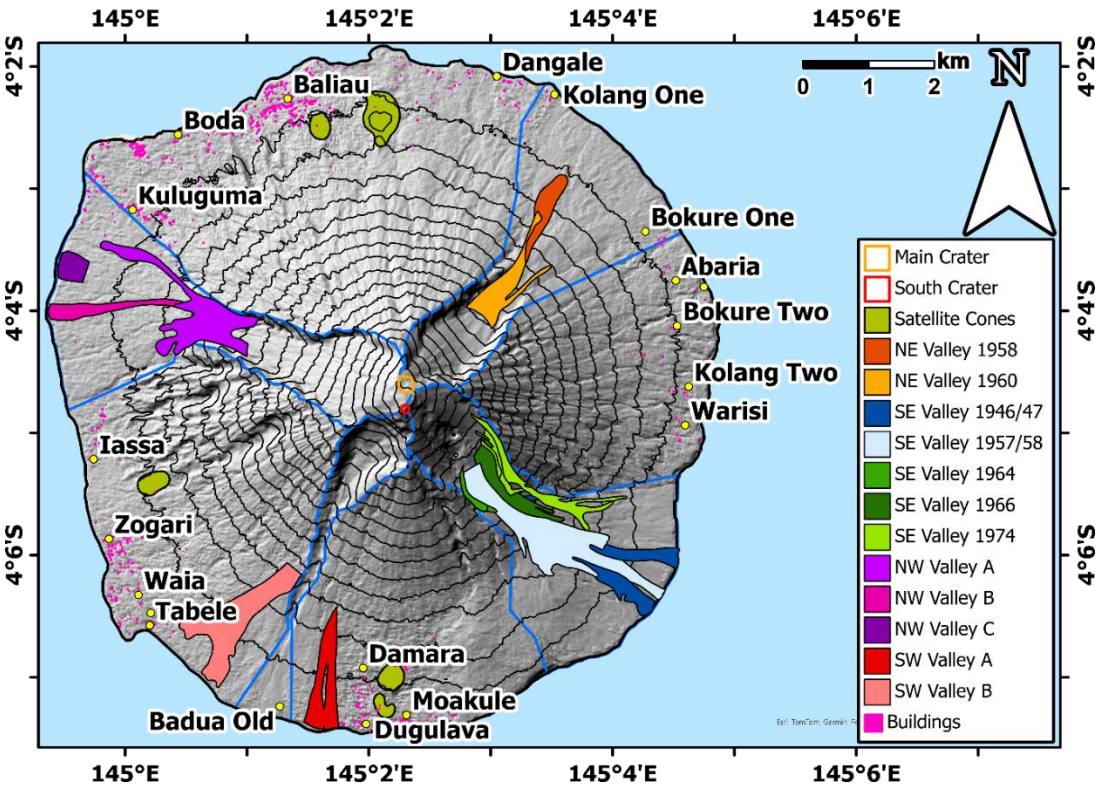

Figure 4.1 Historical lava flows (pre-1981) mapped by McKee 1981. NW Valley A flow (light purple) is likely to be the 1958 lava flow observed by Taylor (1958). The SE Valley 1946/47 flow (dark blue) is debated in the literature as to whether it was a true lava flow (Best 1953) or debris flow (avalanche) (Reynolds 1957).

4.1.2.1 Northeast Valley

Lava flows in the northeast valley emanate from Main Crater, which (in its current topographical form) has an opening in its eastern wall directly into the valley itself (Best 1953; Palfreyman and Cooke 1976). The lava flows mapped by McKee (1981) (**Figure 4.1**) show two lava flows in the northeast valley from 1958 (Taylor 1958a) and 1960 (Taylor 1963) reaching within ~900 m and ~1600 m of the coast respectively. These are the first two observed lava flows in the written history of Manam's eruptions (Palfreyman and Cooke, 1976).

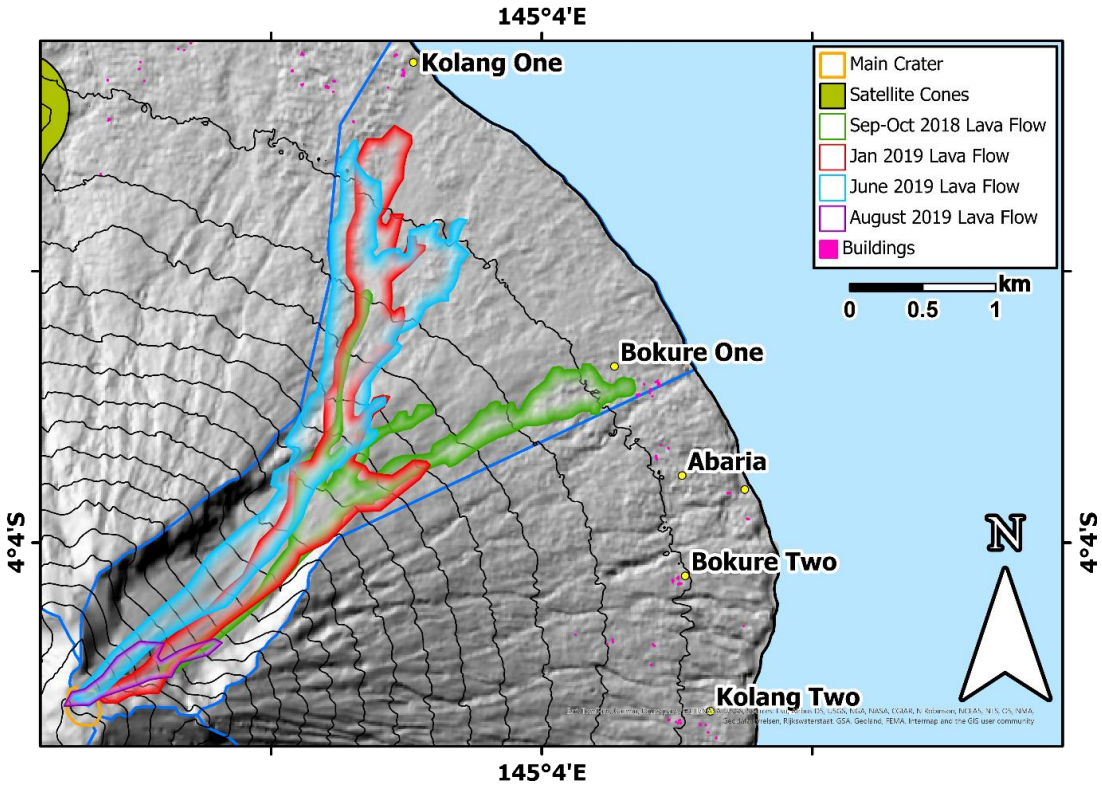

Figure 4.2 Recent (August 2018 – December) northeast valley flows visible in and mapped from Sentinel-2 MSI and Landsat 8 OLI shortwave infrared (SWIR) imagery. 25th September – 2 October 2018 flow – Sentinel-2 MSI 02/10/2018 SWIR, 8 January 2019 flow Landsat 8 OLI 22/01/2019 SWIR, 28 June 2019 and August 2019 flows – Sentinel-2 MSI 13/08/2019 SWIR.

Despite Manam's frequent eruptions through this intervening period, the next lava flows into the northeast valley only occurred on 13 April 1992 (Global Volcanism Program 1992d), followed by another seven lava flows in 1992, three of which that reached the coast. Notably, the 1992 flows destroyed 28 houses on the south side of the northeast valley (Global Volcanism Program 1992a, 1992b, 1992c).

Three shorter lava flows were emplaced in 1996, the longest reaching only to 600-700 m asl (Global Volcanism Program 1996a). The major explosive eruptions in October and December 2004 were accompanied by two longer lava flows, one reaching within 1 km of the coast in October and the other entering the sea in November and within 100 m of Bokure village (Global Volcanism Program 2004d)

The eruptive activity from August 2018 to December 2021 (see Chapter 2) produced several lava flows that propagated down the northeast valley; including three that came within 400-650 m of the ocean (**Figure 4.2**). A lava flow stopped within metres of Bokure on the southern side of the northeast valley 1 October 2018 and had threatened Kolang on the north side. A subsequent lava flow on 8 December 2018 prompted the evacuation of both villages (Global Volcanism Program 2019a) and their later relocation to the south between the northeast and southeast valleys (**Figure 4.1**).

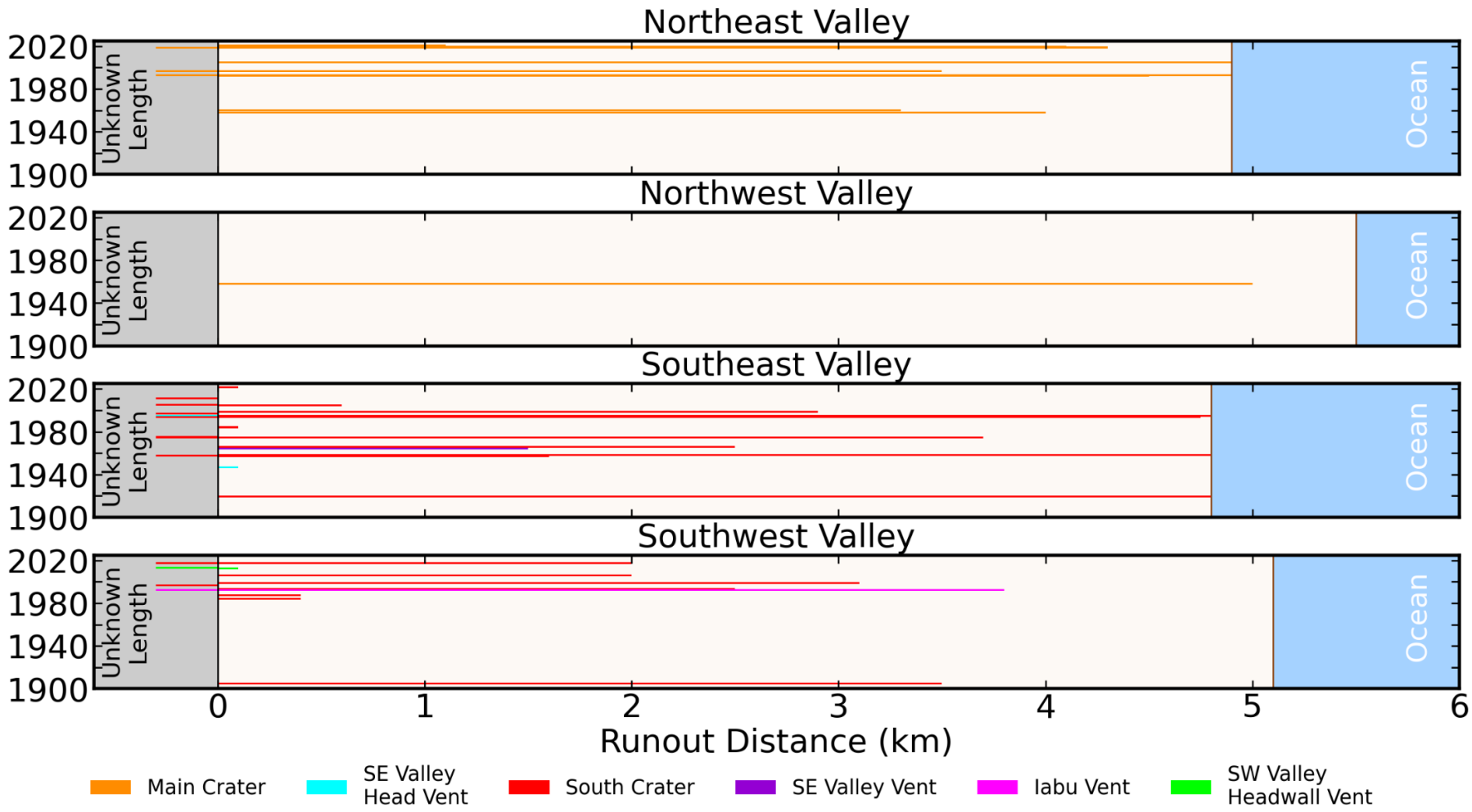

Figure 4.3 Graphical representation of the lava flow runout distances observed (Global Volcanism Program 2024) or mapped by McKee (1981) or measured as part of this work from satellite imagery. Grey zone represents observed flows with no reported runout distance.

4.1.2.2 Northwest Valley

Manam's northwest valley is described as being the most mature valley with well established drainage patterns (McKee 1981), which alludes to the fact that volcanic flows have travelled down this valley the least frequently, historically (Global Volcanism Program 2024). Two young but undated lava flows were identified by McKee (1981) with one of these (NW Valley A in **Figure 4.1**) likely to be the 14 January 1958 flow that reportedly reached within 0.5 miles (800 m) of the coast (Taylor, 1958). McKee (1981) did not map the upper slopes of the avalanche valleys (**Figure 4.1**) and Taylor (1958a) does not describe the source of this lava flow other than that Main Crater was the more active crater during this eruptive phase. The source remains unclear: if Main Crater had been the source, the lava would have had to overcome the high back wall of the crater, or if it had been South Crater lava might have been directed down the northwest valley but this seems unlikely as this behaviour has never been documented. A remaining option is that another vent opened somewhere in the northwest valley. The circumstances under which lava flows may descend the northwest valley are thus uncertain at this time.

4.1.2.3 Southwest Valley

The southeast valley is the narrowest of the four avalanche valleys on Manam. It reaches its widest point (~1000 m) at 1200 m asl but then narrows to ~300 m at 700 m asl, a width it approximately maintains until ~150 m asl, where it opens up on the shallow slopes of the coastal areas. It would therefore be expected that lava flows are contained within this narrow valley. However, the mapped lava flows by McKee (1981) show two undated flows that reached the ocean but are outside the current

valley geometry but taper towards the head of the valley (**Figure 4.1**). In Palfreyman and Cooke's (1976) compilation of Manam's eruptive history there is only one observed lava flow that flowed down the southwest valley: the 26 October 1904 flow was observed to have stopped where the valley's slope angle reduced and it is explicitly stated not to have reached the sea (Palfreyman and Cooke 1976) meaning that it is unlikely this event corresponds to either of the two mapped flows (McKee, 1981, **Figure 4.1**). Furthermore, all observed southwest valley lava flows have been contained within the valley's boundaries (Global Volcanism Program 2024), raising questions about how these two mapped flows had overcome the valley walls and whether future flows in this valley could do the same. These questions have very practical relevance towards understanding the potential risk to settlements situated near to the bottom of this valley.

At least three sources have been reported from which lava flows entered into the southwest valley. The first is the South Crater, which has been the confirmed source of nine lava flows between 1984 and 1998 and a possible source for a further five flows (Cooke et al. 1976; Palfreyman and Cooke 1976; Global Volcanism Program 2024). Lava flows from South Crater have been observed exiting the crater via a collapsed portion of the crater wall that is periodically destroyed and rebuilt (Global Volcanism Program 1984). This lower section of crater wall was observed by an UAS flight in 2019 (Liu et al., 2020, Figure 4.4). Lava flows sourced from South Crater must descend the steep headwall of the southwest valley; this often results in the brecciation and breakup of the lava as it cascades down the steep terrain (Global Volcanism Program 1984, 1992d). Flows that are able to negotiate the headwall

without disintegrating typically reach the upper part of the narrow neck of the valley around 600 m asl and obtain a maximum runout of ~2.5 km down to approximately 450 m asl **Figure 4.3**.

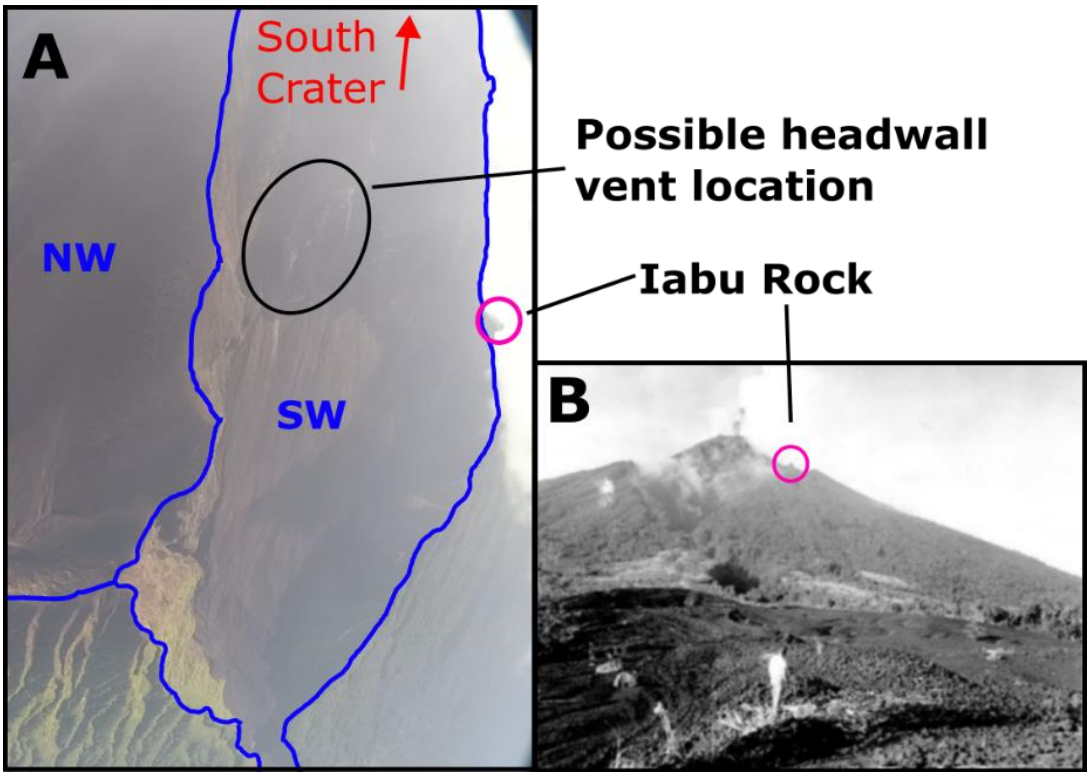

Figure 4.4 Location of Iabu Rock (pink ring) after which the Iabu Vent is named and is presumably in located in nearby. The black ring image A indicates a vent-like feature on the southwest valley headwall. A – Imagery of fixed wing overpass of the southwest valley in October 2018 (Courtesy of E. Nicholson). B – Photo of from the bottom of the southwest valley looking up towards the summit (Adapted from (Johnson 2013).

In 1992, lava flows in the southwest valley were reported to come from a vent named Iabu Vent (Global Volcanism Program 1992e). This vent is not mentioned before or after these reports and the exact position is not published. However, Iabu Rock is a prominent skyward protrusion of angular rock situated on the boundary between the southwest and southeast valley (Johnson, 2013, **Figure 4.4**). Flows from Iabu Vent reached as far as 200 m asl (~3.8 km) on 14 May 1992 (Global Volcanism Program 1992e) (**Figure 4.3**). On 15 April 2013, two vents opened on the

headwall of the southwest valley sending lava flows into the valley (Global Volcanism Program 2013). Further reports of lava flows on 14 and 15 May 2017 from a unspecified vent and a shortwave infrared hotspot located on valley headwall on 14 July 2017 (Sentinel-2 Multispectral Instrument imagery (MSI), indicate that new vents are capable of opening across the breadth of the headwall.

4.1.2.4 Southeast Valley

Of all Manam's avalanche valleys, the southeast valley has the most recorded lava flows since 1919 (**Figure 4.3**), where a large flow reached the ocean during the major eruption of 2 August 1919 (Fisher 1939). In 1946/47 a lava flow from South Crater is reported to have reached the ocean (Best 1953) and was subsequently mapped as a lava flow by McKee (1981, **Figure 4.1**). However, the observation in January 1957 of lava accumulating at the top of the valley, collapsing and then moving down hill as debris flows led to the reclassification of the 1946/46 lava flow as a debris flow (Reynolds 1957; Taylor 1958a). Since the 1919 flow, only two more flows have been recorded reaching the ocean via the southeast valley. The first was on 6 March 1958 (reportedly from South Crater; Taylor, 1958, **Figure 4.1**) and the second on 18 October 1994 (the source of which was not reported; Global Volcanism Program, 1994). Other lava flows originating from South Crater have remained in the upper reaches of the valley (Taylor 1958a; Global Volcanism Program 2024) and, of the three lava flows supposedly entering the ocean, only that in 1958 was explicitly stated to have originated from South Crater (Taylor 1958a).

Other vents have been observed to produce lava flows in the southeast valley. A vent or fissure has been regularly observed at the top of the southeast valley

estimated to be situated 400-500 yards (365-457 m) from the rim South Crater in 1964 (Branch 1965). Although these lavas flows typically travelled only short distances before disintegrating downslope (Reynolds 1957), some reached halfway down the valley (Branch 1965) and even to 150 m asl, ~500 m from the coast (Global Volcanism Program 1993b). An active vent was observed on 15 April 2013 was reported as being at the same elevation as those formed in 2012 (Global Volcanism Program 2013); however, the position of these 2012 vents are not recorded in any publicly-available report.

The historical record has shown that multiple lava flow producing vents have been active over the last 100 years and that they each have undergone periods of quiescence with activity shifting to other locations, often nearby within the same valley. The origin of the longest runout lava flows in the southeast valley is the most unclear and represents an area in which this work seeks to clarify. Additionally, the circumstances required for lava to flow down the northwest valley are unresolved at present. Given that there is clearly a possibility of lava flows issuing from many locations it is therefore important that the hazard represented by each of these vents quantified. The assessment of the hazard represented by each vent will enable local communities to respond appropriately when a particular vent opens and produces lava.

4.1.3 Aims and Objectives

This chapter aims to quantify the potential runout lengths of future lava flows at Manam and, from this, assess the hazard posed by effusive eruptions to local

settlements and their resident populations. Although most villages are situated away from the areas typically affected by volcanic flows at the bottom of the avalanche valleys, some remain proximal including Kulaguma, Dangale, and Abaria (**Figure 4.1**). In addition to assessing the likelihood of direct inundation of lava flows, this chapter seeks to evaluate the probability of a lava flow entering the ocean, and therefore generating secondary hazards, for a range of eruptive scenarios. Additionally this work looks to test whether the FLOWGO model embedded in Q-LavHA is fit for purpose. The *Q-LavHA* probabilistic modelling platform (Mossoux et al. 2016) will be used to achieve the following objectives:

1. By varying the vent location and effusion rate within relevant bounds, determine which (if any) eruption scenarios are capable of producing lava flows that inundate settlements on Manam.
2. Generate a distribution of future satellite cones based on the location of existing cones and model the potential lava flows generated by the opening of such lower flank vents to reveal potential inundation of settlements.
3. Evaluate the potential for different vents and effusion rates to generate lava flow ocean entry sites, which may produce secondary hazards such as a laze plume or littoral explosions.
4. Reconcile previously mapped flows (McKee, 1981) with simulated model outputs, specifically testing (a) whether historically-recorded vents are capable of generating lava flows in the northwest valley or if another source was responsible for the lava flows mapped in this valley (McKee 1981) and (b) determining the likelihood that future lava flows may overtop the

southwest valley walls and following similar paths to the undated flows mapped by McKee (1981).

4.2 Methods

This section describes the procedures followed to assess the spatial distribution of lava flow hazard at Manam including (a) the selection of vent locations and eruption scenarios, (b) background detail on *Q-LavHA* (Mossoux et al. 2016) and the underlying *FLOWGO* model (Harris and Rowland 2001, 2015b), and (c) the selection of the model input parameters. This section includes preliminary model runs of *Q-LavHA* to test the sensitivity of the model output to varying individual parameters over relevant value ranges; this informs the definition of eruptive scenarios and selection of model starting conditions. Two different resolution digital elevation models (DEMs) are also tested against recently mapped flows to determine the optimal option for replicating past and modelling future Manam lava flows. For clarity, throughout this chapter the use of *Q-LavHA* refers to the model in its entirety including the elements from *FLOWGO* (unless otherwise stated) and when *FLOWGO* is used specifically it should be understood as the lava flow length constraint method provided by *FLOWGO* and not the full *Q-LavHA* model platform.

4.2.1 *Q-LavHA*

Q-LavHA is a plugin for Quantum GIS (Q-GIS) that simulates the probability of 'a'ā lava inundation over a DEM for a given vent location (Mossoux et al. 2016). The vent location can be given as a point source, line (or fissure) source, or as a surface area. Point and line sources are intended to model lava flows originating from well

defined vents or fissures. Surface area sources allow the simulation of flows from a broader area where the exact location may be unknown or changeable. For line and surface area defined vents flows are generated at regular, user defined, intervals with the minimum being that of the pixel resolution of the underlying DEM (Mossoux et al. 2016).

The advance of channelised 'a'ā flows is simulated following the model of Felpeto et al. (2001), which allows the lava flow to overcome topographic obstacles. Beginning at the vent pixel, the model advances the flow pixel by pixel, by selecting one of the eight surrounding pixels. This is done by calculating a flow probability (P_i) for each of the surrounding pixels according to **Equation 4.1**:

$$\boldsymbol{P_i = \frac{\Delta h_i}{\sum_{j=i}^{8} \Delta h_j}, i = 1, 2, \ldots, 8} \qquad \textbf{\textit{(4.1)}}$$

where Δh_i represents the difference in elevation between the central pixel ($i = 0$) and each of the eight surrounding pixels. If the elevation difference between the central pixel and a surrounding pixel is negative, Δh_i is set to 0 as uphill propagation is impossible. Backward propagation to the pixel the flow has come from is not allowed and Δh_i is also set to 0.

Following Felpeto et al. (2001), corrective factors are included to enable the lava flows to overcome small topographic barriers or depressions. The factor H_c represents the thickness of the lava flow and is added to the central pixel before calculating the elevation difference between it and the surrounding pixels. H_p is a higher corrective factor that allows the lava flow to attempt to fill a topographic depression and continue to flow. This factor is only applied if the flow front

occupies a pixel where all the surrounding pixels are at a higher elevation that the central pixel with H_c applied (see Mossoux et al., 2016 for full procedure of applying $\mathrm{H_p}$). These corrective factors are applied to the DEM temporarily and are not carried over to subsequent simulation runs.

Once P_i has been calculated for all surrounding pixels, a cumulative probability value S_i (**Equation 4.2**) and a random number ($\boldsymbol{rnd}$) is generated between zero and one. If the randomly generated number falls within the interval $[S_{i-1,}\ S_i]$, pixel i selected as the pixel for the flow to move to (**Equation 4.3**, Felpeto et al., 2001; Mossoux et al., 2016):

$$\boldsymbol{S_i = \sum_{j=1}^{i} P_j, i = 1, 2 \ldots, 8} \qquad \textit{(4.2)}$$

$$\boldsymbol{S_{i-1} \leq rnd < S_i, 1, 2, \ldots, 8} \qquad \textit{(4.3)}$$

Q-LavHA also includes a method of calculating the pixel flow probability using the second power of Δh_i (**Equation 4.4**). This gives pixels with higher elevation differences higher probabilities for the flow to move to that pixel, therefore increasing the probability of the flow following the steepest flow path. It is the recommended method and so is used in the modelling of Manam lava flows:

$$\boldsymbol{P_i^2 = \frac{(\Delta h_i)^2}{\sum_{j=1}^{8}(\Delta h_j)^2}, i = 1, 2, \ldots 8} \qquad \textit{(4.4)}$$

If the lava flow reaches a depression that cannot be overcome with the application of H_p then *Q-LavHA* also has the provision to allow the flow to propagate to one of the 16 surrounding pixels bordering the initial 8 surrounding pixels. The probability

calculated in the same manner as for the 9 surrounding pixels (Mossoux et al. 2016). This is also a recommended setting and is used in this work.

There are 3 methods available within *Q-LavHA* to determine the runout length of lava flows within each iteration. The first is a user-defined maximum length either by a) Manhattan length, which is the length of the flow line pixel by pixel or b) Euclidean length, which is the straight line distance from vent to terminus (Mossoux et al. 2016). The second is using a decreasing probability method where the user determines a mean Euclidean runout distance ($\bar{x}$) and the standard deviation (σ) (both ideally calculated from historical flow measurements). The flow stops when reaching a max Euclidean distance equal to $\bar{x} + 3 \times \sigma$ and then weighted by a decreasing probability density function (Mossoux et al. 2016). The third method is the application of the *FLOWGO* cooling-limited model (Harris and Rowland 2001); this is the option selected for modelling Manam's lava flows and is discussed in the next section.

The final probability that a pixel will be inundated by a lava flow is given by attributing an incremental probability of inundation ($\boldsymbol{prob_i}$) to each pixel after each iteration is complete (**Equation 4.5**). This probability is added to a matrix that calculates the final probability for a pixel to be inundated ($\boldsymbol{PROB_i}$). Where the eruption source is a line fissure or surface (i.e. where multiple regularly-spaced permutations of the vent location are simulated), all simulations are combined and divided by the total number of vents simulated (**Equation 6**).

$$\boldsymbol{prob_i = 1/(total\ number\ of\ iteration)} \qquad \textbf{\textit{(4.5)}}$$

$$\boldsymbol{PROB_i = \frac{\sum prob_i}{number\ of\ vents\ simulated} \times \varphi \times P_{susc}} \qquad \textbf{(4.6)}$$

The values $\boldsymbol{\varphi}$ and $\boldsymbol{P_{susc}}$ relate to the use of the descending probability runout length method and the use of susceptibility maps, respectively; neither are used in this work and are therefore held as 1.

4.2.1.1 *FLOWGO* Model

The 2001 version of the *FLOWGO* cooling-limited lava flow model (Harris and Rowland 2001) is available within *Q-LavHA* to determine lava flow runout distance. *FLOWGO* is used as the runout length constraint option in this project as it uses physical properties and the simulation of thermodynamic processes within the flow rather than the other options which pre-define the maximum runout length (Mossoux et al. 2016). *FLOWGO* requires a larger set of input parameters than the other runout length constraint methods, but *Q-LavHA* only specifically requires: effusion rate ($m^3\ s^{-1}$), initial lava viscosity (Pa·S), initial phenocryst mass fraction and channel ratio (width/depth) and holds defaults for all other "advanced" parameters, which can also be individually modified. The determination of input parameters will be discussed in section 4.2.4.

FLOWGO simulates the movement of a one-dimensional finite-mass lava parcel down a levee-constrained channel with no mechanically continuous roof, typical for an 'a'ā flow (Kilburn and Guest 1993; Kilburn 2022). The rheological properties of lava change as it loses heat by radiation and convection at the surface and conduction of air across the surface and by conduction through the ground along the base of the flow (Harris and Rowland 2001; Cordonnier et al. 2016). The

FLOWGO model operates under the principle that the velocity of lava flowing in a channel depends on the rheological properties of the lava, environmental factors (e.g. slope angle and gravity) and the dimensions of the lava channel itself. The primary rheological factors are viscosity and yield strength, which depend on the temperature and crystallinity of the lava (Harris and Rowland 2001). As lava flows along a channel, it cools and causes the rheological factors to change (Dragoni 1989; Kilburn and Lopes 1991; Stasiuk et al. 1993). In *FLOWGO*, the finite-mass lava parcel is advanced down the channel until either velocity reaches zero or the temperature of the core of the lava flow reaches its solidus (Harris and Rowland 2001). *Q-LavHA* also stops the flow when the yield strength of basal lava exceeds the stress of the downhill slope (Harris and Rowland 2015b; Mossoux et al. 2016).

4.2.2 Eruption Source Locations

This section describes the location of sources or vents including (a) the summit craters, (b) the flank vents in the southeast and southwest valleys (**Figure 4.5**), and (c) the illustrative potential locations of future satellite cones. Where the exact position of a vent is unclear or not described in the literature, the rationale for the placement of vents will be outlined. The decision to model the vents as a point source or surface area will be explained.

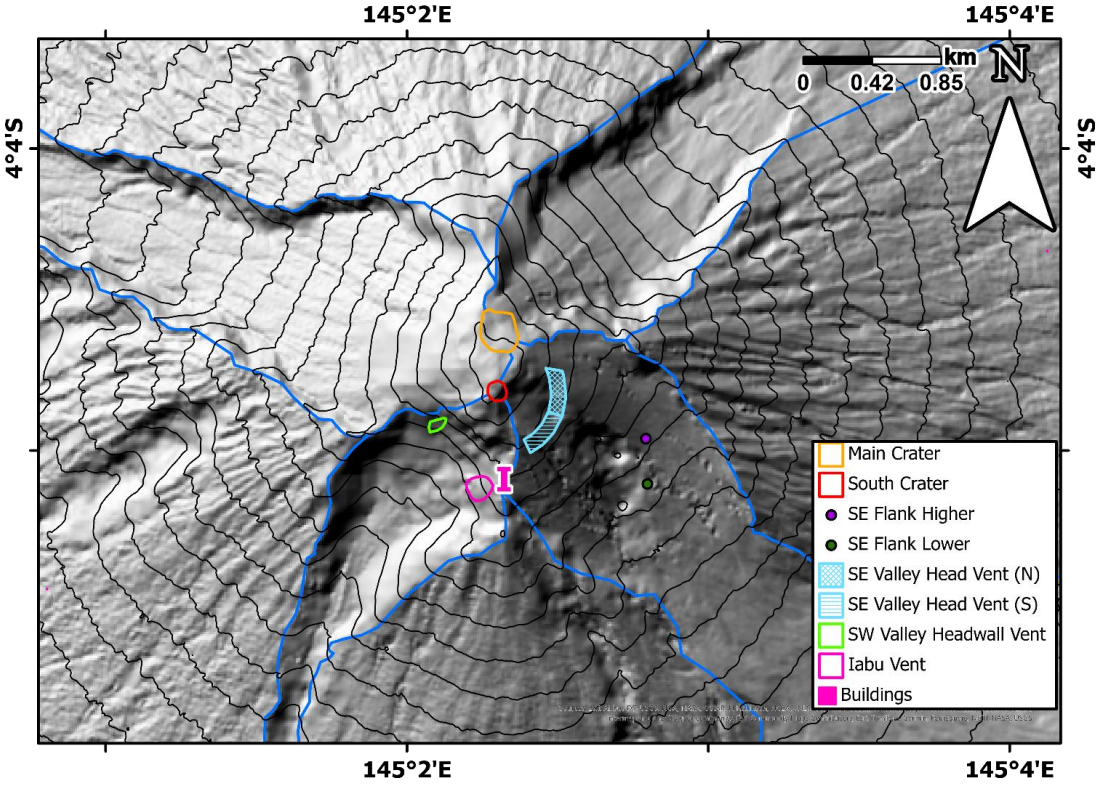

Figure 4.5 Hillshade relief map of the summit area of Manam indicating all eruption source locations modelled. Pink "I" indicates approximate location of Iabu rock from which the assumed location of Iabu Vent is based on.

4.2.2.1 Main Crater

The most recent observations of Main Crater from UAS overflights in October 2018 and May 2019 (Liu et al. 2020a) show that the topography of Main Crater is open on the eastern side into the northeast avalanche valley with the crater wall intact on the western side (**Figure 4.6**). This observation closely matches previous descriptions of Main Crater (Best 1956; Palfreyman and Cooke 1976; McKee 1981) implying that no substantial alterations to this crater have occurred since at least the 1950s. Main Crater is the source of all confirmed lava flows that have flowed down the northeast valley (Palfreyman and Cooke 1976; Global Volcanism Program 2024) and its current morphology explains why lava flows in the historical record

are preferentially directed down the northeast valley. The higher western crater wall, which appears visually as the headwall of the northeast valley, presents a significant barrier to lava entering the northwest valley (**Figure 4.6**). The historical northwest valley lava flows are undated (McKee 1981) and the literature does not record their origin. Although, as discussed in section 4.1.2.1, the NW Valley A flow in **Figure 4.1** is likely to be the 1958 flow described by Taylor (1958a) potentially originating from Main Crater. In this case it is unclear whether lava overcame the western crater wall or whether the wall had been broken or opened to facilitate lava flowing down the northwest valley.

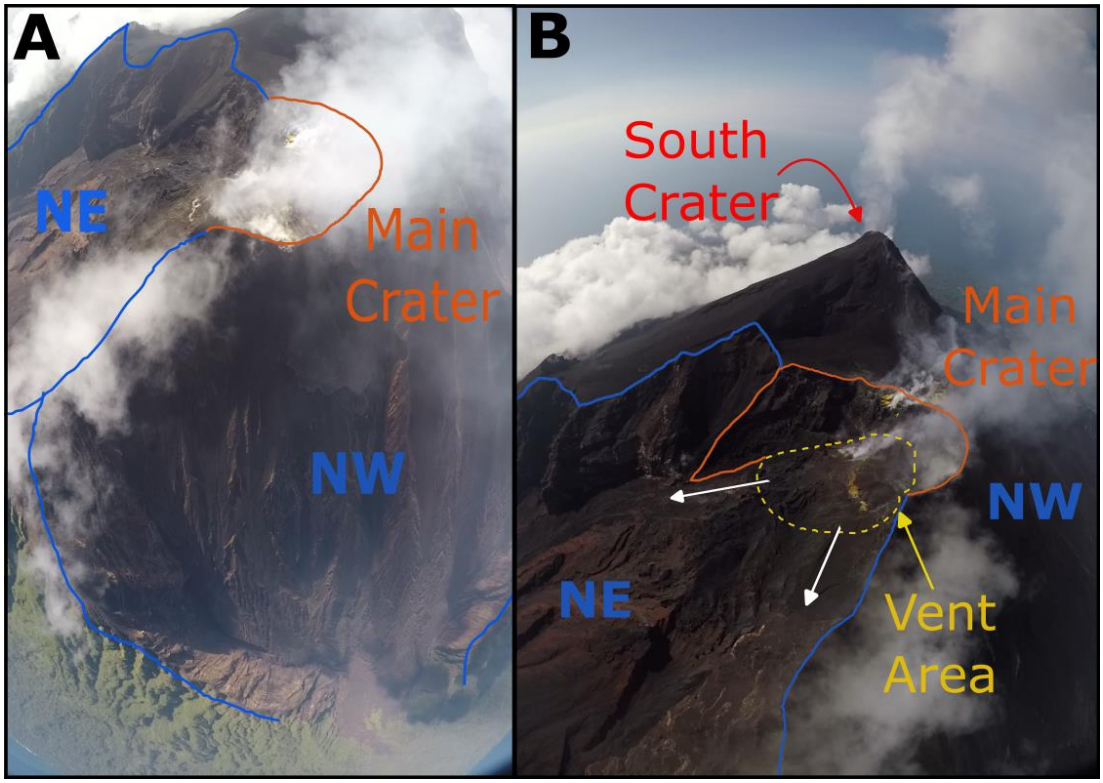

Figure 4.6 Fixed-wing drone overpass imagery of Main Crater from October 2018 (Courtesy of E. Nicholson). Topography of Main Crater shown from behind the crater wall looking approximately southeast (A) and into the crater from the north (B). Orange line indicates the high back wall that separates Main Crater and the northeast valley from the northwest valley. Yellow dashed area indicates the area in which vents form and lava flows originate. White arrows indicate two channels into which lava typically flow from the Main Crater. South Crater is situated behind Auroka Peak (Manam's summit), the plume from which can be seen in B.

In December 1996 and September 2003, two vents were seen to be emitting ash within Main Crater (Global Volcanism Program 1996b, 2003). This demonstrated that that there is not one fixed vent within Main Crater. Consequently, the locations of lava flow sources may vary between eruptions. The variable position of the vent(s) within Main Crater, was thus modelled as a surface area within *Q-LavHA*.

4.2.2.2 South Crater

Direct observation of South Crater in May 2019 showed that, the crater rim was lower on the southwestern side and opened out onto the headwall of the southwest valley (Liu et al., 2020, **Figure 4.6**). This open side may have resulted from a reopening of the "V-shaped channel" which formed during the 2005 eruptions and was filled up in 2011 (Global Volcanism Program 2013). The crater itself was estimated to be 60 m deep in 1987 (Global Volcanism Program 1987) while the diameter of the crater rim was estimated at 94 m based on satellite imagery from 2020 **(**Chapter 2 calculates depth of 64 m based off an assumed 30° crater flare angle and conduit radius of 10 m, close to the estimated depth in 1987). The size of the crater rim, in addition to observations of multiple vents active within the crater (Palfreyman and Cooke 1976) and its ability to direct lava into either of the southern valleys, mean that modelling South Crater as a surface area source is the most appropriate option to capture the variability in where lava exits the crater (**Figure 4.5**)

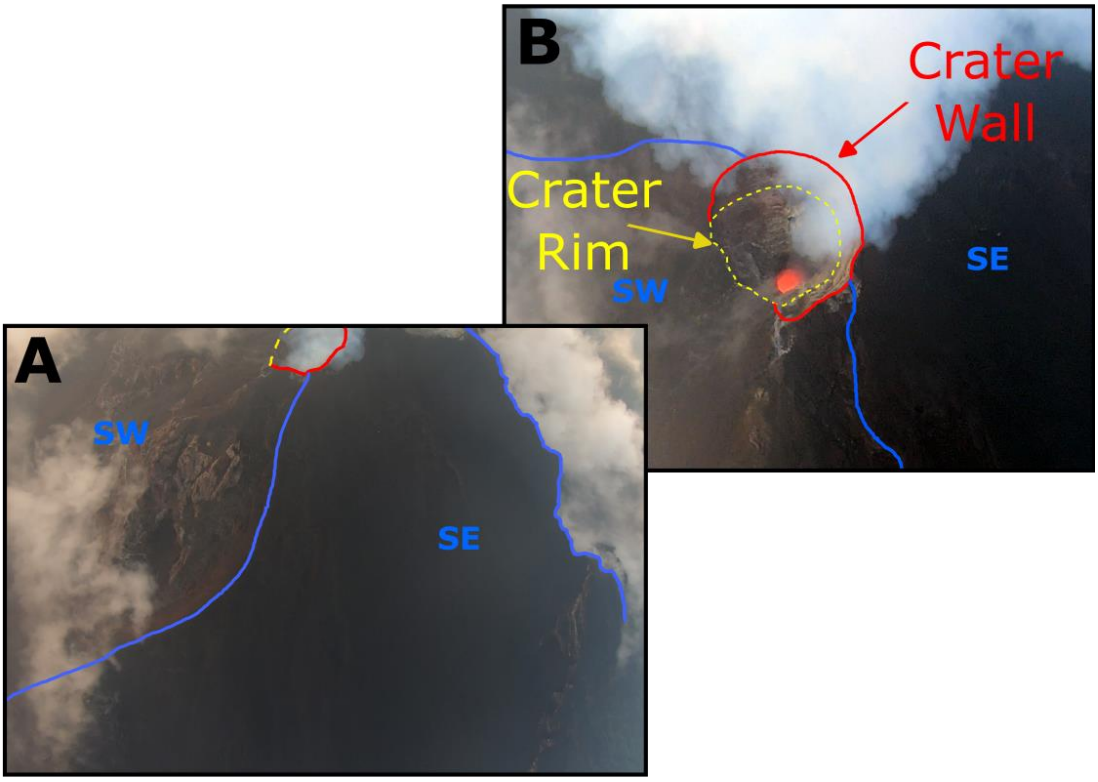

Figure 4.7 Fixed-wing drone overpass imagery of South Crater from 22 May 2019 (Courtesy of E. Nicholson). Red line indicates the high crater wall that runs from the west side all the way round to the south side. The crater wall is lower on the southwest side and is indicated here as the "crater rim" to differentiate the two. A – View of the southwest and southeast valley heads below South Crater looking approximately westward. B – Nadir view of the South Crater where incandescent lava can be seen.

4.2.2.3 Southeast Valley Vents

The most detailed description of the vent that has periodically opened up at the head of the southeast valley places it between 400-500 yards (365-457 m) below the rim of South Crater (Branch 1965). Hereafter, this vent is referred to as the "Southeast Valley Head Vent". Using QGIS, a band representing where this vent could reopen was drawn below the South Crater rim. Areas on the steep valley walls were removed and the band was divided into a northern and southern section so that the potential flow paths from these two different areas could be compared. These two areas will be modelled as surface areas to represent the uncertainty in the exact location the vent will open.

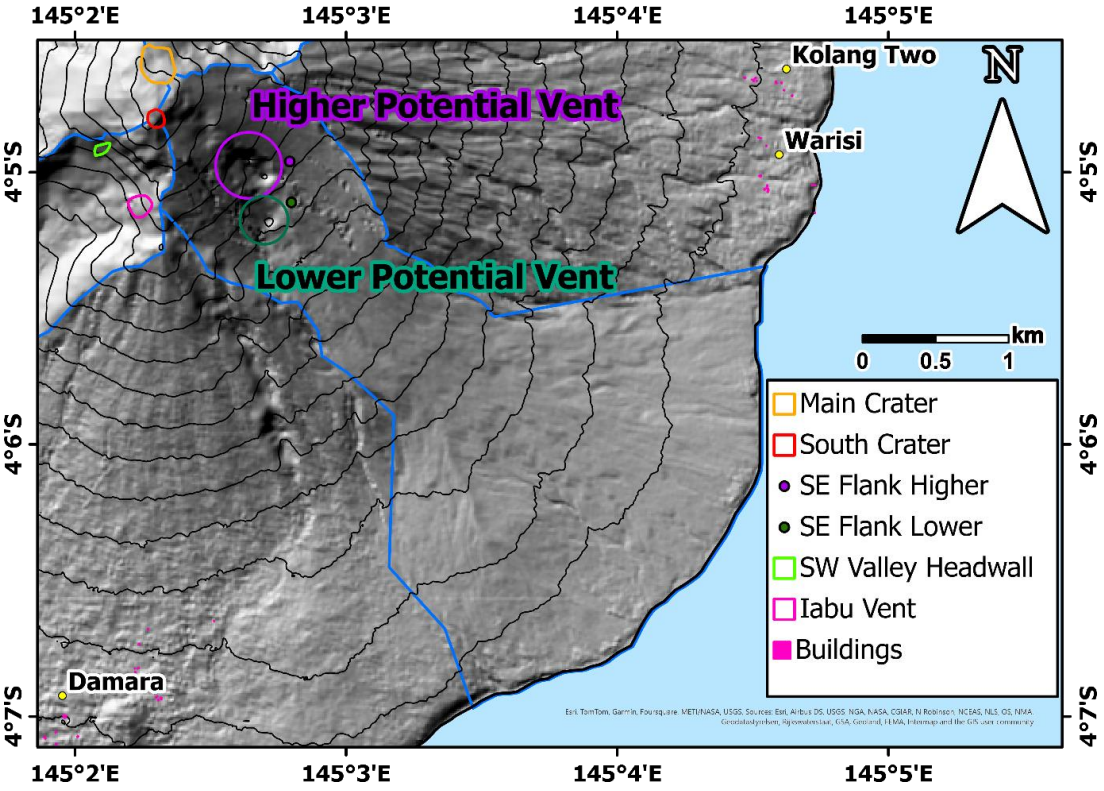

Figure 4.8 Hillshade map of Manam's southeast valley. The two coloured rings indicate the two depression features in the mid to upper valley that are potential locations for the flank vents that opened in 2012 and 2013 (Global Volcanism Program 2013).

Reports that vents opened somewhere in the southeast valley in 2012 and 2013 (Global Volcanism Program 2013) are vague and do not provide any positional information. However, when examining the 12 m resolution TanDEM-X DEM (Krieger et al., 2007; Rizzoli et al., 2017), two depressions can be seen within the southeast valley at 1000-1150 m asl and 1150-1250 m asl (**Figure 4.8**). These depressions are assumed to be the approximate location of the 2012-2013 "missing" vents for the purpose of hazard assessment, and are named the Higher and Lower Southeast Flank Vents. They are modelled as point sources ~100 m to the northeast (**Figure 4.5**) in order to model a worst case scenario of vents opening at a similar elevations without being influenced by the depressions highlighted in **Figure 4.8**.

4.2.2.4 Southwest Valley Vents

In addition to South Crater, two sources of lava flows mentioned throughout the literature that are here referred to as the Iabu Vent and the Southwest Headwall Vent. However, the exact positions of these two vents are not given (Global Volcanism Program 1992e, 2013). It is assumed that to be given the name Iabu Vent, the source must be close to Iabu Rock on the boundary of the southwest and southeast valleys (**Figure 4.4 & Figure 4.5**). Therefore, an area below Iabu Rock on the eastern headwall of the valley was selected to represent Iabu Vent. The vent itself was modelled as a surface area source to include the uncertainty of the exact location but also to present the wider potential of vents to form on this eastern side of the headwall. The Southwest Headwall Vent is modelled as a surface area source corresponding to the shortwave infrared hotspot partially obscured by the gas plume emanating from South Crater on 14 July 2017 (**Figure 4.9**).

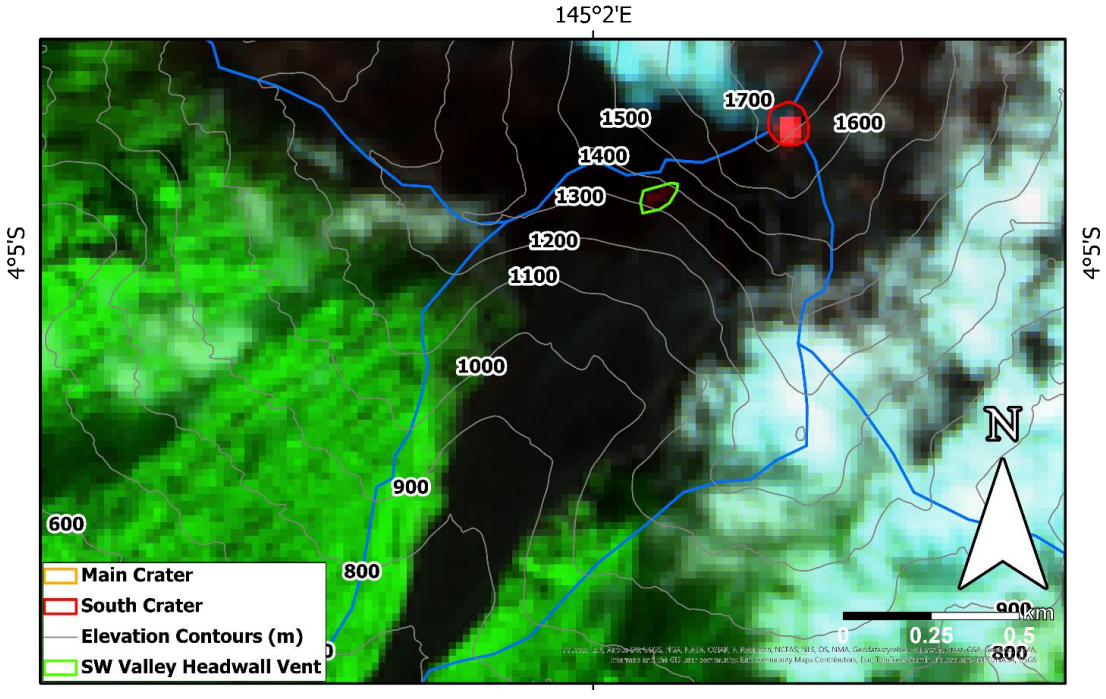

Figure 4.9 Sentinel-2 MSI shortwave infrared imagery on 9 December 2017 showing the location of the recurring faint hotspot on the headwall of the south valley.

4.2.2.5 Satellite Cones

Satellite cones are formed by dykes propagating either: a) laterally away from a magma-filled conduit (common at persistently-degassing open-vent volcanoes, and known as L-type dykes; Acocella and Neri, 2009; Harp and Valentine, 2018) or b) sub-vertically from a source beneath the volcano (associated with closed conduit systems with a lack of summit activity, known as V-type dykes; Acocella and Neri, 2009; Harp and Valentine, 2018). Given Manam's persistent open vent activity throughout historical records it is likely that the five satellite cones were formed by L-type dykes. However, the satellite cones are undated and therefore it is unclear whether they formed during Manam's current open vent state or in a period of where it the vent may have been closed, and thus the cones may more likely have been formed by V-type dykes. Dykes propagate parallel to the maximum compressive stress (Gudmundsson 2005; Tibaldi 2015; Di Vito et al. 2016), which at Manam would likely be controlled by the vertical loading of the edifice itself on the crust below. Dykes directly beneath the main edifice would therefore preferentially propagate laterally away from the conduit unless the loading stress changes (Kervyn et al. 2009). Where the load is approximately circular, dykes typically will propagate radially and, where they reach the surface, produce cones in a ring away from the central cone (Di Vito et al. 2016).

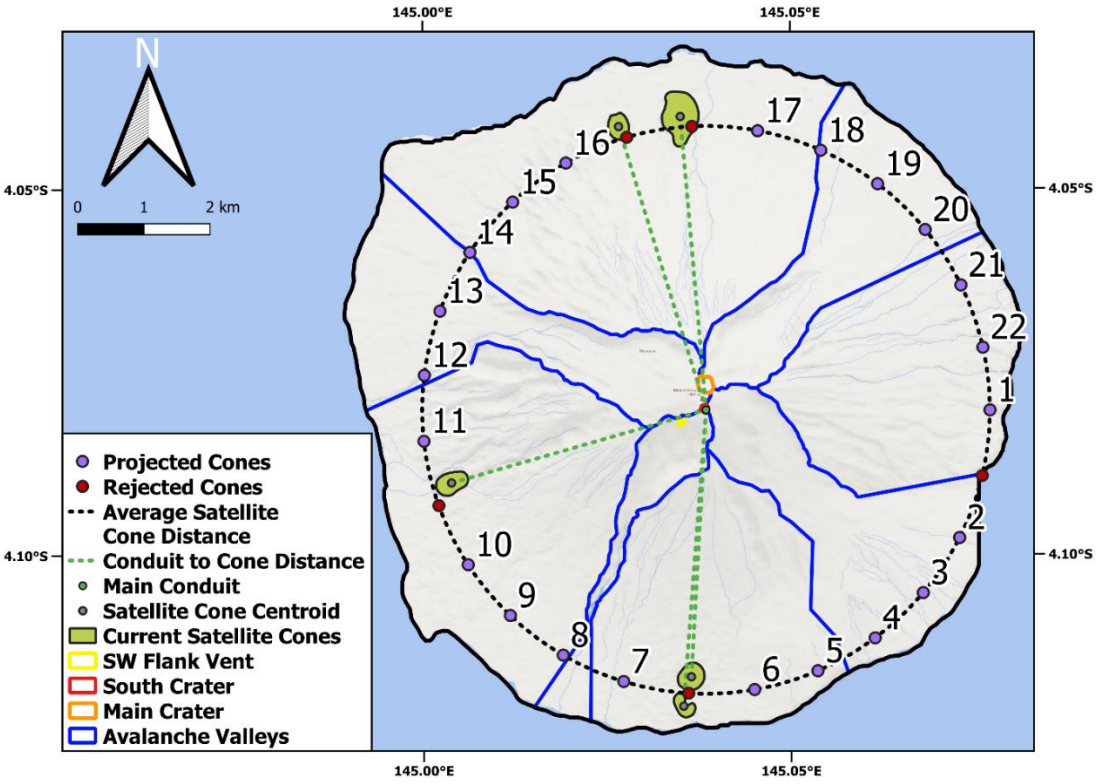

Figure 4.10 Locations of the projected satellite cones. The green dashed lines were used to measure the distance between the South Crater (assumed location of the central conduit) and the centre of the current satellite cones. The average distance of these were used as the radius to draw the black dashed circle to show the calculated mean distance from the central conduit. Projected satellite locations (purple dots) were placed at 1 km intervals along this circle. Those overlapping or close to current cones were removed (see main text) as was one point in the sea.

Given most activity historically has been centred at South Crater, it likely represents the approximate location of the central conduit and the five existing satellite cones are all a similar distance from this crater, with a range of 4-4.5 km (mean = 4.3 km). Given Manam's symmetrical circular shape, it may be that the stresses caused by the load of the central edifice produces a compressive stress trajectories which causes dykes to reach the surface at a radial distance of approximately 4.3 km from the central conduit. Therefore, in order to represent the potential for flank eruptions at similar distances to the existing satellite cones, lava flows were modelled at "projected cones" placed at 1 km intervals around a ring with a 4.3 km radius (**Figure 4.10**). Emplaced dykes enhance the strength of the surrounding rock impeding the ability of later dykes to propagate along a similar paths to the initial

dyke, known as the piling effect (Yokoyama 2015). Therefore projected cones that fell within or close to the current cones were discounted as it is more likely for new vents to open away from previously emplaced cones. One projected cone fell within the ocean and was discounted as *Q-LavHA* is not capable of modelling sub-marine eruptions (**Figure 4.10**).

4.2.3 Initial Input Parameter Selection

This section describes the process used to determine the input parameters for modelling Manam's lava flows using the *FLOWGO* lava flow length constraint method within *Q-LavHA*. Firstly, the methods are described for estimating or calculating effusion rate, initial viscosity, phenocryst mass fraction, channel ratio, eruption temperature, dense rock equivalent (DRE) density and vesicularity. Secondly, sensitivity testing is used to determine how well the chosen parameters replicate two recent flows in the northeast valley and whether other values for these parameters would be more appropriate. The final parameters and scenarios for modelling are then presented.

wt. %	Sample 1	Sample 2	Sample 3	Sample 4	Sample 5	Sample 6	Sample 7	Sample 8	Sample 9	Sample 10	Sample 11	Mean
SiO_2	53.9	53.05	52.7	51.1	51.01	51.19	51.96	52.42	52.6	53.5	53.93	52.49
TiO_2	0.38	0.35	0.37	0.58	0.35	0.39	0.3	0.33	0.37	0.49	0.35	0.39
Al_2O_3	16.6	13.9	17	16.65	17.05	15.39	14.74	15.59	16.9	16.6	17.02	16.13
Fe_2O_3	4.9	6.07	4.45	4.98	4.78	4.01	3.34	4.04	4.6	4.4	4.55	4.56
FeO	3.9	3.99	4.4	4	4.6	5.29	5.19	4.7	4.1	3.95	3.7	4.35
MnO	0.17	0.16	0.17	0.16	0.18	0.17	0.17	0.17	0.16	0.16	0.15	0.17
MgO	6.7	8.6	6.8	6.8	6.63	7.83	9	7.89	6.7	6.4	5.7	7.19
CaO	10.5	10.68	0.75	10.6	11.31	11.76	11.28	11.2	10.7	9.7	10.29	9.89
Na_2O	2.4	2.57	2.5	4.25	2.41	2.44	2.37	2.41	2.65	2.75	2.66	2.67
K_2O	0.69	0.9	0.66	0.88	0.55	0.63	0.6	0.62	0.73	1.03	0.83	0.74

P_2O_5	0.12	0.25	0.11	0.19	0.12	0.13	0.1	0.11	0.12	0.2	0.15	0.15
H_2O+	0.06	-	0.08	-	0.41	0.42	0.52	0.09	0.04	0.41	0.22	0.25
H_2O-	0.07	-	-	-	0.07	0.01	0.13	0.03	0.04	0.14	0.04	0.07
CO_2	0.05	-	0.02	-	0.05	-	-	0.05	0.05	0.05	0.05	0.05
S	**-**	-	-	-	-	-	-	-	0.01	0.01	-	0.01

Table 4.1 Bulk rock compositional analysis of Manam lava samples. Sample 1 – Lava from South Crater, January 1957 (Morgan, 1966, specimen 6), Sample 2 – Lava from Main Crater, 1957/58 (Morgan, 1966, specimen 6), Sample 3 – Lava from unknown crater, 1962 (Morgan, 1966, specimen 19), Sample 4 – Lava from South Crater, April 1964 (Branch 1967), Sample 5 – Lava flow in stream bed near Warisi (McKee, 1981, registered sample 75710007), Sample 6 – Lava flow at southeast coast forming part of low-profile, grass-covered hill (McKee, 1981, 78710015), Sample 7 – Lava flow at coast north of Godagi cone (McKee, 1981, 78710009), Sample 8 – December 1974 lava flow in southeast valley (McKee, 1981, 74710013), Sample 9 – Lower 1964 lava flow in upper part of southeast valley, (McKee, 1981, 74710028), Sample 10 – Lava flow near Iassa cone (McKee, 1981, 78710030), Sample 11 – 1946-47 lava flow in southeast valley, north lobe at coast (McKee, 1981, 78710014)

4.2.3.1 Lava Temperature, Density, Viscosity and Phenocryst Mass Fraction

Eruption Temperature

The eruption temperature of lava is classed as an advanced *FLOWGO* input parameter within the *Q-LavHA* user interface and was also used here to calculate initial viscosity and density. The temperature was calculated from lava composition using a simplified method requiring only the liquid MgO content (Putirka 2008) (**Equation 4.7**):

$$\boldsymbol{T(^{\circ}C) = 26.3\ MgO^{liq} + 994.4^{\circ}C} \qquad \textit{(4.7)}$$

Mean bulk rock MgO content was used as a proxy for the unavailable liquid MgO content. The value of 7.19 wt%, from **Table 4.1** for $\boldsymbol{MgO^{liq}}$ yields a temperature of 1183 ± 71°C (this error is a standard error of estimate calculated by Putirka (2008)). This value falls within the ranges of eruption temperatures for basalts (1050-1200°C) and andesites (950-1170°C) (Kilburn 2000) and given Manam's lavas are generally classified as basaltic to basaltic-andesite (Cooke et al. 1976; Palfreyman and Cooke 1976; McKee 1981) this value is taken as the eruption temperature input parameter value throughout this chapter.

Density

The method of Bottinga and Weill (1970) was used to calculate the DRE bulk density of the lava on eruption. Using the mean compositions of Manam lavas in **Table 4.1**, the calculated eruption temperature of 1183°C, and a pressure of 0.1 MPa (approximately atmospheric pressure) gives a density of 2640 kg/m^3.

Initial Viscosity

Initial viscosity was calculated using the model proposed by Giordano et al. (2008), based on the eruption temperature of 1183°C and the mean composition of Manam lavas in **Table 4.1**. Given these inputs the model calculates the viscosity of Manam's lava as 44 ± [6, 860] Pa·S.

Initial Phenocryst Mass Fraction

The seven lava samples compiled by McKee (1981) (samples 5-11, **Table 4.1**) are the only samples with reported phenocrysts volume fraction (**Table 4.2**). We convert the total PVF to total phenocryst mass fraction using **Equation 4.8**.

$$\boldsymbol{PMF = \frac{Mean\ Crystal\ Density}{Total\ Melt\ Density} \times PVF} \qquad \textbf{(4.8)}$$

Typical densities of the phenocrysts were used as reported by Deer et al. (2013) and a representative mean density for opaques was calculated from the densities of commonly occurring opaque crystals in mafic rock *(Wilson 1989)*. The phenocryst densities used are shown in **Table 4.3**. The calculated phenocryst mass fraction of the halted lava was 0.41. *FLOWGO*, however, requires the initial phenocryst mass fraction and so the value calculated here is used as a basis for the parameter sensitivity testing in section 4.2.4.2 from which final input parameters are determined.

Phenocryst volume fraction (%)	Sample 5	Sample 6	Sample 7	Sample 8	Sample 9	Sample 10	Sample 11	Mean
Plagioclase	21	31	9	14.5	23.5	21	13.5	19.07
Olivine	2.5	4.5	3	2.5	1.5	2.5	1	2.50
Orthopyroxene	0.5	0.5	0.5	0.5	0	0.5	0.5	0.43
Clinopyroxene	7.5	15.5	16	11	8.5	8	3.5	10.00
Opaques	0.5	1	0.5	0.5	0.5	0.5	0.5	0.57
Total	32.00	52.50	29.00	29.00	34.00	32.50	19.00	32.57

*Table 4.2 Phenocryst volume fractions of Manam lavas (McKee 1981). Sample numbers correspond to those given in Table 4.1****Error! Reference source not found.****.*

Phenocryst	Typical Density (kg/m^3)
Plagioclase	**2620**
Olivine	**3222**
Orthopyroxene	**3210**
Clinopyroxene	**3375**
Graphite (Opaque)	2260
Magnetite (Opaque)	5170
Ilmenite (Opaque)	2400
Pyrite (Opaque)	5000
Pyrrhotite (Opaque)	4610
Chalcopyrite (Opaque)	4190
Opaques Mean	**4316**

Table 4.3 Typical densities of phenocrysts present in McKee (1981) lava samples as reported by (Deer et al. 2013). A mean density for opaque phenocrysts was calculated using the densities of common opaque crystals in mafic rocks (Wilson 1989).

4.2.3.2 Channel Ratio

To calculate the channel ratio for lava flows at Manam requires knowledge of the width of lava flow channels and the height or thickness of the flow. The height of the September & October 2018 northeast valley lava flows is calculated to be ~3.5 m using a 3D orthomosaic model generated from UAS imagery (see Chapter 2). The widths of lava flows were estimated from a simple method based on that used by Dietterich and Cashman (2014) to determine the morphology of lava flow networks. The morphological features (e.g. the flow extent and levees) are digitised into a geographical information system (GIS). Centre lines are then generated through the flow and every ten metres a transect is drawn through the centre line to the levees. This enables a width profile along the flow of the channel to be produced.

Ideally lava flows are digitised in using an ultra-high resolution DEM that allows the identification of the levees. Unfortunately no such DEM exists for Manam other than for the lower portion of the September & October 2018 lava flow. Here we use a combination of the digitised lava flow maps from McKee (1981) (**Figure 4.1**) and the four lava flows mapped from shortwave infrared Sentinel-2 MSI and Landsat 8 Operational Land Imager (OLI) satellite imagery (see Chapter 2) (**Figure 4.2**). It is recognised that utilising McKee's map (1981) adds an unquantifiable element of uncertainty to the measurements. The uncertainty of measurements based on satellite imagery is directly related to the pixel resolutions: MSI and OLI shortwave infrared imagery resolutions are 20 and 30 m respectively. Therefore, flows digitised from these satellites have a maximum potential error equal to the pixel resolution of the platform and imagery were used. Levees were not marked on

McKee's map (1981) and is difficult to identify the levees in the satellite imagery. Instead, the whole channel width was measured (**Figure 4.11**) and therefore strictly the flow extent ratio is calculated, which is used as proxy for the channel ratio. Transect lines were generated every 10 m along the centre line but transect lines were discounted if they a) intersected another transect, which was often due to a small meander along a centre line, or b) crossed two centrelines which would represent a bifurcation of the flow and so would result in an exaggerated channel width here as the levees cannot be identified. The range of mean channel widths per flow was 29-404 m and a mean lava flow width for all Manam flows is 159 m, resulting in a channel ratio of 45.

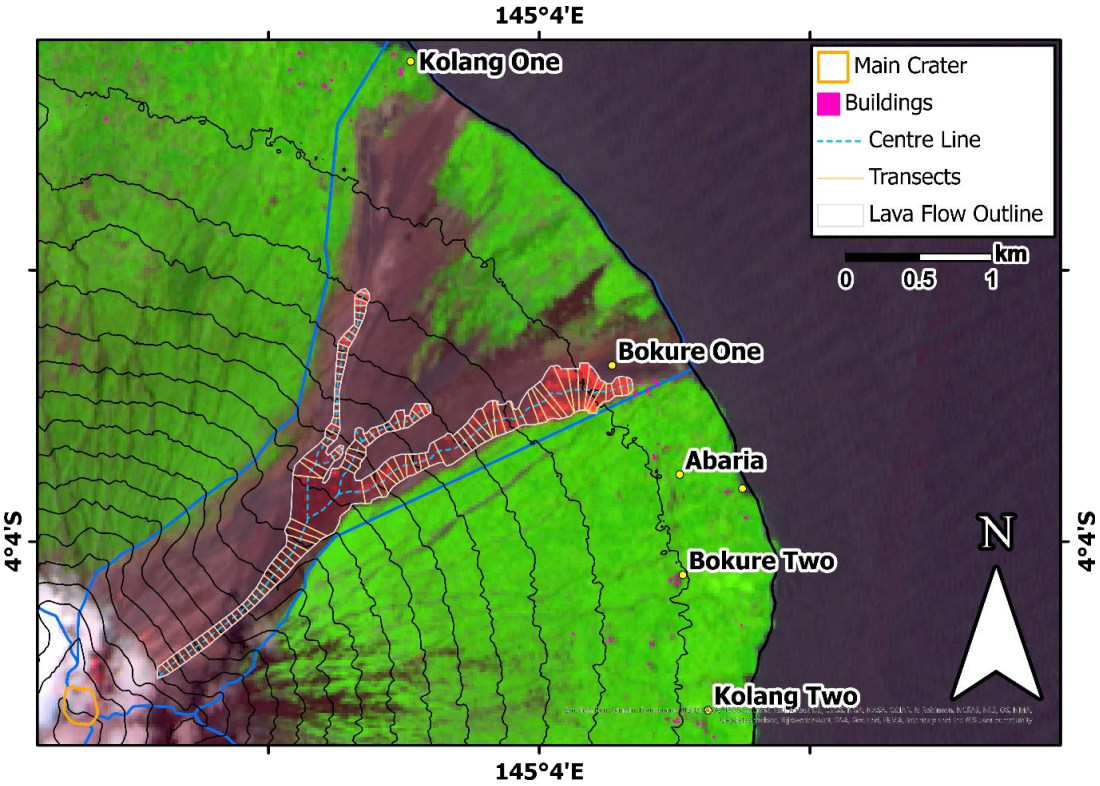

Figure 4.11 Example of the flow width measurement method used to calculate the channel ratio input parameter for the FLOWGO lava flow length constraint method in Q-LavHA. In this exampled the 25 September – 10 October 2018 lava flow extent was digitised (light grey outline) using QGIS from Sentinel-2 MSI SWIR imagery (02/10/2018). Centre lines (light blue) were generated from the extent and transects were drawn every 10 m. The average lengths of these transects was used as the average width of the lava flow. The channel ratio was calculated using an average 3.5 m thickness.

Lava Flow (Mapping Source)	Mean Width (m)	Channel Ratio
Northeast Valley 1958 ***(McKee 1981)***	178	51
Northeast Valley 1960 ***(McKee 1981)***	128	37
Northeast Valley October 2018 ***(S2 MSI SWIR)***	125	36
Northeast Valley January 2019 ***(L8 OLI SWIR)***	217	62
Northeast Valley June 2019 ***(S2 MSI SWIR)***	264	76
Northeast Valley August 2019 ***(S2 MSI SWIR)***	120	34
Southeast Valley 1964a ***(McKee 1981)***	65	18
Southeast Valley 1964b ***(McKee 1981)***	79	22
Southeast Valley 1966a ***(McKee 1981)***	133	38
Southeast Valley 1974a ***(McKee 1981)***	79	23
Southeast Valley 1974b ***(McKee 1981)***	65	19
Southeast Valley 1974c ***(McKee 1981)***	46	13
Southeast Valley 1974d ***(McKee 1981)***	29	8
Southeast Valley 1946a ***(McKee 1981)***	248	71
Southeast Valley 1946b ***(McKee 1981)***	189	54
Northwest Valley A ***(McKee 1981)***	132	38
Northwest Valley B ***(McKee 1981)***	144	41
Northwest Valley C ***(McKee 1981)***	404	115
Southwest Valley A ***(McKee 1981)***	349	100
Southwest Valley B ***(McKee 1981)***	163	47
Mean	**159**	**45**

Table 4.4 Mean lava flow widths and channel ratios

4.2.3.3 Effusion Rate

Lava flow effusion rates have not been published for Manam and so this parameter must be estimated. A compilation of effusion rates from mafic lava flows (**Appendix D, Table 7.1**) was used to determine appropriate effusion rate scenarios. The range and means for historic lava flows originating from summit, flank, fissure and satellite cone type vents **Table 4.1** shows that effusion rates range over 4 orders of magnitude (10^{-1}–10^{2} m^3 s^{-1}).

Vent Type	Min Effusion Rate (m^3 s^{-1})	Mean Effusion Rate (m^3 s^{-1})	Max Effusion Rate (m^3 s^{-1})
Summit	0.07	2	10
Flank	0.04	60	800
Fissure	8	132	374
Satellite Cone	1	30	80
All	**0.04**	**43**	**800**

Table 4.5 Summary table for effusion rates of mafic lava flows. See Appendix D for full table of lava flow effusion rates used here.

The three scenarios chosen for this study are based on the mean summit effusion rate (2 m^3 s^{-1}) (**Table 4.1**) across the three largest orders of magnitude yielding effusion rate scenarios of 2 m^3 s^{-1}, 20 m^3 s^{-1}, and 200 m^3 s^{-1}. The mean summit effusion rate is used as the basis of the scenarios as most of Manam's lava flows originate from summit vents (Palfreyman and Cooke 1976; McKee 1981; Global Volcanism Program 2024). The same effusion rates scenarios were used so that all modelled flows from all vent types would be easily compared whilst ensuring that

the range of modelled effusion rates encapsulates the potential of all vent types. The three scenarios representing best to least to worst case scenarios from a hazard assessment perspective.

4.2.4 Parameter Testing

Q-LavHA is able to calculate three fitness indexes (FI), which assess the accuracy of a simulated lava flow by comparing it to a historical flow of known extent. The overlapping area between the simulated flow and the historical flow ($\boldsymbol{FI_{true\ positive}}$) is calculated by **Equation 4.9** (Mossoux et al. 2016):

$$\boldsymbol{FI_{true\ positive}} = \frac{\boldsymbol{A_s \cap A_r}}{\boldsymbol{A_s \cup A_r}} \qquad \textbf{(4.9)}$$

where $\boldsymbol{A_s}$ is the area covered by the simulated flow and $\boldsymbol{A_r}$ is the area covered by the real flow. $\boldsymbol{FI_{true\ positive}}$ varies between 0 and 1 where values closer to 1 represent a greater overlap between the simulated and real flows. To determine whether the discrepancy between the simulated and real flows is due to overestimation or underestimation by the simulation requires calculating the $\boldsymbol{FI_{false\ positive}}$ (**Equation 4.10**) and $\boldsymbol{FI_{false\ negative}}$ (**Equation 4.11**) respectively (Mossoux et al. 2016):

$$\boldsymbol{FI_{false\ positive}} = \frac{\boldsymbol{A_s - (A_s \cap A_r)}}{\boldsymbol{A_s \cup A_r}} \qquad \textbf{(4.10)}$$

$$\boldsymbol{FI_{false\ negative}} = \frac{\boldsymbol{A_r - (A_s \cap A_r)}}{\boldsymbol{A_s \cup A_r}} \qquad \textbf{(4.11)}$$

The composite score (CS) (**Equation 4.12**) enables the fits of different simulated lava flows to be compared by giving more importance to high $\boldsymbol{FI_{true\ positive}}$ values and

very low $\boldsymbol{FI_{false\ negative}}$ values. A simulated flow that perfectly matches a real flow would have CS equal to 100 (Mossoux et al. 2016).

$$\boldsymbol{CS = FI_{true\ positive} \times (1 - FI_{false\ positive})^{1/2}) \times (1 - FI_{false\ negative})^{2}) \times 100} \qquad \textbf{(4.12)}$$

The *Q-LavHA* sensitivity testing function was used to test the initially selected input parameters (described in the section 4.2.4.1) in conjunction with the fitness indexes to determine whether any adjustments to the input parameter values should be made for the final modelling. The sensitivity testing function allows one parameter to be varied by a regular value inclusive of and between a minimum and maximum value, while holding all other parameters as constants. This testing was performed against effusion rate (between 10 and 100 $m^3\ s^{-1}$ at 10 $m^3\ s^{-1}$ intervals and between 100 and 1000 $m^3\ s^{-1}$ at 100 $m^3\ s^{-1}$ intervals), channel ratio (10-50 in intervals of 10), initial viscosity (between 50 and 1000 Pa·s in 50 Pa·s intervals), phenocryst mass fraction (0.05-50 in intervals of 0.05) and threshold (0.01-0.2 in intervals of 0.01). Threshold is a *Q-LavHA* value that allows the user to discount any pixels with a probability below the given threshold from being included in the final output, for example a threshold of 0.05 would discount any pixels with a 5% probability of lava inundation from being included in the final results.

4.2.4.1 Digital Elevation Model Testing

Using the most recent digital elevation model (DEM) is critical to accurate modelling and forecasting of lava flows because changes in topography may alter the flow direction of lava (Tarquini and Favalli 2010). The spatial resolution of a DEM has also been shown to impact the modelled runout length when using *FLOWGO* to

constrain the runout length in *Q-LavHA* (Rodriguez-Gonzalez et al. 2021). On steep slopes runout distances are shown to be closer to true lengths on coarser resolution DEMs, whereas on shallower slopes higher resolution DEMs more closely replicate the true runout distance (Mossoux et al. 2016). Therefore, two different resolution DEMs were tested alongside the sensitivity testing of the input parameters to find the best combination for replicating Manam's lava flows. The TanDEM-X 12 m resolution DEM (the data for which was acquired in 2015; Krieger et al., 2007; Rizzoli et al., 2017) and the ASTER GDEM v3 30 m resolution DEM (constructed with imagery from 2000-2013; Abrams et al., 2022, 2020) are both tested. While neither of these DEMs represent current topography given numerous lava effusion events since their acquisition dates, they are, especially in the case of TanDEM-X, the most recent high resolution DEMs available for Papua New Guinea.

4.2.4.2 Final Parameter Selection

The initial parameter selections and the two DEMs were tested against the September-October 2018 and the January 2019 lava flows (**Figure 4.1**). These are the two of the most recent lava flows mapped as part of this project in the northeast valley and have come within 1 km of the coast. Both were used for parameter testing because they represent two possible flow paths down the northern (January 2019) and southern sides (September and October 2018) of the upper valley. Overall the composite scores across the different parameters are low with maximum scores ranging between 15 and 20. These low scores are likely to be a result of a) the fitness index methodology which looks for the difference in the cumulative area covered by the model flows and the real flow b) the shape of the

two previous flows used for testing. The *Q-LavHA* propagation method enables lower probability initial flow paths to be simulated meaning that many potential flow routes are modelled. Where topography does not constrain the initial flow paths it is to be expected that fitness index values are produced because the modelled flows are able to flow in many directions but also do not spread.

Specifically in this testing, the wide northeast valley has many potential flow paths but the two test flows have an initially narrow channel until reaching shallower parts of the valley where upon they spread and bifurcate. Therefore the 5,000 iterations produce many flows that take routes outside the real flow extents and thus the cumulative modelled flows have a high level of high overestimation ($\boldsymbol{FI}_{\boldsymbol{false\ positive}}$) in the upper reaches of the valley. As *Q-LavHA* does not model the spreading of flows, the relatively few modelled flows that do reach the lower coastal areas appear to underestimate compared to the real flows resulting in low $\boldsymbol{FI}_{\boldsymbol{true\ positive}}$ scores. Therefore these discrepancies in both the upper and lower parts of the valley result in low composite scores. However given these explanations it is still of merit to compare the composite scores across the two DEMs and the different values within each parameter.

Generally across all parameters tested the TanDEM-X 12 m resolution DEM produces higher composite scores compared to the ASTER GDEM 30 m resolution DEM (**Figure 4.12**). The only exceptions to this are at channel ratios of 15-25 and at effusion rates of 350-550 m^3s^{-1} for the January 2019 flow. The TanDEM-X 12 m DEM produces higher composite scores for the September and October 2018 flow in all

parameters. Therefore it is clear that the higher resolution DEM is the preferred option the final modelling.

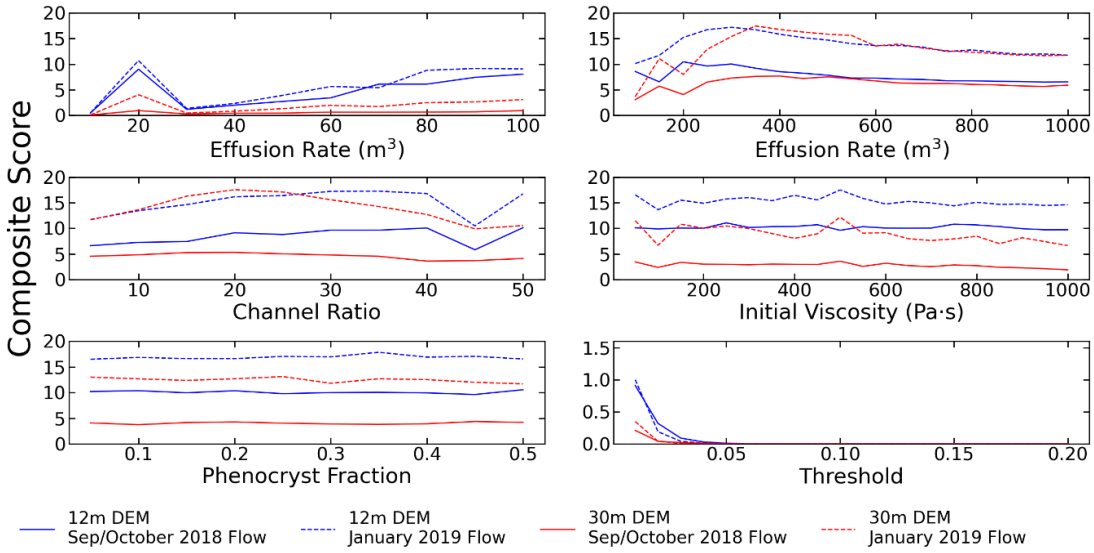

Figure 4.12 Q-LavHA composite scores representing best fits of simulated flows to real flows, the September & October 2018 flows and the January 2019 flow. Composite scores range between 0-100 with 100 representing a perfectly replicated flow.

The effusion rate sensitivity testing showed composite score peaks of ~10 for both flows in the 12 m DEM at 20 m^3s^{-1} and 200 m^3s^{-1} and has a score of 15 for the January 2019 flow that increases to 17 at 300 m^3s^{-1} (**Figure 4.12**). The effusion rate composite score peaks at 200 m^3s^{-1} for the September and October 2018. This therefore suggests that the two higher effusion rate scenarios (20 and 200 m^3s^{-1}) are appropriate for use in the final modelling of Manam's lava flows (**Figure 4.12**). The lowest effusion rate scenario (2 m^3s^{-1}) will also be used as it represents a smaller event than those that seem to have produced the two test lava flows.

Composite scores for the channel ratio parameter show that the best fit is for the January 2019 lava flow using the 30m DEM at a ratio of 20 and also at a ratio of 30 for the 12 m DEM for the same flow (**Figure 4.12**). The calculated ratio of 45

produces the lowest composite scores for all flows across both DEMs (**Figure 4.12**). However, since this metric was directly measured and that the highest composite scores are relatively low overall (17) it was decided to keep the measured channel ratio of 45 for the final modelling.

The sensitivity testing for the initial viscosity shows that changing the viscosity between the tested values of 50 and 1000 makes relatively little difference (**Figure 4.12**). The highest composite scores across all lava flows were found at 50 Pa·s with a comparable peak at 500 Pa·s for the January 2019 flow tests (16 and 17 respectively) (**Figure 4.12**). Therefore, the calculated initial viscosity of 42 Pa·s was kept for the final modelling. Initial phenocryst mass fraction was shown to have very little impact on the composite scores of both flows across both DEMs when varied between 0.05 and 0.5 (**Figure 4.12**). As such, final modelling used the calculated phenocryst mass fraction of 0.41.

The threshold parameter testing showed that utilising this parameter drastically lowers the composite score for both flows and DEMs (**Figure 4.12**). This is due to the highly variable potential flow paths within the northeast valley, which itself lowers the range of inundation probabilities, in conjunction with the previously noted observation that higher resolution DEMs also increases the possible permutations of potential flow paths (Tarquini and Favalli 2010; Mossoux et al. 2016). Therefore, it was decided not to set a threshold value so that all potential flow paths can be viewed.

Parameter	Value	Source
Lava Flow Propagation		
H_c (m)	3.5	This Study
H_p (m)	10	(Global Volcanism Program 1992d)
P_i^2	Activated	
H_{16}	Activated	
Lava Flow Length Constraints		
Basic Parameters		
Effusion Rate ($m^3\ s^{-1}$)	2, 20, 200	This Study
Initial Lava Viscosity (Pa · s)	42	This Study – (Giordano et al. 2008)
Initial Phenocryst Mass Fraction	0.41	McKee (1981)
Channel Ratio (width/depth)	45	This Study
Advanced Parameters		
Thermal Parameters		
T(eruption) (°C)	1183	This Study (Putirka 2008)
T(crust) (°C)	500	(Mossoux et al., 2016)
Offset (°C)	160	(Mossoux et al., 2016)
d (constant)	-0.16	(Mossoux et al., 2016)
Viscosity & Elasticity		
a (1/K)	0.04	(Dragoni 1989)
b (Pa)	0.01	(Dragoni 1989)
c (1/K)	0.08	(Dragoni 1989)
Convection Parameters		
Wind Speed ($m\ s^{-1}$)	5	(Mossoux et al., 2016)
Ch (related to the friction wind speed)	0.0036	(Mossoux et al., 2016)
T(air) (°C) (ambient air temperature)	20	(Mossoux et al., 2016)
Density (air) ($kg\ m^{-3}$)	0.4412	(Mossoux et al., 2016)
Specific Heat Capacity (air) (J/kg · K)	1099	(Mossoux et al., 2016)
Velocity Constant		
Gravity (m/s^2)	9.81	(Mossoux et al., 2016)
Lava Density & Vesicularity		
DRE Density ($kg\ m^{-3}$)	2640	This Study - (Bottinga and Weill 1970)
Vesicularity	0.18	This study
Crystal Parameters		
Growth Rate	0.0027	(Mossoux et al., 2016)
L (J/kg) (latent heat of crystallization)	350000	(Mossoux et al., 2016)
R (inverse of maximum solid fraction)	1.51	(Mossoux et al., 2016)
Radiation Parameters		
Stefan-Boltzmann Constant ($W/m^2 \cdot K4$)	5.67×10^{-8}	(Mossoux et al., 2016)
Emissivity	0.95	(Mossoux et al., 2016)
Conduction Parameters		
Thickness of Lava Crust (%)	10	(Mossoux et al., 2016)
T (base of lava crust) (%)	700	(Mossoux et al., 2016)
Lava Thermal Conductivity (W/ m · K)	2.5	(Mossoux et al. 2016)

Table 4.6 Final input parameters for Q-LavHA modelling of Manam lava flows using the FLOWGO lava flow length constraint method. Q-LavHA defaults can be found in (2016)

All final modelling parameters are given in **Table 4.6**. Of note are the *Thermal Parameters* T(crust), (°C) Offset (°C), and d (constant) which describe the thermal insulation efficiency of the lava flow (Harris and Rowland 2001). These defaults given by Q-LavHA (Mossoux et al. 2016) describe a lava flow that is thermally inefficient at retaining heat that would result in much shorter runouts than those that have a continuous crust (i.e. those with no or few cracks) which are responsible for the majority of heat loss from a lava flow. This should be kept in mind when viewing the modelled lava flow results .

4.3 Results

The results of the *Q-LavHA* modelling are presented here, with specific attention on the lava flow runout distance and the proximity of the potential inundation areas to settlements. The results are organised according to the different vent scenarios, beginning first with the summit craters followed by the flank vents from the two southern valleys and finally the projected satellite cones. The modelled outputs show the probability of flows to inundate each pixel for a given effusion rate scenario. These probabilities are relative within each scenario and are not strictly comparable between scenarios. Hence, instead of being presented as absolute low to high probabilities, they are described as having lower or higher probabilities. The lava flow inundation probability maps are divided into five categories representing differing levels of relative probability: Lowest (>0% - <12.5%), Lower (≥12.5% - <25%), Moderate (≥25% - <37.5%), Higher (≥37.5% - <50%), and Highest (≥50%). The outputs as the sum of the trajectories (Mossoux et al. 2016) and the possible total area inundated and the maximum runout length are the key metrics for comparison

between scenarios. Maximum runout lengths are given as straight line distances in this section as the model outputs do not show individual modelled flows paths.

4.3.1 Main Crater

For an effusion rate of 2 m^3 s^{-1}, flows originating at Main Crater are likely to remain within the crater area or reach no lower than 1600 m asl in the northeast valley (**Figure 4.13**). The maximum runout distance of the modelled flows is ~580 m, reaching approximately 1350 m asl. In comparison, the 20 m^3 s^{-1} flows exhibit a moderate probability of reaching the maximum runout of distance of the 2 m^3 s^{-1} scenario (**Figure 4.13**). The maximum runout distance for a 20 m^3 s^{-1} flow is modelled at ~1800 m, reaching to 700 m asl. The 200 m^3 s^{-1} effusion rate scenario results show that, close to source, three flow paths are more likely than others, as outlined by the moderate to higher probability areas in **Figure 4.13**. These three preferred flow routes include: one path that flows down the southern side of the valley; a second that initially flows down the centre of the valley and then transitions to the north side between 900-1000 m asl; and a third that follows the centre route and then moves to the north side of the valley at 700 m asl (**Figure 4.13**). These three higher probability areas approximately correspond to the three flows emplaced in 2018-2019 (**Figure 4.2**). The maximum flow length for this highest effusion rate scenario is 4.8 km, reaching the coast, though very few flow paths reach the ocean and these have the lowest relative probability (**Figure 4.13**). Lava ocean entry it remains a potential high hazard scenario for the highest effusion rates. There are several flow paths that reach approximately 4 km, which closely replicates the runout distances of the mapped flows illustrated in **Figure 4.2**.

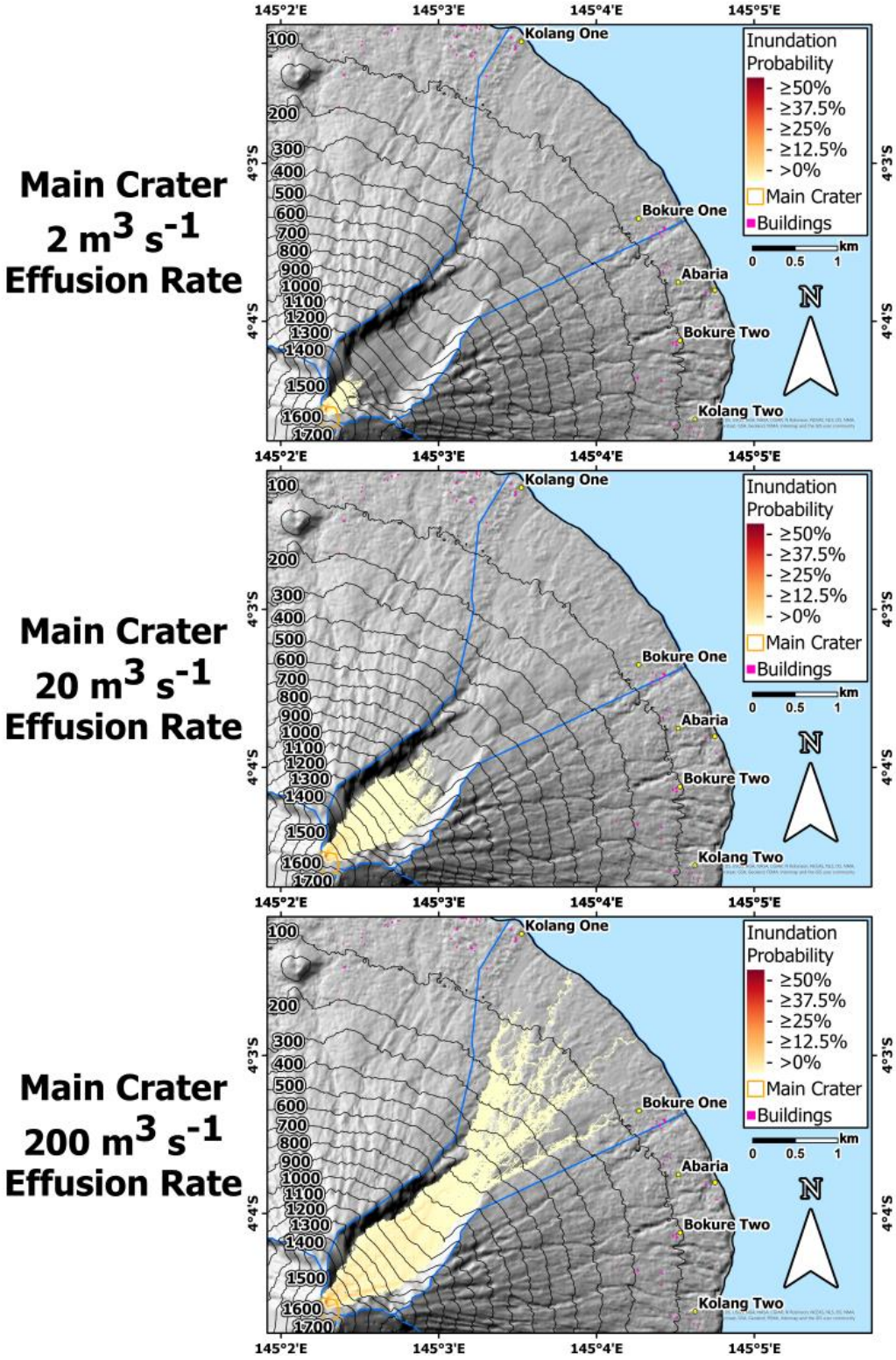

Figure 4.13 Results of the Q-LavHA modelling of lava flows from Main Crater at 20 m^3 s^{-1} (top), 20 m^3 s^{-1} (middle), and 200 m^3 s^{-1} (bottom) effusion rate scenarios.

4.3.2 South Crater

For a 2 m^3 s^{-1} effusion rate scenario from South Crater, it is most likely that lava flows would remain within the vent area (**Figure 4.14**). The maximum runout length for this scenario is ~130 m with flows capable of reaching to ~1650 m asl in the southeast, southwest and northwest valleys. Results for the 20 m^3 s^{-1} scenario show that the same three valleys could be affected. The pixel inundation probabilities in this scenario reveal three preferred flow paths. The first flows into the south east valley with a maximum runout length of ~630 m, reaching ~1300 m asl, and overrunning the postulated position of the southeast valley head vent area. The second path takes a fairly central route down the southwest valley headwall between the modelled locations of the southwest headwall and Iabu vents with a maximum runout of 600 m, reaching ~1250 m asl (**Figure 4.14**). The third route flows into the southern portion of the northwest valley but suggests that flows may potentially returning back into the southwest valley at around 1500 m asl, passing over the area of the southwest headwall vent with a maximum runout length of 630 m (**Figure 4.14**).

The 200 m^3 s^{-1} scenario at South Crater shows that the two southwest valley paths identified in the 20 m^3 s^{-1} scenario converge around 1000 m asl (**Figure 4.14**). Following this convergence, an area of higher inundation probability is shown in the centre of the valley between the steep valley walls, which converge at ~600 m asl. Longer runout flows are confined by these walls and the maximum flow length is ~1740 m, reaching to 700 m asl (**Figure 4.14**).

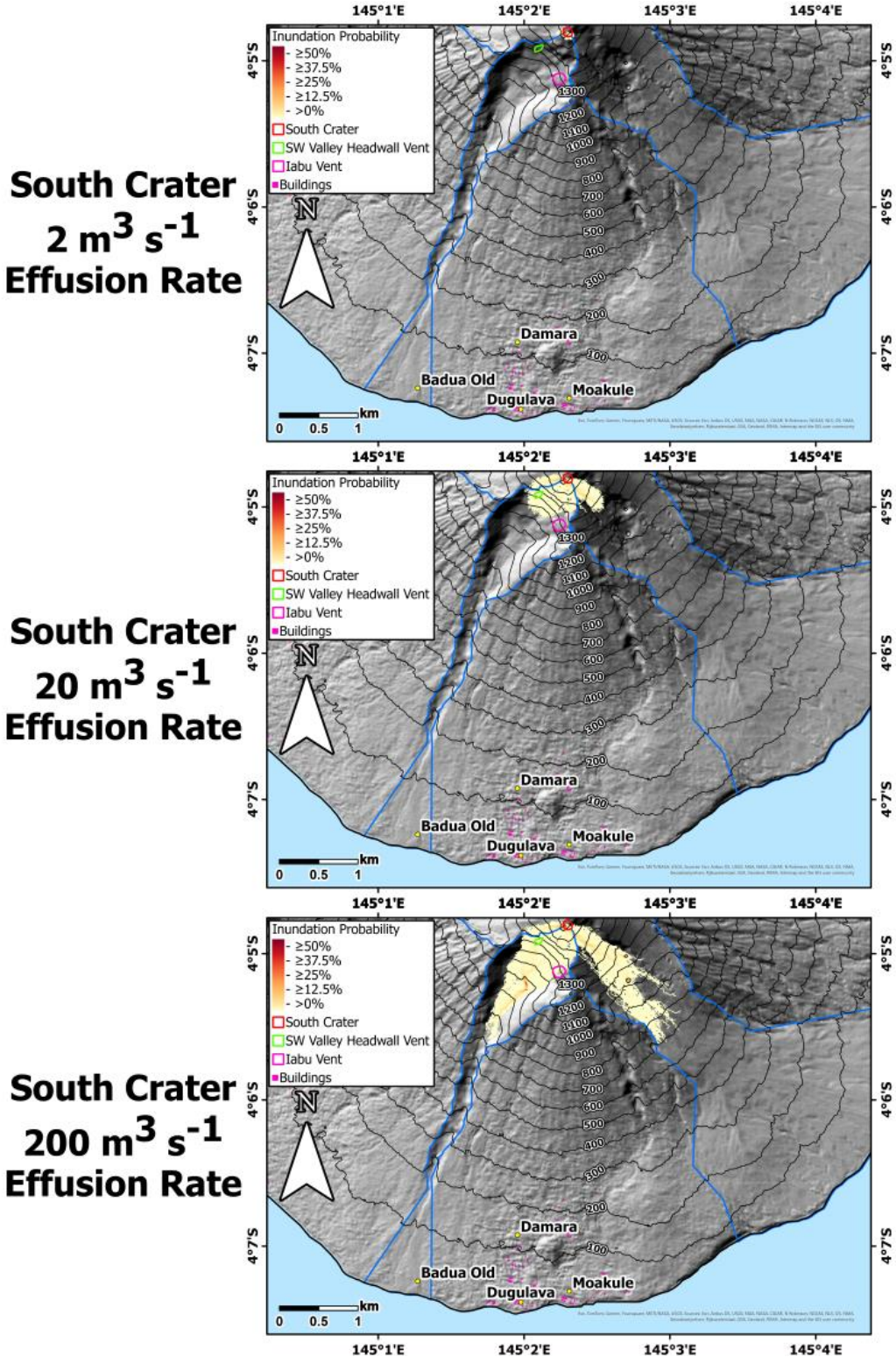

Figure 4.14 Results of the Q-LavHA modelling of lava flows from South Crater at 20 m^3 s^{-1} (top), 20 m^3 s^{-1} (middle), and 200 m^3 s^{-1} (bottom) effusion rate scenarios.

The flow paths that initially pass into the northwest valley indicate that the delineation of the northwest and southwest valleys is not an abrupt watershed and instead represents a transitional plateau area, as suggested by the flow paths in the 20 and 200 m^3 s^{-1} scenarios that return to the southwest valley.

The higher probability pixels in the southeast valley show that there is preferred path over the south sector of the headwall vent. Flow trajectories then become more variable below approximately 1350 m asl. Here, flows have higher probabilities to either move more northwards and flow into the higher of the two depressions, to maintain a central path and flow into the lower depression feature, or to flow slightly further south within the valley. The maximum runout distances in this valley are observed along the southern side at 1950 m, reaching around 700 m asl (**Figure 4.14**).

4.3.3 Southeast Valley Vents

4.3.3.1 Southeast Valley Head Vent

The 2 m^3 s^{-1} effusion rate scenario for the northern and southern sectors of the southeast valley head vent both have relatively low inundation probabilities across all flow paths. Lower to moderate probabilities are focused around the proposed vent location area (**Figure 4.15 &Figure** 4.16). Flows from the southern sector have a maximum runout length of around 1840 m, reaching just short of 600 m asl along the southern side of the valley (**Figure 4.16**). The northern sector maximum length is ~2070 m reaching ~550 m asl (**Figure 4.15**). The maximum lengths for both flows are outliers, with most flow paths much shorter and terminating at the elevation of the two topographic depressions. Notably, the maximum runouts under these two

scenarios reach lower elevations than the South Crater 20 m^3 s^{-1} effusion rate scenario in this valley (**Figure 4.15 &Figure** 4.16).

For an effusion rate of 20 m^3 s^{-1}, the southeast valley head vent scenarios both have flow pathways capable of reaching the ocean, albeit within the lowest probability range (**Figure 4.15 &Figure** 4.16). The southern sector flows have moderate to higher probabilities of reaching ~1250 m asl. However, the modelled outputs suggest that at lower inundation probabilities, flows would be capable of flowing further predominantly down the south side of the valley (**Figure 4.16**). Although flows are also capable of passing between the two depressions and reaching the northern side of the valley, reaching to around 180 m asl, this appears unlikely given the very small number of model runs that suggest this trajectory. Lava flows from the southern sector also could migrate into the centre of the valley from 900 m asl paths, which appear to facilitate reaching the ocean (**Figure 4.16**). Some lowest probability flows are shown to escape the southern boundary of the valley between 600-700 m asl (**Figure 4.16**). Flows originating from the southern sector of this vent are also able to enter the upper southwest valley flowing to 1200 m asl.

The modelled flows from the southeast valley head vent at an effusion rate of 200 m^3 s^{-1} show multiple pathways where lava flows can reach the ocean. Northern and southern sector eruptions both are able to produce flows affecting the breadth of the southeast valley and produce lava ocean entry locations in multiple regions (**Figure 4.15 & Figure 4.16**). The highest inundation probability pixels from flows originating in the northern sector suggest a dominant path into the upper valley depression, whereas southern sector flows show a higher probability to either flow

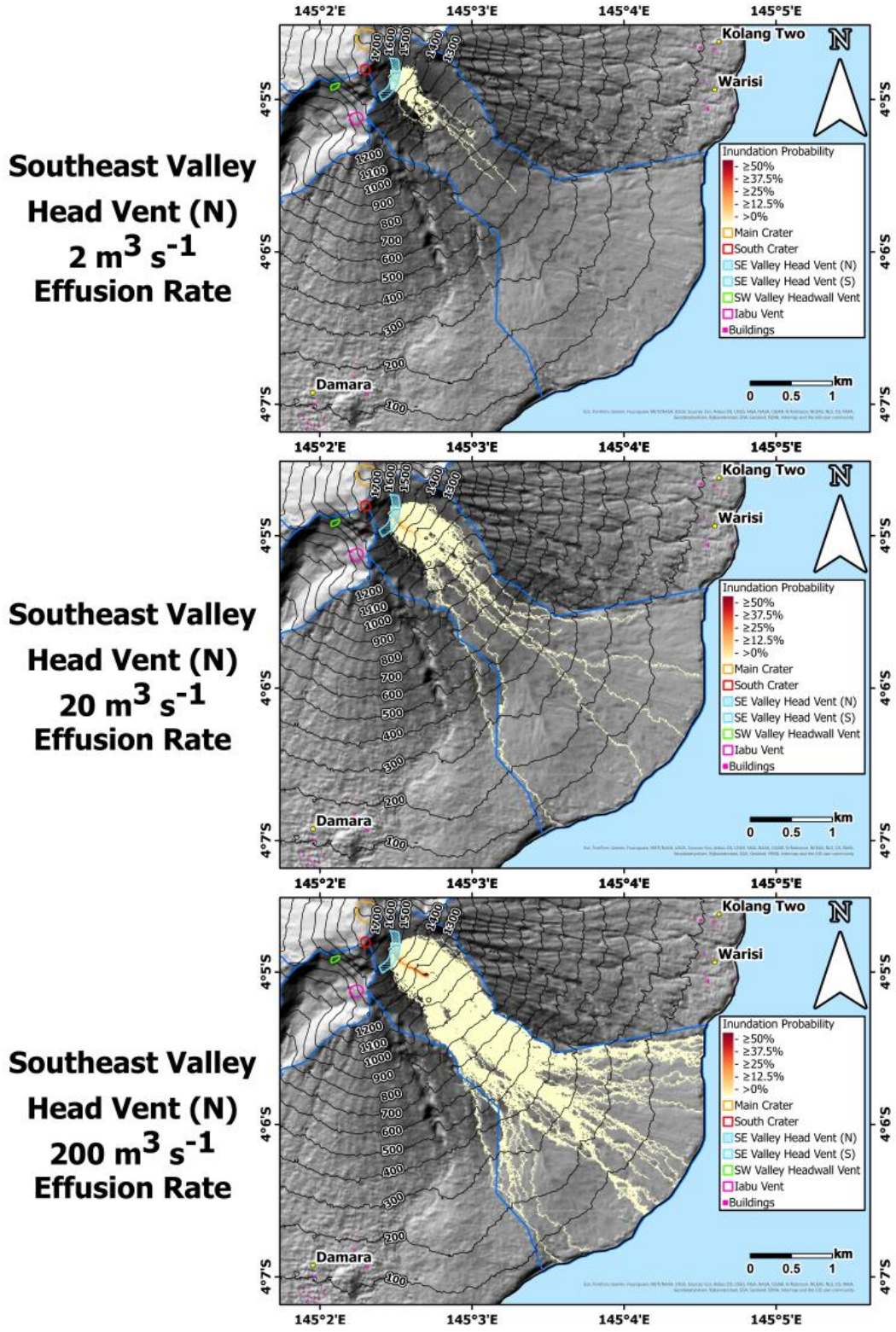

Figure 4.15 Results of the Q-LavHA modelling of lava flows from the northern sector of the southeast valley head vent area at 20 $m^3 s^{-1}$ (top), 20 $m^3 s^{-1}$ (middle), and 200 $m^3 s^{-1}$ (bottom) effusion rate scenarios.

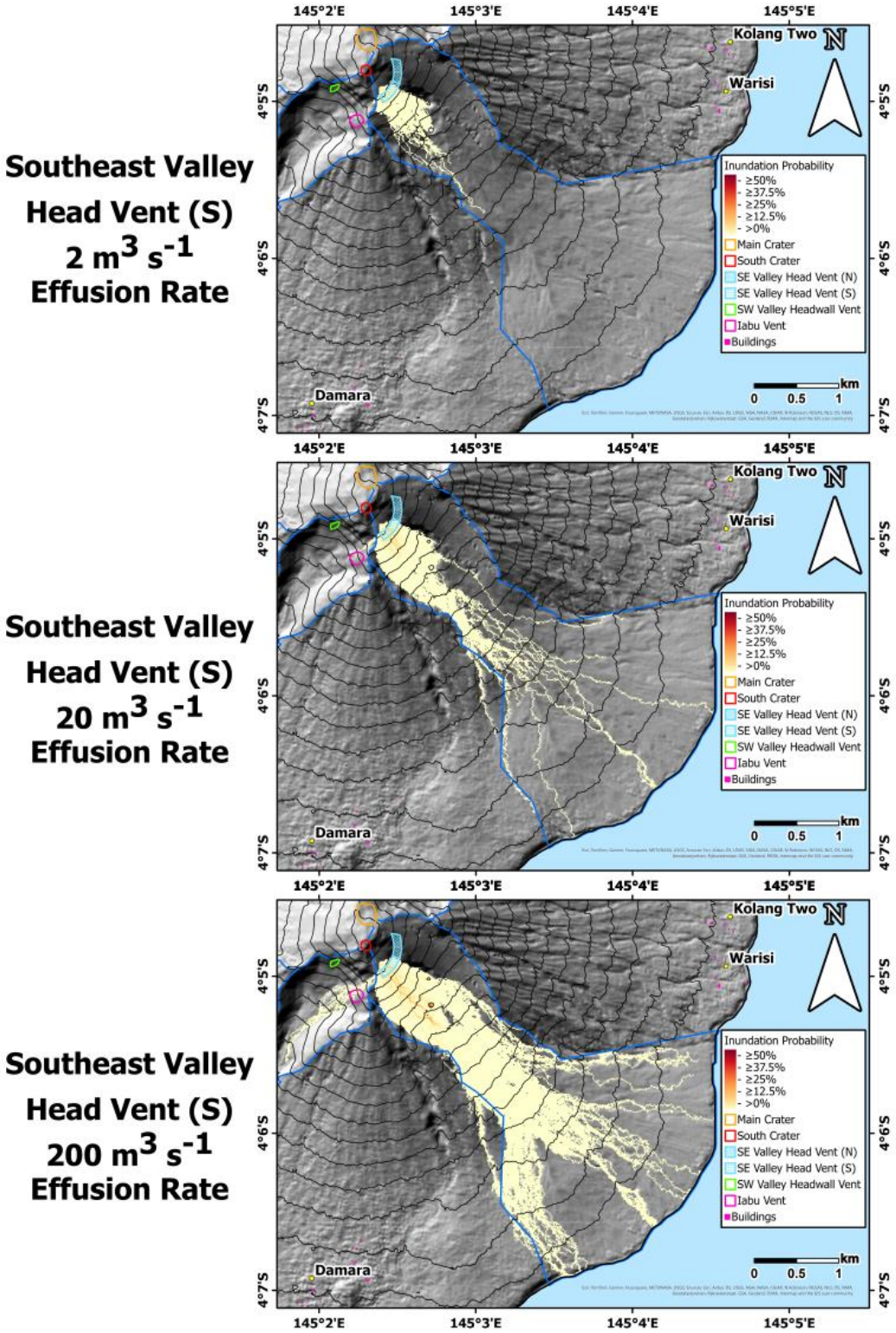

Figure 4.16 Results of the Q-LavHA modelling of lava flows from the southern sector of the southeast valley head vent area at 20 m^3 s^{-1} (top), 20 m^3 s^{-1} (middle), and 200 m^3 s^{-1} (bottom) effusion rate scenarios.

towards the lower depression or pass south of this feature (**Figure 4.16**). As with the 20 m^3 s^{-1} scenario, southern sector flows with a 200 m^3 s^{-1} effusion rate may also enter the southwest valley and flow centrally to ~750 m asl, a maximum runout in this valley of ~1500 m. Additionally, a greater area beyond the southern boundary of the southeast valley can be inundated by lava flows, regardless of whether flows are emitted from northern or southern regions (**Figure 4.15**).

4.3.3.2 Southeast Valley Flank Vents

The higher and lower flank vents both feed short flow paths when the effusion rate is 2 m^3 s^{-1}. The higher vent has a maximum flow distance of 210 m compared to 75 m for the lower vent (**Figure 4.17**). In comparison, the flow paths modelled under the 20 m^3 s^{-1} effusion rate scenario for both vents produce moderate to highest probability areas of inundation directly downslope from the point-defined eruption source (**Figure 4.17 &Figure** 4.18**)**. The maximum modelled runout distance for the lower vent is ~380 m, reaching just below 900 m asl, whereas the higher vent is capable of producing longer flows of approximately 770 m down to ~820 m asl (**Figure 4.18**).

At an effusion rate of 200 m^3 s^{-1}, the lower vent is able to generate lava flows reaching down to elevations of ~500 m asl, with a maximum distance of ~1390 m (**Figure 4.18**). The probabilistic output from this modelling shows that the preferred central flow trajectory from the 20 m^3 s^{-1} scenario is maintained with highest probabilities of inundation at around 800 m asl and moderate to higher probabilities maintained as far as 600 m asl (**Figure 4.18**). The higher vent is capable of producing maximum runout distances of 2450 m, 1060 m longer than those from

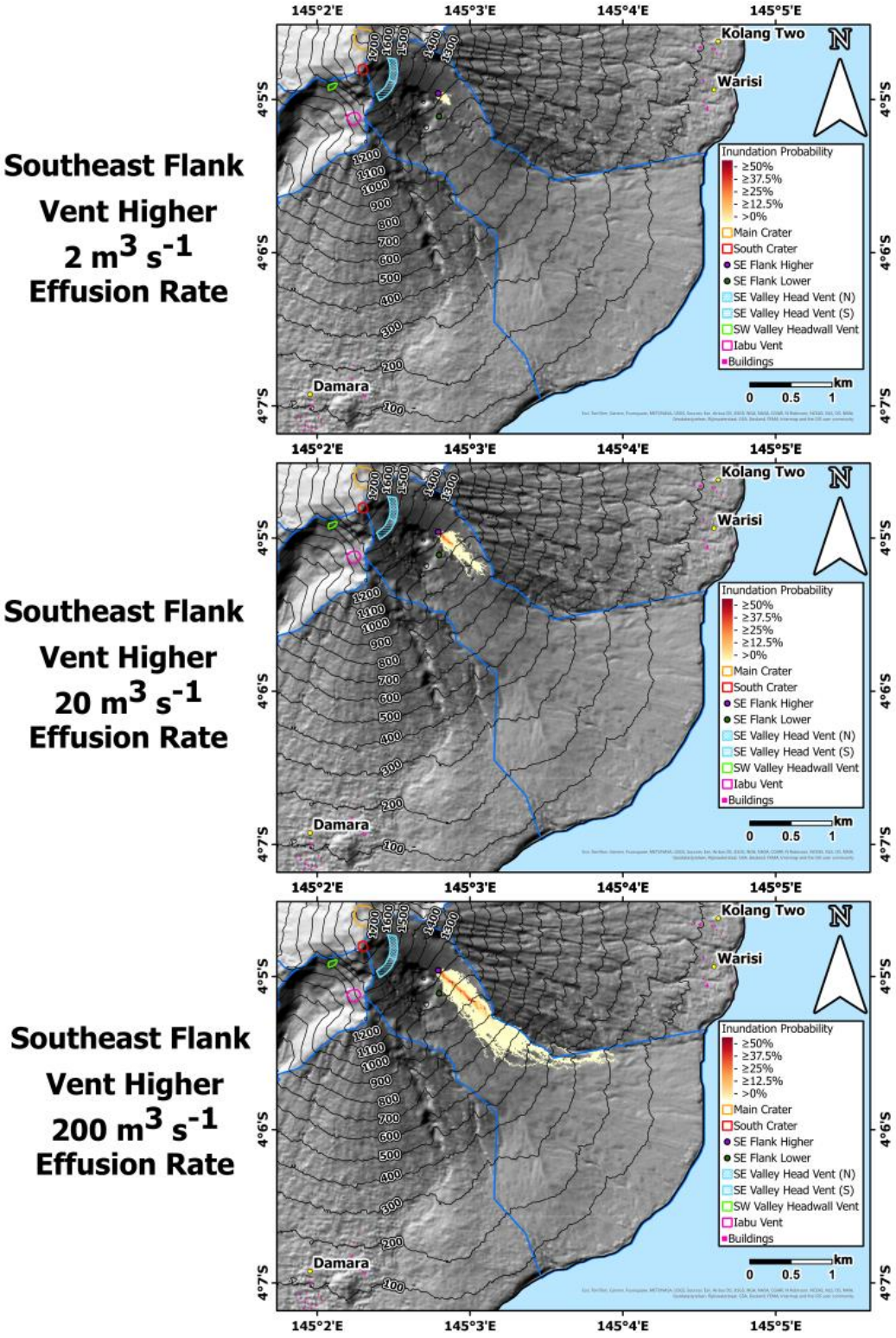

Figure 4.17 Results of the Q-LavHA modelling of lava flows from the higher Southeast Flank Vent position at 20 $m^3 s^{-1}$ (top), 20 $m^3 s^{-1}$ (middle), and 200 $m^3 s^{-1}$ (bottom) effusion rate scenarios.

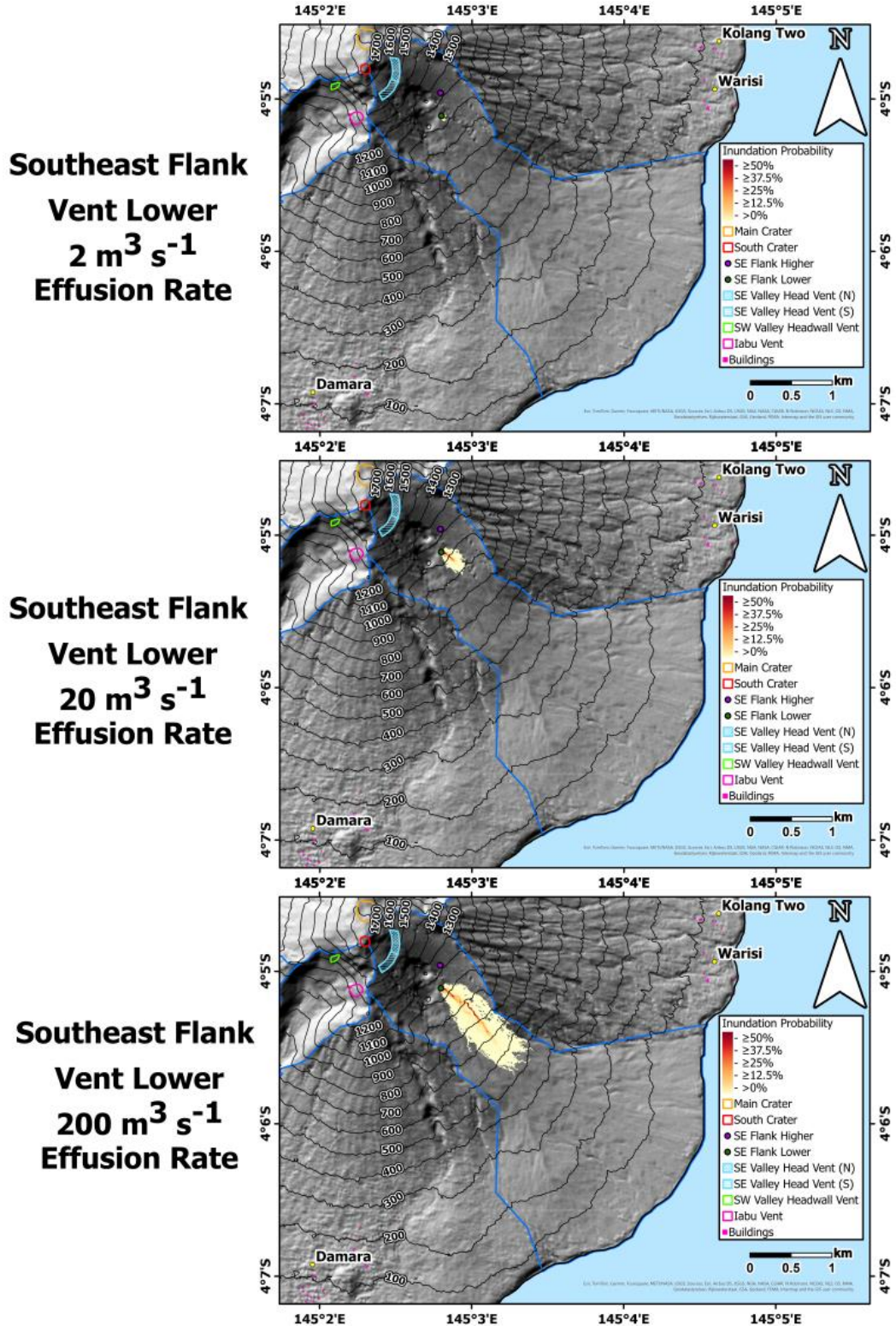

Figure 4.18 Results of the Q-LavHA modelling of lava flows from the lower Southeast Flank Vent position at 20 $m^3 s^{-1}$ (top), 20 $m^3 s^{-1}$ (middle), and 200 $m^3 s^{-1}$ (bottom) effusion rate scenarios.

the lower vent, and reaching to ~180 m asl (**Figure 4.17**); the position of the higher vent therefore has a greater ability to produce flows that reach further towards the coast than the lower vent. This scenario has moderate to highest probabilities of inundation on the northern side of the valley to approximately 850 m asl (**Figure 4.17**).

4.3.4 Southwest Valley Vents

4.3.4.1 Southwest Valley Headwall Vent

At a 2 $m^3 s^{-1}$ effusion rate the southwest valley headwall vent produces a maximum runout of ~160 m, with flows reaching between 1250 and 1400 m asl (**Figure 4.19**). The highest probabilities are found within or immediately adjacent to the proposed vent area. In the 20 $m^3 s^{-1}$ effusion rate scenario, the area of moderate to highest probabilities extends to 1200 m asl with the maximum runout extending ~530 m down to 1000 m asl (**Figure 4.19**). The flows produced under a 200 $m^3 s^{-1}$ effusion rate scenario from this vent descend to 700 m asl, a maximum distance of 1560 m. The highest probabilities of inundation occur just below 1000 m asl where it appears that flows begin to be channelled by the steep side walls (**Figure 4.19**); this was also seen in the South Crater flows reaching these elevations (**Figure 4.14**). Overall, flows from the southwest valley vent are capable of occupying most of the upper valley except the eastern portion around the proposed Iabu vent (**Figure 4.19**).

4.3.4.2 Iabu Vent

All Iabu vent flow scenarios have greater maximum runout distances than their southwest valley headwall counterparts (**Figure 4.20**). An effusion rate 2 $m^3 s^{-1}$ from Iabu vent is able to produce a flow reaching 850 m asl, approximately 850 m from the vent. Higher inundation probabilities are located just north of the proposed vent, suggesting a topographically-controlled exit geometry from the vent area. Lower probability flows reach to around 1100 m asl (**Figure 4.20**). The 20 $m^3 s^{-1}$ effusion rate scenario has a maximum runout of 1940 m down to ~470 m asl within the narrow portion of the southwest valley (**Figure 4.20**) and, similar to the previous scenario, the highest inundation probabilities occur just north of the vent. In the 200 $m^3 s^{-1}$ effusion rate scenario, the highest probabilities exist in the same area to the north of the vent and within the same part of the valley just below 1000 m asl where lava flows appear to be preferentially channelled regardless of source (**Figure 4.20**). The maximum flow distance for Iabu vent is ~3300 m reaching to ~160 m asl where the narrow section of the southwest valley opens up onto the shallower coastal areas (**Figure 4.20**).

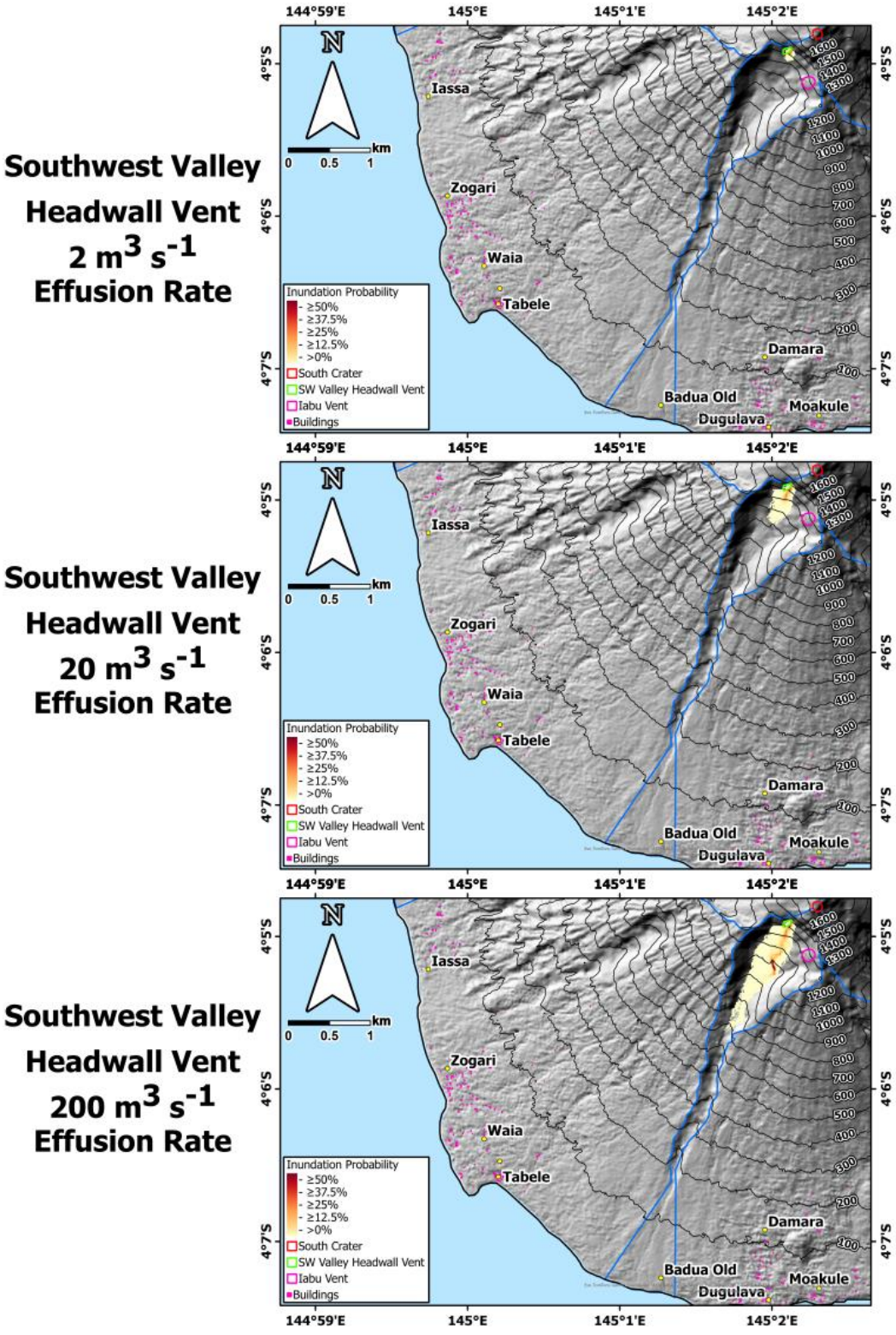

Figure 4.19 Results of the Q-LavHA modelling of lava flows from the Southwest Headwall Vent at 20 m^3 s^{-1} (top), 20 m^3 s^{-1} (middle), and 200 m^3 s^{-1} (bottom) effusion rate scenarios.

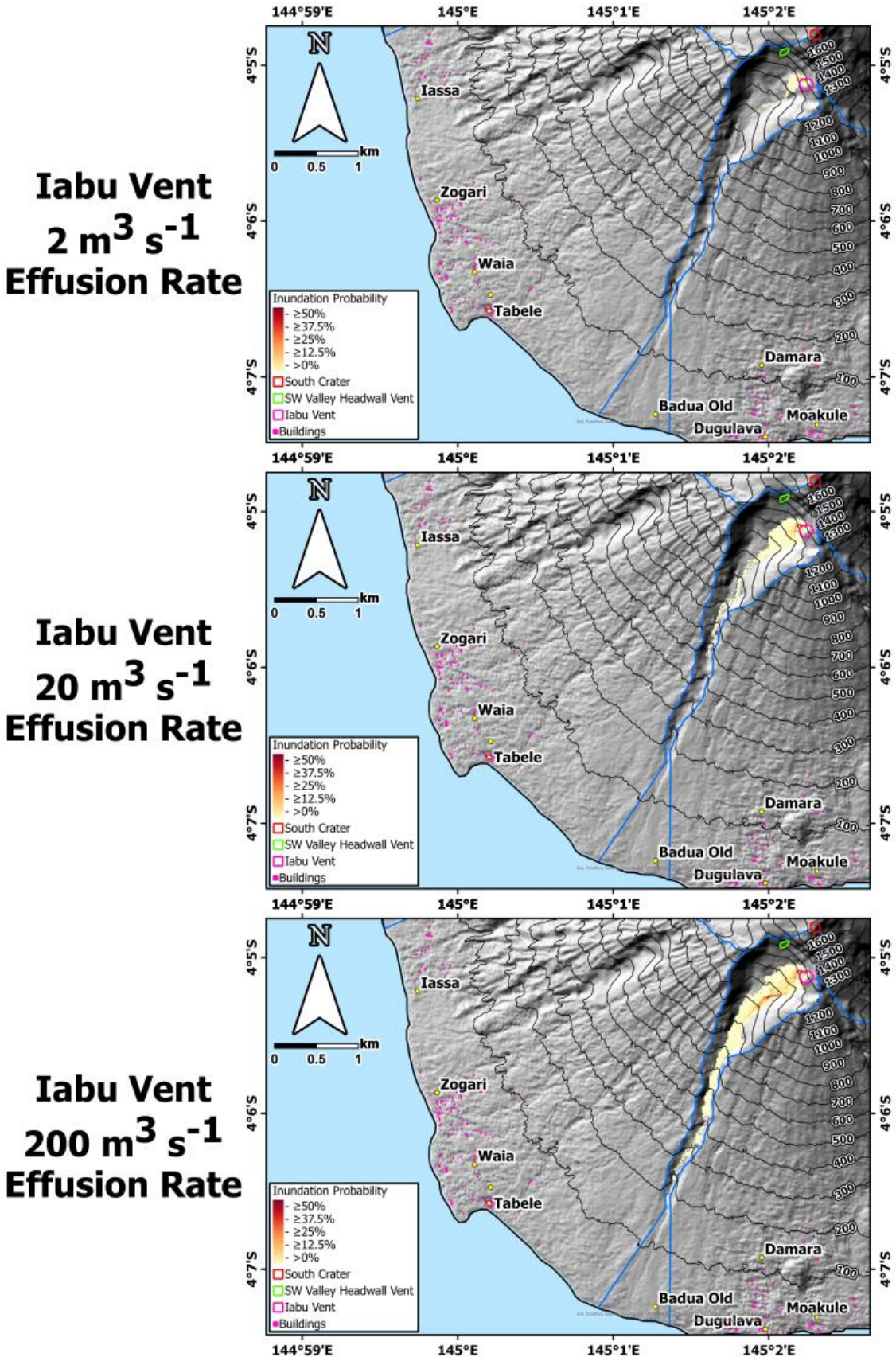

Figure 4.20 Results of the Q-LavHA modelling of lava flows from the Iabu Vent at 20 m^3 s^{-1} (top), 20 m^3 s^{-1} (middle), and 200 m^3 s^{-1} (bottom) effusion rate scenarios.

4.3.5 Satellite Cones

For an effusion rate of 2 $m^3 s^{-1}$ within the satellite cone scenario, model simulations show that most flows from the projected cones would be very localised, travelling no more than 150 m. Notable exceptions are cones 6 and 20 which have maximum runouts of ~400 and ~780 m, respectively, with the latter reaching the ocean (**Figure 4.21**). An effusion rate of 20 $m^3 s^{-1}$ at these cones produces possible lava ocean entry locations at Cones 1, 2, 3, 4, 5, 6, and 20 (**Figure 4.21**); though for south and eastern sides of the island are closer to the coast due to the single radial mean distance used to define the projected cone locations (**Figure 4.10**). An effusion rate of 200 $m^3 s^{-1}$ produces far more flows that result in an ocean entry. Cones 1, 6, 7, 9, 10, 11, 14, 15, 16, 17, 18, 21 and 22 produce flow paths that overlap mapped buildings of nearby settlements (**Figure 4.21**). The flows are generally well constrained by topography, with projected cones situated in river channels (Cones 15 and 16) producing narrow inundation footprints. In contrast, those forming in more open terrain, especially nearer the coast, have many more flow path permutations (**Figure 4.21**). Regardless of topography, cone generated flows with a 200 $m^3 s^{-1}$ effusion rate are capable of runout distances of more than 700 m, with Cone 13 producing a flow of approximately 1350 m (**Figure 4.21**).

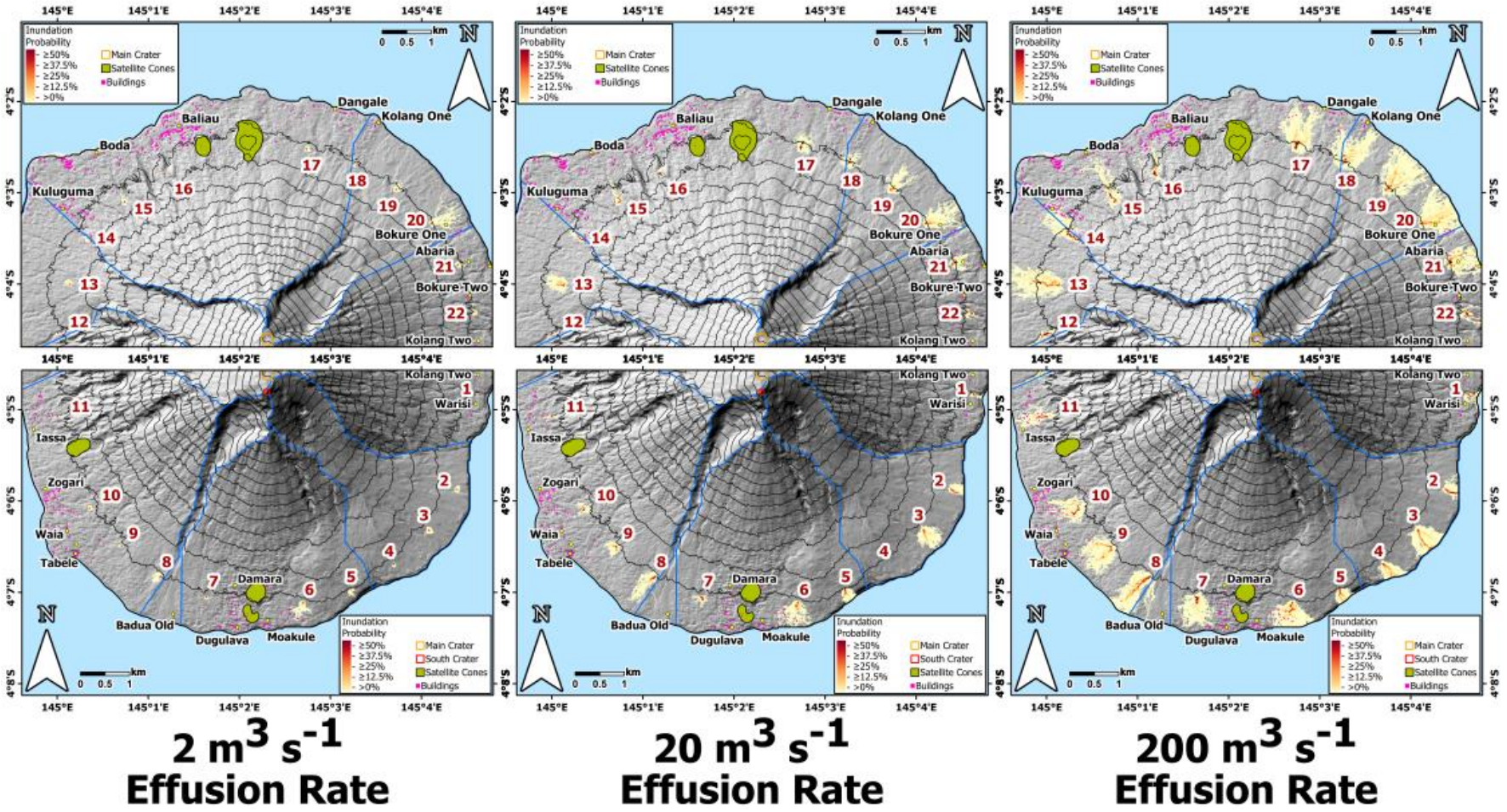

Figure 4.21 Results of the Q-LavHA modelling of lava flows from projected satellite cone positions (red numbers) at 20 m^3 s^{-1} (left), 20 m^3 s^{-1} (middle), and 200 m^3 s^{-1} (right) effusion rate scenarios.

4.4 Discussion

The main aim of this chapter is to assess the hazard posed by lava flows to settlements on Manam. Probabilistic modelling of lava flow inundation areas at Manam, for a suite of pre-defined eruptive scenarios, shows considerable variability in the distances that the flows can reach depending on the eruption source. Therefore, this section will draw on the modelling results presented to discuss the overall potential for lava flows to directly impact settlements across a range of relevant eruption scenarios. The results also indicate that future flows will not produce similar runouts lengths as the mapped flows in the northwest and southwest valleys (McKee 1981) and possible explanations will presented. Lava flow ocean entry situations are a frequently under-recognised hazard during effusive eruptions at ocean island volcanoes, and yet have implications for public health. The modelling analysis suggests that lava flows are capable of reaching the ocean under several eruptive scenarios, although generally only at higher effusion rates. The analysis presented demonstrates clearly that the ability for lava flows to reach the ocean is largely dependent on the vent location and this is critical information for local response when assessing the potential hazard posed by a newly-formed and active lava flow. Consequently, the final section of this discussion will consider mechanisms that may explain the discrepancy between historical records and modelled results regarding the ability of flows to reach the coast within the southeast valley.

4.4.1 Can Valley Channelled Lava Flows Impact Settlements?

The September and October 2018 northeast valley lava flows threatened the villages of Bokure and Kolang prompting the relocation of these settlements to the coastal region between the northeast and southeast valleys (Global Volcanism Program 2019a). The closest villages to the lower avalanche valleys are now Dangale and Abaria (both less than 1 km from the lower reaches of the northeast valley), Kuluguma (parts of which are within 100 m of the northwest valley) and Iassa (<1 km from the northwest valley). In the northeast valley the longest modelled flows reach between 4 and 5 km in runout distance, with most of these flows fronts being located in the centre of the valley down to ~100 m asl, a considerable distance from Dangale and Abaria (**Figure 4.13**). None of the modelled scenarios produced flows that propagated down the northwest valley which means that the circumstances leading to the 1958 flow that threatened Kuluguma (Taylor 1958a) remain unclear.

4.4.1.1 Flow Field Development in the Northeast Valley

The modelled runout distances match the 2018-2019 lava flows in the northeast valley (**Figure 4.2**) relatively well but do not replicate the full northerly and southerly extents reached by recent flows. *Q-LavHA* does not model the lateral spreading of flows, nor the development of flow fields, as each iteration does not take into account the emplacement of previous iterations (Mossoux et al. 2016). The maximum widths of the lower reaches of the recently emplaced flows are between 200-500 m. Even with this amount of spreading at the distal lobes, the modelled flows do not threaten Dangale or Abaria.

As *Q-LavHA* only models a single lava flow channel, the hazard posed by flow field extension is not represented. Flow fields develop when the pressure within the channel exceeds the strength of the levees containing the flow, causing breaches from which lava escapes from the main channel (Kilburn and Lopes 1991; Kilburn 2000). The 1983 and 1989 flow fields on Etna (Italy) were shown to have extended beyond the limit of the initial flow by 67% and 22% respectively (Kilburn and Lopez 1988; Barberi 1990; Kilburn and Guest 1993). If flows extended down the most northern or southern extremities of the northeast valley it is possible that Dangale and Abaria villages could be inundated. However, the likelihood of such an event at Manam is very unlikely given the eruption durations required for extensive flow fields to develop. Flow fields observed globally commonly take weeks to months to develop (Kilburn and Guest 1993; Mattox et al. 1993; Pedersen et al. 2017), whereas lava flows at Manam are typically emplaced within hours to days (Taylor 1958a; Palfreyman and Cooke 1976; Global Volcanism Program 2024). The exact emplacement duration of the September-October 2018 flow is uncertain but at most may have been active for 8 days based on observations of lava flowing in the valley on 25 September 2018 and later reports of a flow halting on 2 October 2018 but with no confirmation if the two were the same flow (Global Volcanism Program 2019a). However, while this lava flow did develop three distinct lobes (**Figure 4.2**) this cannot be described as a flow field. From a forecasting perspective it would be unlikely that Dangale and Abaria villages would be considered under threat from flows in the initial days of lava flow emplacement in the northeast valley. These villages could be considered at risk if effusions from Main Crater continued for one week or more and breakouts began to form on the northern or southern most

extremities of the valleys. However, given the typical duration of Manam lava flows being less than one week this is currently unlikely.

4.4.1.2 Possible Topographic Change in the Northwest and Southwest Valleys

The greatest discrepancy between the mapped and observed real flows and the modelled lava flows can be seen in the northwest and southwest valleys. The mapped flows in these valleys are within hundreds of metres of current buildings and settlements and so investigating what circumstances may have led to lava emplacement previously is an important part of understanding lava flow hazard in these areas particularly. The modelled flows reflect observed behaviour of flows in the southwest valley where most flows remain within the wider upper reaches of the valley with some flows advancing down into the narrower section below ~600-700 m asl. Although, all flows remain within the confines of the valley walls, the divergence between the modelled and true lava flows relates to the two undated flows mapped by McKee (1981). These flows were mapped from the coast to ~300-350 m asl and originally drawn as if extensions of the southwest valley; however, current topography indicates they fall outside the valley confines and the modelling suggests that these flow paths are not currently possible. There are three options that are considered here to explain the inundation of these areas: 1) the vent position feeding these historical flows was different from observed vents, 2) a higher effusion rate enabled lava to overcome the valley walls, or 3) a topographic change has since occurred in the southwest valley. The direction of the mapped flows indicate they flowed from the narrow mid-section of the valley (McKee 1981) suggesting a vent source in the upper valley, as with recently observed flows. The

200 m^3 s^{-1} effusion rate modelling scenario has already been acknowledged as reflecting the upper limit at Manam based on observations at analogue volcanoes such as Etna (Kilburn and Guest 1993; Andronico and Lodato 2005; Zuccarello et al. 2022). Even this scenario does not favour overflows in the southwest valley, so that an elevated effusion rate cannot explain how the flows mapped by McKee (1981) were emplaced.

It is also unlikely that the vent location has changed significantly. Topographic change within the valley is thus considered the most likely explanation for the difference between these undated flows and the more recently observed and modelled flows. McKee (1981) recognised that the undated flows were recent, thus the topographic alteration must have taken place relatively quickly, with only 34 or so years between mapping and the TanDEM-X acquisition in 2015 (Rizzoli et al. 2017). Assuming the undated flows overcame the valley walls then subsequently either the valley wall height has increased, the valley became deeper or a combination of the two. If the flows did overcome the valley walls, their emplacement may have impeded future flows from overcoming the walls, either by adding to the height of the walls or by making other flow paths within the valley more favourable. In terms of deepening of the valley, it is possible that erosion by PDCs or lahars may have gouged out a deeper valley floor, in the upper reaches and depositing material in the coastal areas at the bottom of the valley (Palfreyman and Cooke 1976; McKee 1981) that would now mean that lava flows cannot escape the confines of the channel. PDCs are capable of entraining finer particle substrate and larger, more coarse material (Roche et al. 2013) resulting in the erosion of flow

channels (Cole et al. 1998; Calder et al. 2000; Brand et al. 2014). Frequent PDCs in the southwest valley over the last 100 years or more (Global Volcanism Program 2024) would thus be capable of deepening the valley to such an extent that all future lava flows are constrained by the deeper valley topography. This has had the effect of limiting the hazard posed by lava flows to the villages near to the southwest valley.

Model simulations of flows originating Main Crater do not show any propagation of lava into the northwest valley, suggesting that there is no hazard posed to Kuluguma and Yassa villages. However, the NW Valley A flow in **Figure 4.1**, likely the 1958 flow described by Taylor (1958a), was emplaced within metres of current structures on Manam and within 1 km of the main area of Kuluguma. Therefore it is necessary to understand the circumstances, eruptive and topographical, that led to this flow's emplacement, and what would be required for similar flows to be emplaced in the future.

The account of the 1958 northwest valley lava flow describes explosive and effusive eruptions at Main Crater and then states that on 14 January "a more powerful eruption poured a much larger lava flow into the northwestern valley" (Taylor 1958a). This description implies that the flow did indeed originate from Main Crater and flowed over the northwestern crater wall. Since the scientific record of Manam's activity began in 1939 (Fisher 1939), explosive eruptions at Main Crater have been uncommon with most explosive activity centred on South Crater (Palfreyman and Cooke 1976). Paroxysmal explosive eruptions followed by substantial effusion of lava has been linked to the release of trapped volatiles

beneath a low permeability plug, followed by subsequent depressurisation of the shallow magmatic system and rapid magma ascent (Cassidy et al. 2018a). Therefore, precursory explosive behaviour may be an indicator of the potential conditions required for lava propagation in the northwest valley. However, the magmatic processes responsible for the triggering of effusive eruptions do not necessarily dictate the flow path of the effused lava as this is primarily topographically-controlled. Therefore, similar to discussion of the southwest valley flows above, there must have been different topography at the time of effusion to that of the present day.

Pre-existing topography strongly controls the emplacement geometry of lava flows (Miyamoto and Papp 2004) and, in turn, lava flows change the topography during emplacement (Ebmeier et al. 2012). As such, the lava flows preceding the 1958 northeast flow may have been emplaced in such a way as to direct future flows into the northwest valley. To investigate this possibility, **Figure 4.22** shows a *Q-LavHA* model of a Main Crater lava flow with a 200 m^3 s^{-1} effusion rate over a modified version of the TanDEM-X DEM. This DEM was modified by adding 3.5 m (the calculated average Manam lava flow thickness) to any pixel where one of the four lava flows from 2018-2019 (**Figure 4.2**) had been emplaced; a maximum increase of 14m where all flows cover a given pixel. The probabilistic output from the modelling on this modified DEM show that there are possible flow paths where lava is able to pass over the northern wall of Main Crater and flow down the northwest valley to around 750 m asl, a 1660 m maximum runout (**Figure 4.22**). Although highly simplified, this rudimentary example demonstrates how successive lava flows can

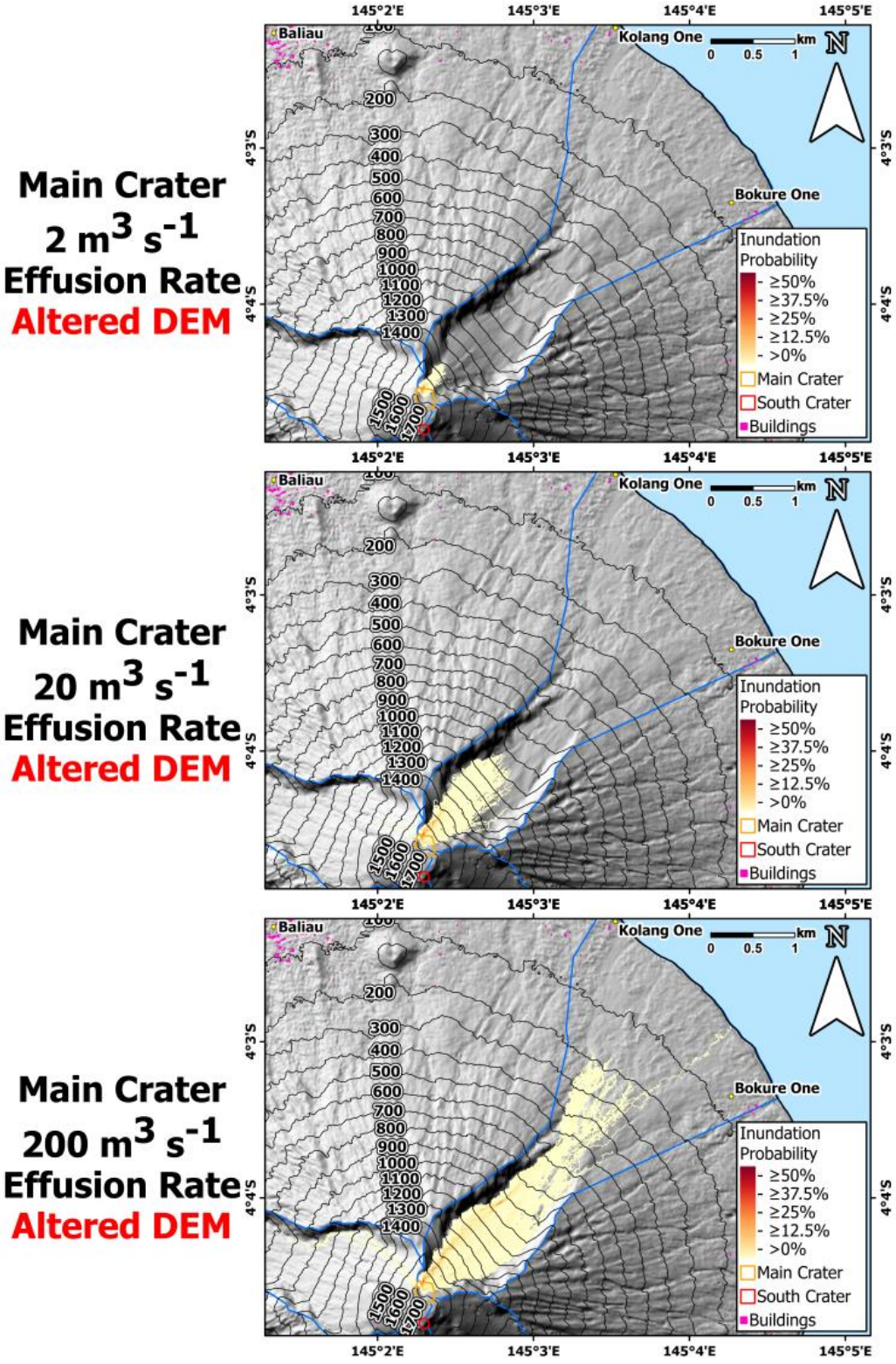

Figure 4.22 Results of the Q-LavHA modelling of lava flows from Main Crater over an altered DEM. In these results lava flows from Main Crater are shown to be able to flow into the northeast valley. The DEM had the average thickness of 3.5 m added to the elevation of pixels where the recent September-October 2018, January 2019, June 2019, and August 2019 had inundated for a maximum elevation increase of 14 m. These results show the 20 m^3 s^{-1} (top), 20 m^3 s^{-1} (middle), and 200 m^3 s^{-1} (bottom) effusion rate scenarios.

change the underlying topography sufficiently to cause future flows to be directed down the northwest valley. Ultimately, under this example there is still a low probability of Main Crater flows entering the northwest valley. However, the build-up of lava within the crater area should still be monitored, especially if the open northeastern side of the crater begins to fill in as a result of successive overflows.

Overall the modelling of Manam's lava flows indicate that there is a low probability direct inundation of villages in their current locations, especially given the relocation of Bokure and Kolang in recent years. Topographic changes over the last 70 or more years has likely prevented lava from threatening villages around the northwest and southwest valleys. It has been shown that Main Crater generated flows may be capable of entering the northwest valley due to successive build up of lava flows in the crater area but these are not expected to travel far enough to threaten villages (**Figure 4.22**). Therefore more substantial topographical change is thought to be required for lava flows to directly threaten settlements situated around the base of the northwest and southwest valleys

4.4.2 Southern Villages Most at Risk from Future Satellite Eruptions

The primary issue facing volcanic hazard assessment of monogenetic cone fields is that typically activity is centred in one location with subsequent eruptions moving location (Schmidt et al. 2022). This adds additional uncertainty to hazard modelling where the vent location is normally a well constrained parameter. As such hazard assessments attempt to statistically analyse the distribution of cones to infer future locations (Kereszturi et al. 2014; Sieron et al. 2021; Bevilacqua et al. 2022) and may

randomly generate cone location within a known field (Marrero et al. 2019). Due to the unpredictability of where a cone will form, it represents a significant challenge for planning and response to these events from large monogenetic fields (Kereszturi et al. 2014; Charlton et al. 2020; Bevilacqua et al. 2022) to small island volcanoes like Manam (Marrero et al. 2019; Barragan et al. 2022; Biass et al. 2024). Given that only five satellite cones have been emplaced at Manam it was not possible to replicate these approaches but they do point to the general difficulty in modelling satellite cone hazard. In this section the hazard to Manam's settlements given the assumption that cones form at approximately similar distances due to stresses produced the loading effect of the central edifice, whilst recognising the difficultly in representing the probability of cones forming in any one particular part of the island.

The modelled results for lava flows produced by satellite cones reveal that the potential inundationextent is sensitive to the effusion rate (**Figure 4.21**). The 2 m^3 s^{-1} effusion rate scenario shows very limited flow mobility, likely due to shallower slope gradients the lower flanks, and generally flows are not able to flow far enough to reach populated areas unless the vent itself is close (<500 m) to settlements (e.g. Cones 1, 6, 11, 14, 11, 21 and 22). The 20 m^3 s^{-1} scenario flows are capable of longer runouts of up to ~800m (Cones 8, 13 and 20, **Figure 4.21**) but are typically shorter, especially if they are topographically-constrained (Cones 1, 7, 9, 10, 11, 12, 16, **Figure 4.21**). The 200 m^3 s^{-1} scenario shows that all projected vent positions are capable of longer runouts of 600-1000 m; only when source vents are located on steeper slope gradients (projected cones 12, 16 and 22, **Figure 4.21**). At analogue

volcanoes, satellite cone effusion rates are typically between 1 and 20 m^3 s^{-1} (Andronico and Lodato 2005; Branca et al. 2013; Larrea et al. 2017; Pedersen et al. 2022; Zuccarello et al. 2022) and so the hazard represented by the 2 and 20 m^3 s^{-1} scenarios should be considered the most realistic, with the 200 m^3 s^{-1} scenario representing a low probability but high consequence (i.e. worst case) scenario.

The regular placement of vents at the average distance of current satellite cones from South Crater attempts to capture an approximation of the hazard posed by lava flows from satellite vents. However, this cannot be considered as a comprehensive hazard assessment as the vent placement is arbitrary and future flank eruptions may initiate at any position, closer to or further from Manam's coastal settlements. The locations of existing satellite cones provide some indication as to the position of future vents and cones. Clustered distributions of monogenetic cones around the central cone have been identified at composite volcanoes globally (e.g. Springer Volcanic Field (USA) - Connor et al., 1992; Etna (Italy) - Corazzato and Tibaldi, 2006; Kadovar, Long Island and Langila (Papua New Guinea) McKee, 1981; Bazman (Iran) Saadat and Stern, 2011; Jeju Island (South Korea) Yokoyama, 2020). Clustering typically follows either an annular pattern or more linear pattern where cones concentrate along identifiable axes from the main conduit (Yokoyama 2015). Manam's satellite cones seem to follow a linear axes distribution with four cones situated along a north-south axis and the fifth located on in the west (**Figure 4.10**). The north-south and west axes represent more viable pathways for dyke propagation. The absence of cones to the east may indicate that sub-surface conditions, such as stress field and emplaced strata (Gudmundsson

2005, 2006; Bazargan and Gudmundsson 2019) are conducive to vent-forming dyke propagation on eastern Manam or that such behaviour is rarer than along the other directions. Thus the north-south axis and tentative western branch represent the most likely locations for future satellite vents. Piling effects, whereby solidified dykes improve the strength of surrounding rock hampering successive dyke propagation (Yokoyama 2015), may also influence future location of satellite vents. Future dykes are less likely to reach the surface in close proximity to previously emplaced cones and so could instead surface 500-1000 m away from previous cones, based on the distance between the two northern and two southern satellite cones on Manam (**Figure 4.1**).

The position of existing cones indicate that villages on the north, south and west coasts are more at risk from lava flows produced by future cone-forming eruptions than those on the east cost. In addition the mean distance of existing cones from the South Crater conduit suggest that future cones forming in southern Manam would likely open within hundreds of metres away from or potentially within villages themselves. Thus overall southern villages are most at risk from future cone formation given this potential proximity to future forming cones and the indicated preference for cones along the north-south axis.

4.4.3 Secondary Lava Degassing Hazard

This research has indicated that the likelihood for lava flows inundated a populated area of the island is low without topographic alteration to the avalanche valleys or a change in effusive behaviour to become more long-lived. However, an often

overlooked aspect of lava flow hazard is that of its degassing as volatiles continue to exsolve from the lava during and continue for weeks to months after emplacement (Simmons et al. 2017; Kern et al. 2020). The reaction of atmospheric moisture with volcanic gas emissions, especially SO_2, produces volcanic smog increasingly known as “vog” (Sutton et al. 2001). The primary constituent of vog is sulphate aerosols a particulate matter with a mean diameter of less than 2.5 μm ($PM_{2.5}$) (Mather et al. 2012). Vog has been shown to result in respiratory health issues (Longo et al. 2010; Edmonds et al. 2018) when communities are overexposed and as such particulate dispersal models are increasingly used to forecast the impact of vog generation (Perrone et al. 2012; Moisseeva et al. 2023) however this remains outside the scope of this work. Communities on Hawaii within several kilometres of vog sources have been show to be regularly exposed to SO_2 and $PM_{2.5}$ levels exceeding 24 hour safe levels (Businger et al. 2015). The modelling presented in this chapter show that lava flows are capable of reaching within 1-2 kilometres of settlements and therefore may pose a health hazard due to ongoing degassing and possible vog production.

Lava-seawater interaction can result in explosive behaviour capable of generating ballistics (Mattox and Mangan 1997) and also produce a gas and aerosol plume known as laze (“lava haze”), which is rich in chlorine from volatilised seawater (Edmonds and Gerlach 2006; Mason et al. 2021). It has long been clear that lava flows have been capable of reaching the ocean via the northeast (Global Volcanism Program 1992c, b, 2004d) and southeast valleys (Fisher 1939; Taylor 1958a; Global Volcanism Program 1994). Similarly to vog, laze contains volatile trace elements, which are emitted initially in their gaseous form and then condense rapidly to

particulate aerosols, predominantly complexed with sulphur or chlorine ligands (Edmonds et al. 2022b). Many of the trace elements are classified as environmental pollutants (Ilyinskaya et al. 2021b) and exposure can negatively impact on regional air and water quality and be detrimental to human health, especially over prolonged exposure timescales (Sabra et al. 2017; Rehman et al. 2018; Ilyinskaya et al. 2021b; Stewart et al. 2021). Even short-term exposure to volcanic plume, and particularly laze, can cause significant respiratory aggravation and eye irritation (Stewart et al., 2021). Persistent degassing from Manam is generally thermally energetic, producing a buoyant gas plume that rises from the summit craters (~1600-1800 m asl) to an elevation of around 3000 m asl (Liu et al. 2020a) where it is then transported laterally. Consequently, under quiescence conditions, gases and aerosols within the plume do not present a significant hazard to local populations. Laze however, forming at sea level, and with an unfavourable wind direction could potentially expose populated areas to highly acidic chlorine-rich gases and elevated concentrations of particulate aerosols. Deposition of these aerosols into stored open drinking water containers may contaminate water supplies, and so planning for the extended use of well water and only covered water storage sites would be an important preparedness measure. The impact of volcanic trace element aerosol on agriculture is less well understood; although supplying additional nutrients to soils may be beneficial to productivity over long timescales, the uptake of high concentrations of metallic elements into growing produce may prove hazardous for consumption. As such it is important to understand what the conditions are required for lava flows to reach the sea.

The ability for lava flows in the northeast valley to reach the ocean is dependent on the effusion rate. Only the 200 m^3 s^{-1} effusion rate scenario was capable of producing flows that reach the ocean, which in itself would be considered a low likelihood eruptive intensity, and may explain why just four northeast valley lava flows have reached the ocean according to the historical records (Global Volcanism Program 1992c, b, 2004d). The conditions for southeast valley flows to reach the ocean is less clear. Three confirmed southeast valley lava flows are known to have reached the ocean: the 2 August 1919 flow which was not directly observed (Fisher 1939), the 6 March 1958 which reportedly came from South Crater (Taylor 1958a) and the 18 October 1994 flow which came from a breach on the east side of South Crater (Global Volcanism Program 1994). The modelled results in this study indicate that lava flows sourced directly form South Crater with high effusion rates of 200 m^3 s^{-1} are not capable of reaching the ocean (**Figure 4.14**). In contrast, flows from the southeast valley head vent can reach the ocean under both the 20 and 200 m^3 s^{-1} scenarios (**Figure 4.15 &Figure** 4.16), indicating that a flank eruption promotes the formation of ocean entry sites relative to summit overflows.

4.4.3.1 Anticipating Ocean-Entry Hazards in the Southeast Valley

This subsection seeks to reconcile the inconsistency between the modelled South Crater flows and the account of the 6 March 1958 ocean-entering lava flow. Modelling suggests that a South Crater flow cannot result in a ocean-entry and therefore there is no risk of laze but the account of the 1958 flow suggests otherwise. Determining how the 6 March 1958 lava flow reached the ocean informs

whether local communities should prepare for potential laze hazard when observing South Crater generated flows in the southeast valley.

The ocean entry of the 1958 flow can be explained in one of three ways: 1) the rheology of the 6 March 1958 lava was markedly different than modelled, enabling a more mobile flow, 2) since the 6 March 1958 flow was emplaced the topography of the southeast valley has changed to prevent flows advancing to the ocean, or 3) the 6 March 1958 flow did not originate from the South Crater. The physical properties of the 6 March 1958 lava flow may well have been different from those modelled; however, the simulated flows from Main Crater and the southeast valley head vent were able to reach the coast (**Figure 4.13,Figure 4.15, & Figure 4.16**) where South Crater flows were only projected to flow to ~700 m asl (**Figure 4.14**). This suggests that topography may be the limiting factor for the modelled South Crater flows. However, if TanDEM-X topography as of 2015 is the limiting factor for modelled South Crater flows to reach the sea then, surely, modelled southeast valley head vent flows may also be expected to have been limited. Instead, more viable flow paths to lower elevations are found by flows simulated from this vent (**Figure 4.15 & Figure 4.16**). Given that differences in rheology and topography did prevent the modelled South Crater flows from reaching the ocean, it follows that the 6 March 1958 flow may not have originated from South Crater but from a vent at a lower altitude. It is common for longer lavas to be fed from lower-altitude vents. At Etna (Italy), for example, lavas from flank vents have longer average and maximum runout distances than summit-fed flows (Chester et al. 1985; Andronico and Lodato 2005). It is therefore suggested that the 1958 flow may in fact have

issued from either a breach in the crater wall, similar to the 18 October 1994 flow (Global Volcanism Program 1994) or from the southeast valley head vent region based on the modelled results (**Figure 4.15 & Figure** 4.16).

Misidentification of the source of the 6 March 1958 flow may therefore have been similar to the discredited 1946/47 lava flow that reportedly reached the ocean (Best 1953). This was later interpreted to have been an accumulation of lava at the top of the valley that collapsed and descended the valley as a debris flow (Reynolds 1957). These debris flows were noted to leave deposits superficially similar to an 'a'ā lava flow (Taylor 1958a). McKee (1981) did subsequently map these 1946/47 deposits as a lava flow. Here, it is suggested that both the 1946/47 and 6 March 1958 flows may have indeed been lava flows that issued from a vent high up in the southeast valley which, from the modelling (**Figure 4.14, Figure 4.15, Figure 4.16)**, is the only vent location capable of generating flows that enter the ocean in this valley. Therefore, as per the modelled results, local communities should only be concerned of potential lava sea-entry hazards if flows are generated below South Crater's rim.

4.4.4 Limitations and Future Work

There are no published effusion rates for Manam's lava flow and publicly available reports are generally not detailed enough for any estimations. Therefore, this chapter used published effusion rates at analogous systems to define the three effusion rate scenarios used in the modelling. Effusion rates have been estimated using thermal satellite remote sensing methods (Wright et al. 2001; Harris and Baloga 2009a) at volcanoes such as Etna (Italy) (Vicari et al. 2009; Harris et al. 2011),

Kilauea (USA) (Harris et al. 1998; Plank et al. 2021), Piton de la Fournaise (La Reunion) (Coppola et al. 2009), Holuhraun (Iceland) (Bonny et al. 2018), and Pacaya (Guatemala) (Morgan et al. 2013). These method relates the radiated energy from a lava flow to the time averaged discharge rate (TADR) by assuming the temperature of the lava (Harris et al. 1997) typically using satellite-borne thermal infrared sensors such as NASA's Advanced Very High Resolution Radiometer (AVHRR) and Moderate Resolution Imaging Spectrometer (MODIS) instruments (Harris et al. 1997, 2011; Coppola et al. 2009). These satellites-based data sources are open-access and provide robust estimations of effusion rates and so therefore represent a natural next progression for lava hazard assessment at Manam.

The lava flow properties selected as input parameters for *Q-LavHA* were based on compositional analyses of lava flows from 1974 or earlier (Palfreyman and Cooke 1976; McKee 1981; Johnson et al. 1985). To better constrain the properties of Manam's lava flows, samples from more recent flows should be collected and analysed, and used to update the representative Manam lava bulk composition. These data would also enable evaluation of whether the bulk composition of erupted products from Manam has evolved over time, which would yield independent yet complementary constraints on magma storage conditions and potential eruption triggering mechanisms such as magma recharge, mixing, protracted crystallisation and volatile exsolution.

Most critically, the TanDEM-X DEM used as the topographic input for *Q-LavHA* represents the topography in 2015 (Rizzoli et al. 2017). Since then, Manam has generated both explosive and effusive eruptions capable of altering the topography

of the summit areas and avalanche valleys. Up to date DEMs are critical for accurate lava flow hazard assessment (Tarquini and Favalli 2010). The TanDEM-X product is the most recent satellite derived DEM and in addition to this its high-resolution means that it represents the best possible basis for current modelling. However, an updated DEM ideally should be produced during future field work, potentially using ground-based LIDAR (Fornaciai et al. 2010; Bisson et al. 2016; Hunt et al. 2020) or UAS photogrammetric surveys (Müller et al. 2017; Granados-Bolaños et al. 2021; Vieira et al. 2021). LIDAR or UAS photogrammetric derived DEMs typically produce very high-resolution DEMs (in the range of millimetres to centimetres per pixel compared to metres for satellite-derived DEMs). High-resolution DEMs produce lower inundation probabilities in *Q-LavHA* due to the increased number of potential flow paths (Mossoux et al. 2016) and so any field data based DEMs would need to be smoothed to lower resolutions on the orders of metres for use with lava flow models.

As indicated in **section 4.1.3** the default *Thermal Parameters* for Q-LavHA are thermally inefficient and limit the runout distances of lava flows. Future iterations of this study should either determine these parameters through analysing lava flow samples from Manam or utilising a newer version of FLOWGO (Harris and Rowland 2015b) coupled with *DOWNFLOW* (Tarquini and Favalli 2011, 2016) in place of Q-LavHA for the flow direction propagation (Gurioli and Paris 2015; Harris et al. 2016).The *DOWNFLOW* code simulates the propagation of lava flows by way of steepest descent path and perturbates the topography within user defined elevation intervals and number of iterations (Tarquini and Favalli 2011, 2016). This

enables more realistic simulation of lava flow bifurcation and spreading (Favalli et al. 2005; Tarquini and Favalli 2016) which are not well represented in Q-LavHA as it is unable to alter topography between iterations (Mossoux et al. 2016).

A further area of work to comprehensively assess lava hazards at Manam would be to quantify the lava degassing hazards posed by both vog and laze. Initially particulate dispersal models such as VogCast (Moisseeva et al. 2023) or FLEXPART (Perrone et al. 2012) should be used to model scenarios based upon the rainy (November-April) and wet seasons (May-October), which have different prevailing wind directions, and varied wind speeds. This would allow for Manam residents to be more aware of whether a volcanic gas and particulate plumes from an active or recently emplaced lava flow is likely to affect their settlement. A further improvement to this would be to measure the lava plume gas specie composition using a MultiGAS (Shinohara 2005; Aiuppa et al. 2007) and the particulate matter within the plume (Ilyinskaya et al. 2021b; Mason et al. 2021) where possible. These could then be fed into the particulate dispersal model to better constrain the exposure hazard from the lava degassing vog and laze hazards.

4.5 Conclusions

The aim of this chapter was to assess the potential for lava flows to impact settlements on Manam through direct inundation and through lava-seawater interaction at ocean entry sites generating harmful gas plumes. This chapter shows that Q-LavHA is capable of assessing lava flow hazard on Manam but needs to invoke high effusion rates to produce runout distances comparable to observed

flows. This is most likely due to the thermally inefficient default *Thermal Parameters* (**Table 4.6)** (Mossoux et al. 2016) and so it is recommended to better constrain these parameters for Manam's lava flows for future hazard assessments.

The probabilistic results of *Q-LavHA* lava flow modelling indicates that direct inundation of settlements does not currently pose a significant threat to existing settlements. Manam's four radial avalanche valleys direct lava flows generated from the summit and flank vents and direct them to uninhabited regions of the island. This chapter also shows that Q-LavHA is capable of assessing lava flow hazard on Manam but needs to invoke high effusion rates to produce runout distances comparable to observed flows. This is most likely due to the thermally inefficient default *Thermal Parameters* (**Table 4.6)** (Mossoux et al. 2016) and so it is recommended to better constrain these parameters for Manam's lava flows for future hazard assessments.

The potential threat from satellite cone formation was also explored by systematically simulating the formation of cones around the island at the mean distance of the five current cones from South Crater. This analysis showed that flows emitted at lower effusion rates (~2 m^3 s^{-1}) are largely contained by local topography and have limited runout capability. Flows erupted at higher effusion rates (20-200m^3 s^{-1}) are capable of reaching between ~500 and 1300 m putting most settlements on Manam at risk. Settlements located on the northern coast of Manam, such as Baliau, Boda and Dangale are further from the assumed cone forming region, whereas other regions, especially south coast settlements, are closer to this region (**Figure 4.10**). However, the likelihood of future lower flank

eruptions forming satellite cones is uncertain, as those in the eruptive record are undated so the repose time is unconstrained.

Modelling results have shown that, under the suite of eruptive conditions explored, only lava flows descending via the northeast and southeast valleys are capable of entering the ocean and generating secondary hazards, primarily laze. Only high effusion rate scenario flows (200 $m^3 s^{-1}$) from any source vent were shown to be capable of reaching the ocean and the probability of this occurring was relatively low. In the southeast valley, only lava flows generated from the southeast valley head vent were able to reach the ocean under the 20 and 200 $m^3 s^{-1}$ effusion rate scenarios. Although the probability of a lava flow reaching the ocean was similar between the two valleys, the number of simulated flow paths that reached the sea was greater in the southeast valley.

This work has demonstrated the application of open-source lava flow models to assess hazard at a frequently active island-arc volcano. The different mobility and resulting hazard footprint of lava flows generated by flank eruptions compared to summit overflows, as observed at other mafic volcanoes, is also reflected quantitatively here in the modelled outputs. These results provide actionable information for local communities and eruption response agencies when observing and responding to effusive eruptions at Manam by highlighting the maximum potential runout for Manam's recent and current vent configurations. To extend the results, further research into the geochemical and rheological properties of more recent lava flows and the production of up to date topographic models are suggested for future evaluations of Manam's lava flow hazard.

5 Chapter Five - Summary and Conclusions

5.1 Summary

This thesis set out to achieve two main aims, which were a) to interpret the volcanological processes responsible for the observed open-vent activity of Manam volcano using satellite remote sensing of thermal and SO_2 emissions, and b) to assess the hazard posed by tephra deposition and lava flows to human activity and infrastructure on Manam and the nearby Papua New Guinea mainland.

5.1.1 What are the Processes Governing Manam's Activity?

Satellite remote sensing of Manam enabled the production of the first multi-annual and multi-parametric timeseries of Manam's emissions, which was used to gain insights into the magmatic processes operating between May 2018 and December 2021. Specifically, this work identified the arrival of a volatile-rich magma into Manam's shallow plumbing system. This recharge event is inferred to have triggered a series of eruptions, which evolved in character as residual degassed magma was progressively removed from the conduit and replaced by buoyant gas-rich melt, and to have been responsible for subsequent elevated SO_2 emissions due to enhanced fluxing of volatiles through the shallow plumbing system. These heightened gas emissions resulted in further eruptions that are consistent with the emplacement and subsequent failure of a conduit plug formed as a result of rapid degassing-driven dehydration and crystallisation. Furthermore, this chapter quantified the excess degassing at Manam and found that, over the full study period, more magma was erupted than supplied. However, this was interpreted as including the removal of the residual degassed magma. From March 2019 to

December 2021, after which we invoke that only the recharge magma remains, Manam degassed an excess of 0.1 km^3 more magma than was erupted.

5.1.2 What are the Likely Impacts of Tephra and Lava Flows?

Modelling of lava flows and tephra deposition using *Q-LavHA* and *TephraProb* quantitatively assessed the future exposure areas of these hazards across a range of scenarios, enabling discussion of the potential impacts. It was found that lava flows source from Manam's summit and flank vents were not likely to inundate settlements in their current locations but that lava-seawater interaction (and the resulting laze plume) was a more likely mechanism of which to impact Manam's population. This work shows that satellite cone eruptions on the lower flanks of Manam represent a direct threat to populations and infrastructure but recognises the ambiguity related to the location and probability of these types of eruption on Manam. This source location ambiguity represents a considerable source of uncertainty to eruption preparedness and planning. Vulcanian and sub-Plinian eruptions generating >10km eruptions columns are likely to deposit 10-1000 mm of tephra across much of Manam, which may require at least a temporary evacuation of the island. These major eruptions would also impact the coastal mainland areas of Bogia district; in particular, this work highlighted vulnerability in the road network, which would be relied on to facilitate evacuations and the receipt of incoming relief aid to Bogia and on to surrounding settlements, due to reliance on single access points located within the footprint of tephra fall. The influence of changing prevailing wind directions during the wet season would promote an east-

southeast dominated tephra dispersal leading to the key town of Bogia being impacted as well as both road routes from the provincial capital Madang.

5.2 Implications

This project set out to improve understanding of the behaviour and lava flow and tephra hazards of Manam volcano. In doing so, some of the findings have ramifications not just for Manam and Papua New Guinea, but also for the wider study of open-vent volcanoes and it is these implications that this section will examine.

5.2.1 Excess Degassing Timescales

The excess degassing phenomenon, where seemingly more magma is degassed than erupted, is frequently observed at persistently degassing open-vent volcanoes (Kazahaya et al. 1994; Shinohara 2008; Edmonds et al. 2010; Coppola et al. 2022; Lages et al. 2024). Generally excess degassing has been identified solely based on the persistent degassing in the absence of eruption (Allard 1997; Delgado-Granados et al. 2001; Beckett et al. 2014) or calculation mass flux using thermal radiance typically at lava lakes or domes (Harris et al. 1999; González et al. 2015; Coppola et al. 2022; Lages et al. 2024). The analysis of Manam's magma budget between 2018-2021 indicated that more magma was being erupted over the whole time series, but that excess degassing dominated from degassing Phase 2 onwards. This shows that there can be some intricacies regarding the timescales over which excess degassing is observed. The implication for the wider study of excess degassing is that volcanoes can be in a state of excess degassing over shorter timescales (e.g. daily,

weekly, monthly) but when analysed over longer timescales (e.g. annual, multi-annual, decadal) a volcano may have a balanced magma budget or even a deficit; or vice versa. This therefore suggests that timescale-based excess degassing definitions would benefit future classification and understanding of the phenomenon, in a similar way that Harris et al. (2007) sought to define classifications of lava effusion rates over different timescales. These more robust definitions would also provide an avenue for theoretically identifying systems that predominantly facilitate excess degassing by conduit convection and endogenous growth (Coppola et al. 2019) or those that expel their degassed magma when triggered by pressure fluctuations within subsurface storage regions. Such as the proposed magma recharge arrival at Manam in 2018 that was heralded by the extrusion and eruption of residual degassed magma (**Figure 2.31**), or a combination of both. Overall this work has shown the variability of the magma budget at one system over 4 years and in doing so has highlighted need to better constrain definitions of excess degassing in order to achieve a greater holistic view of the phenomenon globally. This work has also highlighted the utility of satellite remote sensing to reconstruct such chronologies.

5.2.2 Towards Forecasting Manam's Eruptions

Predicting or forecasting volcanic eruptions is widely considered to be the primary goal of volcanology (Scarpa 2001; Sparks 2003b; Poland and Anderson 2020; Acocella et al. 2024). This is particular challenge at open-vent volcanoes where geophysical signals that typically herald the movement of magma towards the surface at closed-vent systems are not often present (Palma et al. 2008). Instead,

rather than identifying the onset of renewed activity (e.g. recommenced inflation), changes in monitoring parameters from background typically need to be identified and these can often be subtle or difficult to detect except in hindsight (Palma et al. 2011; Johnson et al. 2018; Naismith et al. 2019). Chapter Two presented a conceptual model based on the thermal and SO_2 emissions at Manam, which explained explosive eruptions at Manam being the result of the repeated formation and failure of semi-permeable plugs in the conduit. A sharp decrease in SO_2 emissions occurred prior to the series of minor eruptions in June 2019 and again prior to the major 28 June 2019 eruption, and this is inferred to reflect the conduit sealing that led, ultimately, to the partial failure and subsequent complete failure of a plug.

Sealing is the reduction in permeability of a plug or lava dome reducing the ability for volatiles to escape to the atmosphere and can be inferred from reduced gas emissions (Edmonds et al. 2003a; Diller et al. 2006). Therefore, this project leads to two recommendations towards identifying precursory signals from Manam's SO_2 emissions. The first is to expand the analysis of thermal and SO_2 emissions alongside observed activity into the preceding and succeeding years. Satellite derived SO_2 emissions prior to May 2018 would require the integration of MODIS thermal anomaly detections alongside SO_2 emissions measured by the Ozone Monitoring Instrument (OMI) aboard NASA's Aura satellite (Carn et al. 2013; Fioletov et al. 2015). This would allow the examination of more eruptions to see if there is a pattern of reduced SO_2 emissions prior to explosive eruptions during normal open-vent behaviour. The second recommendation is to install ground-based SO_2

monitoring equipment such as an ultraviolet camera (Tamburello et al. 2011; Lages et al. 2019; Delle Donne et al. 2022) or scanning differential optical absorption spectrometer (ScanDOAS) (Arellano et al. 2021). This would provide high spatio-temporal resolution measurement of Manam's SO_2 emissions allowing the identification of eruption related SO_2 flux changes more precisely that may identify sealing events or other precursory signals in real time. The combination of these two recommendations would greatly improve the understanding of the mechanisms of plug-failure triggered eruptions at Manam and improve the ability for forecasting of future eruptions, allowing monitoring agencies, policy makers, and communities to be able to respond quicker to potential hazards that may result.

5.2.3 Hazard Awareness and Resilience

The most important implications of this work relate to how the new hazard information can be utilised by local communities and policy makers to augment hazard resilience and response measures. This project has modelled extents of lava flows and tephra deposition across various eruption scenarios, which provide a basis for renewed volcanic eruption response procedures and for long-term land use planning. This work indicates areas most likely to experience impactful tephra deposition, thus giving stakeholders (communities on Manam and the mainland, and monitoring agencies) quantitative and visual hazard information with which to make informed decisions regarding construction methods or the implementation of new agricultural practices that can increase food security resilience. This modelling of lava flow hazard also suggests that lava flows are unlikely to inundate Manam's

settlements but does highlight the requirement for improved awareness of how lava flow ocean entry sites may generate gas plumes that present a health risk. The modelling critically identifies the vent locations that are most likely to generate flows capable of reaching the coast, providing communities and policy makers with a simple way of assessing hazard at the beginning of an effusive eruption. The analysis of Manam's thermal and gas emissions have provided an interpretation of the processes at work in the shallow magmatic system that can be used to infer the state of the system by observing future emissions. Alongside the continued analysis of these emissions, and the seismic monitoring already in place, these findings represent a foundation from which to begin assessing the eruptive potential of Manam in the future.

To enable these results to be effective in a practical sense, the insights into the volcanological processes potentially driving Manam's activity and the modelled extents of lava flow and tephra hazards require communicating in an understandable format for non-specialists (Fearnley et al. 2018). Hazard maps that integrate individual hazard extents into combined zones of varying degrees of relative hazard are shown to be the most effective for communication to local populations (Lindsay and Robertson 2018; Thompson et al. 2018). Clear communication of hazard is vital for achieving appropriate hazard awareness and perception, as was found in the aftermath of the 1985 Nevado del Ruiz (Colombia) eruption where residents and local policymakers underestimated the hazard posed prior to the eruption (Voight 1990) and conversely the success of which was seen

from the mass self-evacuations during the 1994 eruptions of Rabaul (Papua New Guinea) (McKee et al. 2018).

5.3 Directions for Future Work

5.3.1 Fieldwork

The greatest limitation placed on this project was the inability to perform fieldwork on Manam, largely as a result of travel restrictions during a substantial portion of the study period. Each of the main chapters in this thesis would have benefited from data derived from field work. Therefore, for future iterations of this work it is suggested that field-based data collection be undertaken where possible. The collection of lava and tephra samples would offer improved constraints on input parameters used in modelling of both hazards including: updated compositional data (used to calculate multiple parameters for lava flow modelling), representative quantification of the range in vesicularity of both products, and specific tephra densities. UAS photogrammetric surveys of the avalanche valleys would allow the production of an up-to-date DEM on which to model future lava flows (Favalli et al. 2018; Vieira et al. 2021). This would have also enabled the accurate measurement of previously emplaced lava flow geometric properties (e.g. length, width, thicknesses, channel ratios) (Bretar et al. 2013; Cashman et al. 2013) to improve upon those estimated from satellite imagery used in this work.

Field-based data collection of SO_2 emissions using a ultraviolet camera would enable the creation of a high spatio-temporal resolution timeseries, which would provide insights into the timescales of the processes proposed to explain Manam's

activity (Tamburello et al. 2011; Lages et al. 2019). Specifically, this dataset would quantify outgassing dynamics on much shorter (sub-daily) timescales compared to satellite remote sensing observations; this may aid the identification of geochemical eruptive precursors. Additionally, in-situ gas plume compositional data acquired using a UAS-mounted MultiGAS would allow a) the calculation of CO_2 and H_2S fluxes based on combining measured mixing ratios with the SO_2 flux measured independently using the ultraviolet camera, and b) enabled the inference of the depths of the magmatic degassing through comparing measured ratios to thermodynamic decompression degassing models, initiated using petrological constraints on Manam's primary melt and volatile compositions (Shinohara 2005; Aiuppa et al. 2007; Liu et al. 2019, 2020a).

5.3.2 Seismo-Acoustic Monitoring

This project sought to demonstrate the utility of satellite remote sensing techniques to study the behaviour of a lesser studied, remote and largely inaccessible volcano. A future enhancement of this work would to incorporate seismic and infrasound monitoring of Manam to achieve another dimension to the multi-parameter approach used here. Utilising data from the regional seismometer network or installing additional seismometers on Manam itself would provide further insight into sub-surface processes operating at Manam over the study period. Seismic monitoring of open-vent systems has played a key part in studies that have identified cyclic behaviour at open-vent volcanoes and has enabled the identification of various types of sub-aerial and sub-surface explosions and their generating mechanisms (Palma et al. 2008; Lyons et al. 2010; Naismith et al. 2019).

Open-vent volcanic systems have been shown to be particularly effective producers of resonant infrasound tones and these have been used to infer the height of magma columns (Ripepe et al. 2007; Sciotto et al. 2022) and lava lakes (Johnson et al. 2018; Barrière et al. 2018), which has been shown to provide a surface representation of changes in shallow reservoir pressure and has been observed at some systems as a repeated precursor to passive to explosive transitions (e.g., Villarrica, Fuego, Stromboli). A future research avenue here would be to test and calibrate the method for estimating intra-crater magma level at Manam (presented in Chapter 2) against infrasound calculated lava lake levels. A further ambition would be to implement infrasound monitoring equipment at Manam to provide estimates of sub-surface magma column depths alongside thermal remote sensing to gauge system pressure (Patrick et al. 2015a).

5.3.3 Pyroclastic Density Current and Lahar Hazards

In addition to lava flow and tephra deposition hazard, Manam is also capable of generating lahars and pyroclastic density currents (PDC). Lahars are volcanic mudflows consisting generally of tephra and other volcanic products generated from heavy rainfall or melting of glaciers during volcanic unrest (Thouret et al. 2020). Lahars on Manam pose a direct threat to life as demonstrated by the 13 March 2007 lahar which killed four people (Global Volcanism Program). Manam's is able to generate both block and ash flow and column collapse PDCs, with the former generally constrained within the avalanche valleys (Palfreyman and Cooke 1976; McKee et al. 2018; Global Volcanism Program 2024). Notable recent examples were the southwest valley channelled 28 November 1992 PDC which

destroyed Budua Old Village killing 13 and those generated during the 28 June 2019 eruption that flowed down the northeast and western flanks (Global Volcanism Program 2019b). To undertake a comprehensive hazard assessment it is suggested that lahars and PDCs should be modelled using a scenario-based approach (such as those adopted in Chapters 3 and 4) using numerical models such as *LAHARZ* (Schilling 1998) and *TITAN2D* (Sheridan et al. 2005). The output from these modelled hazard assessments would ideally be combined with the lava and tephra deposition modelling presented in this work to produce a comprehensive view of hazard of Manam volcano in accessible and useful formats for all stakeholders.

6 References

Abbott LD (1995) Neogene tectonic reconstruction of the Adelbert-Finisterre-New Britain collision, northern Papua New Guinea. J Southeast Asian Earth Sci 11:33–51. https://doi.org/10.1016/0743-9547(94)00032-A

Abbott LD, Silver EA, Galewsky J (1994) Structural evolution of a modern arc-continent collision in Papua New Guinea. Tectonics 13:1007–1034. https://doi.org/10.1029/94TC01623

Abers GA, Roecker SW (1991) Deep structure of an arc-continent collision: Earthquake relocation and inversion for upper mantle P and S wave velocities beneath Papua New Guinea. J Geophys Res Solid Earth 96:6379–6401. https://doi.org/10.1029/91JB00145

Abrams M, Crippen R, Fujisada H (2020) ASTER global digital elevation model (GDEM) and ASTER global water body dataset (ASTWBD). Remote Sens 12:1156

Abrams M, Yamaguchi Y, Crippen R (2022) Aster Global Dem (GDEM) Version 3. Int Arch Photogramm Remote Sens Spat Inf Sci 43:593–598

Acocella V, Neri M (2009) Dike propagation in volcanic edifices: Overview and possible developments. Tectonophysics 471:67–77. https://doi.org/10.1016/j.tecto.2008.10.002

Acocella V, Ripepe M, Rivalta E, et al (2024) Towards scientific forecasting of magmatic eruptions. Nat Rev Earth Environ 5:5–22. https://doi.org/10.1038/s43017-023-00492-z

Aiuppa A (2015) Volcanic-gas monitoring. In: Volcanism and Global Environmental Change. Cambridge University Press, pp 81–96

Aiuppa A, Bitetto M, Calabrese S, et al (2022) Mafic magma feeds degassing unrest at Vulcano Island, Italy. Commun Earth Environ 3:1–15. https://doi.org/10.1038/s43247-022-00589-1

Aiuppa A, Bitetto M, Delle Donne D, et al (2021) Volcanic CO2 tracks the incubation period of basaltic paroxysms. Sci Adv 7:eabh0191. https://doi.org/10.1126/sciadv.abh0191

Aiuppa A, Bitetto M, Francofonte V, et al (2017) A CO2-gas precursor to the March 2015 Villarrica volcano eruption. Geochem Geophys Geosystems 18:2120–2132. https://doi.org/10.1002/2017GC006892

Aiuppa A, Burton M, Caltabiano T, et al (2010) Unusually large magmatic CO2 gas emissions prior to a basaltic paroxysm. Geophys Res Lett 37:. https://doi.org/10.1029/2010GL043837

Aiuppa A, de Moor JM, Arellano S, et al (2018) Tracking Formation of a Lava Lake From Ground and Space: Masaya Volcano (Nicaragua), 2014–2017. Geochem Geophys Geosystems 19:496–515. https://doi.org/10.1002/2017GC007227

Aiuppa A, Fischer TP, Plank T, Bani P (2019) CO2 flux emissions from the Earth's most actively degassing volcanoes, 2005–2015. Sci Rep 9:5442. https://doi.org/10.1038/s41598-019-41901-y

Aiuppa A, Moretti R, Federico C, et al (2007) Forecasting Etna eruptions by real-time observation of volcanic gas composition. Geology 35:1115–1118. https://doi.org/10.1130/G24149A.1

Aiuppa A, Robidoux P, Tamburello G, et al (2014) Gas measurements from the Costa Rica–Nicaragua volcanic segment suggest possible along-arc variations in volcanic gas chemistry. Earth Planet Sci Lett 407:134–147. https://doi.org/10.1016/j.epsl.2014.09.041

Albino F, Biggs J, Yu C, Li Z (2020) Automated Methods for Detecting Volcanic Deformation Using Sentinel-1 InSAR Time Series Illustrated by the 2017–2018 Unrest at Agung, Indonesia. J Geophys Res Solid Earth 125:e2019JB017908. https://doi.org/10.1029/2019JB017908

Alfano F, Bonadonna C, Volentik ACM, et al (2011) Tephra stratigraphy and eruptive volume of the May, 2008, Chaitén eruption, Chile. Bull Volcanol 73:613–630. https://doi.org/10.1007/s00445-010-0428-x

Alfano F, Bonadonna C, Watt S, et al (2016) Reconstruction of total grain size distribution of the climactic phase of a long-lasting eruption: the example of the 2008–2013 Chaitén eruption. Bull Volcanol 78:46. https://doi.org/10.1007/s00445-016-1040-5

Allard P (1997) Endogenous magma degassing and storage at Mount Etna. Geophys Res Lett 24:2219–2222. https://doi.org/10.1029/97GL02101

Allard P, Burton M, Muré F (2005) Spectroscopic evidence for a lava fountain driven by previously accumulated magmatic gas. Nature 433:407–410. https://doi.org/10.1038/nature03246

Allard P, Carbonnelle J, Métrich N, et al (1994) Sulphur output and magma degassing budget of Stromboli volcano. Nature 368:326–330. https://doi.org/10.1038/368326a0

Anderson KR, Poland MP, Johnson JH, Miklius A (2015) Episodic Deflation–Inflation Events at Kīlauea Volcano and Implications for the Shallow Magma System. In: Hawaiian Volcanoes. American Geophysical Union (AGU), pp 229–250

Andreastuti S, Paripurno E, Gunawan H, et al (2019) Character of community response to volcanic crises at Sinabung and Kelud volcanoes. J Volcanol Geotherm Res 382:298–310. https://doi.org/10.1016/j.jvolgeores.2017.01.022

Andres RJ, Kasgnoc AD (1998) A time-averaged inventory of subaerial volcanic sulfur emissions. J Geophys Res Atmospheres 103:25251–25261. https://doi.org/10.1029/98JD02091

Andronico D, Corsaro RA (2011) Lava fountains during the episodic eruption of South–East Crater (Mt. Etna), 2000: insights into magma-gas dynamics within the shallow volcano plumbing system. Bull Volcanol 73:1165–1178. https://doi.org/10.1007/s00445-011-0467-y

Andronico D, Del Bello E, D'Oriano C, et al (2021) Uncovering the eruptive patterns of the 2019 double paroxysm eruption crisis of Stromboli volcano. Nat Commun 12:4213. https://doi.org/10.1038/s41467-021-24420-1

Andronico D, Del Carlo P (2016) PM_{10} measurements in urban settlements after lava fountain episodes at Mt. Etna, Italy: pilot test to assess volcanic ash hazard to human health. Nat Hazards Earth Syst Sci 16:29–40. https://doi.org/10.5194/nhess-16-29-2016

Andronico D, Lodato L (2005) Effusive Activity at Mount Etna Volcano (Italy) During the 20th Century: A Contribution to Volcanic Hazard Assessment. Nat Hazards 36:407–443. https://doi.org/10.1007/s11069-005-1938-2

Applegarth LJ, Tuffen H, James MR, Pinkerton H (2013a) Degassing-driven crystallisation in basalts. Earth-Sci Rev 116:1–16. https://doi.org/10.1016/j.earscirev.2012.10.007

Applegarth LJane, Tuffen H, James MR, et al (2013b) Direct observations of degassing-induced crystallization in basalts. Geology 41:243–246. https://doi.org/10.1130/G33641.1

Arellano S, Galle B, Apaza F, et al (2021) Synoptic analysis of a decade of daily measurements of SO_2 emission in the troposphere from volcanoes of the global ground-based Network for Observation of Volcanic and Atmospheric Change. Earth Syst Sci Data 13:1167–1188. https://doi.org/10.5194/essd-13-1167-2021

Arnalds O (2013) Chapter Six - The Influence of Volcanic Tephra (Ash) on Ecosystems. In: Sparks DL (ed) Advances in Agronomy. Academic Press, pp 331–380

Arzilli F, Morgavi D, Petrelli M, et al (2019) The unexpected explosive sub-Plinian eruption of Calbuco volcano (22–23 April 2015; southern Chile): Triggering mechanism implications. J Volcanol Geotherm Res 378:35–50. https://doi.org/10.1016/j.jvolgeores.2019.04.006

Aso N, Tsai VC (2014) Cooling magma model for deep volcanic long-period earthquakes. J Geophys Res Solid Earth 119:8442–8456. https://doi.org/10.1002/2014JB011180

Augustus E, Murphy MM, Guell C, et al (2023) The double burden of COVID-19 and a major volcanic eruption on local food production and food security in a Small Island Developing State. Front Sustain Food Syst 7:. https://doi.org/10.3389/fsufs.2023.1268330

Auker MR, Sparks RSJ, Siebert L, et al (2013) A statistical analysis of the global historical volcanic fatalities record. J Appl Volcanol 2:2. https://doi.org/10.1186/2191-5040-2-2

Avolio MV, Crisci GM, Di Gregorio S, et al (2006) SCIARA *γ*2: An improved cellular automata model for lava flows and applications to the 2002 Etnean crisis. Comput Geosci 32:876–889. https://doi.org/10.1016/j.cageo.2005.10.026

Ayris PM, Delmelle P (2012) The immediate environmental effects of tephra emission. Bull Volcanol 74:1905–1936

Baloga S, Spudis PD, Guest JE (1995) The dynamics of rapidly emplaced terrestrial lava flows and implications for planetary volcanism. J Geophys Res Solid Earth 100:24509–24519. https://doi.org/10.1029/95JB02844

Bamber EC, Arzilli F, Polacci M, et al (2020) Pre- and syn-eruptive conditions of a basaltic Plinian eruption at Masaya Volcano, Nicaragua: The Masaya Triple Layer (2.1 ka). J Volcanol Geotherm Res 392:106761. https://doi.org/10.1016/j.jvolgeores.2019.106761

Bamber EC, La Spina G, Arzilli F, et al (2022) Basaltic Plinian eruptions at Las Sierras-Masaya volcano driven by cool storage of crystal-rich magmas. Commun Earth Environ 3:1–17. https://doi.org/10.1038/s43247-022-00585-5

Barberi F (1990) Mt. Etna: the 1989 eruption. American Geophysical Union

Barclay J, Few R, Armijos MT, et al (2019) Livelihoods, wellbeing and the risk to life during volcanic eruptions. Front Earth Sci 7:205

Barragan LD, Maio LD, Hardy M-PR, et al (2022) Impact assessment of buildings exposed to the tephra fallout of the 2021 Cumbre Vieja eruption in La Palma, Spain. Copernicus Meetings

Barrière J, d'Oreye N, Oth A, et al (2018) Single-Station Seismo-Acoustic Monitoring of Nyiragongo's Lava Lake Activity (D.R. Congo). Front Earth Sci 6:. https://doi.org/10.3389/feart.2018.00082

Barrière J, d'Oreye N, Smets B, et al (2022) Intra-Crater Eruption Dynamics at Nyiragongo (D.R. Congo), 2002–2021. J Geophys Res Solid Earth 127:e2021JB023858. https://doi.org/10.1029/2021JB023858

Barsotti S, Andronico D, Neri A, et al (2010) Quantitative assessment of volcanic ash hazards for health and infrastructure at Mt. Etna (Italy) by numerical simulation. J Volcanol Geotherm Res 192:85–96. https://doi.org/10.1016/j.jvolgeores.2010.02.011

Barsotti S, Di Rienzo DI, Thordarson T, et al (2018) Assessing Impact to Infrastructures Due to Tephra Fallout From Öræfajökull Volcano (Iceland) by Using a Scenario-Based Approach and a Numerical Model. Front Earth Sci 6:

Battaglia J, Hidalgo S, Bernard B, et al (2019) Autopsy of an eruptive phase of Tungurahua volcano (Ecuador) through coupling of seismo-acoustic and SO2 recordings with ash characteristics. Earth Planet Sci Lett 511:223–232. https://doi.org/10.1016/j.epsl.2019.01.042

Bazargan M, Gudmundsson A (2019) Dike-induced stresses and displacements in layered volcanic zones. J Volcanol Geotherm Res 384:189–205. https://doi.org/10.1016/j.jvolgeores.2019.07.010

Bebbington M, Cronin SJ, Chapman I, Turner MB (2008) Quantifying volcanic ash fall hazard to electricity infrastructure. J Volcanol Geotherm Res 177:1055–1062. https://doi.org/10.1016/j.jvolgeores.2008.07.023

Beckett FM, Burton M, Mader HM, et al (2014) Conduit convection driving persistent degassing at basaltic volcanoes. J Volcanol Geotherm Res 283:19–35. https://doi.org/10.1016/j.jvolgeores.2014.06.006

Beckett FM, Mader HM, Phillips JC, et al (2011) An experimental study of low-Reynolds-number exchange flow of two Newtonian fluids in a vertical pipe. J Fluid Mech 682:652–670. https://doi.org/10.1017/jfm.2011.264

Behncke B, Fornaciai A, Neri M, et al (2016) Lidar surveys reveal eruptive volumes and rates at Etna, 2007–2010. Geophys Res Lett 43:4270–4278. https://doi.org/10.1002/2016GL068495

Beirle S, Hörmann C, Penning de Vries M, et al (2014) Estimating the volcanic emission rate and atmospheric lifetime of SO_2 from space: a case study for Kīlauea volcano, Hawai`i. Atmospheric Chem Phys 14:8309–8322. https://doi.org/10.5194/acp-14-8309-2014

Berk A, Conforti P, Kennett R, et al (2014) MODTRAN® 6: A major upgrade of the MODTRAN® radiative transfer code. In: 2014 6th Workshop on Hyperspectral Image and Signal Processing: Evolution in Remote Sensing (WHISPERS). pp 1–4

Best JG (1956) Investigations of recent volcanic activity in the Territory of New Guinea. Proc 8th Pac Sci Congr1953 Manila 2:180–204

Best JG (1953) Territory of Papua and New Guinea, report of investigation of volcanic activity Manam Island, T.N.G., April, 1953. Geoscience Australia, Canberra

Bevilacqua A, Macedonio G, Neri A, et al (2022) Volcanic Hazard Assessment at the Campi Flegrei Caldera, Italy. In: Orsi G, D'Antonio M, Civetta L (eds) Campi Flegrei: A Restless Caldera in a Densely Populated Area. Springer, Berlin, Heidelberg, pp 311–355

Biass S, Bonadonna C, Connor L, Connor C (2016) TephraProb: a Matlab package for probabilistic hazard assessments of tephra fallout. J Appl Volcanol 5:10. https://doi.org/10.1186/s13617-016-0050-5

Biass S, Jenkins SF, Aeberhard WH, et al (2022) Insights into the vulnerability of vegetation to tephra fallouts from interpretable machine learning and big Earth observation data. Nat Hazards Earth Syst Sci 22:2829–2855. https://doi.org/10.5194/nhess-22-2829-2022

Biass S, Reyes-Hardy M-P, Gregg C, et al (2024) The spatiotemporal evolution of compound impacts from lava flow and tephra fallout on buildings: lessons from the 2021 Tajogaite eruption (La Palma, Spain). Bull Volcanol 86:10. https://doi.org/10.1007/s00445-023-01700-w

Biass S, Todde A, Cioni R, et al (2017) Potential impacts of tephra fallout from a large-scale explosive eruption at Sakurajima volcano, Japan. Bull Volcanol 79:73. https://doi.org/10.1007/s00445-017-1153-5

Bird DK, Gísladóttir G, Dominey-Howes D (2011) Different communities, different perspectives: issues affecting residents' response to a volcanic eruption in southern Iceland. Bull Volcanol 73:1209–1227. https://doi.org/10.1007/s00445-011-0464-1

Bisson M, Spinetti C, Neri M, Bonforte A (2016) Mt. Etna volcano high-resolution topography: airborne LiDAR modelling validated by GPS data. Int J Digit Earth 9:710–732. https://doi.org/10.1080/17538947.2015.1119208

Blackett M (2017) An Overview of Infrared Remote Sensing of Volcanic Activity. J Imaging 3:13. https://doi.org/10.3390/jimaging3020013

Blackett M (2013) Review of the utility of infrared remote sensing for detecting and monitoring volcanic activity with the case study of shortwave infrared data for Lascar Volcano from 2001–2005. Geol Soc Lond Spec Publ 380:107–135. https://doi.org/10.1144/SP380.10

Blackett M (2014) Early Analysis of Landsat-8 Thermal Infrared Sensor Imagery of Volcanic Activity. Remote Sens 6:2282–2295. https://doi.org/10.3390/rs6032282

Blake DM, Deligne NI, Wilson TM, Wilson G (2017) Improving volcanic ash fragility functions through laboratory studies: example of surface transportation networks. J Appl Volcanol 6:16. https://doi.org/10.1186/s13617-017-0066-5

Blake DM, Wilson TM, Gomez C (2016) Road marking coverage by volcanic ash: an experimental approach. Environ Earth Sci 75:1348. https://doi.org/10.1007/s12665-016-6154-8

Blong R (2003) Building damage in Rabaul, Papua New Guinea, 1994. Bull Volcanol 65:43–54. https://doi.org/10.1007/s00445-002-0238-x

Blong RJ (1984) Volcanic Hazards: A Sourcebook on the Effects of Eruptions. Elsevier

Blong RJ (1996) Volcanic Hazards Risk Assessment. In: Scarpa R, Tilling RI (eds) Monitoring and Mitigation of Volcano Hazards. Springer, Berlin, Heidelberg, pp 675–698

Boltzmann L (1884) Ableitung des Stefan'schen Gesetzes, betreffend die Abhangigkeit der Warmestrahlung von der Temperatur aus der elctromagenetischen-Lichttheorie. Ann Phys Chem 22:291–294

Bonadonna C, Biass S, Costa A (2015a) Physical characterization of explosive volcanic eruptions based on tephra deposits: Propagation of uncertainties and sensitivity analysis. J Volcanol Geotherm Res 296:80–100. https://doi.org/10.1016/j.jvolgeores.2015.03.009

Bonadonna C, Biass S, Menoni S, Gregg CE (2021a) Chapter 8 - Assessment of risk associated with tephra-related hazards. In: Papale P (ed) Forecasting and Planning for Volcanic Hazards, Risks, and Disasters. Elsevier, pp 329–378

Bonadonna C, Connor CB, Houghton BF, et al (2005) Probabilistic modeling of tephra dispersal: Hazard assessment of a multiphase rhyolitic eruption at Tarawera, New Zealand. J Geophys Res Solid Earth 110:. https://doi.org/10.1029/2003JB002896

Bonadonna C, Connor L, Connor C, Courtland L (2014a) Tephra2

Bonadonna C, Connor LJ, Connor CB, Courtland LM (2014b) Tephra2

Bonadonna C, Costa A (2012) Estimating the volume of tephra deposits: A new simple strategy. Geology 40:415–418. https://doi.org/10.1130/G32769.1

Bonadonna C, Costa A (2013) Modeling of tephra sedimentation from volcanic plumes. Model Volcan Process Phys Math Volcanism 173–202

Bonadonna C, Costa A, Folch A, Koyaguchi T (2015b) Chapter 33 - Tephra Dispersal and Sedimentation. In: Sigurdsson H (ed) The Encyclopedia of Volcanoes (Second Edition). Academic Press, Amsterdam, pp 587–597

Bonadonna C, Frischknecht C, Menoni S, et al (2021b) Integrating hazard, exposure, vulnerability and resilience for risk and emergency management in a volcanic context: the ADVISE model. J Appl Volcanol 10:7. https://doi.org/10.1186/s13617-021-00108-5

Bonadonna C, Houghton BF (2005) Total grain-size distribution and volume of tephra-fall deposits. Bull Volcanol 67:441–456. https://doi.org/10.1007/s00445-004-0386-2

Bonadonna C, Macedonio G, Sparks RSJ (2002) Numerical modelling of tephra fallout associated with dome collapses and Vulcanian explosions: application to hazard assessment on Montserrat. Geol Soc Lond Mem 21:517–537. https://doi.org/10.1144/GSL.MEM.2002.021.01.23

Bonny E, Thordarson T, Wright R, et al (2018) The Volume of Lava Erupted During the 2014 to 2015 Eruption at Holuhraun, Iceland: A Comparison Between Satellite- and Ground-Based Measurements. J Geophys Res Solid Earth 123:5412–5426. https://doi.org/10.1029/2017JB015008

Bottinga Y, Weill DF (1970) Densities of liquid silicate systems calculated from partial molar volumes of oxide components. Am J Sci 269:169–182

Bouche E, Vergniolle S, Staudacher T, et al (2010) The role of large bubbles detected from acoustic measurements on the dynamics of Erta 'Ale lava lake (Ethiopia). Earth Planet Sci Lett 295:37–48. https://doi.org/10.1016/j.epsl.2010.03.020

Branca S, De Beni E, Chester D, et al (2017) The 1928 eruption of Mount Etna (Italy): Reconstructing lava flow evolution and the destruction and recovery of the town of Mascali. J Volcanol Geotherm Res 335:54–70. https://doi.org/10.1016/j.jvolgeores.2017.02.002

Branca S, De Beni E, Proietti C (2013) The large and destructive 1669 AD eruption at Etna volcano: reconstruction of the lava flow field evolution and effusion rate trend. Bull Volcanol 75:694. https://doi.org/10.1007/s00445-013-0694-5

Branch CD (1965) The April 1964 eruption of Manam Volcano. Geoscience Australia, Canberra

Branch CD (1967) Short Papers from the Vulcanological Observatory, Rabaul, New Britain. Department of National Development, Bureau of Mineral Resources, Geology and ...

Brand BD, Mackaman-Lofland C, Pollock NM, et al (2014) Dynamics of pyroclastic density currents: Conditions that promote substrate erosion and self-channelization — Mount St Helens, Washington (USA). J Volcanol Geotherm Res 276:189–214. https://doi.org/10.1016/j.jvolgeores.2014.01.007

Brazier S, Davis AN, Sigurdsson H, Sparks RSJ (1982) Fall-out and deposition of volcanic ash during the 1979 explosive eruption of the soufriere of St. Vincent. J Volcanol Geotherm Res 14:335–359. https://doi.org/10.1016/0377-0273(82)90069-5

Bretar F, Arab-Sedze M, Champion J, et al (2013) An advanced photogrammetric method to measure surface roughness: Application to volcanic terrains in the Piton de la Fournaise, Reunion Island. Remote Sens Environ 135:1–11. https://doi.org/10.1016/j.rse.2013.03.026

Brown RJ, Bonadonna C, Durant AJ (2012) A review of volcanic ash aggregation. Phys Chem Earth Parts ABC 45–46:65–78. https://doi.org/10.1016/j.pce.2011.11.001

Brown SK, Jenkins SF, Sparks RSJ, et al (2017) Volcanic fatalities database: analysis of volcanic threat with distance and victim classification. J Appl Volcanol 6:15. https://doi.org/10.1186/s13617-017-0067-4

Brown SK, Loughlin SC, Sparks RSJ, Vye-Brown C (2015) Global volcanic hazards and risk: Technical background paper for the UN-ISDR Global Assessment Report on Disaster Risk Reduction 2015. Global Volcano Model and the International Association of Volcanology and Chemistry of the Earth's Interior

Buchhorn M, Smets B, Bertels L, et al (2020) Copernicus Global Land Service: Land Cover 100m: collection 3: epoch 2019: Globe

Buckland HM, Mastin LG, Engwell SL, Cashman KV (2022) Modelling the transport and deposition of ash following a magnitude 7 eruption: the distal Mazama tephra. Bull Volcanol 84:87. https://doi.org/10.1007/s00445-022-01593-1

Burgi P-Y, Darrah TH, Tedesco D, Eymold WK (2014) Dynamics of the Mount Nyiragongo lava lake. J Geophys Res Solid Earth 119:4106–4122. https://doi.org/10.1002/2013JB010895

Burgisser A, Arbaret L, Druitt TH, Giachetti T (2011) Pre-explosive conduit conditions of the 1997 Vulcanian explosions at Soufrière Hills Volcano, Montserrat: II. Overpressure and depth distributions. J Volcanol Geotherm Res 199:193–205. https://doi.org/10.1016/j.jvolgeores.2010.11.014

Burgisser A, Degruyter W (2015) Chapter 11 - Magma Ascent and Degassing at Shallow Levels. In: Sigurdsson H (ed) The Encyclopedia of Volcanoes (Second Edition). Academic Press, Amsterdam, pp 225–236

Bursik M (2001) Effect of wind on the rise height of volcanic plumes. Geophys Res Lett 28:3621–3624. https://doi.org/10.1029/2001GL013393

Bursik M (1998) Tephra dispersal. Geol Soc Lond Spec Publ 145:115–144. https://doi.org/10.1144/GSL.SP.1996.145.01.07

Bursik MI, Sparks RSJ, Gilbert JS, Carey SN (1992) Sedimentation of tephra by volcanic plumes: I. Theory and its comparison with a study of the Fogo A plinian deposit, Sao Miguel (Azores). Bull Volcanol 54:329–344. https://doi.org/10.1007/BF00301486

Burton M, Allard P, Muré F, La Spina A (2007) Magmatic Gas Composition Reveals the Source Depth of Slug-Driven Strombolian Explosive Activity. Science 317:227–230. https://doi.org/10.1126/science.1141900

Burton M, Hayer C, Miller C, Christenson B (2021) Insights into the 9 December 2019 eruption of Whakaari/White Island from analysis of TROPOMI SO2 imagery. Sci Adv 7:. https://doi.org/10.1126/sciadv.abg1218

Businger S, Huff R, Pattantyus A, et al (2015) Observing and Forecasting Vog Dispersion from Kīlauea Volcano, Hawaii. Bull Am Meteorol Soc 96:1667–1686. https://doi.org/10.1175/BAMS-D-14-00150.1

Calder ES, Cole PD, Dade WB, et al (1999) Mobility of pyroclastic flows and surges at the Soufriere Hills Volcano, Montserrat. Geophys Res Lett 26:537–540. https://doi.org/10.1029/1999GL900051

Calder ES, Lavallée Y, Kendrick JE, Bernstein M (2015a) Chapter 18 - Lava Dome Eruptions. In: Sigurdsson H (ed) The Encyclopedia of Volcanoes (Second Edition). Academic Press, Amsterdam, pp 343–362

Calder ES, Sparks RSJ, Gardeweg MC (2000) Erosion, transport and segregation of pumice and lithic clasts in pyroclastic flows inferred from ignimbrite at Lascar Volcano, Chile. J Volcanol Geotherm Res 104:201–235. https://doi.org/10.1016/S0377-0273(00)00207-9

Calder ES, Wagner K, Ogburn S (2015b) Volcanic hazard maps. Glob Volcan Hazards Risk 335–342

Calvari S, Biale E, Bonaccorso A, et al (2022a) Explosive Paroxysmal Events at Etna Volcano of Different Magnitude and Intensity Explored through a Multidisciplinary Monitoring System. Remote Sens 14:4006. https://doi.org/10.3390/rs14164006

Calvari S, Di Traglia F, Ganci G, et al (2022b) Multi-parametric study of an eruptive phase comprising unrest, major explosions, crater failure, pyroclastic density currents and lava flows: Stromboli volcano, 1 December 2020–30 June 2021. Front Earth Sci 10:

Calvari S, Lodato L, Spampinato L (2004) Monitoring active volcanoes using a handheld thermal camera. In: Thermosense XXVI. SPIE, pp 199–209

Calvari S, Spampinato L, Bonaccorso A, et al (2011) Lava effusion — A slow fuse for paroxysms at Stromboli volcano? Earth Planet Sci Lett 301:317–323. https://doi.org/10.1016/j.epsl.2010.11.015

Campbell JB, Wynne RH (2011) Introduction to Remote Sensing, Fifth Edition. Guilford Press

Campion R, Coppola D (2023) Classification of lava lakes based on their heat and SO2 emission: Implications for their formation and feeding processes. Front Earth Sci 11:1040199. https://doi.org/10.3389/feart.2023.1040199

Campion R, Delgado-Granados H, Legrand D, et al (2018a) Breathing and Coughing: The Extraordinarily High Degassing of Popocatépetl Volcano Investigated With an SO2 Camera. Front Earth Sci 6:

Campion R, Delgado-Granados H, Legrand D, et al (2018b) Breathing and Coughing: The Extraordinarily High Degassing of Popocatépetl Volcano Investigated With an SO2 Camera. Front Earth Sci 6:. https://doi.org/10.3389/feart.2018.00163

Campus A, Laiolo M, Massimetti F, Coppola D (2022) The Transition from MODIS to VIIRS for Global Volcano Thermal Monitoring. Sensors 22:1713. https://doi.org/10.3390/s22051713

Cannata A, Di Grazia G, Giuffrida M, et al (2018) Space-Time Evolution of Magma Storage and Transfer at Mt. Etna Volcano (Italy): The 2015–2016 Reawakening of Voragine Crater. Geochem Geophys Geosystems 19:471–495. https://doi.org/10.1002/2017GC007296

Cappello A, Hérault A, Bilotta G, et al (2016) MAGFLOW: a physics-based model for the dynamics of lava-flow emplacement. Geol Soc Lond Spec Publ 426:357–373. https://doi.org/10.1144/SP426.16

Carey RJ, Houghton BF, Sable JE, Wilson CJN (2007) Contrasting grain size and componentry in complex proximal deposits of the 1886 Tarawera basaltic Plinian eruption. Bull Volcanol 69:903–926. https://doi.org/10.1007/s00445-007-0117-6

Carey RJ, Manga M, Degruyter W, et al (2013) Convection in a volcanic conduit recorded by bubbles. Geology 41:395–398. https://doi.org/10.1130/G33685.1

Carey S, Sigurdsson H (1989) The intensity of plinian eruptions. Bull Volcanol 51:28–40. https://doi.org/10.1007/BF01086759

Carey S, Sparks RSJ (1986) Quantitative models of the fallout and dispersal of tephra from volcanic eruption columns. Bull Volcanol 48:109–125. https://doi.org/10.1007/BF01046546

Caricchi L, Sheldrake TE, Blundy J (2018) Modulation of magmatic processes by CO2 flushing. Earth Planet Sci Lett 491:160–171. https://doi.org/10.1016/j.epsl.2018.03.042

Caricchi L, Townsend M, Rivalta E, Namiki A (2021) The build-up and triggers of volcanic eruptions. Nat Rev Earth Environ 2:458–476. https://doi.org/10.1038/s43017-021-00174-8

Carn SA, Clarisse L, Prata AJ (2016) Multi-decadal satellite measurements of global volcanic degassing. J Volcanol Geotherm Res 311:99–134. https://doi.org/10.1016/j.jvolgeores.2016.01.002

Carn SA, Fioletov VE, McLinden CA, et al (2017) A decade of global volcanic SO2 emissions measured from space. Sci Rep 7:44095. https://doi.org/10.1038/srep44095

Carn SA, Krotkov NA, Yang K, Krueger AJ (2013) Measuring global volcanic degassing with the Ozone Monitoring Instrument (OMI). Geol Soc Lond Spec Publ 380:229–257. https://doi.org/10.1144/SP380.12

Cashman KV, Rust AC (2020) Far-travelled ash in past and future eruptions: combining tephrochronology with volcanic studies. J Quat Sci 35:11–22. https://doi.org/10.1002/jqs.3159

Cashman KV, Soule SA, Mackey BH, et al (2013) How lava flows: New insights from applications of lidar technologies to lava flow studies. Geosphere 9:1664–1680. https://doi.org/10.1130/GES00706.1

Cassidy M, Manga M, Cashman K, Bachmann O (2018a) Controls on explosive-effusive volcanic eruption styles. Nat Commun 9:2839. https://doi.org/10.1038/s41467-018-05293-3

Cassidy M, Manga M, Cashman K, Bachmann O (2018b) Controls on explosive-effusive volcanic eruption styles. Nat Commun 9:2839. https://doi.org/10.1038/s41467-018-05293-3

Castruccio A, Contreras MA (2016) The influence of effusion rate and rheology on lava flow dynamics and morphology: A case study from the 1971 and 1988–1990 eruptions at Villarrica and Lonquimay volcanoes, Southern Andes of Chile. J Volcanol Geotherm Res 327:469–483. https://doi.org/10.1016/j.jvolgeores.2016.09.015

Charbonnier SJ, Gertisser R (2008) Field observations and surface characteristics of pristine block-and-ash flow deposits from the 2006 eruption of Merapi Volcano, Java, Indonesia. J Volcanol Geotherm Res 177:971–982. https://doi.org/10.1016/j.jvolgeores.2008.07.008

Charlton D, Kilburn C, Edwards S (2020) Volcanic unrest scenarios and impact assessment at Campi Flegrei caldera, Southern Italy. J Appl Volcanol 9:7. https://doi.org/10.1186/s13617-020-00097-x

Chaussard E, Amelung F, Aoki Y (2013) Characterization of open and closed volcanic systems in Indonesia and Mexico using InSAR time series. J Geophys Res Solid Earth 118:3957–3969. https://doi.org/10.1002/jgrb.50288

Chester DK, Duncan AM, Guest JE, Kilburn CRJ (1985) Geological setting and volcanic history. In: Chester DK, Duncan AM, Guest JE, Kilburn CRJ (eds) Mount Etna: The anatomy of a volcano. Springer Netherlands, Dordrecht, pp 65–122

Chevrel MO, Labroquère J, Harris AJL, Rowland SK (2018) PyFLOWGO: An open-source platform for simulation of channelized lava thermo-rheological properties. Comput Geosci 111:167–180. https://doi.org/10.1016/j.cageo.2017.11.009

Cioni R, Pistolesi M, Rosi M (2015) Plinian and subplinian eruptions. In: The encyclopedia of volcanoes. Elsevier, pp 519–535

Clarke AB, Ongaro TE, Belousov A (2015) Vulcanian eruptions. In: The encyclopedia of volcanoes. Elsevier, pp 505–518

Cloos M (2005) Collisional Delamination in New Guinea: The Geotectonics of Subducting Slab Breakoff. Geological Society of America

Cole PD, Calder ES, Druitt TH, et al (1998) Pyroclastic flows generated by gravitational instability of the 1996–97 Lava Dome of Soufriere Hills Volcano, Montserrat. Geophys Res Lett 25:3425–3428. https://doi.org/10.1029/98GL01510

Cole PD, Calder ES, Sparks RSJ, et al (2002) Deposits from dome-collapse and fountain-collapse pyroclastic flows at Soufrière Hills Volcano, Montserrat. In: Druitt TH, Kokelaar BP (eds) The Eruption of Soufrière Hills Volcano, Montserrat from 1995 to 1999. Geological Society of London, p 0

Coltelli M, Proietti C, Branca S, et al (2007) Analysis of the 2001 lava flow eruption of Mt. Etna from three-dimensional mapping. J Geophys Res Earth Surf 112:. https://doi.org/10.1029/2006JF000598

Conde V, Robidoux P, Avard G, et al (2014) Measurements of volcanic SO2 and CO2 fluxes by combined DOAS, Multi-GAS and FTIR observations: a case study from Turrialba and Telica volcanoes. Int J Earth Sci 103:2335–2347. https://doi.org/10.1007/s00531-014-1040-7

Connell J, Lutkehaus N (2017) Escaping Zaria's fire? The volcano resettlement problem of Manam Island, Papua New Guinea. Asia Pac Viewp 58:14–26

Connell J, Lutkehaus N (2016) Another Manam? The forced migration of the population of Manam Island, Papua New Guinea, due to volcanic eruptions 2004–2005. International Organisation for Migration

Connor C, Bebbington M, Marzocchi W (2015) Chapter 51 - Probabilistic Volcanic Hazard Assessment. In: Sigurdsson H (ed) The Encyclopedia of Volcanoes (Second Edition). Academic Press, Amsterdam, pp 897–910

Connor CB, Condit CD, Crumpler LS, Aubele JC (1992) Evidence of regional structural controls on vent distribution: Springerville Volcanic Field, Arizona. J Geophys Res Solid Earth 97:12349–12359. https://doi.org/10.1029/92JB00929

Connor CB, Connor LJ, Bonadonna C, et al (2019) Modelling Tephra Thickness and Particle Size Distribution of the 1913 Eruption of Volcán de Colima, Mexico. In:

Varley N, Connor CB, Komorowski J-C (eds) Volcán de Colima: Portrait of a Persistently Hazardous Volcano. Springer, Berlin, Heidelberg, pp 81–110

Connor CB, Hill BE, Winfrey B, et al (2001) Estimation of volcanic hazards from tephra fallout. Nat Hazards Rev 2:33–42

Connor LJ, Connor CB (2006) Inversion is the key to dispersion: understanding eruption dynamics by inverting tephra fallout. In: Mader HM, Coles SG, Connor CB, Connor LJ (eds) Statistics in Volcanology. Geological Society of London, p 0

Constantinescu R, Hopulele-Gligor A, Connor CB, et al (2021) The radius of the umbrella cloud helps characterize large explosive volcanic eruptions. Commun Earth Environ 2:1–8. https://doi.org/10.1038/s43247-020-00078-3

Cooke RJS, McKee CO, Dent VF, Wallace DA (1976) Striking sequence of volcanic eruptions in the Bismarck Volcanic Arc, Papua New Guinea, in 1972–75. Volcanism Australas 149–172

Coppola D (2022) MIROVA

Coppola D, Laiolo M, Cigolini C, et al (2016) Enhanced volcanic hot-spot detection using MODIS IR data: results from the MIROVA system. Geol Soc Lond Spec Publ 426:181–205. https://doi.org/10.1144/SP426.5

Coppola D, Laiolo M, Massimetti F, Cigolini C (2019) Monitoring endogenous growth of open-vent volcanoes by balancing thermal and SO2 emissions data derived from space. Sci Rep 9:9394. https://doi.org/10.1038/s41598-019-45753-4

Coppola D, Laiolo M, Piscopo D, Cigolini C (2013) Rheological control on the radiant density of active lava flows and domes. J Volcanol Geotherm Res 249:39–48. https://doi.org/10.1016/j.jvolgeores.2012.09.005

Coppola D, Piscopo D, Laiolo M, et al (2012) Radiative heat power at Stromboli volcano during 2000–2011: Twelve years of MODIS observations. J Volcanol Geotherm Res 215–216:48–60. https://doi.org/10.1016/j.jvolgeores.2011.12.001

Coppola D, Piscopo D, Staudacher T, Cigolini C (2009) Lava discharge rate and effusive pattern at Piton de la Fournaise from MODIS data. J Volcanol Geotherm Res 184:174–192. https://doi.org/10.1016/j.jvolgeores.2008.11.031

Coppola D, Valade S, Masias P, et al (2022) Shallow magma convection evidenced by excess degassing and thermal radiation during the dome-forming Sabancaya eruption (2012–2020). Bull Volcanol 84:16. https://doi.org/10.1007/s00445-022-01523-1

Corazzato C, Tibaldi A (2006) Fracture control on type, morphology and distribution of parasitic volcanic cones: An example from Mt. Etna, Italy. J Volcanol Geotherm Res 158:177–194. https://doi.org/10.1016/j.jvolgeores.2006.04.018

Cordonnier B, Lev E, Garel F (2016) Benchmarking lava-flow models. Geol Soc Lond Spec Publ 426:425–445. https://doi.org/10.1144/SP426.7

Costa A, Folch A, Macedonio G, et al (2012) Quantifying volcanic ash dispersal and impact of the Campanian Ignimbrite super-eruption. Geophys Res Lett 39:. https://doi.org/10.1029/2012GL051605

Costa A, Macedonio G (2005) Computational modeling of lava flows: A review. In: Kinematics and dynamics of lava flows. Geological Society of America

Costa A, Macedonio G, Folch A (2006) A three-dimensional Eulerian model for transport and deposition of volcanic ashes. Earth Planet Sci Lett 241:634–647. https://doi.org/10.1016/j.epsl.2005.11.019

Costa A, Pioli L, Bonadonna C (2016) Assessing tephra total grain-size distribution: Insights from field data analysis. Earth Planet Sci Lett 443:90–107. https://doi.org/10.1016/j.epsl.2016.02.040

Cottrell E (2015) Chapter 1 - Global Distribution of Active Volcanoes. In: Shroder JF, Papale P (eds) Volcanic Hazards, Risks and Disasters. Elsevier, Boston, pp 1–16

Couch S, Sparks RSJ, Carroll MR (2003) The Kinetics of Degassing-Induced Crystallization at Soufrière Hills Volcano, Montserrat. J Petrol 44:1477–1502. https://doi.org/10.1093/petrology/44.8.1477

Craig H, Wilson T, Magill C, et al (2021) Agriculture and forestry impact assessment for tephra fall hazard: Fragility function development and New Zealand scenario application. Volcanica 4:345–367. https://doi.org/10.30909/vol.04.02.345367

Craig H, Wilson T, Stewart C, et al (2016) Agricultural impact assessment and management after three widespread tephra falls in Patagonia, South America. Nat Hazards 82:1167–1229. https://doi.org/10.1007/s11069-016-2240-1

Crandell DR, Mullineaux DR (1978) Potential hazards from future eruptions of Mount St. Helens Volcano, Washington. U.S. Govt. Print. Off.,

Crisci GM, Rongo R, Di Gregorio S, Spataro W (2004) The simulation model SCIARA: the 1991 and 2001 lava flows at Mount Etna. J Volcanol Geotherm Res 132:253–267. https://doi.org/10.1016/S0377-0273(03)00349-4

Crisp J, Baloga S (1990) A model for lava flows with two thermal components. J Geophys Res Solid Earth 95:1255–1270. https://doi.org/10.1029/JB095iB02p01255

Crummy J, Bekele Y, Engwell S, et al (2023) Towards understanding volcanic risk in low data environments: Integration of tephra fall hazard analysis and exposure data at Corbetti Volcano, Ethiopia. Rotorua New Zealand

Cunningham H, Gill J, Turner S, et al (2012) Rapid magmatic processes accompany arc–continent collision: the Western Bismarck arc, Papua New Guinea. Contrib Mineral Petrol 164:789–804. https://doi.org/10.1007/s00410-012-0776-y

Cutter SL (1996) Vulnerability to environmental hazards. Prog Hum Geogr 20:529–539. https://doi.org/10.1177/030913259602000407

D'Aleo R, Bitetto M, Delle Donne D, et al (2019) Understanding the SO2 Degassing Budget of Mt Etna's Paroxysms: First Clues From the December 2015 Sequence. Front Earth Sci 6:

Damby DE, Horwell CJ, Baxter PJ, et al (2013) The respiratory health hazard of tephra from the 2010 Centennial eruption of Merapi with implications for occupational mining of deposits. J Volcanol Geotherm Res 261:376–387. https://doi.org/10.1016/j.jvolgeores.2012.09.001

Darwin Volcanic Ash Advisory Centre (2021) Darwin Volcanic Ash Advisory Centre. http://www.bom.gov.au/aviation/volcanic-ash/. Accessed 18 Feb 2022

Davaille A, Jaupart C (1993) Thermal convection in lava lakes. Geophys Res Lett 20:1827–1830. https://doi.org/10.1029/93GL02008

Davies AG, Calkins J, Scharenbroich L, et al (2008) Multi-instrument remote and in situ observations of the Erebus Volcano (Antarctica) lava lake in 2005: A comparison with the Pele lava lake on the jovian moon Io. J Volcanol Geotherm Res 177:705–724. https://doi.org/10.1016/j.jvolgeores.2008.02.010

Davies SM, Larsen G, Wastegård S, et al (2010) Widespread dispersal of Icelandic tephra: how does the Eyjafjöll eruption of 2010 compare to past Icelandic events? J Quat Sci 25:605–611. https://doi.org/10.1002/jqs.1421

De Haen H, Hemrich G (2007) The economics of natural disasters: Implications and challenges for food security. Agric Econ 37:31–45

de Moor JM, Aiuppa A, Avard G, et al (2016) Turmoil at Turrialba Volcano (Costa Rica): Degassing and eruptive processes inferred from high-frequency gas monitoring. J Geophys Res Solid Earth 121:5761–5775. https://doi.org/10.1002/2016JB013150

De Saint Ours P, McKee C (1995) Manam. Bull Volcan Erupt 32:37–45

Deer WA, Howie RA, Zussman J (2013) An Introduction to the Rock-Forming Minerals. Mineralogical Society of Great Britain and Ireland

Dehn J, Dean KG, Engle K, Izbekov P (2002) Thermal precursors in satellite images of the 1999 eruption of Shishaldin Volcano. Bull Volcanol 64:525–534. https://doi.org/10.1007/s00445-002-0227-0

Dehn J, Harris AJL (2015) Thermal anomalies at volcanoes. In: Dean KG, Dehn J (eds) Monitoring Volcanoes in the North Pacific: Observations from Space. Springer, Berlin, Heidelberg, pp 49–78

Del Negro C, Fortuna L, Herault A, Vicari A (2008) Simulations of the 2004 lava flow at Etna volcano using the magflow cellular automata model. Bull Volcanol 70:805–812. https://doi.org/10.1007/s00445-007-0168-8

Delgado-Granados H, Cárdenas González L, Piedad Sánchez N (2001) Sulfur dioxide emissions from Popocatépetl volcano (Mexico): case study of a high-emission rate, passively degassing erupting volcano. J Volcanol Geotherm Res 108:107–120. https://doi.org/10.1016/S0377-0273(00)00280-8

Delle Donne D, Lo Coco E, Bitetto M, et al (2022) Spatio-temporal changes in degassing behavior at Stromboli volcano derived from two co-exposed SO2 camera stations. Front Earth Sci 10:. https://doi.org/10.3389/feart.2022.972071

Delmelle P, Opfergelt S, Cornelis J-T, Ping C-L (2015) Chapter 72 - Volcanic Soils. In: Sigurdsson H (ed) The Encyclopedia of Volcanoes (Second Edition). Academic Press, Amsterdam, pp 1253–1264

Derenius R, Gao J (2022) The floor is Q-LavHA A study about Hafnarfjörður and the rising volcanic activity on the Reykjanes peninsula, Iceland

Devine JD, Sigurdsson H, Davis AN, Self S (1984) Estimates of sulfur and chlorine yield to the atmosphere from volcanic eruptions and potential climatic effects. J Geophys Res Solid Earth 89:6309–6325. https://doi.org/10.1029/JB089iB07p06309

Dewanti DS, Ayuwat D, Yongvanit S (2019) Early warning system through sustainability livelihoods approach for volcanic disaster management. IOP Conf Ser Earth Environ Sci 398:012015. https://doi.org/10.1088/1755-1315/398/1/012015

Di Vito MA, Acocella V, Aiello G, et al (2016) Magma transfer at Campi Flegrei caldera (Italy) before the 1538 AD eruption. Sci Rep 6:32245. https://doi.org/10.1038/srep32245

Dietterich HR, Cashman KV (2014) Channel networks within lava flows: Formation, evolution, and implications for flow behavior. J Geophys Res Earth Surf 119:1704–1724. https://doi.org/10.1002/2014JF003103

Diller K, Clarke AB, Voight B, Neri A (2006) Mechanisms of conduit plug formation: Implications for vulcanian explosions. Geophys Res Lett 33:. https://doi.org/10.1029/2006GL027391

Diniega S, Smrekar SE, Anderson S, Stofan ER (2013) The influence of temperature-dependent viscosity on lava flow dynamics. J Geophys Res Earth Surf 118:1516–1532. https://doi.org/10.1002/jgrf.20111

Dominguez C, Layana S, Aguilera F (2016) Satellite surveillance of the last eruptive period of Villarrica volcano: A predictable eruption?

Dozier J (1981) A method for satellite identification of surface temperature fields of subpixel resolution. Remote Sens Environ 11:221–229. https://doi.org/10.1016/0034-4257(81)90021-3

Dragoni M (1989) A dynamical model of lava flows cooling by radiation. Bull Volcanol 51:88–95. https://doi.org/10.1007/BF01081978

Draxler R, Hess G (1998) An overview of the HYSPLIT_4 modelling system for trajectories. Aust Meteorol Mag 47:

Dzurisin D (2003) A comprehensive approach to monitoring volcano deformation as a window on the eruption cycle. Rev Geophys 41:. https://doi.org/10.1029/2001RG000107

Ebmeier SK, Andrews BJ, Araya MC, et al (2018) Synthesis of global satellite observations of magmatic and volcanic deformation: implications for volcano monitoring & the lateral extent of magmatic domains. J Appl Volcanol 7:2. https://doi.org/10.1186/s13617-018-0071-3

Ebmeier SK, Biggs J, Mather TA, et al (2012) Measuring large topographic change with InSAR: Lava thicknesses, extrusion rate and subsidence rate at Santiaguito volcano, Guatemala. Earth Planet Sci Lett 335–336:216–225. https://doi.org/10.1016/j.epsl.2012.04.027

Edmonds, Liu EJ, Cashman KV (2022a) Open-vent volcanoes fuelled by depth-integrated magma degassing. Bull Volcanol 84:28. https://doi.org/10.1007/s00445-021-01522-8

Edmonds M, Aiuppa A, Humphreys M, et al (2010) Excess volatiles supplied by mingling of mafic magma at an andesite arc volcano. Geochem Geophys Geosystems 11:. https://doi.org/10.1029/2009GC002781

Edmonds M, Gerlach TM (2006) The airborne lava–seawater interaction plume at Kīlauea Volcano, Hawai'i. Earth Planet Sci Lett 244:83–96. https://doi.org/10.1016/j.epsl.2006.02.005

Edmonds M, Grattan J, Michnowicz S (2018) Volcanic Gases: Silent Killers. In: Fearnley CJ, Bird DK, Haynes K, et al. (eds) Observing the Volcano World: Volcano Crisis Communication. Springer International Publishing, Cham, pp 65–83

Edmonds M, Mason E, Hogg O (2022b) Volcanic Outgassing of Volatile Trace Metals. Annu Rev Earth Planet Sci 50:79–98. https://doi.org/10.1146/annurev-earth-070921-062047

Edmonds M, Oppenheimer C, Pyle DM, et al (2003a) SO2 emissions from Soufrière Hills Volcano and their relationship to conduit permeability, hydrothermal interaction and degassing regime. J Volcanol Geotherm Res 124:23–43. https://doi.org/10.1016/S0377-0273(03)00041-6

Edmonds M, Oppenheimer C, Pyle DM, et al (2003b) SO2 emissions from Soufrière Hills Volcano and their relationship to conduit permeability, hydrothermal interaction and degassing regime. J Volcanol Geotherm Res 124:23–43. https://doi.org/10.1016/S0377-0273(03)00041-6

Edmonds M, Wallace PJ (2017) Volatiles and Exsolved Vapor in Volcanic Systems. Elements 13:29–34. https://doi.org/10.2113/gselements.13.1.29

Edmonds M, Woods AW (2018) Exsolved volatiles in magma reservoirs. J Volcanol Geotherm Res 368:13–30. https://doi.org/10.1016/j.jvolgeores.2018.10.018

Elissondo M, Baumann V, Bonadonna C, et al (2016) Chronology and impact of the 2011 Cordón Caulle eruption, Chile. Nat Hazards Earth Syst Sci 16:675–704. https://doi.org/10.5194/nhess-16-675-2016

Endo ET, Murray T (1991) Real-time Seismic Amplitude Measurement (RSAM): a volcano monitoring and prediction tool. Bull Volcanol 53:533–545. https://doi.org/10.1007/BF00298154

ESA (2022). https://scihub.copernicus.eu/dhus/#/home. Accessed 1 Apr 2022

Favalli M, Chirico GD, Papale P, et al (2009) Lava flow hazard at Nyiragongo volcano, D.R.C. Bull Volcanol 71:363–374. https://doi.org/10.1007/s00445-008-0233-y

Favalli M, Fornaciai A, Nannipieri L, et al (2018) UAV-based remote sensing surveys of lava flow fields: a case study from Etna's 1974 channel-fed lava flows. Bull Volcanol 80:29. https://doi.org/10.1007/s00445-018-1192-6

Favalli M, Pareschi MT, Neri A, Isola I (2005) Forecasting lava flow paths by a stochastic approach. Geophys Res Lett 32:. https://doi.org/10.1029/2004GL021718

Fearnley C, Winson AEG, Pallister J, Tilling R (2018) Volcano Crisis Communication: Challenges and Solutions in the 21st Century. In: Fearnley CJ, Bird DK, Haynes K, et al. (eds) Observing the Volcano World: Volcano Crisis Communication. Springer International Publishing, Cham, pp 3–21

Felpeto A, Araña V, Ortiz R, et al (2001) Assessment and Modelling of Lava Flow Hazard on Lanzarote (Canary Islands). Nat Hazards 23:247–257. https://doi.org/10.1023/A:1011112330766

Feng S, Fu Y, Xiao Q (2012) Trends in the global tropopause thickness revealed by radiosondes. Geophys Res Lett 39:. https://doi.org/10.1029/2012GL053460

Few R, Armijos MT, Barclay J (2017) Living with Volcan Tungurahua: The dynamics of vulnerability during prolonged volcanic activity. Geoforum 80:72–81. https://doi.org/10.1016/j.geoforum.2017.01.006

Fioletov VE, McLinden CA, Krotkov N, Li C (2015) Lifetimes and emissions of SO2 from point sources estimated from OMI. Geophys Res Lett 42:1969–1976. https://doi.org/10.1002/2015GL063148

Firth C, Cronin S (2023) Life-cycles of a lava lake: Ambrym volcano, Vanuatu. J Volcanol Geotherm Res 434:107742. https://doi.org/10.1016/j.jvolgeores.2022.107742

Fischer TP, Arellano S, Carn S, et al (2019a) The emissions of CO2 and other volatiles from the world's subaerial volcanoes. Sci Rep 9:18716. https://doi.org/10.1038/s41598-019-54682-1

Fischer TP, Arellano S, Carn S, et al (2019b) The emissions of CO2 and other volatiles from the world's subaerial volcanoes. Sci Rep 9:18716. https://doi.org/10.1038/s41598-019-54682-1

Fischer TP, Chiodini G (2015) Chapter 45 - Volcanic, Magmatic and Hydrothermal Gases. In: Sigurdsson H (ed) The Encyclopedia of Volcanoes (Second Edition). Academic Press, Amsterdam, pp 779–797

Fisher NH (1939) Report on the volcanoes of the territory of New Guinea. Territory of New Guinea, Geol. Bulletin

Flower VJB, Carn SA (2015) Characterising volcanic cycles at Soufriere Hills Volcano, Montserrat: Time series analysis of multi-parameter satellite data. J Volcanol Geotherm Res 304:82–93. https://doi.org/10.1016/j.jvolgeores.2015.07.035

Flynn LP, Harris AJL, Wright R (2001) Improved identification of volcanic features using Landsat 7 ETM+. Remote Sens Environ 78:180–193. https://doi.org/10.1016/S0034-4257(01)00258-9

Flynn LP, Mouginis-Mark PJ, Gradie JC, Lucey PG (1993) Radiative temperature measurements at Kupaianaha Lava Lake, Kilauea Volcano, Hawaii. J Geophys Res Solid Earth 98:6461–6476. https://doi.org/10.1029/92JB02698

Flynn LP, Mouginis-Mark PJ, Horton KA (1994) Distribution of thermal areas on an active lava flow field: Landsat observations of Kilauea, Hawaii, July 1991. Bull Volcanol 56:284–296. https://doi.org/10.1007/BF00302081

Folch A (2012) A review of tephra transport and dispersal models: Evolution, current status, and future perspectives. J Volcanol Geotherm Res 235–236:96–115. https://doi.org/10.1016/j.jvolgeores.2012.05.020

Folch A, Costa A, Durant A, Macedonio G (2010) A model for wet aggregation of ash particles in volcanic plumes and clouds: 2. Model application. J Geophys Res Solid Earth 115:. https://doi.org/10.1029/2009JB007176

Folch A, Costa A, Macedonio G (2009) FALL3D: A computational model for transport and deposition of volcanic ash. Comput Geosci 35:1334–1342. https://doi.org/10.1016/j.cageo.2008.08.008

Folch A, Jorba O, Viramonte J (2008) Volcanic ash forecast – application to the May 2008 Chaitén eruption. Nat Hazards Earth Syst Sci 8:927–940. https://doi.org/10.5194/nhess-8-927-2008

Folch A, Sulpizio R (2010) Evaluating long-range volcanic ash hazard using supercomputing facilities: application to Somma-Vesuvius (Italy), and consequences for civil aviation over the Central Mediterranean Area. Bull Volcanol 72:1039–1059. https://doi.org/10.1007/s00445-010-0386-3

Fornaciai A, Bisson M, Landi P, et al (2010) A LiDAR survey of Stromboli volcano (Italy): Digital elevation model-based geomorphology and intensity analysis. Int J Remote Sens 31:3177–3194. https://doi.org/10.1080/01431160903154416

Francis P, Oppenheimer C, Stevenson D (1993) Endogenous growth of persistently active volcanoes. Nature 366:554–557. https://doi.org/10.1038/366554a0

Francis PW, Rothery DA (1987) Using the Landsat Thematic Mapper to detect and monitor active volcanoes: An example from Lascar volcano, northern Chile. Geology 15:614–617. https://doi.org/10.1130/0091-7613(1987)15<614:UTLTMT>2.0.CO;2

Fraunfelder FT, Kalina RE, Buist AS, et al (1983) Ocular effects following the volcanic eruptions of Mount St Helens. Arch Ophthalmol 101:376–378

Freire S, Florczyk AJ, Pesaresi M, Sliuzas R (2019) An Improved Global Analysis of Population Distribution in Proximity to Active Volcanoes, 1975–2015. ISPRS Int J Geo-Inf 8:341. https://doi.org/10.3390/ijgi8080341

Fuchs S, Birkmann J, Glade T (2012) Vulnerability assessment in natural hazard and risk analysis: current approaches and future challenges. Nat Hazards 64:1969–1975. https://doi.org/10.1007/s11069-012-0352-9

Furtney MA, Pritchard ME, Biggs J, et al (2018) Synthesizing multi-sensor, multi-satellite, multi-decadal datasets for global volcano monitoring. J Volcanol Geotherm Res 365:38–56. https://doi.org/10.1016/j.jvolgeores.2018.10.002

Gaillard J-C, Ercole R d', Leone F (2001) Cartography of population vulnerability to volcanic hazards and lahars of Mount Pinatubo (Philippines): a case study in Pasig-Potrero River basin (province of Pampanga) / Cartographie de la vulnérabilité des populations face aux phénomènes volcaniques et aux lahars du Mont Pinatubo (Philippines) : cas du bassin de la rivière Pasig-Potrero (province de Pampanga). Géomorphologie Relief Process Environ 7:209–221. https://doi.org/10.3406/morfo.2001.1103

Gaunt HE, Burgisser A, Mothes PA, et al (2020) Triggering of the powerful 14 July 2013 Vulcanian explosion at Tungurahua Volcano, Ecuador. J Volcanol Geotherm Res 392:106762. https://doi.org/10.1016/j.jvolgeores.2019.106762

Gaunt HE, Sammonds PR, Meredith PG, et al (2014) Pathways for degassing during the lava dome eruption of Mount St. Helens 2004–2008. Geology 42:947–950. https://doi.org/10.1130/G35940.1

Gaunt HE, Sammonds PR, Meredith PG, Chadderton A (2016) Effect of temperature on the permeability of lava dome rocks from the 2004–2008 eruption of Mount St. Helens. Bull Volcanol 78:30. https://doi.org/10.1007/s00445-016-1024-5

Gerlach TM (2004) Volcanic sources of tropospheric ozone-depleting trace gases. Geochem Geophys Geosystems 5:. https://doi.org/10.1029/2004GC000747

Gerlach TM, McGee KA, Doukas MP (2008) Emission rates of CO2, SO2, and H2S, scrubbing, and preeruption excess volatiles at Mount St. Helens, 2004-2005. U.S. Geological Survey, Reston, VA

Giggenbach WF (1996) Chemical Composition of Volcanic Gases. In: Scarpa R, Tilling RI (eds) Monitoring and Mitigation of Volcano Hazards. Springer, Berlin, Heidelberg, pp 221–256

Giordano D, Russell JK, Dingwell DB (2008) Viscosity of magmatic liquids: A model. Earth Planet Sci Lett 271:123–134. https://doi.org/10.1016/j.epsl.2008.03.038

Girault F, Carazzo G, Tait S, et al (2014) The effect of total grain-size distribution on the dynamics of turbulent volcanic plumes. Earth Planet Sci Lett 394:124–134. https://doi.org/10.1016/j.epsl.2014.03.021

Girina OA (2013) Chronology of Bezymianny Volcano activity, 1956–2010. J Volcanol Geotherm Res 263:22–41. https://doi.org/10.1016/j.jvolgeores.2013.05.002

Girona T, Realmuto V, Lundgren P (2021) Large-scale thermal unrest of volcanoes for years prior to eruption. Nat Geosci 14:238–241. https://doi.org/10.1038/s41561-021-00705-4

Glaze L, Francis PW, Rothery DA (1989) Measuring thermal budgets of active volcanoes by satellite remote sensing. Nature 338:144–146. https://doi.org/10.1038/338144a0

Global Volcanism Program (2024) Manam. Smithsonian Institution

Global Volcanism Program (2005) Report on Manam (Papua New Guinea) February 2005. Smithsonian Institution

Global Volcanism Program (1993a) Report on Manam (Papua New Guinea) July 1993. Smithsonian Institution

Global Volcanism Program (1993b) Report on Manam (Papua New Guinea) October 1993. Smithsonian Institution

Global Volcanism Program (1992a) Report on Manam (Papua New Guinea) — October 1992. Smithsonian Institution

Global Volcanism Program (1992b) Report on Manam (Papua New Guinea) — November 1992. Smithsonian Institution

Global Volcanism Program (1996a) Report on Manam (Papua New Guinea) — December 1996. Smithsonian Institution

Global Volcanism Program (1998) Report on Manam (Papua New Guinea) December 1998. Smithsonian Institution

Global Volcanism Program (2006) Report on Manam (Papua New Guinea) — February 2006. Smithsonian Institution

Global Volcanism Program (2004a) Report on Manam (Papua New Guinea) October 2004. Smithsonian Institution

Global Volcanism Program (2004b) Report on Manam (Papua New Guinea) November 2004. Smithsonian Institution

Global Volcanism Program (2004c) Report on Manam (Papua New Guinea) July 2004. Smithsonian Institution

Global Volcanism Program (2017) Report on Manam (Papua New Guinea) March 2017. Smithsonian Institution

Global Volcanism Program (2018) Report on Manam (Papua New Guinea) — March 2018. Smithsonian Institution

Global Volcanism Program (2019a) Report on Manam (Papua New Guinea) — February 2019. Smithsonian Institution

Global Volcanism Program (2019b) Report on Manam (Papua New Guinea) October 2019. Smithsonian Institution

Global Volcanism Program (2021a) Report on Manam (Papua New Guinea) — November 2021. Smithsonian Institution

Global Volcanism Program (2022a) Report on Manam (Papua New Guinea) — August 2022. Smithsonian Institution

Global Volcanism Program (2022b) Report on Manam (Papua New Guinea) — November 2022. Smithsonian Institution

Global Volcanism Program (2021b) Manam. Smithsonian Institution

Global Volcanism Program (2021c) Kadovar. Smithsonian Institution

Global Volcanism Program (2021d) Ulawun. Smithsonian Institution

Global Volcanism Program (1987) Report on Manam (Papua New Guinea) June 1987. Smithsonian Institution

Global Volcanism Program (1992c) Report on Manam (Papua New Guinea) — September 1992. Smithsonian Institution

Global Volcanism Program (1992d) Report on Manam (Papua New Guinea) — April 1992. Smithsonian Institution

Global Volcanism Program (2004d) Report on Manam (Papua New Guinea) November 2004. Smithsonian Institution

Global Volcanism Program (1984) Report on Manam (Papua New Guinea) — April 1984. Smithsonian Institution

Global Volcanism Program (1992e) Report on Manam (Papua New Guinea) May 1992. Smithsonian Institution

Global Volcanism Program (2013) Report on Manam (Papua New Guinea) June 2013. Smithsonian Institution

Global Volcanism Program (1994) Report on Manam (Papua New Guinea) October 1994. Smithsonian Institution

Global Volcanism Program (2003) Report on Manam (Papua New Guinea) September 2003. Smithsonian Institution

Global Volcanism Program (1996b) Report on Manam (Papua New Guinea) December 1996. Smithsonian Institution

Global Volcanism Program Report on Manam (Papua New Guinea) — April 2007. Smithsonian Institution

Gómez-Vazquez A, De la Cruz-Reyna S, Mendoza-Rosas AT (2016) The ongoing dome emplacement and destruction cyclic process at Popocatépetl volcano, Central Mexico. Bull Volcanol 78:58. https://doi.org/10.1007/s00445-016-1054-z

Gonnermann HM (2015) Magma Fragmentation. Annu Rev Earth Planet Sci 43:431–458. https://doi.org/10.1146/annurev-earth-060614-105206

Gonnermann HM, Manga M (2007) The Fluid Mechanics Inside a Volcano. Annu Rev Fluid Mech 39:321–356. https://doi.org/10.1146/annurev.fluid.39.050905.110207

González C, Inostroza M, Aguilera F, et al (2015) Heat and mass flux measurements using Landsat images from the 2000–2004 period, Lascar volcano, northern Chile. J Volcanol Geotherm Res 301:277–292. https://doi.org/10.1016/j.jvolgeores.2015.05.009

González-Santana D, Santana-Casiano JM, González AG, González-Dávila M (2022) Coastal carbonate system variability along an active lava–seawater interface. Front Mar Sci 9:. https://doi.org/10.3389/fmars.2022.952203

Granados-Bolaños S, Quesada-Román A, Alvarado GE (2021) Low-cost UAV applications in dynamic tropical volcanic landforms. J Volcanol Geotherm Res 410:107143. https://doi.org/10.1016/j.jvolgeores.2020.107143

Grapenthin R, Kyle P, Aster RC, et al (2022) Deformation at the open-vent Erebus volcano, Antarctica, from more than 20 years of GNSS observations. J Volcanol Geotherm Res 432:107703. https://doi.org/10.1016/j.jvolgeores.2022.107703

Gray DM, Burton-Johnson A, Fretwell PT (2019) Evidence for a lava lake on Mt. Michael volcano, Saunders Island (South Sandwich Islands) from Landsat, Sentinel-2 and ASTER satellite imagery. J Volcanol Geotherm Res 379:60–71. https://doi.org/10.1016/j.jvolgeores.2019.05.002

Green RM, Bebbington MS, Jones G, et al (2016) Estimation of tephra volumes from sparse and incompletely observed deposit thicknesses. Bull Volcanol 78:25. https://doi.org/10.1007/s00445-016-1016-5

Griffiths RW (2000) The Dynamics of Lava Flows. Annu Rev Fluid Mech 32:477–518. https://doi.org/10.1146/annurev.fluid.32.1.477

Gudmundsson A (2005) The effects of layering and local stresses in composite volcanoes on dyke emplacement and volcanic hazards. Comptes Rendus Geosci 337:1216–1222. https://doi.org/10.1016/j.crte.2005.07.001

Gudmundsson A (2006) How local stresses control magma-chamber ruptures, dyke injections, and eruptions in composite volcanoes. Earth-Sci Rev 79:1–31. https://doi.org/10.1016/j.earscirev.2006.06.006

Gudmundsson G (2011) Respiratory health effects of volcanic ash with special reference to Iceland. A review. Clin Respir J 5:2–9. https://doi.org/10.1111/j.1752-699X.2010.00231.x

Gudnason J, Thordarson T, Houghton BF, Larsen G (2018) The 1845 Hekla eruption: Grain-size characteristics of a tephra layer. J Volcanol Geotherm Res 350:33–46. https://doi.org/10.1016/j.jvolgeores.2017.11.025

Guest JE, Murray JB (1979) An analysis of hazard from Mount Etna volcano. J Geol Soc 136:347–354. https://doi.org/10.1144/gsjgs.136.3.0347

Gurioli L, Colo' L, Bollasina AJ, et al (2014) Dynamics of Strombolian explosions: Inferences from field and laboratory studies of erupted bombs from Stromboli volcano. J Geophys Res Solid Earth 119:319–345. https://doi.org/10.1002/2013JB010355

Gurioli L, Paris R (2015) Simulating the thermorheological evolution of channel-contained lava: FLOWGO and its implementation...

Hall ML, Steele AL, Bernard B, et al (2015) Sequential plug formation, disintegration by Vulcanian explosions, and the generation of granular Pyroclastic Density Currents at Tungurahua volcano (2013–2014), Ecuador. J Volcanol Geotherm Res 306:90–103. https://doi.org/10.1016/j.jvolgeores.2015.09.009

Hansell AL, Horwell CJ, Oppenheimer C (2006) The health hazards of volcanoes and geothermal areas. Occup Environ Med 63:149–156. https://doi.org/10.1136/oem.2005.022459

Harp AG, Valentine GA (2018) Emplacement controls for the basaltic-andesitic radial dikes of Summer Coon volcano and implications for flank vents at stratovolcanoes. Bull Volcanol 80:16. https://doi.org/10.1007/s00445-018-1194-4

Harris A (2013a) Thermal Remote Sensing of Active Volcanoes: A User's Manual. Cambridge University Press

Harris A (ed) (2013b) The mixed pixel, the dual-band technique, heat loss and volume flux. In: Thermal Remote Sensing of Active Volcanoes: A User's Manual. Cambridge University Press, Cambridge, pp 155–273

Harris A, Steffke A, Calvari S, Spampinato L (2011) Thirty years of satellite-derived lava discharge rates at Etna: Implications for steady volumetric output. J Geophys Res Solid Earth 116:. https://doi.org/10.1029/2011JB008237

Harris AJ, Chevrel MO, Coppola D, et al (2019) Validation of an integrated satellite-data-driven response to an effusive crisis: the April–May 2018 eruption of Piton de la Fournaise. Ann Geophys 61:

Harris AJ, Rowland S (2001) FLOWGO: a kinematic thermo-rheological model for lava flowing in a channel. Bull Volcanol 63:20–44. https://doi.org/10.1007/s004450000120

Harris AJL (2008) Modeling lava lake heat loss, rheology, and convection. Geophys Res Lett 35:. https://doi.org/10.1029/2008GL033190

Harris AJL, Baloga SM (2009a) Lava discharge rates from satellite-measured heat flux. Geophys Res Lett 36:. https://doi.org/10.1029/2009GL039717

Harris AJL, Baloga SM (2009b) Lava discharge rates from satellite-measured heat flux. Geophys Res Lett 36:. https://doi.org/10.1029/2009GL039717

Harris AJL, Blake S, Rothery DA, Stevens NF (1997) A chronology of the 1991 to 1993 Mount Etna eruption using advanced very high resolution radiometer data: Implications for real-time thermal volcano monitoring. J Geophys Res Solid Earth 102:7985–8003. https://doi.org/10.1029/96JB03388

Harris AJL, Carniel R, Jones J (2005) Identification of variable convective regimes at Erta Ale Lava Lake. J Volcanol Geotherm Res 142:207–223. https://doi.org/10.1016/j.jvolgeores.2004.11.011

Harris AJL, Dehn J, Calvari S (2007) Lava effusion rate definition and measurement: a review. Bull Volcanol 70:1. https://doi.org/10.1007/s00445-007-0120-y

Harris AJL, Flynn LP, Keszthelyi L, et al (1998) Calculation of lava effusion rates from Landsat TM data. Bull Volcanol 60:52–71. https://doi.org/10.1007/s004450050216

Harris AJL, Flynn LP, Rothery DA, et al (1999) Mass flux measurements at active lava lakes: Implications for magma recycling. J Geophys Res Solid Earth 104:7117–7136. https://doi.org/10.1029/98JB02731

Harris AJL, Rhéty M, Gurioli L, et al (2016) Simulating the thermorheological evolution of channel-contained lava: FLOWGO and its implementation in EXCEL. Geol Soc Lond Spec Publ 426:313–336. https://doi.org/10.1144/SP426.9

Harris AJL, Rowland SK (2009) Effusion rate controls on lava flow length and the role of heat loss: a review. In: Thordarson T, Self S, Larsen G, et al. (eds) Studies in Volcanology: The Legacy of George Walker, First. The Geological Society of London on behalf of The International Association of Volcanology and Chemistry of the Earth's Interior, pp 33–51

Harris AJL, Rowland SK (2015a) Chapter 17 - Lava Flows and Rheology. In: Sigurdsson H (ed) The Encyclopedia of Volcanoes (Second Edition). Academic Press, Amsterdam, pp 321–342

Harris AJL, Rowland SK (2015b) Flowgo 2012. In: Hawaiian Volcanoes. American Geophysical Union (AGU), pp 457–481

Hayes JL, Biass S, Jenkins SF, et al (2022) Integrating criticality concepts into road network disruption assessments for volcanic eruptions. J Appl Volcanol 11:8. https://doi.org/10.1186/s13617-022-00118-x

Hayes JL, Calderón B R, Deligne NI, et al (2019) Timber-framed building damage from tephra fall and lahar: 2015 Calbuco eruption, Chile. J Volcanol Geotherm Res 374:142–159. https://doi.org/10.1016/j.jvolgeores.2019.02.017

Hayes JL, Wilson TM, Magill C (2015) Tephra fall clean-up in urban environments. J Volcanol Geotherm Res 304:359–377. https://doi.org/10.1016/j.jvolgeores.2015.09.014

Haynes K, Barclay J, Pidgeon N (2007) Volcanic hazard communication using maps: an evaluation of their effectiveness. Bull Volcanol 70:123–138. https://doi.org/10.1007/s00445-007-0124-7

Heiken G, Wohletz K (1991) Fragmentation Processes in Explosive Volcanic Eruptions. In: Fisher RV, Smith GA (eds) Sedimentation in Volcanic Settings. SEPM Society for Sedimentary Geology, p 0

Hellweg M (2000) Physical models for the source of Lascar's harmonic tremor. J Volcanol Geotherm Res 101:183–198. https://doi.org/10.1016/S0377-0273(00)00163-3

Herault A, Vicari A, Ciraudo A, Del Negro C (2009) Forecasting lava flow hazards during the 2006 Etna eruption: Using the MAGFLOW cellular automata model. Comput Geosci 35:1050–1060. https://doi.org/10.1016/j.cageo.2007.10.008

Hicks A, Barclay J (2018) Citizen-centric risk communication. Geoscientist 28:16–19. https://doi.org/10.1144/geosci2018-004

Hidalgo S, Battaglia J, Arellano S, et al (2015) SO2 degassing at Tungurahua volcano (Ecuador) between 2007 and 2013: Transition from continuous to episodic activity. J Volcanol Geotherm Res 298:1–14. https://doi.org/10.1016/j.jvolgeores.2015.03.022

Holm RJ, Richards SW (2013) A re-evaluation of arc–continent collision and along-arc variation in the Bismarck Sea region, Papua New Guinea. Aust J Earth Sci 60:605–619. https://doi.org/10.1080/08120099.2013.824505

Hooper A, Zebker H, Segall P, Kampes B (2004) A new method for measuring deformation on volcanoes and other natural terrains using InSAR persistent scatterers: A NEW PERSISTENT SCATTERERS METHOD. Geophys Res Lett 31:. https://doi.org/10.1029/2004GL021737

Horwell CJ, Baxter PJ (2006) The respiratory health hazards of volcanic ash: a review for volcanic risk mitigation. Bull Volcanol 69:1–24. https://doi.org/10.1007/s00445-006-0052-y

Hunt JA, Mather TA, Pyle DM (2020) Morphological comparison of distributed volcanic fields in the Main Ethiopian Rift using high-resolution digital elevation models. J Volcanol Geotherm Res 393:106732. https://doi.org/10.1016/j.jvolgeores.2019.106732

Huppert HE, Hallworth MA (2007) Bi-directional flows in constrained systems. J Fluid Mech 578:95–112. https://doi.org/10.1017/S0022112007004661

Hurst T, Smith W (2004) A Monte Carlo methodology for modelling ashfall hazards. J Volcanol Geotherm Res 138:393–403. https://doi.org/10.1016/j.jvolgeores.2004.08.001

Hurst T, Turner R (1999) Performance of the program ASHFALL for forecasting ashfall during the 1995 and 1996 eruptions of Ruapehu volcano. N Z J Geol Geophys - N Z J GEOL GEOPHYS 42:615–622. https://doi.org/10.1080/00288306.1999.9514865

Husain T, Elsworth D, Voight B, et al (2018) Influence of conduit flow mechanics on magma rheology and the growth style of lava domes. Geophys J Int 213:1768–1784. https://doi.org/10.1093/gji/ggy073

Ilyinskaya E, Mason E, Wieser PE, et al (2021a) Rapid metal pollutant deposition from the volcanic plume of Kīlauea, Hawai'i. Commun Earth Environ 2:78. https://doi.org/10.1038/s43247-021-00146-2

Ilyinskaya E, Mason E, Wieser PE, et al (2021b) Rapid metal pollutant deposition from the volcanic plume of Kīlauea, Hawai'i. Commun Earth Environ 2:1–15. https://doi.org/10.1038/s43247-021-00146-2

Jackson G, McNamara KE, Witt B (2020) "System of hunger": Understanding causal disaster vulnerability of indigenous food systems. J Rural Stud 73:163–175. https://doi.org/10.1016/j.jrurstud.2019.10.042

James MR, Varley N (2012) Identification of structural controls in an active lava dome with high resolution DEMs: Volcán de Colima, Mexico. Geophys Res Lett 39:. https://doi.org/10.1029/2012GL054245

Jenkins SF, Biass S, Williams GT, et al (2022) Evaluating and ranking Southeast Asia's exposure to explosive volcanic hazards. Nat Hazards Earth Syst Sci 22:1233–1265. https://doi.org/10.5194/nhess-22-1233-2022

Jenkins SF, Day SJ, Faria BVE, Fonseca JFBD (2017) Damage from lava flows: insights from the 2014–2015 eruption of Fogo, Cape Verde. J Appl Volcanol 6:6. https://doi.org/10.1186/s13617-017-0057-6

Jenkins SF, Wilson TM, Magill C, et al (2015) Volcanic ash fall hazard and risk. In: Loughlin SC, Sparks S, Brown SK, et al. (eds) Global Volcanic Hazards and Risk, 1st edn. Cambridge University Press, pp 173–222

Jensen JR (2000) Remote Sensing of the Environment. 8

Jiménez D (2020) Forensic human identification during a humanitarian crisis in Guatemala. In: Forensic Science and Humanitarian Action. John Wiley & Sons, Ltd, pp 625–633

Johnson ER, Wallace PJ, Cashman KV, Delgado Granados H (2010) Degassing of volatiles (H2O, CO2, S, Cl) during ascent, crystallization, and eruption at mafic monogenetic volcanoes in central Mexico. J Volcanol Geotherm Res 197:225–238. https://doi.org/10.1016/j.jvolgeores.2010.02.017

Johnson JB, Lees JM (2000) Plugs and chugs—seismic and acoustic observations of degassing explosions at Karymsky, Russia and Sangay, Ecuador. J Volcanol Geotherm Res 101:67–82. https://doi.org/10.1016/S0377-0273(00)00164-5

Johnson JB, Watson LM, Palma JL, et al (2018) Forecasting the Eruption of an Open-Vent Volcano Using Resonant Infrasound Tones. Geophys Res Lett 45:2213–2220. https://doi.org/10.1002/2017GL076506

Johnson JH, Poland MP (2013) Seismic detection of increased degassing before Kīlauea's 2008 summit explosion. Nat Commun 4:1668. https://doi.org/10.1038/ncomms2703

Johnson RW (1977) Distribution and major element chemistry of late Cainozoic volcanoes at the southern margin of the Bismarck Sea, Papua New Guinea. Aust. Bur. Miner. Resour Geol Geophys Rep 188:

Johnson RW (2013) Fire Mountains of the Islands: A History of Volcanic Eruptions and Disaster Management in Papua New Guinea and the Solomon Islands. ANU E Press

Johnson RW, Jaques AL, Hickey RL, et al (1985) Manam Island, Papua New Guinea: Petrology and Geochemistry of a Low-TiO2 Basaltic Island-Arc Volcano. J Petrol 26:283–323. https://doi.org/10.1093/petrology/26.2.283

Jones A, Thomson D, Hort M, Devenish B (2007) The U.K. Met Office's Next-Generation Atmospheric Dispersion Model, NAME III. In: Borrego C, Norman A-L (eds) Air Pollution Modeling and Its Application XVII. Springer US, Boston, MA, pp 580–589

Jost A, Beirle S, Dörner S, et al (2022) Quantification of SO2 emission rates from the Kilauea volcano in Hawaii by the divergence of the SO2 flux using S5P-TROPOMI satellite measurements and comparison to results from ground-based observations. EGU22-6159. https://doi.org/10.5194/egusphere-egu22-6159

Jumadi, Carver S, Quincey D (2017) A conceptual design of spatio-temporal agent-based model for volcanic evacuation. Systems 5:53

Kadavi PR, Lee C-W (2018) Land cover classification analysis of volcanic island in Aleutian Arc using an artificial neural network (ANN) and a support vector machine (SVM) from Landsat imagery. Geosci J 22:653–665. https://doi.org/10.1007/s12303-018-0023-2

Kaminski E, Jaupart C (1998) The size distribution of pyroclasts and the fragmentation sequence in explosive volcanic eruptions. J Geophys Res Solid Earth 103:29759–29779. https://doi.org/10.1029/98JB02795

Kanamitsu M, Ebisuzaki W, Yang S-K, et al (2002) NCEP-DOE AMIP-II REANALYSIS (R-2)

Kantzas EP, McGonigle AJS, Tamburello G, et al (2010) Protocols for UV camera volcanic SO2 measurements. J Volcanol Geotherm Res 194:55–60. https://doi.org/10.1016/j.jvolgeores.2010.05.003

Kazahaya K, Shinohara H, Saito G (1994) Excessive degassing of Izu-Oshima volcano: magma convection in a conduit. Bull Volcanol 56:207–216. https://doi.org/10.1007/BF00279605

Kazahaya K, Shinohara H, Uto K, et al (2004) Gigantic SO2 emission from Miyakejima volcano, Japan, caused by caldera collapse. Geology 32:425–428. https://doi.org/10.1130/G20399.1

Kelfoun K, Druitt TH (2005) Numerical modeling of the emplacement of Socompa rock avalanche, Chile. J Geophys Res Solid Earth 110:. https://doi.org/10.1029/2005JB003758

Kelman I, Mather TA (2008) Living with volcanoes: The sustainable livelihoods approach for volcano-related opportunities. J Volcanol Geotherm Res 172:189–198. https://doi.org/10.1016/j.jvolgeores.2007.12.007

Kereszturi G, Cappello A, Ganci G, et al (2014) Numerical simulation of basaltic lava flows in the Auckland Volcanic Field, New Zealand—implication for volcanic hazard assessment. Bull Volcanol 76:879. https://doi.org/10.1007/s00445-014-0879-6

Kerle N, Huurneman GC, Janssen LLF (eds) (2009) Principles of Remote Sensing

Kern C, Aiuppa A, de Moor JM (2022) A golden era for volcanic gas geochemistry? Bull Volcanol 84:43. https://doi.org/10.1007/s00445-022-01556-6

Kern C, Lerner AH, Elias T, et al (2020) Quantifying gas emissions associated with the 2018 rift eruption of Kīlauea Volcano using ground-based DOAS measurements. Bull Volcanol 82:55. https://doi.org/10.1007/s00445-020-01390-8

Kervyn M, Ernst GGJ, van Wyk de Vries B, et al (2009) Volcano load control on dyke propagation and vent distribution: Insights from analogue modeling. J Geophys Res Solid Earth 114:. https://doi.org/10.1029/2008JB005653

Kilbride BM, Edmonds M, Biggs J (2016) Observing eruptions of gas-rich compressible magmas from space. Nat Commun 7:13744. https://doi.org/10.1038/ncomms13744

Kilburn C (2012) Precursory deformation and fracture before brittle rock failure and potential application to volcanic unrest. J Geophys Res Solid Earth 117:. https://doi.org/10.1029/2011JB008703

Kilburn CR (2000) Lava flows and flow fields. Encycl Volcanoes 291–305

Kilburn CR (2022) Lava crusts, aa flow lengthening and the pahoehoe-aa transition. In: Active lavas. Routledge, pp 263–280

Kilburn CR, Guest JE (1993) aa lavas of Mount Etna, Sicily. In: Active lavas. Routledge, pp 73–106

Kilburn CRJ (2004) Fracturing as a quantitative indicator of lava flow dynamics. J Volcanol Geotherm Res 132:209–224. https://doi.org/10.1016/S0377-0273(03)00346-9

Kilburn CRJ, Carlino S, Danesi S, Pino NA (2023) Potential for rupture before eruption at Campi Flegrei caldera, Southern Italy. Commun Earth Environ 4:1–12. https://doi.org/10.1038/s43247-023-00842-1

Kilburn CRJ, Lopes RMC (1991) General patterns of flow field growth: Aa and blocky lavas. J Geophys Res Solid Earth 96:19721–19732. https://doi.org/10.1029/91JB01924

Kilburn CRJ, Lopez RMC (1988) The growth of a ‘a lava flow field on Mount Etna. Sicily J Geophys Res 93:14,759-14,772

Kim K, Pant P, Yamashita E, Ghimire J (2019) Analysis of Transportation Disruptions from Recent Flooding and Volcanic Disasters in Hawai’i. Transp Res Rec 2673:194–208. https://doi.org/10.1177/0361198118825460

Klees R, Massonnet D (1998) Deformation measurements using SAR interferometry: potential and limitations. Geol En Mijnb 77:161–176

Komorowski JC (2002) The January 2002 eruption - The January 2002 flank eruption of Nyiragongo Volcano (Democratic Republic of Congo): chronology, evidence for a tectonic rift trigger, and impact of lava flows on the city of Goma. Acta Vulcanol J Natl Volcanicn Group Italy 1415 12 20022003 Sample Copy 1000–1035. https://doi.org/10.1400/19077

Kondo G, Aoyama H, Nishimura T, et al (2019) Gas flux cyclic regime at an open vent magmatic column inferred from seismic and acoustic records. Sci Rep 9:5678. https://doi.org/10.1038/s41598-019-42033-z

Krieger G, Moreira A, Fiedler H, et al (2007) TanDEM-X: A Satellite Formation for High-Resolution SAR Interferometry. IEEE Trans Geosci Remote Sens 45:3317–3341. https://doi.org/10.1109/TGRS.2007.900693

Kullman GJ, Jones WG, Cornwell RJ, Parker JE (1994) Characterization of air contaminants formed by the interaction of lava and sea water. Environ Health Perspect 102:478–482. https://doi.org/10.1289/ehp.94102478

La Spina G, Arzilli F, Llewellin EW, et al (2021) Explosivity of basaltic lava fountains is controlled by magma rheology, ascent rate and outgassing. Earth Planet Sci Lett 553:116658. https://doi.org/10.1016/j.epsl.2020.116658

Lages J, Chacón Z, Burbano V, et al (2019) Volcanic Gas Emissions Along the Colombian Arc Segment of the Northern Volcanic Zone (CAS-NVZ): Implications for volcano monitoring and volatile budget of the Andean Volcanic Belt. Geochem Geophys Geosystems 20:5057–5081. https://doi.org/10.1029/2019GC008573

Lages J, Chacón Z, Ramirez J, et al (2024) Excess degassing drives long-term volcanic unrest at Nevado del Ruiz. Sci Rep 14:1230. https://doi.org/10.1038/s41598-024-51380-5

Lages J, Moussallam Y, Bani P, et al (2020) First In-Situ Measurements of Plume Chemistry at Mount Garet Volcano, Island of Gaua (Vanuatu). Appl Sci 10:7293. https://doi.org/10.3390/app10207293

Laiolo M, Coppola D, Barahona F, et al (2017) Evidences of volcanic unrest on high-temperature fumaroles by satellite thermal monitoring: The case of Santa Ana

volcano, El Salvador. J Volcanol Geotherm Res 340:170–179. https://doi.org/10.1016/j.jvolgeores.2017.04.013

Laiolo M, Delle Donne D, Coppola D, et al (2022) Shallow magma dynamics at open-vent volcanoes tracked by coupled thermal and SO2 observations. Earth Planet Sci Lett 594:117726. https://doi.org/10.1016/j.epsl.2022.117726

Laiolo M, Massimetti F, Cigolini C, et al (2018) Long-term eruptive trends from space-based thermal and SO2 emissions: a comparative analysis of Stromboli, Batu Tara and Tinakula volcanoes. Bull Volcanol 80:68. https://doi.org/10.1007/s00445-018-1242-0

Lamb OD, Gestrich JE, Barnie TD, et al (2022) Acoustic observations of lava fountain activity during the 2021 Fagradalsfjall eruption, Iceland. Bull Volcanol 84:96. https://doi.org/10.1007/s00445-022-01602-3

Landi P, Métrich N, Bertagnini A, Rosi M (2008) Recycling and “re-hydration” of degassed magma inducing transient dissolution/crystallization events at Stromboli (Italy). J Volcanol Geotherm Res 174:325–336. https://doi.org/10.1016/j.jvolgeores.2008.02.013

Larrea P, Salinas S, Widom E, et al (2017) Compositional and volumetric development of a monogenetic lava flow field: The historical case of Paricutin (Michoacán, Mexico). J Volcanol Geotherm Res 348:36–48. https://doi.org/10.1016/j.jvolgeores.2017.10.016

Lerner AH, Wallace PJ, Shea T, et al (2021) The petrologic and degassing behavior of sulfur and other magmatic volatiles from the 2018 eruption of Kīlauea, Hawai‘i: melt concentrations, magma storage depths, and magma recycling. Bull Volcanol 83:43. https://doi.org/10.1007/s00445-021-01459-y

Lesage P, Mora MM, Alvarado GE, et al (2006) Complex behavior and source model of the tremor at Arenal volcano, Costa Rica. J Volcanol Geotherm Res 157:49–59. https://doi.org/10.1016/j.jvolgeores.2006.03.047

Lev E, Ruprecht P, Oppenheimer C, et al (2019) A global synthesis of lava lake dynamics. J Volcanol Geotherm Res 381:16–31. https://doi.org/10.1016/j.jvolgeores.2019.04.010

Lev E, Spiegelman M, Wysocki RJ, Karson JA (2012) Investigating lava flow rheology using video analysis and numerical flow models. J Volcanol Geotherm Res 247–248:62–73. https://doi.org/10.1016/j.jvolgeores.2012.08.002

Ligot N, Guevara A, Delmelle P (2022) Drivers of crop impacts from tephra fallout: Insights from interviews with farming communities around Tungurahua volcano, Ecuador. Volcanica 5:163–181. https://doi.org/10.30909/vol.05.01.163181

Lindsay JM, Robertson REA (2018) Integrating Volcanic Hazard Data in a Systematic Approach to Develop Volcanic Hazard Maps in the Lesser Antilles. Front Earth Sci 6:. https://doi.org/10.3389/feart.2018.00042

Lipman PW, Banks NG, Rhodes JM (1985) Degassing-induced crystallization of basaltic magma and effects on lava rheology. Nature 317:604–607. https://doi.org/10.1038/317604a0

Liu EJ, Aiuppa A, Alan A, et al (2020a) Aerial strategies advance volcanic gas measurements at inaccessible, strongly degassing volcanoes. Sci Adv 6:eabb9103. https://doi.org/10.1126/sciadv.abb9103

Liu EJ, Cashman KV, Beckett FM, et al (2014) Ash mists and brown snow: Remobilization of volcanic ash from recent Icelandic eruptions: ASH MISTS AND BROWN SNOW. J Geophys Res Atmospheres 119:9463–9480. https://doi.org/10.1002/2014JD021598

Liu EJ, Cashman KV, Miller E, et al (2020b) Petrologic monitoring at Volcán de Fuego, Guatemala. J Volcanol Geotherm Res 405:107044. https://doi.org/10.1016/j.jvolgeores.2020.107044

Liu EJ, Wood K, Mason E, et al (2019) Dynamics of Outgassing and Plume Transport Revealed by Proximal Unmanned Aerial System (UAS) Measurements at Volcán Villarrica, Chile. Geochem Geophys Geosystems 20:730–750. https://doi.org/10.1029/2018GC007692

Lloyd AS, Ruprecht P, Hauri EH, et al (2014) NanoSIMS results from olivine-hosted melt embayments: Magma ascent rate during explosive basaltic eruptions. J Volcanol Geotherm Res 283:1–18. https://doi.org/10.1016/j.jvolgeores.2014.06.002

Lombardo V, Buongiorno MF, Amici S (2006) Characterization of volcanic thermal anomalies by means of sub-pixel temperature distribution analysis. Bull Volcanol 68:641–651. https://doi.org/10.1007/s00445-005-0037-2

Lombardo V, Buongiorno MF, Pieri D, Merucci L (2004) Differences in Landsat TM derived lava flow thermal structures during summit and flank eruption at Mount Etna. J Volcanol Geotherm Res 134:15–34. https://doi.org/10.1016/j.jvolgeores.2003.12.006

Lombardo V, Musacchio M, Buongiorno MF (2012) Error analysis of subpixel lava temperature measurements using infrared remotely sensed data. Geophys J Int 191:112–125. https://doi.org/10.1111/j.1365-246X.2012.05632.x

Longo BM, Yang W, Green JB, et al (2010) An Indoor Air Quality Assessment for Vulnerable Populations Exposed to Volcanic Vog From Kilauea Volcano. Fam Community Health 33:21. https://doi.org/10.1097/FCH.0b013e3181c4e26b

Loop PNG (2024) Awar Plantation. In: Loop PNG. https://www.looppng.com/tags/awar-plantation. Accessed 3 Feb 2024

López-Saavedra M, Martí J (2023) Reviewing the multi-hazard concept. Application to volcanic islands. Earth-Sci Rev 236:104286. https://doi.org/10.1016/j.earscirev.2022.104286

Loughlin SC, Sparks RSJ, Sparks S, et al (2015) Global Volcanic Hazards and Risk. Cambridge University Press

Lyons JJ, Waite GP, Rose WI, Chigna G (2010) Patterns in open vent, strombolian behavior at Fuego volcano, Guatemala, 2005–2007. Bull Volcanol 72:1–15. https://doi.org/10.1007/s00445-009-0305-7

Lyons JJ, Waite GP, Rose WI, Chigna G (2009) Patterns in open vent, strombolian behavior at Fuego volcano, Guatemala, 2005–2007. Bull Volcanol 72:1. https://doi.org/10.1007/s00445-009-0305-7

Macedonio G, Costa A (2012) Brief Communication "Rain effect on the load of tephra deposits." Nat Hazards Earth Syst Sci 12:1229–1233. https://doi.org/10.5194/nhess-12-1229-2012

Macedonio G, Costa A, Longo A (2005) A computer model for volcanic ash fallout and assessment of subsequent hazard. Comput Geosci 31:837–845. https://doi.org/10.1016/j.cageo.2005.01.013

Madang Provincial Government (2024) Madang Province. https://www.madang.gov.pg/. Accessed 30 Jan 2024

Mafuko Nyandwi B, Kervyn M, Muhashy Habiyaremye F, et al (2023) To go or not to go when the lava flow is coming? Understanding evacuation decisions of Goma inhabitants during the 2021 Nyiragongo eruption crisis. J Volcanol Geotherm Res 444:107947. https://doi.org/10.1016/j.jvolgeores.2023.107947

Mann D, Freymueller J, Lu Z (2002) Deformation associated with the 1997 eruption of Okmok volcano, Alaska. J Geophys Res Solid Earth 107:ETG 7-1-ETG 7-12. https://doi.org/10.1029/2001JB000163

Manzella I, Bonadonna C, Phillips JC, Monnard H (2015) The role of gravitational instabilities in deposition of volcanic ash. Geology 43:211–214. https://doi.org/10.1130/G36252.1

Marotta E, Peluso R, Avino R, et al (2019) Thermal Energy Release Measurement with Thermal Camera: The Case of La Solfatara Volcano (Italy). Remote Sens 11:167. https://doi.org/10.3390/rs11020167

Marrero JM, García A, Berrocoso M, et al (2019) Strategies for the development of volcanic hazard maps in monogenetic volcanic fields: the example of La Palma (Canary Islands). J Appl Volcanol 8:6. https://doi.org/10.1186/s13617-019-0085-5

Martinez-Villegas MaM, Solidum RU, Saludadez JA, et al (2021) Moving for safety: a qualitative analysis of affected communities' evacuation response during the 2014 Mayon Volcano eruption. J Appl Volcanol 10:6. https://doi.org/10.1186/s13617-021-00109-4

Marzocchi W, Sandri L, Gasparini P, et al (2004) Quantifying probabilities of volcanic events: The example of volcanic hazard at Mount Vesuvius. J Geophys Res Solid Earth 109:. https://doi.org/10.1029/2004JB003155

Mason E, Wieser PE, Liu EJ, et al (2021) Volatile metal emissions from volcanic degassing and lava–seawater interactions at Kīlauea Volcano, Hawai'i. Commun Earth Environ 2:79. https://doi.org/10.1038/s43247-021-00145-3

Massimetti F, Coppola D, Laiolo M, et al (2018) FIRST COMPARATIVE RESULTS FROM SENTINEL-2 AND MODIS-MIROVA VOLCANIC THERMAL DATASERIES

Mastin LG, Guffanti M, Servranckx R, et al (2009) A multidisciplinary effort to assign realistic source parameters to models of volcanic ash-cloud transport and dispersion during eruptions. J Volcanol Geotherm Res 186:10–21. https://doi.org/10.1016/j.jvolgeores.2009.01.008

Mastin LG, Schwaiger H, Schneider DJ, et al (2013) Injection, transport, and deposition of tephra during event 5 at Redoubt Volcano, 23 March, 2009. J Volcanol Geotherm Res 259:201–213. https://doi.org/10.1016/j.jvolgeores.2012.04.025

Mastrolorenzo G, Pappalardo L, Troise C, et al (2008) Probabilistic tephra hazard maps for the Neapolitan area: Quantitative volcanological study of Campi Flegrei eruptions. J Geophys Res Solid Earth 113:. https://doi.org/10.1029/2007JB004954

Mather TA, Witt MLI, Pyle DM, et al (2012) Halogens and trace metal emissions from the ongoing 2008 summit eruption of Kīlauea volcano, Hawai`i. Geochim Cosmochim Acta 83:292–323. https://doi.org/10.1016/j.gca.2011.11.029

Matthews NE, Smith VC, Costa A, et al (2012) Ultra-distal tephra deposits from super-eruptions: Examples from Toba, Indonesia and Taupo Volcanic Zone, New Zealand. Quat Int 258:54–79. https://doi.org/10.1016/j.quaint.2011.07.010

Mattioli GS, Dixon TH, Farina F, et al (1998) GPS measurement of surface deformation around Soufriere Hills Volcano, Montserrat from October 1995 to July 1996. Geophys Res Lett 3417–3420. https://doi.org/10.1029/98GL00931@10.1002/(ISSN)1944-8007.SOURFVOL1

Mattox TN, Heliker C, Kauahikaua J, Hon K (1993) Development of the 1990 Kalapana Flow Field, Kilauea Volcano, Hawaii. Bull Volcanol 55:407–413. https://doi.org/10.1007/BF00302000

Mattox TN, Mangan MT (1997) Littoral hydrovolcanic explosions: a case study of lava–seawater interaction at Kilauea Volcano. J Volcanol Geotherm Res 75:1–17. https://doi.org/10.1016/S0377-0273(96)00048-0

McCormick B, Popp C, Andrews B, Cottrell E (2015) Ten years of satellite observations reveal highly variable sulphur dioxide emissions at Anatahan Volcano, Mariana Islands. J Geophys Res Atmospheres 120:7258–7282. https://doi.org/10.1002/2014JD022856

McCormick BT, Edmonds M, Mather TA, Carn SA (2012) First synoptic analysis of volcanic degassing in Papua New Guinea. Geochem Geophys Geosystems 13:. https://doi.org/10.1029/2011GC003945

McCormick Kilbride BT, Mulina K, Wadge G, et al (2019) Multi-year Satellite Observations of Sulfur Dioxide Gas Emissions and Lava Extrusion at Bagana Volcano, Papua New Guinea. Front Earth Sci 7:. https://doi.org/10.3389/feart.2019.00009

McCormick Kilbride BT, Nicholson EJ, Wood KT, et al (2023) Temporal Variability in Gas Emissions at Bagana Volcano Revealed by Aerial, Ground, and Satellite Observations. Geochem Geophys Geosystems 24:e2022GC010786. https://doi.org/10.1029/2022GC010786

McGuire WJ, Kilburn CR, Murray J (1995) Monitoring active volcanoes: strategies, procedures and techniques. UCL Press

McKee C, Itikarai I, Davies H (2018) Instrumental Volcano Surveillance and Community Awareness in the Lead-Up to the 1994 Eruptions at Rabaul, Papua New Guinea. In: Fearnley CJ, Bird DK, Haynes K, et al. (eds) Observing the Volcano World: Volcano Crisis Communication. Springer International Publishing, Cham, pp 205–233

McKee CO (1981) Geomorphology, geology and petrology of Manam volcano. Cooke-Ravian Vol Volcanol Pap 23–38

McKee K, Smith CM, Reath K, et al (2021) Evaluating the state-of-the-art in remote volcanic eruption characterization Part II: Ulawun volcano, Papua New Guinea. J Volcanol Geotherm Res 420:107381. https://doi.org/10.1016/j.jvolgeores.2021.107381

McNutt SR (1996) Seismic monitoring and eruption forecasting of volcanoes: a review of the state-of-the-art and case histories. In: Monitoring and mitigation of volcano hazards. Springer, pp 99–146

Meerdink SK, Hook SJ, Roberts DA, Abbott EA (2019) The ECOSTRESS spectral library version 1.0. Remote Sens Environ 230:111196. https://doi.org/10.1016/j.rse.2019.05.015

Mei ETW, Lavigne F, Picquout A, et al (2013) Lessons learned from the 2010 evacuations at Merapi volcano. J Volcanol Geotherm Res 261:348–365. https://doi.org/10.1016/j.jvolgeores.2013.03.010

Melnik O, Lyakhovsky V, Shapiro NM, et al (2020) Deep long period volcanic earthquakes generated by degassing of volatile-rich basaltic magmas. Nat Commun 11 (1): 3918

Melnik O, Sparks RSJ (2005) Controls on conduit magma flow dynamics during lava dome building eruptions. J Geophys Res Solid Earth 110:. https://doi.org/10.1029/2004JB003183

Melnik O, Sparks RSJ (2002) Dynamics of magma ascent and lava extrusion at Soufrière Hills Volcano, Montserrat. Geol Soc Lond Mem 21:153–171. https://doi.org/10.1144/GSL.MEM.2002.021.01.07

Mercer J, Kelman I (2010) Living alongside a volcano in Baliau, Papua New Guinea. Disaster Prev Manag Int J 19:412–422. https://doi.org/10.1108/09653561011070349

Mercer J, Kelman I, Suchet-pearson S, Lloyd K (2009) Integrating indigenous and scientific knowledge bases for disaster risk reduction in papua new guinea.

Geogr Ann Ser B Hum Geogr 91:157–183. https://doi.org/10.1111/j.1468-0467.2009.00312.x

Meredith ES, Jenkins SF, Hayes JL, et al (2024) Lava flow impacts on the built environment: insights from a new global dataset. J Appl Volcanol 13:1. https://doi.org/10.1186/s13617-023-00140-7

Meredith ES, Jenkins SF, Hayes JL, et al (2022) Damage assessment for the 2018 lower East Rift Zone lava flows of Kīlauea volcano, Hawai'i. Bull Volcanol 84:65. https://doi.org/10.1007/s00445-022-01568-2

Métrich N, Bertagnini A, Pistolesi M (2021) Paroxysms at Stromboli Volcano (Italy): Source, Genesis and Dynamics. Front Earth Sci 9:

Michellier C, Kervyn M, Barette F, et al (2020) Evaluating population vulnerability to volcanic risk in a data scarcity context: The case of Goma city, Virunga volcanic province (DRCongo). Int J Disaster Risk Reduct 45:101460. https://doi.org/10.1016/j.ijdrr.2019.101460

Miller VL, Joseph EP, Sapkota N, Szarzynski J (2022) Challenges and Opportunities for Risk Management of Volcanic Hazards in Small-Island Developing States. Mt Res Dev 42:D22–D31. https://doi.org/10.1659/MRD-JOURNAL-D-22-00001.1

Mitchell JJ, Shrestha R, Moore-Ellison CA, Glenn NF (2013) Single and Multi-Date Landsat Classifications of Basalt to Support Soil Survey Efforts. Remote Sens 5:4857–4876. https://doi.org/10.3390/rs5104857

Miyamoto H, Papp KR (2004) Rheology and topography control the path of a lava flow: Insight from numerical simulations over a preexisting topography. Geophys Res Lett 31:. https://doi.org/10.1029/2004GL020626

Moisseeva N, Businger S, Elias T (2023) VogCast: A Framework for Modeling Volcanic Air Pollution and Its Application to the 2022 Eruption of Mauna Loa Volcano, Hawai'i. J Geophys Res Atmospheres 128:e2023JD039281. https://doi.org/10.1029/2023JD039281

Morales Rivera AM, Amelung F, Mothes P, et al (2017) Ground deformation before the 2015 eruptions of Cotopaxi volcano detected by InSAR. Geophys Res Lett 44:6607–6615. https://doi.org/10.1002/2017GL073720

Moretti R, Papale P (2004) On the oxidation state and volatile behavior in multicomponent gas–melt equilibria. Chem Geol 213:265–280. https://doi.org/10.1016/j.chemgeo.2004.08.048

Morgan HA, Harris AJL, Gurioli L (2013) Lava discharge rate estimates from thermal infrared satellite data for Pacaya Volcano during 2004–2010. J Volcanol Geotherm Res 264:1–11. https://doi.org/10.1016/j.jvolgeores.2013.07.008

Morgan WR (1966) A note on the petrology of some lava types from East New Guinea. J Geol Soc Aust 13:583–591. https://doi.org/10.1080/00167616608728633

Mori J, McKee C, Itikarai I, et al (1987) Recent inflationary tilt at Manam volcano, Papua New Guinea, as recorded on a water-tube tiltmeter. J Volcanol Geotherm Res 33:361–362. https://doi.org/10.1016/0377-0273(87)90027-8

Mossoux S, Saey M, Bartolini S, et al (2016) Q-LAVHA: A flexible GIS plugin to simulate lava flows. Comput Geosci 97:98–109

Moussallam Y, Bani P, Curtis A, et al (2016) Sustaining persistent lava lakes: Observations from high-resolution gas measurements at Villarrica volcano, Chile. Earth Planet Sci Lett 454:237–247. https://doi.org/10.1016/j.epsl.2016.09.012

Mueller SB, Varley NR, Kueppers U, et al (2013) Quantification of magma ascent rate through rockfall monitoring at the growing/collapsing lava dome of Volcán de Colima, Mexico. Solid Earth 4:201–213. https://doi.org/10.5194/se-4-201-2013

Müller D, Walter TR, Schöpa A, et al (2017) High-Resolution Digital Elevation Modeling from TLS and UAV Campaign Reveals Structural Complexity at the 2014/2015 Holuhraun Eruption Site, Iceland. Front Earth Sci 5:

Murray JB (1995) Ground deformation surveying of active volcanoes. Monit Act Volcanoes

Murray JB, Stevens NF (2000) New formulae for estimating lava flow volumes at Mt. Etna Volcano, Sicily. Bull Volcanol 61:515–526. https://doi.org/10.1007/s004450050002

Nadeau PA, Palma JL, Waite GP (2011) Linking volcanic tremor, degassing, and eruption dynamics via SO2 imaging. Geophys Res Lett 38:. https://doi.org/10.1029/2010GL045820

Naismith AK, Matthew Watson I, Escobar-Wolf R, et al (2019) Eruption frequency patterns through time for the current (1999–2018) activity cycle at Volcán de Fuego derived from remote sensing data: Evidence for an accelerating cycle of explosive paroxysms and potential implications of eruptive activity. J Volcanol Geotherm Res 371:206–219. https://doi.org/10.1016/j.jvolgeores.2019.01.001

Namiki A, Manga M (2008) Transition between fragmentation and permeable outgassing of low viscosity magmas. J Volcanol Geotherm Res 169:48–60. https://doi.org/10.1016/j.jvolgeores.2007.07.020

Naranjo JL, Sigurdsson H, Carey SN, Fritz W (1986) Eruption of the Nevado del Ruiz Volcano, Colombia, On 13 November 1985: Tephra Fall and Lahars. Science 233:961–963. https://doi.org/10.1126/science.233.4767.961

Naranjo MF, Ebmeier SK, Vallejo S, et al (2016) Mapping and measuring lava volumes from 2002 to 2009 at El Reventador Volcano, Ecuador, from field measurements and satellite remote sensing. J Appl Volcanol 5:8. https://doi.org/10.1186/s13617-016-0048-z

National Statistics Office [PNG] (2011) PNG National Report 2011 Census. National Statistics Office [PNG]

National Statistics Office [PNG], ICF (2019) Papua New Guinea Demographic Health Survey 2016-18 Report. NSO and ICF, Port Moresby, Papua New Guinea and Rockville, Maryland, USA

Németh K, Moufti MR (2023) Lava Flow Hazard and Its Implication in Geopark Development for the Active Harrat Khaybar Intracontinental Monogenetic Volcanic Field, Saudi Arabia. Land 12:705. https://doi.org/10.3390/land12030705

Neuberg J (2006) Multi-parameter monitoring and modelling of volcanic processes. Stat Volcanol Lond Spec Publ IAVCEI 1:215–230

Newnham RM, Dirks KN, Samaranayake D (2010) An investigation into long-distance health impacts of the 1996 eruption of Mt Ruapehu, New Zealand. Atmos Environ 44:1568–1578. https://doi.org/10.1016/j.atmosenv.2009.12.040

Nguyen K-A, Liou Y-A, Terry JP (2019) Vulnerability of Vietnam to typhoons: A spatial assessment based on hazards, exposure and adaptive capacity. Sci Total Environ 682:31–46. https://doi.org/10.1016/j.scitotenv.2019.04.069

Obermann A, Sánchez-Pastor P, Planès T, Durand V (2019) Innovative passive seismic methods for imaging and monitoring volcanoes. In: Geophysical Research Abstracts

OpenStreetMap contributors (2023) Planet dump retrieved from https://planet.osm.org

Oppenheimer C (1993) Infrared surveillance of crater lakes using satellite data. J Volcanol Geotherm Res 55:117–128. https://doi.org/10.1016/0377-0273(93)90093-7

Oppenheimer C (1991) Lava flow cooling estimated from Landsat Thematic Mapper infrared data: The Lonquimay Eruption (Chile, 1989). J Geophys Res Solid Earth 96:21865–21878. https://doi.org/10.1029/91JB01902

Oppenheimer C, Francis PW, Rothery DA, et al (1993) Infrared image analysis of volcanic thermal features: Láscar Volcano, Chile, 1984–1992. J Geophys Res Solid Earth 98:4269–4286. https://doi.org/10.1029/92JB02134

Oppenheimer C, McGonigle AJS, Allard P, et al (2004) Sulfur, heat, and magma budget of Erta ‘Ale lava lake, Ethiopia. Geology 32:509–512. https://doi.org/10.1130/G20281.1

Oppenheimer C, Yirgu G (2002) Thermal imaging of an active lava lake: Erta ’Ale volcano, Ethiopia. Int J Remote Sens 23:4777–4782. https://doi.org/10.1080/01431160110114637

Orr TR, Rea JC (2012) Time-lapse camera observations of gas piston activity at Pu ‘u ‘Ō ‘ō, Kīlauea volcano, Hawai ‘i. Bull Volcanol 74:2353–2362

Osman S, Thomas M, Crummy J, et al (2023) Laboratory tests to understand tephra sliding behaviour on roofs. J Appl Volcanol 12:11. https://doi.org/10.1186/s13617-023-00137-2

Palfreyman W, Cooke R (1976) Eruptive history of Manam volcano, Papua New Guinea. Volcanism Australas 201–210

Pallister J, McNutt SR (2015) Chapter 66 - Synthesis of Volcano Monitoring. In: Sigurdsson H (ed) The Encyclopedia of Volcanoes (Second Edition). Academic Press, Amsterdam, pp 1151–1171

Palma JL, Blake S, Calder ES (2011) Constraints on the rates of degassing and convection in basaltic open-vent volcanoes. Geochem Geophys Geosystems 12:. https://doi.org/10.1029/2011GC003715

Palma JL, Calder ES, Basualto D, et al (2008) Correlations between SO2 flux, seismicity, and outgassing activity at the open vent of Villarrica volcano, Chile. J Geophys Res Solid Earth 113:. https://doi.org/10.1029/2008JB005577

Pardo N, Wilson H, Procter JN, et al (2015) Bridging Māori indigenous knowledge and western geosciences to reduce social vulnerability in active volcanic regions. J Appl Volcanol 4:5. https://doi.org/10.1186/s13617-014-0019-1

Patra AK, Bauer AC, Nichita CC, et al (2005) Parallel adaptive numerical simulation of dry avalanches over natural terrain. J Volcanol Geotherm Res 139:1–21

Patrick M, Swanson D, Orr T (2019a) A review of controls on lava lake level: insights from Halema‘uma‘u Crater, Kīlauea Volcano. Bull Volcanol 81:13. https://doi.org/10.1007/s00445-019-1268-y

Patrick M, Swanson D, Orr T (2019b) A review of controls on lava lake level: insights from Halema‘uma‘u Crater, Kīlauea Volcano. Bull Volcanol 81:13. https://doi.org/10.1007/s00445-019-1268-y

Patrick MR, Anderson KR, Poland MP, et al (2015a) Lava lake level as a gauge of magma reservoir pressure and eruptive hazard. Geology 43:831–834. https://doi.org/10.1130/G36896.1

Patrick MR, Anderson KR, Poland MP, et al (2015b) Lava lake level as a gauge of magma reservoir pressure and eruptive hazard. Geology 43:831–834. https://doi.org/10.1130/G36896.1

Patrick MR, Houghton BF, Anderson KR, et al (2020) The cascading origin of the 2018 Kīlauea eruption and implications for future forecasting. Nat Commun 11:5646. https://doi.org/10.1038/s41467-020-19190-1

Patrick MR, Orr T, Antolik L, et al (2014) Continuous monitoring of Hawaiian volcanoes with thermal cameras. J Appl Volcanol 3:1. https://doi.org/10.1186/2191-5040-3-1

Patrick MR, Orr T, Sutton AJ, et al (2016) Shallowly driven fluctuations in lava lake outgassing (gas pistoning), Kīlauea Volcano. Earth Planet Sci Lett 433:326–338

Pedersen GBM, Belart JMC, Óskarsson BV, et al (2022) Volume, Effusion Rate, and Lava Transport During the 2021 Fagradalsfjall Eruption: Results From Near Real-Time Photogrammetric Monitoring. Geophys Res Lett 49:e2021GL097125. https://doi.org/10.1029/2021GL097125

Pedersen GBM, Höskuldsson A, Dürig T, et al (2017) Lava field evolution and emplacement dynamics of the 2014–2015 basaltic fissure eruption at Holuhraun, Iceland. J Volcanol Geotherm Res 340:155–169. https://doi.org/10.1016/j.jvolgeores.2017.02.027

Pereira FB, Renagi O, Panakal JJ, Anduwan G (2019) A Study of Climate Variability in Papua New Guinea. J Geosci Environ Prot 07:45–52. https://doi.org/10.4236/gep.2019.75005

Pering TD, Ilanko T, Wilkes TC, et al (2019) A Rapidly Convecting Lava Lake at Masaya Volcano, Nicaragua. Front Earth Sci 6:. https://doi.org/10.3389/feart.2018.00241

Pering TD, Liu EJ, Wood K, et al (2020) Combined ground and aerial measurements resolve vent-specific gas fluxes from a multi-vent volcano. Nat Commun 11:3039. https://doi.org/10.1038/s41467-020-16862-w

Perrone MR, De Tomasi F, Stohl A, Kristiansen NI (2012) Characterization of Eyjafjallajökull volcanic aerosols over Southeastern Italy. Atmospheric Chem Phys Discuss 12:

Peters N, Oppenheimer C, Killingsworth DR, et al (2014) Correlation of cycles in Lava Lake motion and degassing at Erebus Volcano, Antarctica. Geochem Geophys Geosystems 15:3244–3257. https://doi.org/10.1002/2014GC005399

Peterson DW, Tilling RI (2000) Lava Flow Hazards: in Encyclopedia of Volcanology. Academic Press

Petrone CM, Mollo S, Gertisser R, et al (2022) Magma recharge and mush rejuvenation drive paroxysmal activity at Stromboli volcano. Nat Commun 13:7717. https://doi.org/10.1038/s41467-022-35405-z

Pieri DC, Baloga SM (1986) Eruption rate, area, and length relationships for some Hawaiian lava flows. J Volcanol Geotherm Res 30:29–45. https://doi.org/10.1016/0377-0273(86)90066-1

Pieri DC, Glaze LS, Abrams MJ (1990) Thermal radiance observations of an active lava flow during the June 1984 eruption of Mount Etna. Geology 18:1018–1022. https://doi.org/10.1130/0091-7613(1990)018<1018:TROOAA>2.3.CO;2

Planck M (1901) On the Law of Distribution of Energy in the Normal Spectrum. Ann Phys 4:1–11

Plank S, Massimetti F, Soldati A, et al (2021) Estimates of lava discharge rate of 2018 Kīlauea Volcano, Hawai'i eruption using multi-sensor satellite and laboratory measurements. Int J Remote Sens 42:1492–1511. https://doi.org/10.1080/01431161.2020.1834165

Plank S, Walter T, Martinis S, Cesca S (2020) Multi-sensor satellite imagery analysis of the growth and collapse of a littoral lava dome during the 2018/19 eruption of Kadovar Volcano, Papua New Guinea. 22:1423

Plank S, Walter TR, Martinis S, Cesca S (2019) Growth and collapse of a littoral lava dome during the 2018/19 eruption of Kadovar Volcano, Papua New Guinea, analyzed by multi-sensor satellite imagery. J Volcanol Geotherm Res 388:106704. https://doi.org/10.1016/j.jvolgeores.2019.106704

PNG Dept. of Minear Policy and Geohazards Management (2024) Manam Volcano Monitoring Outstation. In: Manam Volcano Monit. Outstation. http://dmpgm.webdev.datec.net.pg/monitoring_stations/manam-volcano-monitoring-outstation/. Accessed 14 Mar 2024

pngbuzz (2020) Awar Plantation Redevelopment launched in Bogia | pngbuzz.com. https://pngbuzz.com/png-news/6256. Accessed 3 Feb 2024

Poland MP, Anderson KR (2020) Partly Cloudy With a Chance of Lava Flows: Forecasting Volcanic Eruptions in the Twenty-First Century. J Geophys Res Solid Earth 125:e2018JB016974. https://doi.org/10.1029/2018JB016974

Poland MP, Zebker HA (2022) Volcano geodesy using InSAR in 2020: the past and next decades. Bull Volcanol 84:27. https://doi.org/10.1007/s00445-022-01531-1

Pothukuchi K (2004) Community Food Assessment: A First Step in Planning for Community Food Security. J Plan Educ Res 23:356–377. https://doi.org/10.1177/0739456X04264908

Poulidis AP, Phillips JC, Renfrew IA, et al (2018) Meteorological Controls on Local and Regional Volcanic Ash Dispersal. Sci Rep 8:6873. https://doi.org/10.1038/s41598-018-24651-1

Prieto-Torrell C, Rodriguez-Gonzalez A, Aulinas M, et al (2021) Modelling and simulation of a lava flow affecting a shore platform: a case study of Montaña de Aguarijo eruption, El Hierro (Canary Islands, Spain). J Maps 17:516–525. https://doi.org/10.1080/17445647.2021.1972853

Putirka KD (2008) Thermometers and Barometers for Volcanic Systems. Rev Mineral Geochem 69:61–120. https://doi.org/10.2138/rmg.2008.69.3

Pyle DM (2016) Chapter 1 - Field Observations of Tephra Fallout Deposits. In: Mackie S, Cashman K, Ricketts H, et al. (eds) Volcanic Ash. Elsevier, pp 25–37

Pyle DM (1989a) The thickness, volume and grainsize of tephra fall deposits. Bull Volcanol 51:1–15. https://doi.org/10.1007/BF01086757

Pyle DM (2015) Sizes of volcanic eruptions. In: The encyclopedia of volcanoes. Elsevier, pp 257–264

Pyle DM (1989b) The thickness, volume and grainsize of tephra fall deposits. Bull Volcanol 51:1–15. https://doi.org/10.1007/BF01086757

Pyle DM, Mather TA, Biggs J (2013) Remote sensing of volcanoes and volcanic processes: integrating observation and modelling – introduction. Geol Soc Lond Spec Publ 380:1–13. https://doi.org/10.1144/SP380.14

Qin Z, Soldati A, Velazquez Santana LC, et al (2018) Slug Stability in Flaring Geometries and Ramifications for Lava Lake Degassing. J Geophys Res Solid Earth 123:10,431-10,448. https://doi.org/10.1029/2018JB016113

Queißer M, Burton M, Theys N, et al (2019) TROPOMI enables high resolution SO 2 flux observations from Mt. Etna, Italy, and beyond. Sci Rep 9:957. https://doi.org/10.1038/s41598-018-37807-w

Rachmawati TA, Hidayat ART, Wahyuningtyas L, Rachmansyah A (2017) The impact of Kelud Volcano eruption to food security case study: Ngantang district, Malang Regencys. AIP Conf Proc 1857:100004. https://doi.org/10.1063/1.4987110

Ramayanti S, Achmad AR, Jung HC, et al (2022) Measurement of surface deformation related to the December 2018 Mt. Etna eruption using time-series interferometry and magma modeling for hazard zone mapping. Geosci J 26:749–765. https://doi.org/10.1007/s12303-022-0021-2

Ramsey MS, Harris AJL (2013) Volcanology 2020: How will thermal remote sensing of volcanic surface activity evolve over the next decade? J Volcanol Geotherm Res 249:217–233. https://doi.org/10.1016/j.jvolgeores.2012.05.011

Rehman K, Fatima F, Waheed I, Akash MSH (2018) Prevalence of exposure of heavy metals and their impact on health consequences. J Cell Biochem 119:157–184. https://doi.org/10.1002/jcb.26234

Resing JA, Sansone FJ (2002) The chemistry of lava-seawater interactions II: the elemental signature. Geochim Cosmochim Acta 66:1925–1941. https://doi.org/10.1016/S0016-7037(01)00897-3

Reynolds MA (1957) Eruption of Manam Volcano, Territory of New Guinea, December, 1956 - February, 1957. Geoscience Australia, Canberra

Richardson JP, Waite GP, Palma JL (2014) Varying seismic-acoustic properties of the fluctuating lava lake at Villarrica volcano, Chile. J Geophys Res Solid Earth 119:5560–5573. https://doi.org/10.1002/2014JB011002

Ripepe M, Marchetti E, Ulivieri G (2007) Infrasonic monitoring at Stromboli volcano during the 2003 effusive eruption: Insights on the explosive and degassing process of an open conduit system. J Geophys Res Solid Earth 112:. https://doi.org/10.1029/2006JB004613

Rizzoli P, Martone M, Gonzalez C, et al (2017) Generation and performance assessment of the global TanDEM-X digital elevation model. ISPRS J Photogramm Remote Sens 132:119–139. https://doi.org/10.1016/j.isprsjprs.2017.08.008

Roberts G, Wooster MJ, Perry GLW, Kaufman YJ (2005) Retrieval of biomass combustion rates and totals from fire radiative power observations: FRP derivation and calibration relationships between biomass consumption and fire radiative energy release. J Geophys Res Atmospheres 110:. https://doi.org/10.1029/2005JD006318

Robin C, Camus G, Gourgaud A (1991) Eruptive and magmatic cycles at Fuego de Colima volcano (Mexico). J Volcanol Geotherm Res 45:209–225. https://doi.org/10.1016/0377-0273(91)90060-D

Roche O, Niño Y, Mangeney A, et al (2013) Dynamic pore-pressure variations induce substrate erosion by pyroclastic flows. Geology 41:1107–1110. https://doi.org/10.1130/G34668.1

Rodriguez-Gonzalez A, Aulinas M, Mossoux S, et al (2021) Comparison of real and simulated lava flows in the Holocene volcanism of Gran Canaria (Canary Islands, Spain) with Q-LavHA: contribution to volcanic hazard management. Nat Hazards 107:1785–1819. https://doi.org/10.1007/s11069-021-04660-6

Rongo R, Lupiano V, Spataro W, et al (2016) SCIARA: cellular automata lava flow modelling and applications in hazard prediction and mitigation. Geol Soc Lond Spec Publ 426:345–356. https://doi.org/10.1144/SP426.22

Rose WI, Palma J, Delgado Granados H, Varley N (2013) Open-vent volcanism and related hazards: Overview. Spec Pap Geol Soc Am 498:vii–xiii. https://doi.org/10.1130/2013.2498(00)

Rose WI, Self S, Murrow PJ, et al (2008a) Nature and significance of small volume fall deposits at composite volcanoes: Insights from the October 14, 1974 Fuego eruption, Guatemala. Bull Volcanol 70:1043–1067. https://doi.org/10.1007/s00445-007-0187-5

Rose WI, Self S, Murrow PJ, et al (2008b) Nature and significance of small volume fall deposits at composite volcanoes: Insights from the October 14, 1974 Fuego eruption, Guatemala. Bull Volcanol 70:1043–1067. https://doi.org/10.1007/s00445-007-0187-5

Rothery DA, Francis PW, Wood CA (1988) Volcano monitoring using short wavelength infrared data from satellites. J Geophys Res Solid Earth 93:7993–8008. https://doi.org/10.1029/JB093iB07p07993

Rowland SK, Garbeil H, Harris AJL (2005) Lengths and hazards from channel-fed lava flows on Mauna Loa, Hawai‘i, determined from thermal and downslope modeling with FLOWGO. Bull Volcanol 67:634–647. https://doi.org/10.1007/s00445-004-0399-x

Rozaki Z, Rahmawati N, Wijaya O, et al (2022) Farmers' food security in the volcanic area: A case in Mount Merapi, Indonesia. Open Agric 7:554–565. https://doi.org/10.1515/opag-2022-0122

Ruggieri F, Forte G, Bocca B, et al (2023) Potentially harmful elements released by volcanic ash of the 2021 Tajogaite eruption (Cumbre Vieja, La Palma Island, Spain): Implications for human health. Sci Total Environ 905:167103. https://doi.org/10.1016/j.scitotenv.2023.167103

Ruth DCS, Costa F (2021) A petrological and conceptual model of Mayon volcano (Philippines) as an example of an open-vent volcano. Bull Volcanol 83:62. https://doi.org/10.1007/s00445-021-01486-9

Rutherford MJ (2008) Magma Ascent Rates. Rev Mineral Geochem 69:241–271. https://doi.org/10.2138/rmg.2008.69.7

Rymer H, Cassidy J, Locke CA, Murray JB (1995) Magma movements in Etna volcano associated with the major 1991–1993 lava eruption: evidence from gravity and deformation. Bull Volcanol 57:451–461. https://doi.org/10.1007/BF00300989

Saadat S, Stern CR (2011) Petrochemistry and genesis of olivine basalts from small monogenetic parasitic cones of Bazman stratovolcano, Makran arc, southeastern Iran. Lithos 125:607–619. https://doi.org/10.1016/j.lithos.2011.03.014

Sabra S, Malmqvist E, Saborit A, et al (2017) Heavy metals exposure levels and their correlation with different clinical forms of fetal growth restriction. PLOS ONE 12:e0185645. https://doi.org/10.1371/journal.pone.0185645

Sansone FJ, Benitez-Nelson CR, Resing JA, et al (2002) Geochemistry of atmospheric aerosols generated from lava-seawater interactions. Geophys Res Lett 29:49-1-49–4. https://doi.org/10.1029/2001GL013882

Scaini C, Folch A, Navarro M (2012) Tephra hazard assessment at Concepción Volcano, Nicaragua. J Volcanol Geotherm Res 219–220:41–51. https://doi.org/10.1016/j.jvolgeores.2012.01.007

Scarpa R (2001) Predicting Volcanic Eruptions. Science 293:615–616. https://doi.org/10.1126/science.1063606

Scarpa R, Gasparini P (1996) A Review of Volcano Geophysics and Volcano-Monitoring Methods. In: Scarpa R, Tilling RI (eds) Monitoring and Mitigation of Volcano Hazards. Springer, Berlin, Heidelberg, pp 3–22

Schellenberg B, Richardson T, Watson M, et al (2019) Remote sensing and identification of volcanic plumes using fixed-wing UAVs over Volcán de Fuego, Guatemala. J Field Robot 36:1192–1211

Schilling SP (1998) LAHARZ; GIS programs for automated mapping of lahar-inundation hazard zones. US Geological Survey; Information Services [distributor],

Schmidt C, Laag C, Whitehead M, et al (2022) The complexities of assessing volcanic hazards along the Cameroon Volcanic Line using spatial distribution of monogenetic volcanoes. J Volcanol Geotherm Res 427:107558. https://doi.org/10.1016/j.jvolgeores.2022.107558

Schmith J, Höskuldsson Á, Holm PM, Larsen G (2018) Large explosive basaltic eruptions at Katla volcano, Iceland: Fragmentation, grain size and eruption dynamics. J Volcanol Geotherm Res 354:140–152. https://doi.org/10.1016/j.jvolgeores.2018.01.024

Schwaiger HF, Denlinger RP, Mastin LG (2012) Ash3d: A finite-volume, conservative numerical model for ash transport and tephra deposition. J Geophys Res Solid Earth 117:. https://doi.org/10.1029/2011JB008968

Sciotto M, Watson LM, Cannata A, et al (2022) Infrasonic gliding reflects a rising magma column at Mount Etna (Italy). Sci Rep 12:16954. https://doi.org/10.1038/s41598-022-20258-9

Scott BJ, McKee CO (1986) Deformation, eruptive activity, and Earth tidal influences at Manam Volcano, Papua New Guinea, 1957–1982. Bull R Soc NZ 24:155–171

Scott S, Pfeffer M, Oppenheimer C, et al (2023) Near-surface magma flow instability drives cyclic lava fountaining at Fagradalsfjall, Iceland. Nat Commun 14:6810. https://doi.org/10.1038/s41467-023-42569-9

Sheridan MF, Stinton AJ, Patra A, et al (2005) Evaluating Titan2D mass-flow model using the 1963 Little Tahoma Peak avalanches, Mount Rainier, Washington. J Volcanol Geotherm Res 139:89–102. https://doi.org/10.1016/j.jvolgeores.2004.06.011

Shevchenko AV, Dvigalo VN, Walter TR, et al (2020) The rebirth and evolution of Bezymianny volcano, Kamchatka after the 1956 sector collapse. Commun Earth Environ 1:1–15. https://doi.org/10.1038/s43247-020-00014-5

Shinohara H (2008) Excess degassing from volcanoes and its role on eruptive and intrusive activity. Rev Geophys 46:

Shinohara H (2005) A new technique to estimate volcanic gas composition: plume measurements with a portable multi-sensor system. J Volcanol Geotherm Res 143:319–333. https://doi.org/10.1016/j.jvolgeores.2004.12.004

Shinohara H, Aiuppa A, Giudice G, et al (2008) Variation of H2O/CO2 and CO2/SO2 ratios of volcanic gases discharged by continuous degassing of Mount Etna volcano, Italy. J Geophys Res Solid Earth 113:. https://doi.org/10.1029/2007JB005185

Shortall R, Davidsdottir B, Axelsson G (2015) A sustainability assessment framework for geothermal energy projects: Development in Iceland, New Zealand and Kenya. Renew Sustain Energy Rev 50:372–407. https://doi.org/10.1016/j.rser.2015.04.175

Shortall R, Kharrazi A (2017) Cultural factors of sustainable energy development: A case study of geothermal energy in Iceland and Japan. Renew Sustain Energy Rev 79:101–109. https://doi.org/10.1016/j.rser.2017.05.029

Shreve T, Grandin R, Boichu M (2022) Reservoir depressurization driven by passive gas emissions at Ambrym volcano. Earth Planet Sci Lett 584:117512. https://doi.org/10.1016/j.epsl.2022.117512

Siagian TH, Purhadi P, Suhartono S, Ritonga H (2014) Social vulnerability to natural hazards in Indonesia: Driving factors and policy implications. Nat Hazards 70:1603–1617

Siebert L, Simkin T, Kimberly P (2011) Volcanoes of the World: Third Edition. University of California Press

Sieron K, Juárez Cerrillo SF, González-Zuccolotto K, et al (2021) Morphology and distribution of monogenetic volcanoes in Los Tuxtlas Volcanic Field, Veracruz, Mexico: implications for hazard assessment. Bull Volcanol 83:47. https://doi.org/10.1007/s00445-021-01467-y

Simkin T, Siebert L, Blong R (2001) Volcano Fatalities--Lessons from the Historical Record. Science 291:255–255. https://doi.org/10.1126/science.291.5502.255

Simmons IC, Pfeffer MA, Calder ES, et al (2017) Extended SO2 outgassing from the 2014–2015 Holuhraun lava flow field, Iceland. Bull Volcanol 79:79. https://doi.org/10.1007/s00445-017-1160-6

Sims K, Reith A, Bright E, et al (2023) LandScan Global 2022

Smets B, d'Oreye N, Kervyn M, Kervyn F (2017) Gas piston activity of the Nyiragongo lava lake: First insights from a Stereographic Time-Lapse Camera system. J Afr Earth Sci 134:874–887. https://doi.org/10.1016/j.jafrearsci.2016.04.010

Spaans K, Hooper A (2016) InSAR processing for volcano monitoring and other near-real time applications. J Geophys Res Solid Earth 121:2947–2960. https://doi.org/10.1002/2015JB012752

Spampinato L, Calvari S, Oppenheimer C, Boschi E (2011) Volcano surveillance using infrared cameras. Earth-Sci Rev 106:63–91. https://doi.org/10.1016/j.earscirev.2011.01.003

Spampinato L, Ganci G, Hernández PA, et al (2013) Thermal insights into the dynamics of Nyiragongo lava lake from ground and satellite measurements. J Geophys Res Solid Earth 118:5771–5784. https://doi.org/10.1002/2013JB010520

Spampinato L, Oppenheimer C, Calvari S, et al (2008) Lava lake surface characterization by thermal imaging: Erta 'Ale volcano (Ethiopia). Geochem Geophys Geosystems 9:. https://doi.org/10.1029/2008GC002164

Sparks R (2003a) Dynamics of magma degassing. Geol Soc Lond Spec Publ 213:5–22

Sparks RSJ (2003b) Forecasting volcanic eruptions. Earth Planet Sci Lett 210:1–15. https://doi.org/10.1016/S0012-821X(03)00124-9

Sparks RSJ (1997) Causes and consequences of pressurisation in lava dome eruptions. Earth Planet Sci Lett 150:177–189. https://doi.org/10.1016/S0012-821X(97)00109-X

Sparks RSJ, Biggs J, Neuberg JW (2012) Monitoring volcanoes. Science 335:1310–1311

Sparks RSJ, Bursik MI, Ablay GJ, et al (1992) Sedimentation of tephra by volcanic plumes. Part 2: controls on thickness and grain-size variations of tephra fall deposits. Bull Volcanol 54:685–695. https://doi.org/10.1007/BF00430779

Sparks SRJ, Aspinall WP, Barclay J, et al (2024) Analysis of magma flux and eruption intensity during the 2021 explosive activity at La Soufrière, St Vincent, West Indies. Geol Soc Lond Spec Publ 539:63–79. https://doi.org/10.1144/SP539-2022-286

Spence RJ, Pomonis A, Baxter PJ, et al (1996) Building damage caused by the Mount Pinatubo eruption of June 15, 1991. Fire Mud Erupt Lahars Mt Pinatubo Philipp Philipp Inst Volcanol Seismol Quezon City

Spence RJS, Kelman I, Baxter PJ, et al (2005) Residential building and occupant vulnerability to tephra fall. Nat Hazards Earth Syst Sci 5:477–494. https://doi.org/10.5194/nhess-5-477-2005

Spina L, Del Bello E, Ricci T, et al (2021) Multi-parametric characterization of explosive activity at Batu Tara Volcano (Flores Sea, Indonesia). J Volcanol Geotherm Res 413:107199. https://doi.org/10.1016/j.jvolgeores.2021.107199

Stasiuk MV, Jaupart C, Stephen R, Sparks J (1993) Influence of cooling on lava-flow dynamics. Geology 21:335–338. https://doi.org/10.1130/0091-7613(1993)021<0335:IOCOLF>2.3.CO;2

Steenbergen DJ, Neihapi PT, Koran D, et al (2020) COVID-19 restrictions amidst cyclones and volcanoes: A rapid assessment of early impacts on livelihoods and food security in coastal communities in Vanuatu. Mar Policy 121:104199. https://doi.org/10.1016/j.marpol.2020.104199

Stefan J (1879) Uber die Beziehung zwischen der Warmestrahlung und der Temperatur, Sitzungsberichte der mathematisch-naturwissenschaftlichen Classe der kaiserlichen. Akad Wiss 79:S-391

Steffke AM, Harris AJL, Burton M, et al (2011) Coupled use of COSPEC and satellite measurements to define the volumetric balance during effusive eruptions at Mt. Etna, Italy. J Volcanol Geotherm Res 205:47–53. https://doi.org/10.1016/j.jvolgeores.2010.06.004

Stevenson DS, Blake S (1998) Modelling the dynamics and thermodynamics of volcanic degassing. Bull Volcanol 60:307–317. https://doi.org/10.1007/s004450050234

Stevenson JA, Loughlin S, Rae C, et al (2012) Distal deposition of tephra from the Eyjafjallajökull 2010 summit eruption. J Geophys Res Solid Earth 117:. https://doi.org/10.1029/2011JB008904

Stewart C, Damby DE, Horwell CJ, et al (2021) Volcanic air pollution and human health: recent advances and future directions. Bull Volcanol 84:11. https://doi.org/10.1007/s00445-021-01513-9

Stix J, Torres RC, Narváez M L, et al (1997) A model of vulcanian eruptions at Galeras volcano, Colombia. J Volcanol Geotherm Res 77:285–303. https://doi.org/10.1016/S0377-0273(96)00100-X

Stoiber RE, Williams SN, Huebert BJ (1986) Sulfur and halogen gases at Masaya Caldera Complex, Nicaragua: Total flux and variations with time. J Geophys Res Solid Earth 91:12215–12231. https://doi.org/10.1029/JB091iB12p12215

Sutton AJ, Elias T, Gerlach TM, Stokes JB (2001) Implications for eruptive processes as indicated by sulfur dioxide emissions from Kīlauea Volcano, Hawai'i, 1979–1997. J Volcanol Geotherm Res 108:283–302. https://doi.org/10.1016/S0377-0273(00)00291-2

Suzuki T (1983) A theoretical model for dispersion of tephra. Arc Volcanism Phys Tecton 95:113

Taddeucci J, Alatorre-Ibargüengoitia MA, Cruz-Vázquez O, et al (2017) In-flight dynamics of volcanic ballistic projectiles. Rev Geophys 55:675–718. https://doi.org/10.1002/2017RG000564

Taddeucci J, Edmonds M, Houghton B, et al (2015) Chapter 27 - Hawaiian and Strombolian Eruptions. In: Sigurdsson H (ed) The Encyclopedia of Volcanoes (Second Edition). Academic Press, Amsterdam, pp 485–503

Taddeucci J, Scarlato P, Del Bello E, et al (2021) Chapter 9 - The dynamics of explosive mafic eruptions: New insights from multiparametric observations. In: Papale P (ed) Forecasting and Planning for Volcanic Hazards, Risks, and Disasters. Elsevier, pp 379–411

Tamburello G, McGonigle AJS, Kantzas EP, Aiuppa A (2011) Recent advances in ground-based ultraviolet remote sensing of volcanic SO2 fluxes. Ann Geophys 54:. https://doi.org/10.4401/ag-5179

Tanaka HKM (2020) Development of the muographic tephra deposit monitoring system. Sci Rep 10:14820. https://doi.org/10.1038/s41598-020-71902-1

Taracsák Z, Longpré M-A, Tartèse R, et al (2022) Highly Oxidising Conditions in Volatile-Rich El Hierro Magmas: Implications for Ocean Island Magmatism. J Petrol 63:egac011. https://doi.org/10.1093/petrology/egac011

Tarquini S, Favalli M (2011) Mapping and DOWNFLOW simulation of recent lava flow fields at Mount Etna. J Volcanol Geotherm Res 204:27–39. https://doi.org/10.1016/j.jvolgeores.2011.05.001

Tarquini S, Favalli M (2010) Changes of the susceptibility to lava flow invasion induced by morphological modifications of an active volcano: the case of Mount Etna, Italy. Nat Hazards 54:537–546. https://doi.org/10.1007/s11069-009-9484-y

Tarquini S, Favalli M (2016) Simulating the area covered by lava flows using the DOWNFLOW code. Geol Soc Lond Spec Publ 426:293–312. https://doi.org/10.1144/SP426.15

Tarquini S, Favalli M (2013) Uncertainties in lava flow hazard maps derived from numerical simulations: The case study of Mount Etna. J Volcanol Geotherm Res 260:90–102. https://doi.org/10.1016/j.jvolgeores.2013.04.017

Taylor G (1963) Seismic and tilt phenomena preceding a Pelean type eruption from a basaltic volcano. Bull Volcanol 26:5–11

Taylor GA (1958a) Notes on the current eruption at Manam. Geoscience Australia, Canberra

Taylor GA (1958b) The eruptive trend of Manam Volcano. Geoscience Australia, Canberra

Tazieff H (1977) An exceptional eruption: Mt. Niragongo, Jan. 10th, 1977. Bull Volcanol 40:189–200. https://doi.org/10.1007/BF02596999

Texier-Teixeira P, Chouraqui F, Perrillat-Collomb A, et al (2014) Reducing volcanic risk on Fogo Volcano, Cape Verde, through a participatory approach: which outcome? Nat Hazards Earth Syst Sci 14:2347–2358

Theys N, De Smedt I, Yu H, et al (2017) Sulfur dioxide retrievals from TROPOMI onboard Sentinel-5 Precursor: algorithm theoretical basis. Atmospheric Meas Tech 10:119–153. https://doi.org/10.5194/amt-10-119-2017

Theys N, Hedelt P, De Smedt I, et al (2019) Global monitoring of volcanic SO2 degassing with unprecedented resolution from TROPOMI onboard Sentinel-5 Precursor. Sci Rep 9:2643. https://doi.org/10.1038/s41598-019-39279-y

Thompson MA, Lindsay JM, Gaillard J (2015) The influence of probabilistic volcanic hazard map properties on hazard communication. J Appl Volcanol 4:6. https://doi.org/10.1186/s13617-015-0023-0

Thompson MA, Lindsay JM, Leonard GS (2018) More Than Meets the Eye: Volcanic Hazard Map Design and Visual Communication. In: Fearnley CJ, Bird DK, Haynes K, et al. (eds) Observing the Volcano World: Volcano Crisis Communication. Springer International Publishing, Cham, pp 621–640

Thouret J-C, Antoine S, Magill C, Ollier C (2020) Lahars and debris flows: Characteristics and impacts. Earth-Sci Rev 201:103003. https://doi.org/10.1016/j.earscirev.2019.103003

Tibaldi A (2015) Structure of volcano plumbing systems: A review of multi-parametric effects. J Volcanol Geotherm Res 298:85–135. https://doi.org/10.1016/j.jvolgeores.2015.03.023

Tilling RI (1987) Fluctuations in surface height of active lava lakes during 1972–1974 Mauna Ulu Eruption, Kilauea Volcano, Hawaii. J Geophys Res Solid Earth 92:13721–13730. https://doi.org/10.1029/JB092iB13p13721

Tollan PME, Dale CW, Hermann J, et al (2017) Generation and Modification of the Mantle Wedge and Lithosphere beneath the West Bismarck Island Arc: Melting, Metasomatism and Thermal History of Peridotite Xenoliths from Ritter Island. J Petrol 58:1475–1510. https://doi.org/10.1093/petrology/egx062

Tregoning P, Jackson RJ, McQueen H, et al (1999) Motion of the South Bismarck Plate, Papua New Guinea. Geophys Res Lett 26:3517–3520. https://doi.org/10.1029/1999GL010840

Tupper A, Itikarai I, Richards M, et al (2007) Facing the Challenges of the International Airways Volcano Watch: The 2004/05 Eruptions of Manam, Papua New Guinea. Weather Forecast 22:175–191. https://doi.org/10.1175/WAF974.1

Tupper A, Textor C, Herzog M, et al (2009) Tall clouds from small eruptions: the sensitivity of eruption height and fine ash content to tropospheric instability. Nat Hazards 51:375–401. https://doi.org/10.1007/s11069-009-9433-9

Tupper A, Wunderman R (2009) Reducing discrepancies in ground and satellite-observed eruption heights. J Volcanol Geotherm Res 186:22–31. https://doi.org/10.1016/j.jvolgeores.2009.02.015

Valade S, Coppola D, Campion R, et al (2023) Lava dome cycles reveal rise and fall of magma column at Popocatépetl volcano. Nat Commun 14:3254. https://doi.org/10.1038/s41467-023-38386-9

Valade S, Donnadieu F, Lesage P, et al (2012) Explosion mechanisms at Arenal volcano, Costa Rica: An interpretation from integration of seismic and Doppler radar data. J Geophys Res Solid Earth 117:. https://doi.org/10.1029/2011JB008623

Valade S, Ley A, Massimetti F, et al (2019) Towards Global Volcano Monitoring Using Multisensor Sentinel Missions and Artificial Intelligence: The MOUNTS Monitoring System. Remote Sens 11:1528. https://doi.org/10.3390/rs11131528

Vásconez F, Moussallam Y, Bani P, et al (2022) Ash and gas discharge during open vent activity at El Reventador (Ecuador): explosion-style transitions driven by conduit capping. Bull Volcanol 84:77. https://doi.org/10.1007/s00445-022-01585-1

Vergniolle S, Bouche E (2016) Gas-driven lava lake fluctuations at Erta 'Ale volcano (Ethiopia) revealed by MODIS measurements. Bull Volcanol 78:60. https://doi.org/10.1007/s00445-016-1047-y

Vergniolle S, Métrich N (2021) Open-vent volcanoes: a preface to the special issue. Bull Volcanol 83:29, s00445-021-01454–3. https://doi.org/10.1007/s00445-021-01454-3

Vergniolle S, Métrich N (2022) An interpretative view of open-vent volcanoes. Bull Volcanol 84:83. https://doi.org/10.1007/s00445-022-01581-5

Verolino A, Jenkins SF, Sieh K, et al (2022) Assessing volcanic hazard and exposure to lava flows at remote volcanic fields: a case study from the Bolaven Volcanic Field, Laos. J Appl Volcanol 11:6. https://doi.org/10.1186/s13617-022-00116-z

Vicari A, Alexis H, Del Negro C, et al (2007) Modeling of the 2001 lava flow at Etna volcano by a Cellular Automata approach. Environ Model Softw 22:1465–1471. https://doi.org/10.1016/j.envsoft.2006.10.005

Vicari A, Ciraudo A, Del Negro C, et al (2009) Lava flow simulations using discharge rates from thermal infrared satellite imagery during the 2006 Etna eruption. Nat Hazards 50:539–550. https://doi.org/10.1007/s11069-008-9306-7

Viccaro M, Calcagno R, Garozzo I, et al (2015) Continuous magma recharge at Mt. Etna during the 2011–2013 period controls the style of volcanic activity and compositions of erupted lavas. Mineral Petrol 109:67–83. https://doi.org/10.1007/s00710-014-0352-4

Viccaro M, Cannata A, Cannavò F, et al (2021) Shallow conduit dynamics fuel the unexpected paroxysms of Stromboli volcano during the summer 2019. Sci Rep 11:266. https://doi.org/10.1038/s41598-020-79558-7

Vieira G, Mora C, Pina P, et al (2021) UAV-based very high resolution point cloud, digital surface model and orthomosaic of the Chã das Caldeiras lava fields (Fogo, Cabo Verde). Earth Syst Sci Data 13:3179–3201. https://doi.org/10.5194/essd-13-3179-2021

Vilches M, Ureta G, Grosse P, et al (2022) Effusion rate estimation based on solidified lava flows: Implications for volcanic hazard assessment in the Negros de Aras monogenetic volcanic field, northern Chile. J Volcanol Geotherm Res 422:107454. https://doi.org/10.1016/j.jvolgeores.2021.107454

Voight B (1990) The 1985 Nevado del Ruiz volcano catastrophe: anatomy and retrospection. J Volcanol Geotherm Res 44:349–386

Volentik ACM, Connor CB, Connor LJ, Bonadonna C (2009) Aspects of volcanic hazard assessment for the Bataan nuclear power plant, Luzon Peninsula, Philippines. Volcan Tecton Hazard Assess Nucl Facil 229–256

Waite GP, Nadeau PA, Lyons JJ (2013) Variability in eruption style and associated very long period events at Fuego volcano, Guatemala. J Geophys Res Solid Earth 118:1526–1533. https://doi.org/10.1002/jgrb.50075

Wakeford ZE, Chmielewska M, Hole MJ, et al (2019) Combining thermal imaging with photogrammetry of an active volcano using UAV: an example from Stromboli, Italy. Photogramm Rec 34:445–466. https://doi.org/10.1111/phor.12301

Walker GPL (1973) Mount Etna and the 1971 eruption-lengths of lava flows. Philos Trans R Soc Lond Ser Math Phys Sci 274:107–118

Walker GPL, Self S, Wilson L (1984) Tarawera 1886, New Zealand — A basaltic plinian fissure eruption. J Volcanol Geotherm Res 21:61–78. https://doi.org/10.1016/0377-0273(84)90016-7

Wallace LM, Stevens C, Silver E, et al (2004) GPS and seismological constraints on active tectonics and arc-continent collision in Papua New Guinea: Implications for mechanics of microplate rotations in a plate boundary zone. J Geophys Res Solid Earth 109:. https://doi.org/10.1029/2003JB002481

Wallace PJ (2001) Volcanic SO2 emissions and the abundance and distribution of exsolved gas in magma bodies. J Volcanol Geotherm Res 108:85–106. https://doi.org/10.1016/S0377-0273(00)00279-1

Wallace PJ (2005) Volatiles in subduction zone magmas: concentrations and fluxes based on melt inclusion and volcanic gas data. J Volcanol Geotherm Res 140:217–240. https://doi.org/10.1016/j.jvolgeores.2004.07.023

Wallace PJ, Edmonds M (2011) The Sulfur Budget in Magmas: Evidence from Melt Inclusions, Submarine Glasses, and Volcanic Gas Emissions. Rev Mineral Geochem 73:215–246. https://doi.org/10.2138/rmg.2011.73.8

Wallace PJ, Kamenetsky VS, Cervantes P (2015a) Special Collection: Glasses, Melts, and Fluids, as Tools for Understanding Volcanic Processes and Hazards. Melt inclusion CO2 contents, pressures of olivine crystallization, and the problem of

shrinkage bubbles. Am Mineral 100:787–794. https://doi.org/10.2138/am-2015-5029

Wallace PJ, Plank T, Edmonds M, Hauri EH (2015b) Chapter 7 - Volatiles in Magmas. In: Sigurdsson H (ed) The Encyclopedia of Volcanoes (Second Edition). Academic Press, Amsterdam, pp 163–183

Wantim MN, Kervyn M, Ernst GGJ, et al (2013) Numerical experiments on the dynamics of channelised lava flows at Mount Cameroon volcano with the FLOWGO thermo-rheological model. J Volcanol Geotherm Res 253:35–53. https://doi.org/10.1016/j.jvolgeores.2012.12.003

Wardman JB, Wilson TM, Bodger PS, et al (2012) Potential impacts from tephra fall to electric power systems: a review and mitigation strategies. Bull Volcanol 74:2221–2241. https://doi.org/10.1007/s00445-012-0664-3

Warwick R, Williams-Jones G, Kelman M, Witter J (2022) A scenario-based volcanic hazard assessment for the Mount Meager Volcanic Complex, British Columbia. J Appl Volcanol 11:5. https://doi.org/10.1186/s13617-022-00114-1

Wech AG, Thelen WA, Thomas AM (2020) Deep long-period earthquakes generated by second boiling beneath Mauna Kea volcano. Science 368:775–779. https://doi.org/10.1126/science.aba4798

Wehrmann H, Bonadonna C, Freundt A, et al (2006) Fontana Tephra: A basaltic Plinian eruption in Nicaragua. https://doi.org/10.1130/2006.2412(11)

Weissel JK, Czuchlewski KR, Kim Y (2004) Synthetic aperture radar (SAR)-based mapping of volcanic flows: Manam Island, Papua New Guinea. Nat Hazards Earth Syst Sci 4:339–346. https://doi.org/10.5194/nhess-4-339-2004

Werner C, Kelly PJ, Doukas M, et al (2013) Degassing of CO2, SO2, and H2S associated with the 2009 eruption of Redoubt Volcano, Alaska. J Volcanol Geotherm Res 259:270–284. https://doi.org/10.1016/j.jvolgeores.2012.04.012

White JT, Connor CB, Connor L, Hasenaka T (2017) Efficient inversion and uncertainty quantification of a tephra fallout model. J Geophys Res Solid Earth 122:281–294. https://doi.org/10.1002/2016JB013682

White R, McCausland W (2016) Volcano-tectonic earthquakes: A new tool for estimating intrusive volumes and forecasting eruptions. J Volcanol Geotherm Res 309:139–155. https://doi.org/10.1016/j.jvolgeores.2015.10.020

Wilkinson E, Lovell E, Carby B, et al (2016) The Dilemmas of Risk-Sensitive Development on a Small Volcanic Island. Resources 5:21. https://doi.org/10.3390/resources5020021

Williams GT, Jenkins SF, Biass S, et al (2020) Remotely assessing tephra fall building damage and vulnerability: Kelud Volcano, Indonesia. J Appl Volcanol 9:10. https://doi.org/10.1186/s13617-020-00100-5

Williams GT, Jenkins SF, Lee DWJ, Wee SJ (2021) How rainfall influences tephra fall loading — an experimental approach. Bull Volcanol 83:42. https://doi.org/10.1007/s00445-021-01465-0

Williams-Jones G, Rymer H (2015) Chapter 57 - Hazards of Volcanic Gases. In: Sigurdsson H (ed) The Encyclopedia of Volcanoes (Second Edition). Academic Press, Amsterdam, pp 985–992

Williamson BJ, Di Muro A, Horwell CJ, et al (2010) Injection of vesicular magma into an andesitic dome at the effusive–explosive transition. Earth Planet Sci Lett 295:83–90. https://doi.org/10.1016/j.epsl.2010.03.027

Wilson G, Wilson TM, Deligne NI, Cole JW (2014) Volcanic hazard impacts to critical infrastructure: A review. J Volcanol Geotherm Res 286:148–182. https://doi.org/10.1016/j.jvolgeores.2014.08.030

Wilson M (1989) Igneous petrogenesis. Springer

Wilson T, Stewart C, Bickerton H, et al (2013) Impacts of the June 2011 Puyehue-Cordón Caulle volcanic complex eruption on urban infrastructure, agriculture and public health

Wilson TM, Cole JW, Stewart C, et al (2011) Ash storms: impacts of wind-remobilised volcanic ash on rural communities and agriculture following the 1991 Hudson eruption, southern Patagonia, Chile. Bull Volcanol 73:223–239. https://doi.org/10.1007/s00445-010-0396-1

Wilson TM, Jenkins S, Stewart C (2015a) Chapter 3 - Impacts from Volcanic Ash Fall. In: Shroder JF, Papale P (eds) Volcanic Hazards, Risks and Disasters. Elsevier, Boston, pp 47–86

Wilson TM, Jenkins SF, Stewart C (2015b) Volcanic ash fall impacts. Glob Volcan Hazards Risk 281–288

Witham F, Woods AW, Gladstone C (2006) An analogue experimental model of depth fluctuations in lava lakes. Bull Volcanol 69:51–56. https://doi.org/10.1007/s00445-006-0055-8

Witter JB, Kress VC, Delmelle P, Stix J (2004) Volatile degassing, petrology, and magma dynamics of the Villarrica Lava Lake, Southern Chile. J Volcanol Geotherm Res 134:303–337. https://doi.org/10.1016/j.jvolgeores.2004.03.002

Woitischek J, Edmonds M, Woods AW (2020a) The control of magma crystallinity on the fluctuations in gas composition at open vent basaltic volcanoes. Sci Rep 10:14862. https://doi.org/10.1038/s41598-020-71667-7

Woitischek J, Woods AW, Edmonds M, et al (2020b) Strombolian eruptions and dynamics of magma degassing at Yasur Volcano (Vanuatu). J Volcanol Geotherm Res 398:106869. https://doi.org/10.1016/j.jvolgeores.2020.106869

Woo G (2008) Probabilistic criteria for volcano evacuation decisions. Nat Hazards 45:87–97. https://doi.org/10.1007/s11069-007-9171-9

Wood M, Foale S, Gabriel J (2019a) Anticipating Ulawun Volcano in New Britain, Papua New Guinea. Anthropol Forum 1–12. https://doi.org/10.1080/00664677.2019.1647831

Wood M, Foale S, Gabriel J (2019b) Anticipating Ulawun Volcano in New Britain, Papua New Guinea. Anthropol Forum 1–12. https://doi.org/10.1080/00664677.2019.1647831

Woodhead J, Hergt J, Sandiford M, Johnson W (2010) The big crunch: Physical and chemical expressions of arc/continent collision in the Western Bismarck arc. J Volcanol Geotherm Res 190:11–24. https://doi.org/10.1016/j.jvolgeores.2009.03.003

Woodhouse MJ, Hogg AJ, Phillips JC, Sparks RSJ (2013) Interaction between volcanic plumes and wind during the 2010 Eyjafjallajökull eruption, Iceland. J Geophys Res Solid Earth 118:92–109. https://doi.org/10.1029/2012JB009592

Wooster M, Kaneko T (1998) Satellite thermal analyses of lava dome effusion rates at Unzen Volcano, Japan. J Geophys Res Solid Earth 103:20935–20947

Wooster MJ, Kaneko T, Nakada S, Shimizu H (2000) Discrimination of lava dome activity styles using satellite-derived thermal structures. J Volcanol Geotherm Res 102:97–118. https://doi.org/10.1016/S0377-0273(00)00183-9

Wooster MJ, Zhukov B, Oertel D (2003) Fire radiative energy for quantitative study of biomass burning: derivation from the BIRD experimental satellite and comparison to MODIS fire products. Remote Sens Environ 86:83–107. https://doi.org/10.1016/S0034-4257(03)00070-1

Wright R (2016a) MODVOLC: 14 years of autonomous observations of effusive volcanism from space. Geol Soc Lond Spec Publ 426:23–53. https://doi.org/10.1144/SP426.12

Wright R (2016b) MODVOLC: 14 years of autonomous observations of effusive volcanism from space. Geol Soc Lond Spec Publ 426:23–53. https://doi.org/10.1144/SP426.12

Wright R, Blackett M, Hill-Butler C (2015) Some observations regarding the thermal flux from Earth's erupting volcanoes for the period of 2000 to 2014. Geophys Res Lett 42:282–289. https://doi.org/10.1002/2014GL061997

Wright R, Blake S, Harris AJL, Rothery DA (2001) A simple explanation for the space-based calculation of lava eruption rates. Earth Planet Sci Lett 192:223–233. https://doi.org/10.1016/S0012-821X(01)00443-5

Wright R, Flynn L, Garbeil H, et al (2002) Automated volcanic eruption detection using MODIS. Remote Sens Environ 82:135–155. https://doi.org/10.1016/S0034-4257(02)00030-5

Wright R, Flynn LP, Garbeil H, et al (2004) MODVOLC: near-real-time thermal monitoring of global volcanism. J Volcanol Geotherm Res 135:29–49. https://doi.org/10.1016/j.jvolgeores.2003.12.008

Yokoo A, Tameguri T, Iguchi M (2009) Swelling of a lava plug associated with a Vulcanian eruption at Sakurajima Volcano, Japan, as revealed by infrasound record: case study of the eruption on January 2, 2007. Bull Volcanol 71:619–630. https://doi.org/10.1007/s00445-008-0247-5

Yokoyama I (2015) Eruption patterns of parasitic volcanoes. Ann Geophys 58:4. https://doi.org/10.4401/ag-6557

Yokoyama I (2020) Clusters of small monogenetic cones: a particular type of confined volcanism. Ann Geophys 62:1. https://doi.org/10.4401/ag-8176

Yoon DK (2012) Assessment of social vulnerability to natural disasters: a comparative study. Nat Hazards 63:823–843. https://doi.org/10.1007/s11069-012-0189-2

Young S, Voight B, Duffell H (2003) Magma extrusion dynamics revealed by high-frequency gas monitoring at Soufriere Hills Volcano, Montserrat. Geol Soc Lond Spec Publ 213:219–230

Young SR, Sparks RSJ, Aspinall WP, et al (1998) Overview of the eruption of Soufriere Hills Volcano, Montserrat, 18 July 1995 to December 1997. Geophys Res Lett 25:3389–3392. https://doi.org/10.1029/98GL01405

Yun S-H, Chang C, Ewert JW (2018) The History of Volcanic Hazard Map. J Petrol Soc Korea 27:49–66. https://doi.org/10.7854/JPSK.2018.27.1.49

Zakšek K, Shirzaei M, Hort M (2013) Constraining the uncertainties of volcano thermal anomaly monitoring using a Kalman filter technique. Geol Soc Lond Spec Publ 380:137–160. https://doi.org/10.1144/SP380.5

Zuccarello F, Bilotta G, Cappello A, Ganci G (2022) Effusion Rates on Mt. Etna and Their Influence on Lava Flow Hazard Assessment. Remote Sens 14:1366. https://doi.org/10.3390/rs14061366

7 Appendices

Appendix A - Dual-Band Analysis Convergence Testing

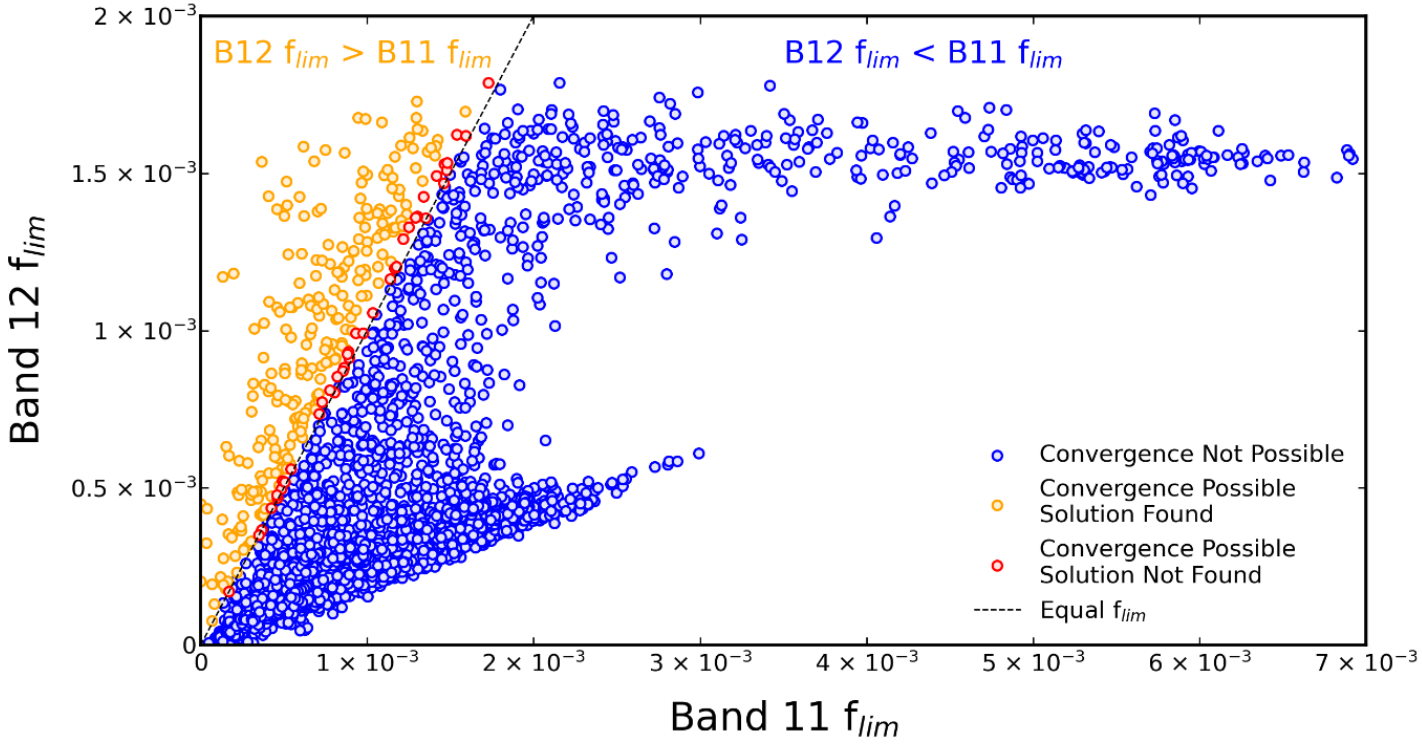

Figure 7.1 The parameter f_{lim} represents the theoretical maximum proportion occupied by the hot portion of a lava covered pixel. When the f_{lim} of Band 12 (2.19 µm) is greater than that of Band 11 (1.61 µm) (orange) a solution to the dual-band simultaneous equations can theoretically found i.e. the two equations can converge (Flynn et.al,1004). It is however possible that where a solution is theoretically possible, a real solution cannot be found (red). Of a total 7710 cloud-free pixels between 17 November 2015 and 31 December 2021 there are 283 theoretically solvable pixels. Of these 243 (86%) actual found a solution (orange).

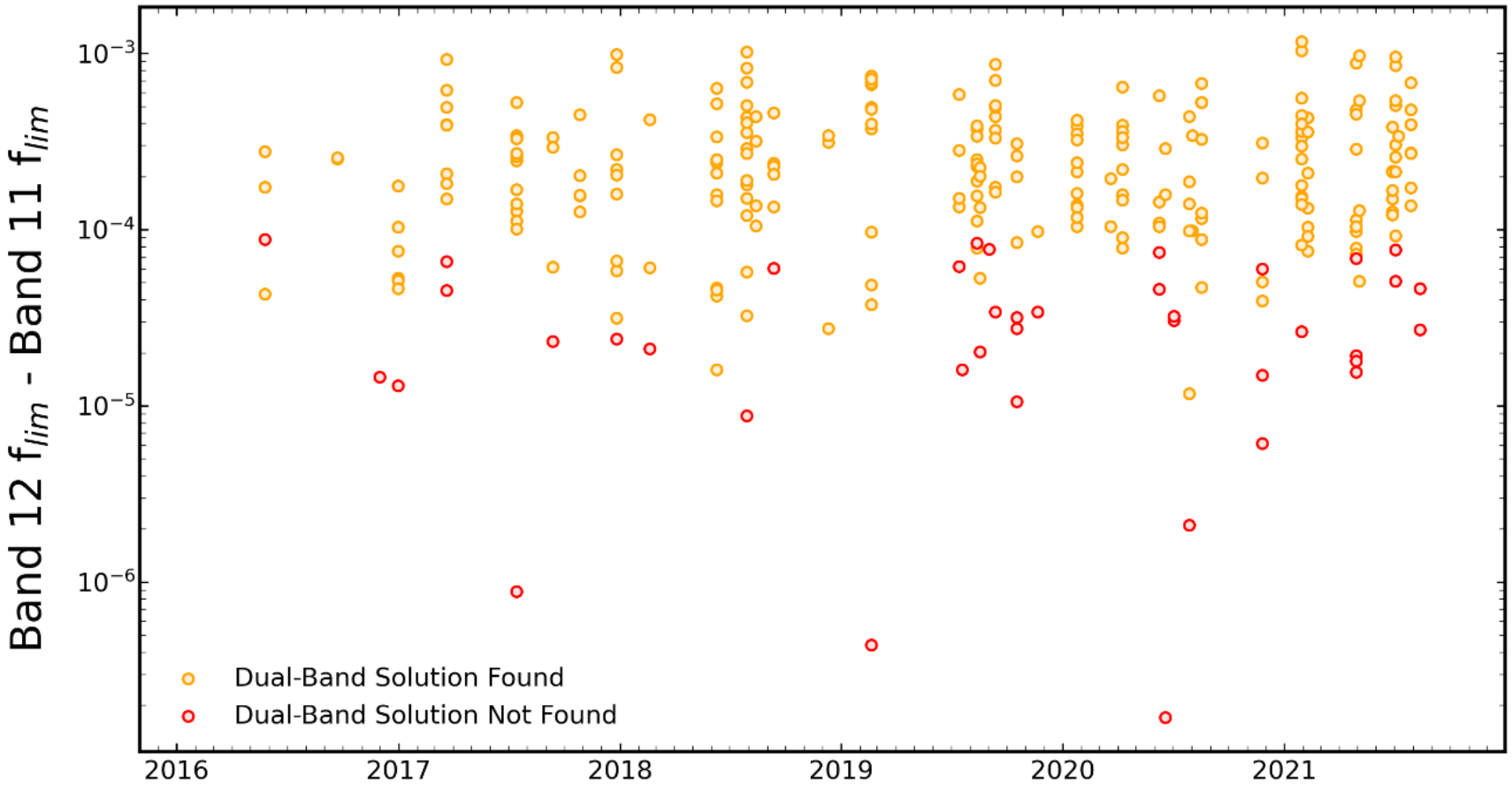

Figure 7.2 Time series of showing the difference between Band 12 and 1 f_{lim} values for all pixels where a solution to the dual-band simultaneous equations is theoretically possible. Instances where a solution was not found all occur at differences less than 10^{-4}. However, solutions are also found between 10^{-5}-10^{-4}.

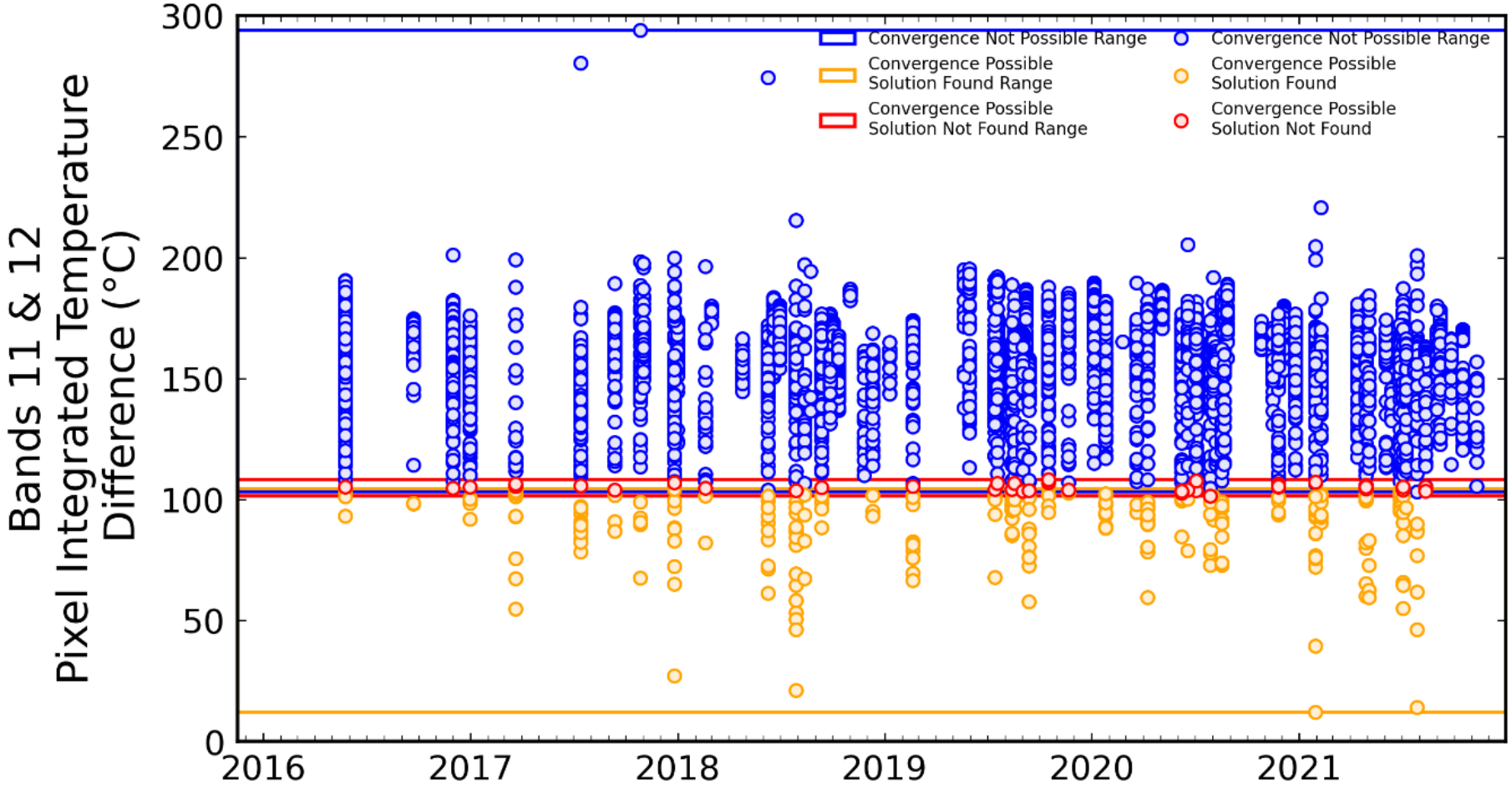

Figure 7.3 Time series showing the difference between the pixel integrated pixels of band 11 and 12. Pixels where a dual-band solution is not possible have a pixel integrated temperature differences range of 109-293°C and where theoretical solutions are possible have a range of 12-104°C. A narrow range of pixel integrated temperatures differences of 101-108°C exists where solutions are theoretically possible but could not be found.

Appendix B - Observed Plume Heights

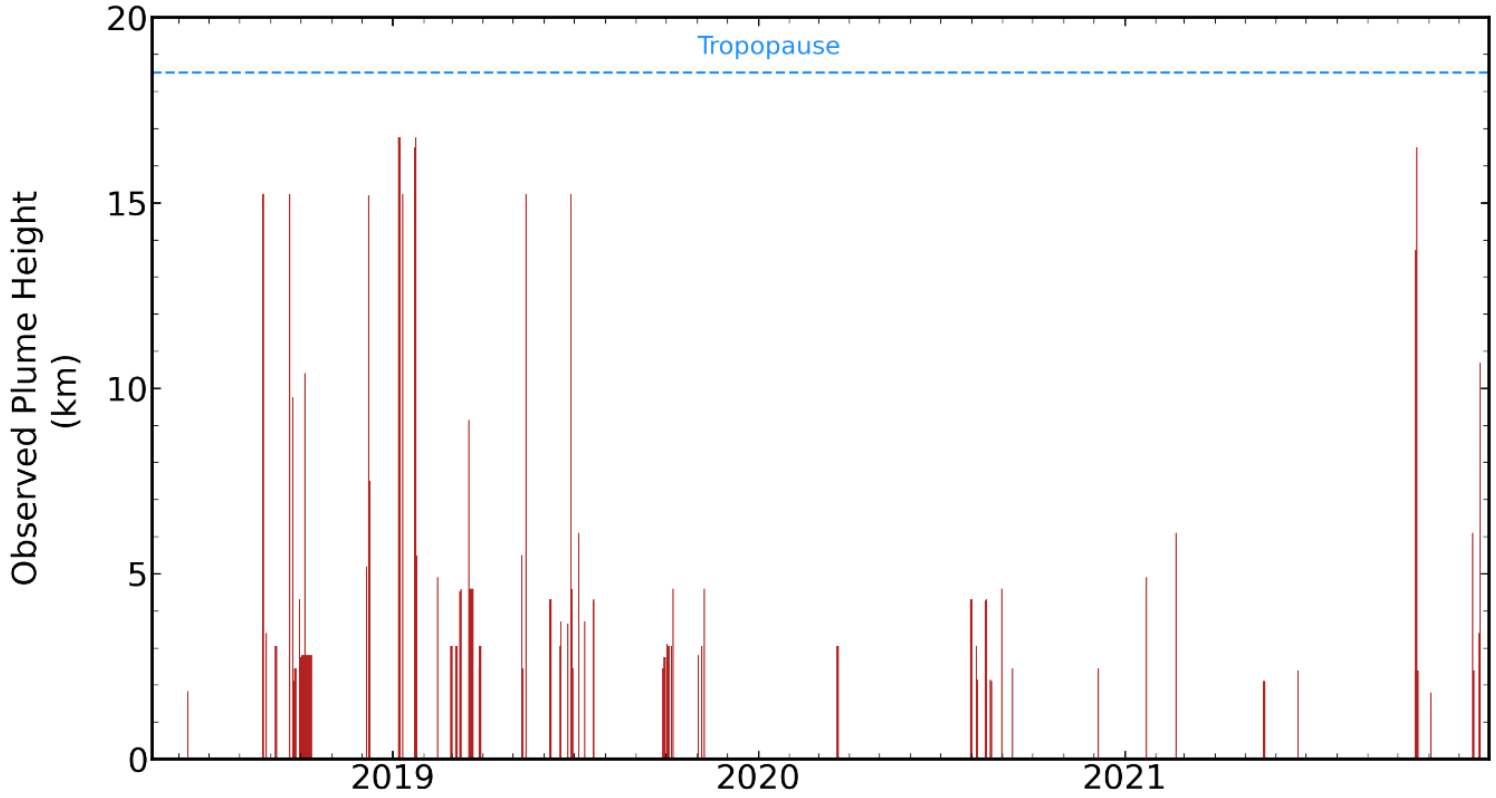

Figure 7.4 Time series of observed ash plume heights by Rabaul Volcanological Observatory (Global Volcanism Program 2024) and Darwin Volcanic Ash Advisory Centre (Darwin Volcanic Ash Advisory Centre 2021). Mean tropopause height as per Feng et al. (2012).

Appendix C - Manam Thermal Anomaly Detections 2002-2021

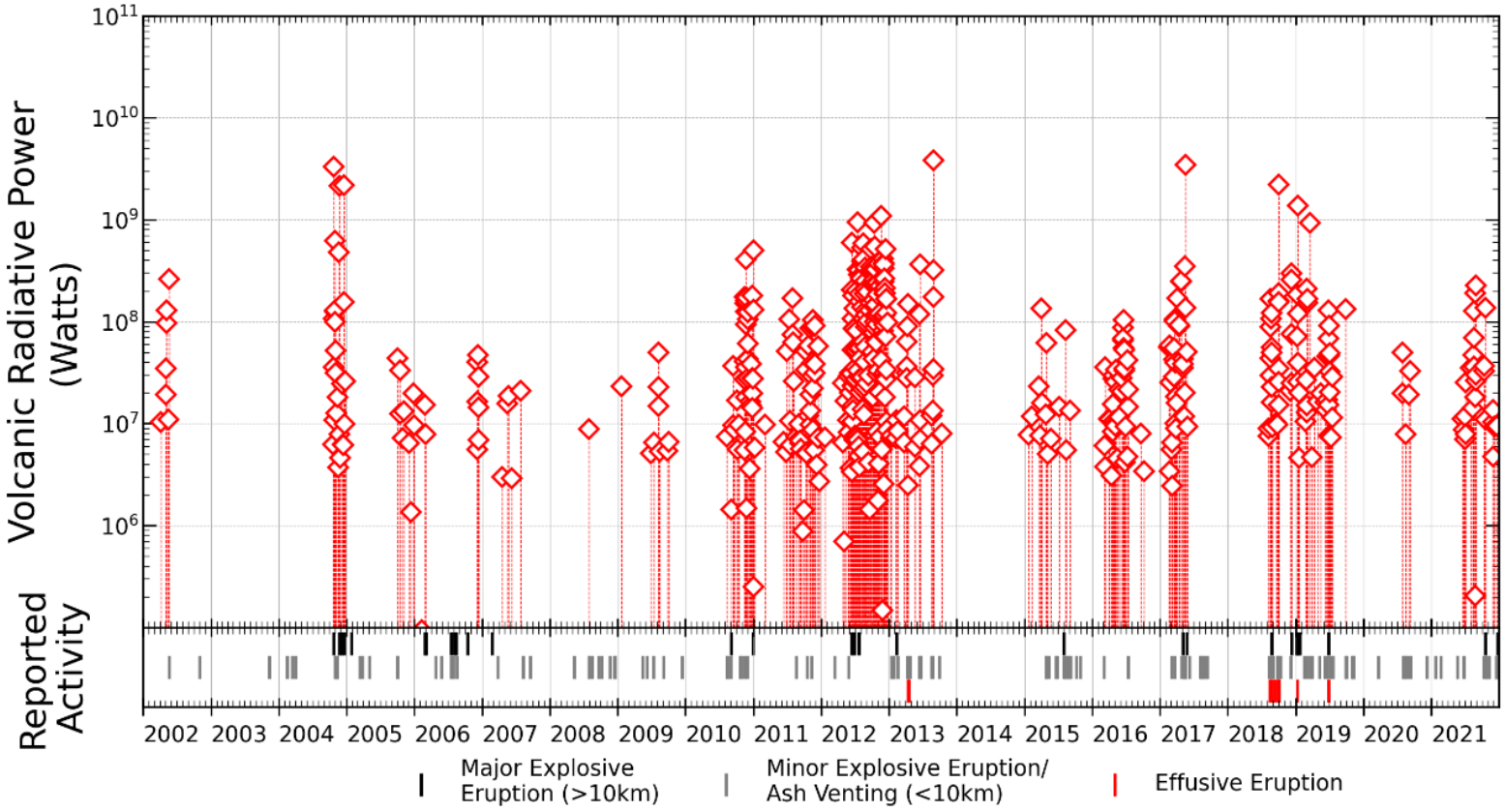

Figure 7.5 Time series of Manam thermal anomaly detections by MODVOLC alongside reported activity (Global Volcanism Program 2024).

Appendix D - Compilation of Effusion Rates of Mafic Lava Flows

Volcano	Eruption	Vent Type	Effusion Rate ($m^3 s^{-1}$)	Source
Villarrica (Chile)	1971	Flank	800	(Castruccio and Contreras 2016)
Etna (Italy)	29/04/1908	Flank	33	(Andronico and Lodato 2005)
Etna (Italy)	23/03/1910	Flank	28	(Andronico and Lodato, 2005)
Etna (Italy)	10/09/1911	Flank	50.8	(Andronico and Lodato, 2005)
Etna (Italy)	30/11/1918	Flank	7	(Andronico and Lodato, 2005)

Etna (Italy)	17/06/1923	Flank	29	(Andronico and Lodato, 2005)
Etna (Italy)	02/11/1928	Flank	27.3	(Andronico and Lodato, 2005)
Etna (Italy)	04/11/1928	Fissure	374.4	(Zuccarello et al. 2022)
Etna (Italy)	30/06/1942	Flank	37.6	(Andronico and Lodato, 2005)
Etna (Italy)	24/02/1947	Flank	9.2	(Andronico and Lodato, 2005)
Etna (Italy)	02/12/1949	Flank	39.3	(Andronico and Lodato, 2005)
Etna (Italy)	25/11/1950	Flank	4.7	(Andronico and Lodato, 2005)
Etna (Italy)	18/07/1955	Summit	3.6	(Andronico and Lodato, 2005)

Etna (Italy)	28/02/1956	Summit	9.9	(Andronico and Lodato, 2005)
Etna (Italy)	01/03/1956	Flank	6.2	(Andronico and Lodato, 2005)
Etna (Italy)	02/04/1956	Summit	3.4	(Andronico and Lodato, 2005)
Etna (Italy)	16/04/1957	Summit	0.9	(Andronico and Lodato, 2005)
Etna (Italy)	01/02/1964	Summit	0.4	(Andronico and Lodato, 2005)
Etna (Italy)	13/01/1966	Summit	0.1	(Andronico and Lodato, 2005)
Etna (Italy)	07/01/1968	Flank	0.04	(Andronico and Lodato, 2005)
Etna (Italy)	08/05/1968	Summit	0.07	(Andronico and Lodato, 2005)

Etna (Italy)	05/04/1971	Flank	13	(Andronico and Lodato, 2005)
Etna (Italy)	30/01/1974	Satellite Cone	3	(Andronico and Lodato, 2005)
Etna (Italy)	11/03/1974	Satellite Cone	1	(Andronico and Lodato, 2005)
Etna (Italy)	10/10/1974	Summit	0.9	(Andronico and Lodato, 2005)
Etna (Italy)	24/02/1975	Flank	0.7	(Andronico and Lodato, 2005)
Etna (Italy)	12/09/1975	Summit	0.9	(Andronico and Lodato, 2005)
Etna (Italy)	29/11/1975	Flank	0.8	(Andronico and Lodato, 2005)
Etna (Italy)	16/07/1977	Summit	0.3	(Andronico and Lodato, 2005)

Etna (Italy)	29/04/1978	Flank	8.6	(Andronico and Lodato, 2005)
Etna (Italy)	25/08/1978	Flank	7.7	(Andronico and Lodato, 2005)
Etna (Italy)	23/11/1978	Flank	10.6	(Andronico and Lodato, 2005)
Etna (Italy)	03/08/1979	Flank	14.5	(Andronico and Lodato, 2005)
Etna (Italy)	01/09/1980	Summit	0.5	(Andronico and Lodato, 2005)
Etna (Italy)	05/02/1981	Summit	0.9	(Andronico and Lodato, 2005)
Etna (Italy)	17/03/1981	Flank	641.4	(Zuccarello et al., 2022)
Etna (Italy)	17/03/1981	Flank	64	(Andronico and Lodato, 2005)

Etna (Italy)	28/03/1983	Flank	8.8	(Andronico and Lodato, 2005)
Etna (Italy)	27/04/1983	Flank	50	(Zuccarello et al., 2022)
Etna (Italy)	28/04/1984	Summit	0.7	(Andronico and Lodato, 2005)
Etna (Italy)	10/03/1985	Flank	2.8	(Andronico and Lodato, 2005)
Etna (Italy)	12/03/1985	Flank	3.2	(Zuccarello et al., 2022)
Etna (Italy)	25/12/1985	Summit	2.1	(Andronico and Lodato, 2005)
Etna (Italy)	13/09/1986	Summit	1	(Andronico and Lodato, 2005)
Etna (Italy)	30/10/1986	Flank	13	(Zuccarello et al., 2022)

Etna (Italy)	30/10/1986	Flank	5.7	(Andronico and Lodato, 2005)
Etna (Italy)	11/09/1989	Flank	15.9	(Andronico and Lodato, 2005)
Lonquimay (Chile)	1988-1990	Satellite Cone	80	(Castruccio and Contreras, 2016)
Etna (Italy)	04/01/1990	Summit	3.1	(Andronico and Lodato, 2005)
Etna (Italy)	14/12/1991	Flank	13.5	(Zuccarello et al., 2022)
Etna (Italy)	14/12/1991	Flank	6.1	(Andronico and Lodato, 2005)
Etna (Italy)	04/07/1996	Summit	0.2	(Andronico and Lodato, 2005)

Etna (Italy)	09/07/1997	Summit	1	(Andronico and Lodato, 2005)
Etna (Italy)	04/02/1999	Summit	1.4	(Andronico and Lodato, 2005)
Etna (Italy)	17/10/1999	Summit	4.3	(Andronico and Lodato, 2005)
Etna (Italy)	17/07/2001	Satellite Cone	34.3	(Zuccarello et al., 2022)
Etna (Italy)	27/10/2002	Flank	39.2	(Zuccarello et al., 2022)
Etna (Italy)	07/09/2004	Flank	21.5	(Zuccarello et al., 2022)
Etna (Italy)	13/05/2008	Flank	15.6	(Zuccarello et al., 2022)
Etna (Italy)	24/12/2018	Flank	80.2	(Zuccarello et al., 2022)

Fagradalsfjall (Iceland)	19/03/2021	Fissure	8	(Pedersen et al. 2022)
Fagradalsfjall (Iceland)	19/05/2021	Fissure	13	(Pedersen et al., 2022)

Table 7.1 Table of effusion rates from mafic lava flows used to determine effusion rate scenarios in Chapter 4. A summary of these flows is shown in Table 4.5.